Geometrical Modeling and Numerical Simulation of Heterogeneous Materials –

Applications to Arterial Walls and Two-Phase Steels

Von der Fakultät für Ingenieurwissenschaften,
Abteilung Bauwissenschaften
der Universität Duisburg-Essen
zur Erlangung des akademischen Grades

Doktor-Ingenieur

genehmigte Dissertation

von

Dipl.-Ing. Dominik Brands

Hauptberichter:	Prof. Dr.-Ing. habil. J. Schröder
Korreferenten:	Prof. Dr. rer. nat. habil. A. Klawonn
	Prof. Dr.-Ing. W.A. Wall

Tag der Einreichung:	25. Januar 2012
Tag der mündlichen Prüfung:	19. September 2012

Fakultät für Ingenieurwissenschaften,
Abteilung Bauwissenschaften
der Universität Duisburg-Essen
Institut für Mechanik
Prof. Dr.-Ing. habil. J. Schröder

Herausgeber:

Prof. Dr.-Ing. habil. J. Schröder

Organisation und Verwaltung:

Prof. Dr.-Ing. habil. J. Schröder
Institut für Mechanik
Fakultät für Ingenieurwissenschaften
Abteilung Bauwissenschaften
Universität Duisburg-Essen
Universitätsstraße 15
45141 Essen
Tel.: 0201 / 183 - 2682
Fax.: 0201 / 183 - 2680

Für Ela und Pia

Vorwort

Die vorliegende Arbeit entstand während meiner Tätigkeit als wissenschaftlicher Mitarbeiter am Institut für Mechanik (Abt. Bauwissenschaften, Fak. Ingenieurwissenschaften) an der Universität Duisburg-Essen im Rahmen der durch die Deutsche Forschungsgemeinschaft (DFG) finanzierten Projekte KL 2094/1-2, SCHR 570/7-2 und SCHR 570/8-1 (Forschergruppe FOR 797 ,,MICROPLAST"). An dieser Stelle möchte ich der DFG für die finanzielle Unterstützung danken und meinen persönlichen Dank an einige Menschen aussprechen, die ihren jeweiligen Anteil zum Gelingen dieser Arbeit beigetragen haben.

Beginnen möchte ich mit meinem sehr geschätzten Doktorvater Professor Jörg Schröder, der mir die Möglichkeit gab, unter seiner Leitung zu promovieren. Ihm gilt der besondere Dank für das entgegengebrachte Vertrauen und die Förderung während der gesamten Promotionszeit. Seine positive Art und Weise der Motivation während der gesamten Zeit waren für mich ein zusätzlicher Ansporn. Gleichzeitig zeigte es mir seine Anerkennung für und das Vertrauen in meine Arbeit, wofür ich im sehr dankbar bin. Mein besonderer Dank gilt auch Professor Axel Klawonn zum einen für die Übernahme des Zweitgutachtens als auch für die erfolgreiche Zusammenarbeit im DFG-Projekt ,,Massiv parallele Simulation von Arterienwänden". Bei vielen Diskussionen habe ich sein weitreichendes Wissen in der Mathematik zu schätzen gelernt. Weiterhin gilt mein Dank auch Professor Wolfgang A. Wall für sein Interesse an der Arbeit und die Übernahme des externen Gutachtens. Seine Veröffentlichungen und Vorträge gerade im Bereich der Biomechanik haben zur Erweiterung meines Wissenstandes auf diesem Gebiet in den letzten Jahren beigetragen.

Ich danke Professor Joachim Bluhm, der sich jederzeit sowohl für fachliche als auch persönliche Angelegenheiten Zeit nahm. Dabei ist er mir bis heute ein Vorbild. Ebenfalls möchte ich Daniel Balzani danken, auf dessen wissenschaftlichen Spuren ich den Weg zur Promotion gegangen bin. Während der gesamten Zusammenarbeit konnte ich auf seine volle Unterstützung zählen und von seinem Wissen provitieren. Oliver Rheinbach gilt mein Dank für die gemeinsame Zeit, die wir im Rahmen des DFG-Projekts mit der massiv parallelen Simulation von Arterienwänden verbracht haben. Dabei hat mich besonders seine Art beeindruckt, die höhere Mathematik auf einfachste Weise verständlich zu machen. Ebenfalls aufs herzlichste möchte ich meinen derzeitigen und ehemaligen Kolleginnen und Kollegen am Institut danken, zu denen Moritz Bloßfeld, Sarah Brinkhues, Vera Ebbing, Bernhard Eidel, Oliver Hilgert, Veronika Jorisch, Matthias Labusch, Marc-André Keip, Ingo Kurzhöfer, Petra Lindner-Roullé, Tim Ricken, Lisa Scheunemann, Thomas Schmidt, Alexander Schwarz, Serdar Serdaş, Steffen Specht, Karl Steeger, Huy Ngoc Thai, Daniel Werner und Robin Wojnowski gehören. Weiterhin gilt mein Dank meinen derzeitigen und ehemaligen studentischen Hilfskräften Marc Misera, Nico Paggen, Stephanie Pitts und Anna Tielke für Ihre hervoragende Unterstützung.

Meinen Eltern Marianne und Gerd Brands, meinen Schwiegereltern Karin und Peter Faßbender und meiner gesamten Familie möchte ich danken für die immerwährende Unterstützung und das Vertrauen. Gabi Khanna möchte ich danken für das mehrfache Korrekturlesen meiner Arbeit.

Abschließend danke ich meiner Frau Manuela und meiner Tochter Pia, die mir in jeder Phase meiner Promotion zur Seite standen. Sie brachten die notwendige Geduld und das Verständnis auf und stärkten mir so jederzeit den Rücken.

Dinslaken, im September 2012 Dominik Brands

Abstract

The discretization of the considered body or material by finite elements is a crucial part of the Finite Element Method in addition to the material modeling and the element formulation. Thereby, the treatment of heterogeneous materials is an advanced challenge, because the interfaces between the individual constituents must be taken into account in addition to the free surfaces. In many materials these interfaces exhibit complex geometries, since they are built up in growth and transformation processes. In the present work the numerical analysis of such materials is presented starting from the geometrical construction and ending up with the evaluation of the computational results. The first part is concerned with the simulation of diseased blood vessels and focusses on the reconstruction of patient-specific arterial geometries. The results of two- and three-dimensional finite element simulations show the field of application of the presented method. The consideration of the heterogeneity of modern two-phase steels in the numerical simulation is given in the following part of the present work. Therein the focus is on the application of geometrically simplified structures, which exhibit a similar mechanical response compared to the real microstructure. The applicability of the proposed method is shown in different boundary value problems using a direct micro-macro transition approach.

Zusammenfassung

Bei Simulationen unter Verwendung der Finite-Elemente-Methode spielt neben der Materialmodellierung und Elementformulierung die Diskretisierung des zu untersuchenden Körpers oder Materials durch finite Elemente eine große Rolle. Diese Aufgabe wird erschwert, wenn es sich um heterogene Materialien handelt. Bei diesen müssen zusätzlich zu den äußeren freien Oberflächen die inneren Grenzschichten zwischen den jeweiligen Individuen berücksichtigt werden. In vielen Materialien sind diese Grenzflächen durch Wachstums- oder Umwandlungsprozesse entstanden, können somit auch komplexe Strukturen aufweisen und erschweren die geometrische Beschreibung. Die vorliegende Arbeit beschäftigt sich im Wesentlichen mit der numerischen Analyse solcher Materialien ausgehend von der Konstruktion der Geometrien bis hin zur Auswertung der Simulationsergebnisse. Der erste Teil der Arbeit beschäftigt sich mit der Simulation von erkrankten Blutgefäßen und geht dort vor allem auf die Rekonstruktion von patienten-spezifischen Arteriengeometrien ein. Die Ergebnisse von zwei- und dreidimensionalen FE-Berechnung verdeutlichen das Einsatzgebiet der vorgestellten Methodik. Die Berücksichtigung der Heterogenität moderner Zweiphasenstähle in der numerischen Simulation wird im anschließenden Teil der Arbeit vorgestellt. Hierbei liegt der Schwerpunkt auf dem Einsatz von geometrisch vereinfachten Ersatzstrukturen, die ein vergleichbares mechanisches Antwortverhalten zur realen Mikrostruktur liefern. Die Anwendbarkeit dieser Methode wird in verschiedenen Randwertproblemen unter Einsatz eines direkten Mikro-Makro Übergangs gezeigt.

Contents

Glossary

Abbreviations

AHSS	advanced high strength steels
BVP, bvp	boundary value problem
CAD	computer-aided design
DP steels	dual-phase steels
FEM	Finite Element Method
FETI	Finite Element Tearing and Interconnecting
HSLA	high strength low alloy
IVUS	intravascular ultrasound
LP	lineal-path function
RVE	representative volume element
SD	spectral density
SSRVE	statistically similar respresentative volume element
VH IVUS	Virtual Histology

Operators

$[\dot{\bullet}] = \frac{\mathrm{d}}{\mathrm{d}t}[\bullet]$	material time derivative
$\partial_{(\bullet)}(\cdot) = \frac{\partial(\cdot)}{\partial(\bullet)}$	partial derivative
Cof	cofactor
det	determinat
dev	deviatoric operator
Div	divergence w.r.t. material coordinates $\boldsymbol{X}$
Grad	gradient w.r.t. material coordinates $\boldsymbol{X}$
grad	gradient w.r.t. spatial coordinates $\boldsymbol{x}$
Lin	linearization
tr	trace operator
Δ	linearization increment
δ	virtual operator
δ	Kronecker operator

Nomenclature

a	spatial surface
$\boldsymbol{a}$	accelaration field
$\boldsymbol{b}$	left Cauchy-Green deformation tensor (Finger deformation tensor)
$\boldsymbol{d}$	vector of nodal displacements
$\boldsymbol{e}$	Euler-Almansi strain tensor

$\boldsymbol{j}$	mapping from isoparametric space to current space
$\boldsymbol{l}$	spatial gradient of the velocity
n_{node}	number of nodes per finite element
n_{ele}	number of elements
$\boldsymbol{n}$	spatial surface normal
r, s	discrete image space
$r_x^{(i)}$, $r_y^{(i)}$, $r_{xy}^{(i)}$	relative mechanical errors at evaulation point i
$\widetilde{r}_x$, $\widetilde{r}_y$, $\widetilde{r}_{xy}$	average error of each virtual experiments
$\widetilde{r}_{\varnothing}$	overall error of mechanical validation
$\boldsymbol{r}^e$	element residual vector
t	time
$\boldsymbol{t}$	spatial traction force vector
$\boldsymbol{u}$	displacement field
v	spatial volume
$\boldsymbol{v}$	velocity field
$\boldsymbol{x}$	coordinates in actual (deformed) configuration
y_0	initial yield strength
A	material surface
$\boldsymbol{B}$	B-matrix
$\boldsymbol{C}$	right Cauchy-Green deformation tensor
$\boldsymbol{D}$	vector of global nodal displacements
$\boldsymbol{E}$	Green-Lagrange strain tensor
$\boldsymbol{F}$	material deformation gradient
G	weak form of equilibrium
J	determinat of the deformation gradient $\boldsymbol{F}$
$\boldsymbol{J}$	mapping from isoparametric space to reference space
$\boldsymbol{I}_1$,$\boldsymbol{I}_2$,$\boldsymbol{I}_3$	principial invariants of $\boldsymbol{C}$
$\boldsymbol{J}_1$,$\boldsymbol{J}_2$,$\boldsymbol{J}_3$	main invariants of $\boldsymbol{C}$
$\boldsymbol{J}_4$, $\boldsymbol{J}_5$	mixed invariants of $\boldsymbol{C}$ and $\boldsymbol{M}$
$\boldsymbol{K}$	global tangent stiffness matrix
$\boldsymbol{K}^e$	element tangent stiffness matrix
$\boldsymbol{L}$	global fluctuation matrix
$\boldsymbol{M}$	structural tensor
N	ansatz function
N_x, N_y	dimension of binary image
$\boldsymbol{N}$	material surface normal
$\boldsymbol{P}$	first Piola-Kirchhoff (or nominal) stress tensor
$\boldsymbol{R}$	global residual vector
$\boldsymbol{S}$	second Piola-Kirchhoff stress tensor

$\boldsymbol{T}$	reference traction force vector
$\boldsymbol{U}$	right (material) stretch tensor
V	material volume
$\boldsymbol{V}$	left (spatial) stretch tensor
$\boldsymbol{X}$	coordinates in reference configuration
$\boldsymbol{\gamma}$	vector of inclusion parametrization of SSRVEs
$\boldsymbol{\epsilon}$	permutation tensor
$\boldsymbol{\lambda}$	vector of Lagrange multipliers
$\boldsymbol{\xi}$	vector of natural coordinates ξ, η, ζ
ξ, η, ζ	natural coordinates
ρ_0, ρ	material and spatial density
σ_V	von Mises stress
$\boldsymbol{\sigma}$	Cauchy stress tensor
$\boldsymbol{\tau}$	Kirchhoff stress tensor
$\boldsymbol{\varphi}(\boldsymbol{X}, t)$	motion of point $\boldsymbol{X}$ at fixed time t
ψ_{c}	(Helmholtz) free energy w.r.t. current unit volume
ψ	(Helmholtz) free energy w.r.t. reference unit volume
ω_{V}, ω_{SD}, ω_{LP}	weighting factor of least-square functionals
Θ	dilatation of volume
$\mathcal{B}_0$, $\mathcal{B}_t$	reference and current configuration
$\mathcal{L}$	objective function
$\mathcal{L}_{\mathrm{V}}$, $\mathcal{L}_{\mathrm{SD}}$, $\mathcal{L}_{\mathrm{LP}}$	least-square functional of individual statistical measures
$\mathcal{P}_{\mathrm{V}}$	volume (or phase) fraction
$\mathcal{P}_{\mathrm{SD}}(r, s)$	value of spectral density at (r, s)
$\mathcal{P}_{\mathrm{LP}}(r, s)$	value of lineal-path function at (r, s)
$\mathbb{A}$	nominal tangent moduli
$\mathbb{C}$	tangent moduli
$\mathbb{R}^3$	three dimensional Euclidean space
$\mathbf{0}$	zero tensor
$\mathbf{1}$	identity tensor
$(\bullet)^h$	finite element approximation
$\overline{(\bullet)}$	macroscopic quantity (in case of two-scale homogenization)

1 Introduction and Motivation

Computer-aided methods developed in several fields of mechanics have got major importance in the analysis of structural components concerning manufactured as well as given by the natural ones. On the one hand the virtual testing using these numerical methods is an integral part of the development of new components and processes in many fields of engineering, e. g. vehicle construction, shipbuilding, plant manufacturing and civil engineering. On the other hand several fields use these methods for the understanding and analysis of the behavior of materials under different loads and the procedure of processes within these materials. To these fields belong the classical ones, e. g. chemistry, biology, medicine and material science, as well as the interdisciplinary ones, e. g. biomechanics, medical engineering, molecular biology and mechatronics. In common, the crucial task in all the above named disciplines is the construction of a simplified model, which represents the reality in a sufficient manner depending on the considered problem. The resulting mathematical formulation will deliver the solution to the problem by suitable algorithms during a numerical simulation. One common technology to build up a simplified or approximated model of a real problem is the Finite Element Method (FEM). Thereby, the considered body is discretized by finite elements and a continuum mechanical description of the material behavior results in a system of equations, which is solved by the application of different numerical solution schemes. But before these tasks can be done the geometrical structure of the considered body or the analyzed material must be provided. Especially in the case of heterogeneous materials the finite element discretization and the assignment of different material laws to these elements require a geometrical description of the body including material interfaces by mathematical relations, i. e. points, lines, areas and volumes. For that reason FEM programs – commercial or research usage – are mostly equipped by a preprocessing unit, which, among other things, enables the user to build a geometrical description of the problem or provide the import of models from computer-aided design (CAD) software. The fields of the application of the implemented tools therein are focused on the construction of geometrical object based on points, lines, areas and volumes, which can directly be described by mathematical relations, e.g. triangles, cubes or splines. Especially, structural components from "constructed" parts like, e. g. machines, bridges or trusses, can be modeled using these tools for the application in a FEM software. But many objects and structures, which are built up in growth and transformation processes, exhibit a complex heterogeneous structure and do not follow those "simple" geometries. Such kind of bodies can be found in nature, e. g. the human and animal body, plants and rocks, as well as in manufactured materials, e. g. steels, plastics and sponges. The treatment of such heterogeneous materials with non-artificial complex geometrical structures and geometries in the framework of the Finite Element Method is the main topic of this thesis.

Chapter 2 starts with the introduction to the general framework of the continuum mechanics as far as necessary in the course of this thesis. Thereby, the relations regarding the kinematics and stresses are recapitulated as well as the fundamental balance principles, since they are the basis for the Finite Element Method. Afterwards several construction principles regarding the modeling of specific material laws like objectivity and material symmetry are described. The chapter closes with a summary of several free energy functions enabling the description of isotropic and anisotropic material behavior.

Starting from a set of differential equation provided by the previous chapter the Finite

Element Method is presented based on a single-field variational formulation in *Chapter 3*. Afterwards we discuss a special finite element formulation – the $\bar{\boldsymbol{F}}$-approach – written in a 3-field formulation due to the volumetric locking arising from the incompressibility, because in the course of this thesis we deal with the simulation of incompressible materials. The treatment of complex geometrical structure often results in a system of equations with a large number of degrees of freedom. For a time-efficient solution of these boundary value problems parallel solution algorithms are a suitable method and therefore we give a brief introduction to the later on used method of Finite Element Tearing and Interconnecting - Dual Primal (FETI-DP).

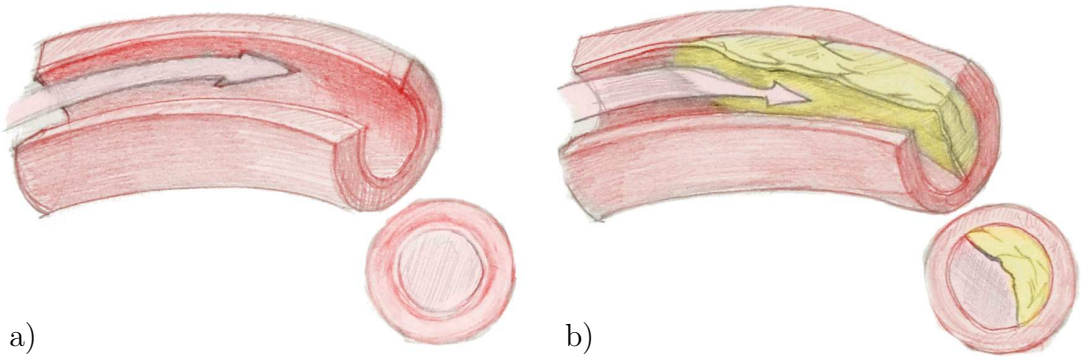

Figure 1.1: Artery a) in its healthy state and b) atherosclerotically diseased and narrowed by plaque deposits. (`www.gefaesschirurgie-klinik.de`)

Both the following chapters are concerned with the modeling and simulation of human arteries, whose walls can be identified as heterogeneous material due to their multi-layered structure and the composition of each layer. In the last years an increasing rate of deaths caused by cardiovascular diseases has been observed and, consequently, the intensity of research regarding the human vessel system has been augmented also in the biomechanical fields. The most widespread disease is the atherosclerosis, whereby the degeneration of the arterial wall causes the evolution of plaque. These deposits arise in the innermost arterial layer causing narrowings, which reduce the blood flow and mainly give rise to hypertension. An illustration of an atherosclerotically degenerated artery is shown in Figure 1.1b and compared to its healthy counterpart (Figure 1.1a). In the healthy state an artery already represents an advanced geometrical object, because it follows a three-dimensional path through the human body, changes its diameter along this path and has a multi-layered wall. But the geometry becomes more complicated when considering a diseased arterial segment, cf. Figure 1.1. Consequently, the reconstruction of such a degenerated artery is a non-trivial task and an essential one for the reliability of the simulation. The development of the reconstruction of a patient-specific arterial geometry is the first main topic in this thesis. Thus, the composition of the arterial wall and its diseases including possible treatments is discussed in *Chapter 4*. Afterwards several medical imaging techniques, which enable "the look into the body", are briefly reviewed. The focus remains on the intravascular ultrasound enhanced by Virtual Histology (VH IVUS), because it allows a deeper analysis of the cross-sectional arterial histology. We use the method in this thesis for the later shown reconstruction of a patient-specific arterial geometry. Since we want to use the resulting geometry in a finite element simulation we close the chapter with the constitutive modeling of the mechanical behavior and the adjustment of the material parameter to experimental data. Based on data resulting from VH IVUS the

reconstruction of a patient-specific arterial geometry is described in *Chapter 5*. The whole reconstruction process was implemented in a self-written MATLAB-code including several tasks of filtering, de-noising and segmentation. Finally, the data are imported to the commercial preprocessing software GAMBIT, wherein the discretization by finite elements is performed. The resulting 2D and 3D discretization of the arterial geometries are applied in finite element simulations. For the three dimensional computations a parallel FETI-DP solution algorithm is used due to the large number of degrees of freedom arising from the finite element discretization. The numerical results are analyzed and discussed as well as the limitations due to the considered approximations.

a)  b) 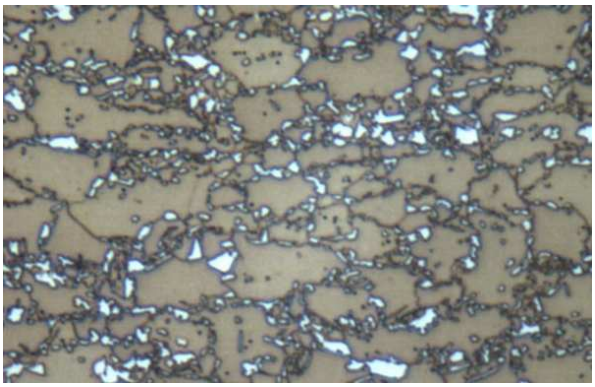

Figure 1.2: a) Wheel web in hot rolled Dual Phase 600 (Patented VersaStyle wheel from Hayes Lemmerz International) and b) the micrograph of a Dual Phase 600 steel. (`www.arcelormittal.com`)

A further group of materials with heterogeneous structures showing complex geometrical compositions are modern advanced high strength steels (AHSS). The simulation of such steels using the Finite Element Method is presented in both the following chapters. These steels are characterized by higher strength and enhanced formability in combination with better energy absorbance compared to other typical types of steels. The multiphase composition at the microscopic level, also called micro-heterogeneity, enables these features in contrast to traditional carbon steels and the high strength low alloy (HSLA) steels. Consequently, in this thesis we focus on the simulation of micro-heterogeneous steels consisting of two phases at the microscopic level. Typical two-phase AHSS are dual-phase steels, which are often used for the manufacturing of automotive parts, see Figure 1.2a. They contain a matrix-inclusion structure based on a ferritic matrix with embedded martensitic inclusions at the microscopic level, cf. Figure 1.2b. This composition mainly influences the mechanical behavior of these steels in contrast to the HSLA steels, whose mechanical properties are influenced by the alloying elements. For the introduction to the main properties of a two-phase steel we exemplarily discuss these aspects for dual-phase steels in *Chapter 6*. Afterwards we outline a constitutive model, the finite J_2-Plasticity model, for the description of the mechanical behavior of each individual phase in a two-phase steel. Since the micro-heterogeneity of the dual-phase steels is the main influencing factor regarding the mechanical properties, the microstructural morphology must be incorporated in the numerical simulation. Additionally, the inhomogeneous stress and strain fields due to the different mechanical properties of the individual phases are the driving force for several damage mechanisms. Finally, they result in macroscopic failures, and also require a consideration of the microstructure during the simulation. In most cases the difference in the length scale between the microstructural multi-phase composition (micrometer)

and the macroscopic dimensions of structural elements (centimeter to meter) is too large. Consequently, a macroscopic discretization of the body at the microstructural resolution level ends up with a highly non-efficient numerical problem or fails due to limits of memory. For this case the method of direct micro-macro homogenization, also referred to as the FE^2-method, enables the numerical treatment of such materials, which is described in *Chapter 7*. Thereby, a representative section of the microstructure is considered at each macroscopic evaluation point, the integration points of the gauss quadrature within a typical finite element. The transition between microscale and macroscale is done by suitable volume averaging over these representative volume elements (RVE). The definition of the size of the RVEs is a crucial part since it influences the reliability of the numerical results as well as the computational efficiency of the simulation. But often a RVE, which is suitable with respect to size, is too complex regarding the geometry and, consequently, has too many degrees of freedom in the finite element discretization, if it is used in a FE^2-framework. On this account in the course of *Chapter 7* a method is presented to construct analogous models for complex two-phase microstructures based on the similarity of statistical measures. These statistically similar representative volume elements (SSRVEs) are supposed to show the same mechanical response as the real microstructure. This statement is verified in several numerical simulations considering macroscopic homogeneous and inhomogeneous boundary value problems. Due to the less complexity of these SSRVEs the number of degrees of freedom in the finite element discretization is reduced and, consequently, the computational cost is decreased in the FE^2-simulation, which is the main advantage of the presented method. The chapter is closed with a discussion concerning the extension of the SSRVE method to three dimensional morphologies and the investigation of the real three dimensional microstructures

Chapter 8 provides a summary of this thesis and gives an outlook for further research.

2 Fundamentals of Continuum Mechanics

The consideration of physical bodies, i.e. solids and fluids, as continuous material is the fundamental character of the method of continuum mechanics. Thereby, the main subjects of continuum mechanics are the description of motion and deformation (kinematics), the concept of stress and the balance principles. These aspects are introduced to the extent necessary in this chapter. Afterwards we present some material models in the form of free energy functions in the context of polyconvexity. Since the continuum mechanics is a larger field in research we give only a short list of references, which is not intended to be exhaustive. Further discussions concerning the continuum mechanics are given by the classic literature Truesdell and Noll [229], Eringen [67] and Ogden [167]. The publications Ciarlet [47], Šilhavý [232] and Stein and Barthold [220] put themselves forward for studies on the theory of elasticity. In addition the textbooks Holzapfel [106] and de Boer and Schröder [56] also give an introduction and include applications in the field of non-linear solid mechanics. For the topic of polyconvexity the reader is referred to the literature given in the associated section 2.6.

2.1 Kinematics

A fundamental assumption in the continuum theory is the definition of the physical body. Therein a physical body, denoted by $\mathcal{B}$ and its surface $\partial\mathcal{B}$, consists of a continuous set of material points $P \in \mathcal{B}$ in a three-dimensional *Euclidean space* $\mathbb{R}^3$. Since we are interested in the descriptions of deformations we introduce two configurations of the continuum body.

The *reference configuration* $\mathcal{B}_0 \in \mathbb{R}^3$ – also called material or Lagrangian configuration – is defined by the position vector $\boldsymbol{X}$ of the material points P at time $t = t_0$, i.e.

$$\boldsymbol{X} = X^J \boldsymbol{E}_J \,, \quad J = 1, 2, 3 \,, \tag{2.1}$$

in terms of the right-handed orthonormal (cartesian) basis $\{\boldsymbol{E}\}_J$ with $J = 1, 2, 3$. The basis of a cartesian system has to fulfill the condition

$$\boldsymbol{E}_I \cdot \boldsymbol{E}_J = \delta_{IJ} \quad \text{and} \quad \boldsymbol{E}_I \times \boldsymbol{E}_J = \epsilon_{IJK} \boldsymbol{E}_K \,. \tag{2.2}$$

At this we use the Kronecker operator δ_{IJ} and the coefficient matrix ϵ_{IJK} of the third-order permutation tensor $\boldsymbol{\epsilon}$, which are defined by

$$\delta_{IJ} = \begin{cases} 0, & \text{if } I \neq J \,, \\ 1, & \text{if } I = J \,, \end{cases} \quad \text{and} \quad \epsilon_{IJK} = \epsilon^{IJK} = \begin{cases} 0, & \text{if two indices are equal,} \\ 1, & \text{for } \epsilon_{123},\, \epsilon_{231},\, \epsilon_{312} \,, \\ -1, & \text{for } \epsilon_{213},\, \epsilon_{132},\, \epsilon_{321} \,. \end{cases} \tag{2.3}$$

The *actual configuration* $\mathcal{B}_t \in \mathbb{R}^3$ – also called spatial or Eulerian configuration – is defined by the position vector $\boldsymbol{x}$ of the material points $P \in \mathcal{B}_t$ at time t, i.e.

$$\boldsymbol{x} = x^j \boldsymbol{e}_j \,, \quad j = 1, 2, 3 \,, \tag{2.4}$$

where $\{e\}_j$ with $j = 1, 2, 3$ is the cartesian basis of the actual configuration.

For the description of the motion of the body $\mathcal{B}$ we introduce the vector field $\boldsymbol{\varphi}$ as the one-to-one mapping of the material points P of $\mathcal{B}_0$ into $\mathcal{B}_t$

$$\boldsymbol{\varphi} \; : \; \mathcal{B}_0 \mapsto \mathcal{B}_t \; . \tag{2.5}$$

At fixed time $t \in \mathbb{R}_+$ the points $\boldsymbol{X} \in \mathcal{B}_0$ of the reference configuration are mapped by the transformation $\boldsymbol{\varphi}$ onto points $\boldsymbol{x} \in \mathcal{B}_t$ of the actual configuration, i.e.

$$\boldsymbol{\varphi}(\boldsymbol{X}, t) : \boldsymbol{X} \mapsto \boldsymbol{x} = \boldsymbol{\varphi}(\boldsymbol{X}, t) \; , \quad \text{with} \quad x^j = x^j(X^1, X^2, X^3, t) \; . \tag{2.6}$$

The motion of the body is assumed to be reversible and so the inverse motion can be written as

$$\boldsymbol{\varphi}^{-1}(\boldsymbol{x}, t) : \boldsymbol{x} \mapsto \boldsymbol{X} = \boldsymbol{\varphi}^{-1}(\boldsymbol{x}, t) \; , \quad \text{with} \quad X^J = X^J(x^1, x^2, x^3, t) \; . \tag{2.7}$$

This condition holds if the vector field $\boldsymbol{\varphi}$ is single-valued and at least once continuously differentiable with respect to its arguments.

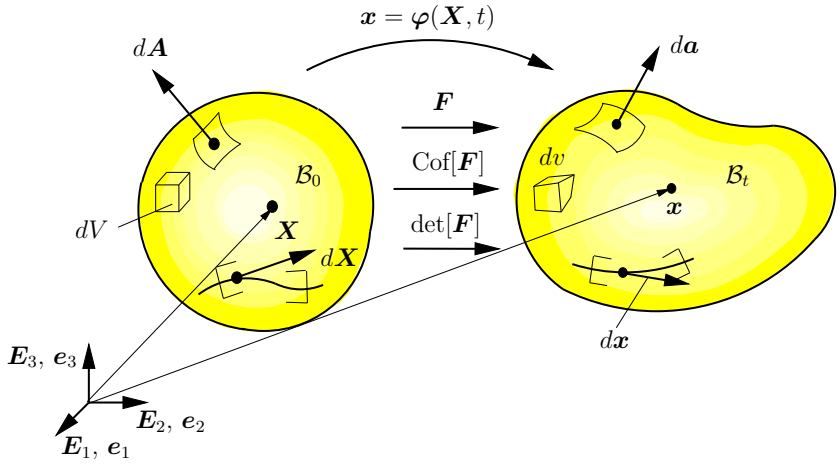

Figure 2.1: Transport theorems: Mapping of infinitesimal geometrical elements from reference configuration to actual configuration

A crucial kinematic quantity in nonlinear continuum mechanics is the *deformation gradient* $\boldsymbol{F}$. This primary measure of deformation is the partial derivative of the deformation mapping $\boldsymbol{x} = \boldsymbol{\varphi}(\boldsymbol{X}, t)$ with respect to the material coordinates $\boldsymbol{X}$, i.e.

$$\boldsymbol{F} = \boldsymbol{F}(\boldsymbol{X}, t) := \operatorname{Grad} \boldsymbol{x} = \frac{\partial \boldsymbol{x}}{\partial \boldsymbol{X}} = F^i{}_J \; \boldsymbol{e}_i \otimes \boldsymbol{E}^J \quad \text{with} \quad F^i{}_j = \frac{\partial x^i}{\partial X^J} = x^i{}_{,J} \; . \tag{2.8}$$

From Equation (2.8) the deformation gradient can be identified as a two-point tensor involving points in two distinct configurations, since the first base vector operates in the actual configuration and the second one in the reference configuration. For the description of the reverse transformation the inverse of the deformation gradient

$$\boldsymbol{F}^{-1}(\boldsymbol{X}, t) = \operatorname{grad} \boldsymbol{X} = \frac{\partial \boldsymbol{X}}{\partial \boldsymbol{x}} = F^{-1\,J}{}_i \; \boldsymbol{E}_J \otimes \boldsymbol{e}^i \quad \text{with} \quad F^{-1\,J}{}_i = \frac{\partial X^J}{\partial x^i} = X^J{}_{,i} \tag{2.9}$$

has to exist. Therefore, the mapping (2.8) must be one-to-one, which is tantamount to a non-singularity of $\boldsymbol{F}(\boldsymbol{X}, t)$. To ensure this condition the determinant of $\boldsymbol{F}(\boldsymbol{X}, t)$, the

Jacobian J, must not be equal zero, i.e. $J = \det \boldsymbol{F}(\boldsymbol{X}, t) \neq 0$. In anticipation of the physical meaning of the Jacobian, it describes the volume ratio between infinitesimal volume elements defined in the reference and actual configuration, cf. Equation (2.15), we will further restrict its scope. Having regarded the continuity of the mapping $\boldsymbol{\varphi}$ we enforce the constraint

$$J = \det \boldsymbol{F}(\boldsymbol{X}, t) > 0 \tag{2.10}$$

for all motions of the body $\mathcal{B}$. From the physical point of view a negative value of J means a penetration of the body by itself – an unphysical deformation.

An alternative representation of the deformation gradient $\boldsymbol{F}$ is achieved by introducing the displacement vector $\boldsymbol{u}(\boldsymbol{X}, t)$ as the difference vector of the position vector in the reference configuration and the actual configuration

$$\boldsymbol{u}(\boldsymbol{X}, t) = \boldsymbol{x} - \boldsymbol{X} = \boldsymbol{\varphi}(\boldsymbol{X}, t) - \boldsymbol{X} \ . \tag{2.11}$$

Considering the definition (2.8) we rewrite

$$\boldsymbol{F} = \operatorname{Grad}[\boldsymbol{X} + \boldsymbol{u}(\boldsymbol{X}, t)] = \mathbf{1} + \operatorname{Grad} \boldsymbol{u} \ , \tag{2.12}$$

where $\mathbf{1}$ denotes the second order identity tensor.

In Figure 2.1 the graphical representation of the *transport theorems* is shown, which are the three fundamental geometric mappings based on the deformation gradient:

(i) Mapping of infinitesimal line elements: $\mathrm{d}\boldsymbol{X} \ \mapsto \ \mathrm{d}\boldsymbol{x}$
The relation between an infinitesimal material line element $\mathrm{d}\boldsymbol{X}$ and an infinitesimal spatial line element $\mathrm{d}\boldsymbol{x}$ is given by

$$\mathrm{d}\boldsymbol{x} = \boldsymbol{F} \, \mathrm{d}\boldsymbol{X} \ . \tag{2.13}$$

(ii) Mapping of infinitesimal area elements: $\mathrm{d}\boldsymbol{A} \ \mapsto \ \mathrm{d}\boldsymbol{a}$
Let $\mathrm{d}\boldsymbol{A} = \boldsymbol{N} \, \mathrm{d}A$ and $\mathrm{d}\boldsymbol{a} = \boldsymbol{n} \, \mathrm{d}a$ be infinitesimal area elements with their outward unit normal vectors $\boldsymbol{N}$ and $\boldsymbol{n}$ defined in the reference and the actual configuration, respectively. The relation between the area elements is calculated by

$$\mathrm{d}\boldsymbol{a} = J\boldsymbol{F}^{-T} \, \mathrm{d}\boldsymbol{A} = \operatorname{Cof}[\boldsymbol{F}] \, \mathrm{d}\boldsymbol{A} \tag{2.14}$$

using *Nanson's Formula* (1878) for the mapping of the normal vectors.

(iii) Mapping of infinitesimal volume elements: $\mathrm{d}\boldsymbol{V} \ \mapsto \ \mathrm{d}\boldsymbol{v}$
The infinitesimal material and spatial volume elements $\mathrm{d}V = \mathrm{d}\boldsymbol{X}_1 \cdot (\mathrm{d}\boldsymbol{X}_2 \times \mathrm{d}\boldsymbol{X}_3)$ and $\mathrm{d}v = \mathrm{d}\boldsymbol{x}_1 \cdot (\mathrm{d}\boldsymbol{x}_2 \times \mathrm{d}\boldsymbol{x}_3)$ are rewritten as the triple product of the corresponding infinitesimal line elements. Together with Equation (2.13) and $J = \det \left[\frac{\partial \boldsymbol{x}}{\partial \boldsymbol{X}}\right] = \frac{\partial \boldsymbol{x}}{\partial X_1} \cdot \left(\frac{\partial \boldsymbol{x}}{\partial X_2} \times \frac{\partial \boldsymbol{x}}{\partial X_3}\right)$ the mapping of the infinitesimal volume element reads

$$\mathrm{d}v = J \, \mathrm{d}V = \det[\boldsymbol{F}] \, \mathrm{d}V \ , \tag{2.15}$$

and from this the Jacobian J is considered as the volume ratio between an infinitesimal material volume element and a spatial one. The relation also provides a further (physical) explanation of the condition (2.10), because volume elements cannot have negative volumes.

Until now we describe the changes of material elements during motion in terms of the deformation gradient. Alternatively, these changes can also be expressed in the form of strain tensors related to either the reference or the actual configuration. First we separate the local deformation gradient $\boldsymbol{F}$ into a pure stretch tensor and a pure rotation tensor by using the *polar decomposition*

$$\boldsymbol{F} = \boldsymbol{R}\boldsymbol{U} = \boldsymbol{V}\boldsymbol{R}\,, \tag{2.16}$$

where the rotation tensor $\boldsymbol{R}$ is a proper orthogonal tensor (with $\boldsymbol{R}^{-1} = \boldsymbol{R}^T$). The *right (material) stretch tensor* $\boldsymbol{U}$ and the *left (spatial) stretch tensor* $\boldsymbol{V}$ are symmetric and defined with respect to the reference and the actual configuration, respectively. Multiplicative combinations of Equation (2.16) lead to the strain measures

$$\begin{aligned} \boldsymbol{C} &:= \boldsymbol{F}^T\boldsymbol{F} = (\boldsymbol{R}\boldsymbol{U})^T(\boldsymbol{R}\boldsymbol{U}) = \boldsymbol{U}^2 \qquad \text{with} \quad C_{AB} = F^a{}_A\, \delta_{ab}\, F^b{}_B\,, \\ \boldsymbol{b} &:= \boldsymbol{F}\boldsymbol{F}^T = (\boldsymbol{V}\boldsymbol{R})(\boldsymbol{V}\boldsymbol{R})^T = \boldsymbol{V}^2 \qquad \text{with} \quad b^{ab} = F^a{}_A\, \delta^{AB}\, F^b{}_B\,, \end{aligned} \tag{2.17}$$

where $\boldsymbol{C}$ is the *right Cauchy-Green tensor* and $\boldsymbol{b}$ the *left Cauchy-Green tensor* (*Finger deformation tensor*). Further important strain measures can be deduced from the half of the difference of the squares of infinitesimal material and spatial line elements, i.e. $\frac{1}{2}(d\boldsymbol{x}\cdot d\boldsymbol{x} - d\boldsymbol{X}\cdot d\boldsymbol{X})$. We achieve the definition of the *Green-Lagrange strain tensor* $\boldsymbol{E}$ and *Euler-Almansi strain tensor* $\boldsymbol{e}$

$$\begin{aligned} \boldsymbol{E} &:= \frac{1}{2}(\boldsymbol{C} - \boldsymbol{1}) \qquad \text{with} \quad E_{AB} = \frac{1}{2}(C_{AB} - \delta_{AB})\,, \\ \boldsymbol{e} &:= \frac{1}{2}(\boldsymbol{1} - \boldsymbol{b}^{-1}) \qquad \text{with} \quad e_{ab} = \frac{1}{2}(\delta_{ab} - \{b^{-1}\}_{ab})\,, \end{aligned} \tag{2.18}$$

under consideration of the mapping of an infinitesimal line element (2.13) and the corresponding inverse operation $\mathrm{d}\boldsymbol{X} = \boldsymbol{F}^{-1}\,\mathrm{d}\boldsymbol{x}$. Since $\boldsymbol{C}$, $\boldsymbol{E}$ and their inverse operate solely on vectors in the reference configuration, we call them material strain tensors. Analogously $\boldsymbol{b}$, $\boldsymbol{e}$ and their inverses are denoted as spatial strain tensors. The four introduced strain measures have in common, that they do not include any rigid body motion.

2.2 Time Derivatives

The derivatives of the kinematic quantities with respect to time have to be considered if we describe non-linear processes like deformation of material with history-dependent behavior, e.g. plasticity. The material time derivative $\frac{\mathrm{d}}{\mathrm{d}t}[\bullet] = \dot{[\bullet]}$ is the temporal change of the quantity $[\bullet]$ at an arbitrary fixed material point $\boldsymbol{X}$ with $\boldsymbol{X} = \text{constant}$. For material quantities $P(\boldsymbol{X}, t)$ – written in coordinates $\boldsymbol{X}$ of the reference configuration – the material time derivative reads

$$\frac{\mathrm{d}P(\boldsymbol{X}, t)}{\mathrm{d}t} = \dot{P}(\boldsymbol{X}, t) = \frac{\partial P}{\partial t}\,, \tag{2.19}$$

because of the independence of $\boldsymbol{X}$ on t. In the case of spatial quantities $p(\boldsymbol{x}, t)$ the describing coordinate $\boldsymbol{x}(\boldsymbol{X}, t)$ is time-dependent and so their material time derivative is calculated by

$$\dot{p} = \frac{\partial p}{\partial \boldsymbol{x}} \cdot \frac{\partial \boldsymbol{x}}{\partial t} + \frac{\partial p}{\partial t} = \operatorname{grad} p \cdot \dot{\boldsymbol{x}} + \frac{\partial p}{\partial t}\,, \tag{2.20}$$

where the first term can be identified as a convective part. The second term is the spatial time derivative of p and is denoted as a local part. Thus, the material velocity $\dot{\boldsymbol{x}}(\boldsymbol{X}, t)$

and the material acceleration $\ddot{\boldsymbol{x}}(\boldsymbol{X},t)$ are defined as the first and second material time derivative of the motion $\boldsymbol{x}=\boldsymbol{\varphi}(\boldsymbol{X},t)$, respectively, i.e.

$$\begin{aligned}\boldsymbol{v}&=\dot{\boldsymbol{x}}(\boldsymbol{X},t)=\frac{\partial\boldsymbol{\varphi}}{\partial t}\ ,\\ \boldsymbol{a}&=\ddot{\boldsymbol{x}}(\boldsymbol{X},t)=\frac{\partial\dot{\boldsymbol{x}}}{\partial t}=\frac{\partial^2\boldsymbol{\varphi}(\boldsymbol{X},t)}{\partial^2 t}\ .\end{aligned}\tag{2.21}$$

For the description of the velocity $\dot{\boldsymbol{x}}$ and acceleration $\dot{\boldsymbol{X}}$ in spatial coordinates we apply the inverse mapping (2.7) to the latter equations and obtain

$$\begin{aligned}\boldsymbol{v}&=\boldsymbol{v}(\boldsymbol{x},t)=\dot{\boldsymbol{x}}(\boldsymbol{\varphi}^{-1}(\boldsymbol{x},t),t)\ ,\\ \boldsymbol{a}&=\boldsymbol{a}(\boldsymbol{x},t)=\ddot{\boldsymbol{x}}(\boldsymbol{\varphi}^{-1}(\boldsymbol{x},t),t)=\frac{\partial\boldsymbol{v}}{\partial\boldsymbol{x}}\frac{\partial\boldsymbol{x}}{\partial t}+\frac{\partial\boldsymbol{v}}{\partial t}=\boldsymbol{l}\boldsymbol{v}+\frac{\partial\boldsymbol{v}}{\partial t}\ ,\end{aligned}\tag{2.22}$$

where $\boldsymbol{l}$ is the spatial gradient of the velocity $\boldsymbol{l}:=\operatorname{grad}\boldsymbol{v}$. This quantity can also be written in terms of the material time derivative of the deformation gradient $\dot{\boldsymbol{F}}=\frac{\partial\dot{\boldsymbol{x}}}{\partial\boldsymbol{X}}$

$$\boldsymbol{l}=\frac{\partial\boldsymbol{v}}{\partial\boldsymbol{x}}=\frac{\partial\dot{\boldsymbol{x}}}{\partial\boldsymbol{X}}\frac{\partial\boldsymbol{X}}{\partial\boldsymbol{x}}=\dot{\boldsymbol{F}}\boldsymbol{F}^{-1}\ .\tag{2.23}$$

The additive decomposition of the spatial velocity gradient into its symmetric part, the *stretching tensor* $\boldsymbol{d}$, and the skew-symmetric part, the *spin tensor* $\boldsymbol{w}$ leads to

$$\boldsymbol{l}=\boldsymbol{d}+\boldsymbol{w}\quad\text{with}\quad\boldsymbol{d}=\frac{1}{2}(\boldsymbol{l}+\boldsymbol{l}^T)\quad\text{and}\quad\boldsymbol{w}=\frac{1}{2}(\boldsymbol{l}-\boldsymbol{l}^T)\ .\tag{2.24}$$

Before we can calculate the material time derivative of infinitesimal geometric elements we calculate the material time derivative of the Jacobian

$$\dot{J}=\frac{\partial\det\boldsymbol{F}}{\partial t}=\frac{\partial\det\boldsymbol{F}}{\partial\boldsymbol{F}}:\frac{\partial\boldsymbol{F}}{\partial t}=\det[\boldsymbol{F}]\boldsymbol{F}^{-T}:\dot{\boldsymbol{F}}=\det[\boldsymbol{F}]\operatorname{tr}[\boldsymbol{l}]=J\operatorname{div}\boldsymbol{v}\ .\tag{2.25}$$

Now the transport theorems (2.13), (2.14) and (2.15) can be derived with respect to time

$$\begin{aligned}\mathrm{d}\dot{\boldsymbol{x}}&=\dot{\boldsymbol{F}}\,\mathrm{d}\boldsymbol{X}=\boldsymbol{l}\boldsymbol{F}\,\mathrm{d}\boldsymbol{X}=\boldsymbol{l}\,\mathrm{d}\boldsymbol{x}\\ \mathrm{d}\dot{\boldsymbol{a}}&=\dot{J}\boldsymbol{F}^{-T}\,\mathrm{d}\boldsymbol{A}+J\,\dot{\overline{\boldsymbol{F}^{-T}}}\,\mathrm{d}\boldsymbol{A}\\ &=J\operatorname{div}[\boldsymbol{v}]\boldsymbol{F}^{-T}\,\mathrm{d}\boldsymbol{A}-J\,\boldsymbol{l}^T\boldsymbol{F}^{-T}\,\mathrm{d}\boldsymbol{A}\\ &=(\operatorname{tr}[\boldsymbol{l}]\mathbf{1}-\boldsymbol{l}^T)\operatorname{Cof}[\boldsymbol{F}]\,\mathrm{d}\boldsymbol{A}=(\operatorname{tr}[\boldsymbol{l}]\mathbf{1}-\boldsymbol{l}^T)\,\mathrm{d}\boldsymbol{a}\\ \mathrm{d}\dot{v}&=\dot{J}\,\mathrm{d}V=J\operatorname{div}[\boldsymbol{v}]\,\mathrm{d}V=\operatorname{div}[\boldsymbol{v}]\,\mathrm{d}v\end{aligned}\tag{2.26}$$

2.3 Stress Concept and Power

In the previous section we discuss the description of motion and deformation of a continuum body. Both cause interactions between the material and neighboring material in the interior part of the body. In continuum mechanics the resulting internal loading state is regarded as stresses, which has physical dimension force per unit of area.

For the introduction of the concept of stresses we consider a deformable continuum body $\mathcal{B}$ in the actual configuration $\mathcal{B}_t$. A virtual cut by a plane surface at point $\boldsymbol{x}\in\mathcal{B}_t$ enables

a view onto the acting internal forces, see Figure 2.2. The traction vector $\boldsymbol{t}$ located at point $\boldsymbol{x}$ is defined by

$$\boldsymbol{t}(\boldsymbol{x},t) := \lim_{a\to 0} \frac{\Delta\overline{\boldsymbol{f}}}{\Delta a} = \frac{\mathrm{d}\overline{\boldsymbol{f}}}{\mathrm{d}a} \,, \tag{2.27}$$

where $\Delta\overline{\boldsymbol{f}}$ denotes the force acting on the area element $\mathrm{d}a$ in $\boldsymbol{x}$. The existence of a unique second-order tensor $\boldsymbol{\sigma}$, which transforms the outward unit normal $\boldsymbol{n}$ of the area element $\mathrm{d}a$ linearly into the traction vector

$$\boldsymbol{t}(\boldsymbol{x},t,\boldsymbol{n}) = \boldsymbol{\sigma}(\boldsymbol{x},t)\,\boldsymbol{n} \,, \tag{2.28}$$

which is refer to the *Cauchy theorem*. Therein the symmetric[1.)] *Cauchy stress* tensor $\boldsymbol{\sigma}$ relates the actual force to the actual area element and therefore denotes the *true stresses*. In addition to the real physical Cauchy stress the associated von Mises stress

$$\sigma_{\mathrm{V}} = \sqrt{\tfrac{3}{2}}\,||\mathrm{dev}\boldsymbol{\sigma}|| \quad \text{with} \quad \mathrm{dev}\,\boldsymbol{\sigma} := \boldsymbol{\sigma} - \tfrac{1}{3}\,\mathrm{tr}[\boldsymbol{\sigma}]\mathbf{1} \tag{2.29}$$

is an important stress quantity for mechanical analysis of complex boundary value problems. Based on Equation (2.27) we formulate the relation for the actual force in terms of the undeformed area element $\mathrm{d}A$, i.e.

$$\mathrm{d}\overline{\boldsymbol{f}} = \boldsymbol{t}\,\mathrm{d}a = \boldsymbol{T}\,\mathrm{d}A \quad \text{with} \quad \boldsymbol{T} = \boldsymbol{T}(\boldsymbol{X},t,\boldsymbol{N}) \,. \tag{2.30}$$

Then the application of the reformulated transport theorem $\boldsymbol{n}\,\mathrm{d}a = \mathrm{Cof}[\boldsymbol{F}]\boldsymbol{N}\,\mathrm{d}A$, obtained from Equation (2.14), and Cauchy's theorem (2.28) to the latter expression results in

$$\boldsymbol{\sigma}\,\mathrm{Cof}[\boldsymbol{F}]\,\boldsymbol{N}\,\mathrm{d}A = \boldsymbol{T}\,\mathrm{d}A \quad \Rightarrow \quad \boldsymbol{P} = \boldsymbol{\sigma}\,\mathrm{Cof}\,\boldsymbol{F} = J\,\boldsymbol{\sigma}\,\boldsymbol{F}^{-T} \,, \tag{2.31}$$

which is the definition of the *first Piola-Kirchhoff* (or *nominal*) *stress tensor* $\boldsymbol{P}$. In contrast to the Cauchy stresses the first Piola-Kirchhoff stress tensor need not be symmetric and is a two-point tensor – like $\boldsymbol{F}$ – involving two points in distinct configurations. Thus, Cauchy's theorem can be rewritten as

$$\boldsymbol{T}\,\mathrm{d}A = \boldsymbol{P}\,\mathrm{d}\boldsymbol{A} = \boldsymbol{P}\boldsymbol{N}\,\mathrm{d}A \quad \Rightarrow \quad \boldsymbol{T} = \boldsymbol{P}\boldsymbol{N} \,, \tag{2.32}$$

and reflects the property of $\boldsymbol{P}$ to relate the actual force to the reference area element. An additional stress measure is the *Kirchhoff stress tensor* $\boldsymbol{\tau}$, which is computed by weighting the Cauchy stresses by the volume ratio J. Therefore it is also known as the

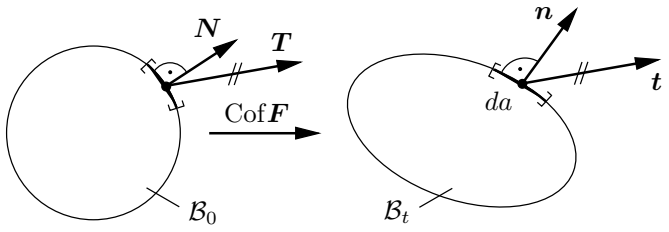

Figure 2.2: Coaxial traction vectors $\boldsymbol{T}$ and $\boldsymbol{t}$ in the reference configuration $\mathcal{B}_0$ and actual configuration $\mathcal{B}_t$, respectively.

[1.)] The symmetry condition is a consequence of the balance of angular momentum, see section 2.4.2.

weighted Cauchy stress tensor. This tensor enables an alternative expression for the first Piola-Kirchhoff stress tensor

$$\boldsymbol{P} = \boldsymbol{\tau}\boldsymbol{F}^{-T} \quad \text{with} \quad \boldsymbol{\tau} = J\boldsymbol{\sigma} \; . \tag{2.33}$$

Furthermore a useful stress measure in computational mechanics is the *second Piola-Kirchhoff stress tensor* $\boldsymbol{S}$. It is calculated by a pull-back operation of the Kirchhoff stress tensor $\boldsymbol{\tau}$

$$\boldsymbol{S} := \boldsymbol{F}^{-1}\boldsymbol{\tau}\boldsymbol{F}^{-T} = \boldsymbol{F}^{-1}\boldsymbol{P} = J\boldsymbol{F}^{-1}\boldsymbol{\sigma}\boldsymbol{F}^{-T} \tag{2.34}$$

and represents the Lagrangian counterpart of $\boldsymbol{\tau}$. Though $\boldsymbol{S}$ does not admit a physical interpretation in terms of surface traction but is symmetric in contrast to the first Piola-Kirchhoff stress tensor. Finally, the relation between both the Piola-Kirchhoff stress tensors is given by

$$\boldsymbol{P} = \boldsymbol{F}\boldsymbol{S} \; . \tag{2.35}$$

The *stress power* or the *rate of the internal mechanical work* $\mathcal{P}_{\text{int}}$ reads as follows

$$\mathcal{P}_{\text{int}} = \int_{\mathcal{B}_t} \boldsymbol{\sigma} : \operatorname{grad} \boldsymbol{v} \, \mathrm{d}v \tag{2.36}$$

and describes the response of the body $\mathcal{B}_t$ as the result of the stress field $\boldsymbol{\sigma}$. Considering the symmetry of $\boldsymbol{\sigma}$, and the split of the spatial velocity gradient (2.24) as well as the transformation of a volume element (2.15) yields

$$\mathcal{P}_{\text{int}} = \int_{\mathcal{B}_t} \boldsymbol{\sigma} : \boldsymbol{d} \, \mathrm{d}v = \int_{\mathcal{B}_0} \boldsymbol{\tau} : \boldsymbol{d} \, \mathrm{d}V \; . \tag{2.37}$$

The alternative descriptions of the stress power in the material setting

$$\mathcal{P}_{\text{int}} \overset{(2.23)}{=} \int_{\mathcal{B}_0} \boldsymbol{\tau} : (\dot{\boldsymbol{F}}\boldsymbol{F}^{-1}) \, \mathrm{d}V \overset{(2.33)}{=} \int_{\mathcal{B}_0} \boldsymbol{P} : \dot{\boldsymbol{F}} \, \mathrm{d}V \overset{(2.35)}{=} \int_{\mathcal{B}_0} \boldsymbol{S} : (\boldsymbol{F}^T\dot{\boldsymbol{F}})_{\text{sym}} \, \mathrm{d}V = \int_{\mathcal{B}_0} \boldsymbol{S} : \dot{\boldsymbol{E}} \, \mathrm{d}V$$

is obtained using the referred equations and the time derivative of the Green-Lagrange strain tensor $\boldsymbol{E}$ written as a pull-back operation of $\boldsymbol{d}$, i.e. $\dot{\boldsymbol{E}} = \frac{1}{2}\dot{\boldsymbol{C}} = \boldsymbol{F}^T\boldsymbol{d}\,\boldsymbol{F} = (\boldsymbol{F}^T\dot{\boldsymbol{F}})_{\text{sym}}$. The pairs of quantities $(\boldsymbol{P}, \dot{\boldsymbol{F}})$, $(\boldsymbol{S}, \dot{\boldsymbol{E}})$ and $(\boldsymbol{\tau}, \boldsymbol{d})$ are called *work-conjugated* pairs.

2.4 Balance Principles

In this section we introduce the fundamental conservation laws and balance principles for physical quantities in continuum mechanics. The four balance equations and one inequality,

- conservation of mass,
- balance of linear momentum,
- balance of angular momentum,
- balance of energy (1^{st} principle of thermodynamics),
- entropy inequality (2^{nd} principle of thermodynamics or *Clausius-Duhem-Inequality*),

are axioms, i.e. the relations are not deduced from other laws, but established by empiric observations. They represent material-independent equations and must be satisfied at all times. Before we discuss each law and its mechanical meaning, we introduce the general form of the balance laws. Therein the variation of a physical quantity $A := \int_{\mathcal{B}_t} a\, dv$, represented by its material time derivative, is balanced for a body in the actual configuration $\mathcal{B}_t$. The balance is governed by sources $\boldsymbol{s} \cdot \boldsymbol{n}$ on the surface, $\boldsymbol{n}$ denotes the outward unit normal of the surface, as well as sources z and production p inside the body. At first we need the relation

$$\operatorname{div}[a\,\boldsymbol{v}] = \operatorname{grad} a \cdot \boldsymbol{v} + a \operatorname{div} \boldsymbol{v} \;\Leftrightarrow\; a \operatorname{div} \boldsymbol{v} = \operatorname{div}[a\,\boldsymbol{v}] - \operatorname{grad} a \cdot \boldsymbol{v}\ , \tag{2.38}$$

with the Eulerian field a and the spatial velocity $\boldsymbol{v} = \boldsymbol{v}(\boldsymbol{x}, t)$, as well as the material time derivative

$$\dot{a} = \frac{\partial a}{\partial t} + \operatorname{grad} a \cdot \boldsymbol{v}\ , \tag{2.39}$$

and the Gauss divergence theorem

$$\int_{\mathcal{B}_t} \operatorname{div}[a\,\boldsymbol{v}]\ \mathrm{d}v = \int_{\partial\mathcal{B}_t} a\,\boldsymbol{v} \cdot \boldsymbol{n}\ \mathrm{d}a\ . \tag{2.40}$$

Then the material time derivative of the integral equation of field a yields

$$\begin{aligned} \dot{A} \quad &= \quad \frac{\partial}{\partial t} A = \frac{\partial}{\partial t} \int_{\mathcal{B}_t} a\ \mathrm{d}v \overset{(2.15)}{=} \frac{\mathrm{d}}{\mathrm{d}t} \int_{\mathcal{B}_0} a\, J\ \mathrm{d}V = \int_{\mathcal{B}_0} \left(\dot{a} J + a \dot{J} \right)\ \mathrm{d}V \\ &\overset{(2.25)}{\underset{(2.15)}{=}} \int_{\mathcal{B}_t} (\dot{a} + a \operatorname{div} \boldsymbol{v})\ \mathrm{d}v \overset{(2.38)}{\underset{(2.40)}{=}} \int_{\mathcal{B}_t} \frac{\partial a}{\partial t}\ \mathrm{d}v + \int_{\partial\mathcal{B}_t} a\,\boldsymbol{v} \cdot \boldsymbol{n}\ \mathrm{d}a \end{aligned} \tag{2.41}$$

using the specified equations and is referred to as *Reynolds' transport theorem*. Thus, the general global form of the spatial balance law appears as

$$\dot{A} = \frac{\mathrm{d}}{\mathrm{d}t} A = \int_{\mathcal{B}_t} \frac{\partial a}{\partial t}\ \mathrm{d}v + \int_{\partial\mathcal{B}_t} a\,\boldsymbol{v} \cdot \boldsymbol{n}\ \mathrm{d}a = \int_{\mathcal{B}_t} z\ \mathrm{d}v + \int_{\partial\mathcal{B}_t} \boldsymbol{s} \cdot \boldsymbol{n}\ \mathrm{d}a + \int_{\mathcal{B}_t} p\ \mathrm{d}v\ . \tag{2.42}$$

For a vanishing production term p the balanced quantity is called conserved quantity. The corresponding local or strong form of the latter equation

$$\dot{a} + a \operatorname{div} \boldsymbol{v} = z + \operatorname{div}[\boldsymbol{s}] + p, \qquad \forall\, \boldsymbol{x} \in \mathcal{B}_t \tag{2.43}$$

is deduced by applying the Gauss divergence theorem (2.40) and the localization theorem. Take note: For the later introduced Clausis-Duhem-Inequality (2.62) the equal sign $=$ in Equation (2.42) and (2.43) is replaced by the greater-than-or-equal sign $\geq$. Thus this balance equation is not denoted as a conserved quantity.

2.4.1 Conservation of Mass

The law of conservation of mass based on the assumption, that during the deformation process neither mass sources nor mass sinks exist, and so the mass M of a body $\mathcal{B}$ is constant, i.e. a conserved quantity. With the corresponding scalar fields ρ_0 and ρ, which

represent the reference and actual density, the *first global form of conservation of mass* reads

$$M := \int_{\mathcal{B}_0} \rho_0(\boldsymbol{X}) \; \mathrm{d}V = \int_{\mathcal{B}_t} \rho(\boldsymbol{x}, t) \; \mathrm{d}v = m = \text{const.} \; . \tag{2.44}$$

This conservation law can be rewritten to the *first local form of conservation of mass*

$$\rho_0 = J\rho, \qquad \forall \, \boldsymbol{X} \in \mathcal{B}_0 \tag{2.45}$$

applying the transport theorem (2.15). Based on the assumption of non-existence of sources and of m as a conserved quantity we set $A = m$, $a = \rho$, $z = 0$, $\boldsymbol{s} = \boldsymbol{0}$ and, $p = 0$ in Equation (2.42) and obtain the *second global form of conservation of mass*

$$\dot{m} = \frac{\mathrm{d}}{\mathrm{d}t} \int_{\mathcal{B}_t} \rho \, \mathrm{d}v = \int_{\mathcal{B}_t} \frac{\partial \rho}{\partial t} \, \mathrm{d}v + \int_{\partial \mathcal{B}_t} \rho \, \boldsymbol{v} \cdot \boldsymbol{n} \, \mathrm{d}a = 0 \; , \tag{2.46}$$

and the *second local form of conservation of mass* reads

$$\dot{\rho} + \rho \, \mathrm{div} \, \boldsymbol{v} = 0, \qquad \forall \, \boldsymbol{x} \in \mathcal{B}_t \; , \tag{2.47}$$

according to Equation (2.43).

2.4.2 Momentum Balance Principles

The *balance of linear momentum* postulates that the material time derivative of the linear momentum $\boldsymbol{L}$ is equal to the external resultant force $\boldsymbol{f}^{\mathrm{ext}}$, i.e.

$$\dot{\boldsymbol{L}} = \boldsymbol{f}^{\mathrm{ext}}, \quad \text{with} \quad \boldsymbol{L} := \int_{\mathcal{B}_t} \rho \boldsymbol{v} \, \mathrm{d}v \quad \text{and} \quad \boldsymbol{f}^{\mathrm{ext}} := \int_{\mathcal{B}_t} \rho \boldsymbol{f} \, \mathrm{d}v + \int_{\partial \mathcal{B}_t} \overline{\boldsymbol{t}} \, \mathrm{d}a \; , \tag{2.48}$$

where $\boldsymbol{f}$ denotes the volume acceleration and $\overline{\boldsymbol{t}}$ the traction vector acting on the surface $\partial \mathcal{B}_t$. Taking Cauchy's Therorem (2.28) and Gauss divergence theorem (2.40) into consideration the second term in the definition of $\boldsymbol{f}^{\mathrm{ext}}$ can be rearranged in

$$\int_{\partial \mathcal{B}_t} \overline{\boldsymbol{t}} \, \mathrm{d}a = \int_{\partial \mathcal{B}_t} \boldsymbol{\sigma} \boldsymbol{n} \, \mathrm{d}a = \int_{\mathcal{B}_t} \mathrm{div} \, \boldsymbol{\sigma} \, \mathrm{d}v \; . \tag{2.49}$$

In the general forms (2.42) and (2.43) we set $A = L$, $a = \rho \boldsymbol{v}$, $z = \rho \boldsymbol{f}$, $\boldsymbol{s} = \boldsymbol{\sigma}$ and, $p = 0$, respectively, and along with the conservation of mass (2.47) we formulate the *global form of the spatial balance of linear momentum*

$$\int_{\mathcal{B}_t} \rho \dot{\boldsymbol{v}} \, \mathrm{d}v = \int_{\mathcal{B}_t} (\rho \boldsymbol{f} + \mathrm{div} \, \boldsymbol{\sigma}) \, \mathrm{d}v \; , \tag{2.50}$$

which is referred to as *Cauchy's first equation of motion* and the corresponding *local form in the spatial configuration*

$$\rho \dot{\boldsymbol{v}} = \mathrm{div} \, \boldsymbol{\sigma} + \rho \boldsymbol{f} \quad \Rightarrow \quad \mathrm{div} \, \boldsymbol{\sigma} + \rho(\boldsymbol{f} - \dot{\boldsymbol{v}}) = \boldsymbol{0} \qquad \forall \, \boldsymbol{x} \in \mathcal{B}_t \; . \tag{2.51}$$

The latter balance equation is transferred to the *local form of the material balance of linear momentum*

$$\mathrm{Div} \, \boldsymbol{P} + \rho_0(\boldsymbol{f} - \dot{\boldsymbol{v}}) = \boldsymbol{0} \tag{2.52}$$

using

$$\int_{\mathcal{B}_t} \operatorname{div} \boldsymbol{\sigma} \, \mathrm{d}v \overset{(2.40)}{=} \int_{\partial\mathcal{B}_t} \boldsymbol{\sigma}\boldsymbol{n} \, \mathrm{d}a \overset{(2.28)}{=} \int_{\partial\mathcal{B}_t} \overline{\boldsymbol{t}} \, \mathrm{d}a \overset{\substack{(2.30)\\(2.32)}}{=} \int_{\partial\mathcal{B}_0} \boldsymbol{P}\boldsymbol{N} \, \mathrm{d}A \overset{(2.40)}{=} \int_{\mathcal{B}_0} \operatorname{Div} \boldsymbol{P} \, \mathrm{d}V \; . \tag{2.53}$$

The *balance of angular momentum* postulates that the material time derivative of the angular momentum $\boldsymbol{h}_{(0)}$ regarding to a point $\boldsymbol{x}_0$ is equal to the resultant moment $\boldsymbol{m}_{(0)}$ of all forces acting on body $\mathcal{B}_t$, i.e.

$$\dot{\boldsymbol{h}}_{(0)} = \boldsymbol{m}_{(0)}, \quad \text{with} \quad \boldsymbol{h}_{(0)} := \int_{\mathcal{B}_t} \boldsymbol{r} \times \rho\boldsymbol{v} \, \mathrm{d}v \; , \quad \boldsymbol{m}_{(0)} := \int_{\mathcal{B}_t} \boldsymbol{r} \times \rho\boldsymbol{f} \, \mathrm{d}v + \int_{\partial\mathcal{B}_t} \boldsymbol{r} \times \overline{\boldsymbol{t}} \, \mathrm{d}a \; , \tag{2.54}$$

where the moment arm is defined as $\boldsymbol{r} := \boldsymbol{x} - \boldsymbol{x}_0$. The second term in the definition of the resultant moment $\boldsymbol{m}_{(0)}$ is reformulated to

$$\int_{\partial\mathcal{B}_t} \boldsymbol{r} \times \overline{\boldsymbol{t}} \, \mathrm{d}a = \int_{\mathcal{B}_t} (\boldsymbol{r} \times \operatorname{div} \boldsymbol{\sigma} + \boldsymbol{\epsilon} : \boldsymbol{\sigma}^T) \, \mathrm{d}v \; , \tag{2.55}$$

using the Gauss divergence theorem for the cross product and the permutation tensor $(2.3)_2$. This relation as well as the balance laws (2.47) and (2.51) applied to the general form (2.42) after setting $A = h_{(0)}$, $a = \boldsymbol{r} \times \rho\boldsymbol{v}$, $z = \boldsymbol{r} \times \rho\boldsymbol{f}$, $s\dot{\boldsymbol{n}} = \boldsymbol{r} \times \overline{\boldsymbol{t}}$ and $p = 0$ yield the *global and local form of the spatial balance of angular momentum*

$$\begin{aligned} &\int_{\mathcal{B}_t} \boldsymbol{r} \times [\operatorname{div} \boldsymbol{\sigma} + \rho(\boldsymbol{f} - \dot{\boldsymbol{v}})] \, \mathrm{d}v + \int_{\mathcal{B}_t} \boldsymbol{\epsilon} : \boldsymbol{\sigma}^T \, \mathrm{d}v = \boldsymbol{0} \\ \overset{(2.51)}{\Rightarrow} &\int_{\mathcal{B}_t} \boldsymbol{\epsilon} : \boldsymbol{\sigma}^T \, \mathrm{d}v = \boldsymbol{0} \quad \Rightarrow \quad \boldsymbol{\epsilon} : \boldsymbol{\sigma}^T = \boldsymbol{0} \quad \forall \; \in \mathcal{B}_t \; . \end{aligned} \tag{2.56}$$

Because of the composition of the permutation tensor $\boldsymbol{\epsilon}$ the latter balance equation is satisfied, if and only if the Cauchy stress tensor $\boldsymbol{\sigma}$ is symmetric, i.e.

$$\boldsymbol{\sigma} = \boldsymbol{\sigma}^T \; , \tag{2.57}$$

which is an important result and named as *Cauchy's second equation of motion*. Based on the symmetry of the Cauchy stress tensor the same condition is deduced for the Kirchhoff stress tensor $\boldsymbol{\tau}$ and the second Piola-Kirchhoff stress tensor $\boldsymbol{S}$, c.f. equations (2.33) and (2.34), respectively.

2.4.3 Thermodynamic principles

For the following investigations we consider only mechanical and thermal energy as they are essential quantities in the field of physics and engineering.

The *first principle of thermodynamics* postulates that the rate of total energy of a physical body is equal to the sum of power which is the result of all forces and all other energies. This context can be written as the *global form of the spatial balance of energy*

$$\frac{\mathrm{d}}{\mathrm{d}t}(\mathcal{K} + \mathcal{E}) = \mathcal{P} + \mathcal{Q} \tag{2.58}$$

with the individual terms of kinetic energy $\mathcal{K}$ and internal energy $\mathcal{E}$ for the total energy on the left side, which are defined as

$$\mathcal{K} := \int_{\mathcal{B}_t} \frac{1}{2}\,\rho \boldsymbol{v}\cdot\boldsymbol{v}\;\mathrm{d}v\;, \quad \mathcal{E} := \int_{\mathcal{B}_t} \rho e\;\mathrm{d}v\;, \tag{2.59}$$

with the specific energy density e defined per unit mass. On the right side of Equation (2.58) the sum of power is represented by the power of mechanical tractions and body forces $\mathcal{P}$ and the power of heat fluxes and heat sources $\mathcal{Q}$. Both these quantities can be expressed by

$$\mathcal{P} := \int_{\mathcal{B}_t} \rho \boldsymbol{f}\cdot\boldsymbol{v}\;\mathrm{d}v + \int_{\partial\mathcal{B}_t} \overline{\boldsymbol{t}}\cdot\boldsymbol{v}\;\mathrm{d}a\;, \quad \mathcal{Q} := \int_{\mathcal{B}_t} \rho r\;\mathrm{d}v - \int_{\partial\mathcal{B}_t} q\;\mathrm{d}a\;, \tag{2.60}$$

under consideration of the heat supply r per unit mass and time. *Stoke's heat flux theorem* supplies the *Cauchy heat flux vector* by $q = \boldsymbol{q}\cdot\boldsymbol{n}$ with the outward normal vector $\boldsymbol{n}$ and is associated with the area element $\mathrm{d}a$. Setting $A = \mathcal{K} + \mathcal{E}$, $a = \rho(e + \frac{1}{2}||\boldsymbol{v}||^2)$, $z = \rho\boldsymbol{v}\cdot\boldsymbol{f}$, $\boldsymbol{s} = (\boldsymbol{v}\cdot\boldsymbol{\sigma} - \boldsymbol{q})$ and $p = \rho r$ and using Cauchy's theroem (2.28) and the divergence theorem (2.40) as well as the momentum balance principles (2.51) and (2.57) leads to the *local form of the spatial balance of energy*

$$\rho\dot{e} = \rho r - \operatorname{div}\boldsymbol{q} + \boldsymbol{\sigma} : \boldsymbol{d}\;, \quad \forall\,\boldsymbol{x}\in\mathcal{B}_t\;. \tag{2.61}$$

The *second principle of thermodynamics* postulates that the material time derivative of total entropy $H_\mathrm{e} = \int_{\mathcal{B}_t}\rho\eta\;\mathrm{d}v$ is greater than or equal to the sum of the supply of entropy by heat flux $(-h/\Theta)$ over surface and internal entropy $(\rho r/\Theta)$ due to evolution of temperature. Thereby η denotes the specific entropy per unit mass and Θ the absolute temperature. In addition to the first principle, which only states the conservation of energy during a thermodynamic process, the second one declares the direction of the process. Rudolf Julius Emmanuel Clausius (1822–1888) formulated this context by:

> "*Es kann nie Wärme aus einem kälteren in einen wärmeren Körper übergehen, wenn nicht gleichzeitig eine andere damit zusammenhängende Aenderung eintritt.*" (Heat can never pass from a colder to a warmer body, if not an other change occurs at the same time.) Clausius [50]

This statement exemplifies the daily experience that heat does not flow from cold to hot without input of work. The axiom can be expressed by the so-called *Clausius-Duhem Inequality* (*global form of spatial entropy inequality*)

$$\frac{\mathrm{d}}{\mathrm{d}t}\int_{\mathcal{B}_t}\rho\eta\;\mathrm{d}v \geq \int_{\mathcal{B}_t}\frac{\rho r}{\Theta}\;\mathrm{d}v - \int_{\partial\mathcal{B}_t}\frac{q}{\Theta}\;\mathrm{d}a\;. \tag{2.62}$$

To yield the *local form of spatial entropy inequality*

$$\rho(\Theta\dot{\eta} - \dot{e}) + \boldsymbol{\sigma} : \boldsymbol{d} - \frac{1}{\Theta} \geq 0\;, \quad \forall\,\boldsymbol{x}\in\mathcal{B}_t\;, \tag{2.63}$$

we set $A = H_\mathrm{e}$, $a = \rho\eta$, $z = 0$, $\boldsymbol{s} = -\boldsymbol{q}/\Theta$ and $p = \rho r/\Theta$ in the general local balance form (2.43) and consider the conservation of mass (2.47) and the balance of energy (2.61).

Since we restricted ourselves to isothermal processes ($\Theta = \text{const.} \Rightarrow \dot{\Theta} = 0$) and chose the *Helmholtz free energy* ψ_c per current unit volume defined by $\psi_c = \rho(e - \Theta\eta)$ the local form of the Clausius-Duhem inequality (2.63) reads

$$-\dot{\psi}_c + \boldsymbol{\sigma} : \boldsymbol{d} \geq 0 \ , \quad \forall \ \boldsymbol{x} \in \mathcal{B}_t \ . \tag{2.64}$$

The material form of the latter equation

$$\boldsymbol{S} : \dot{\boldsymbol{E}} - \dot{\psi} \geq 0 \ , \quad \forall \ \boldsymbol{X} \in \mathcal{B}_0 \tag{2.65}$$

is achieved by considering the work-conjugated pair $(\boldsymbol{S}, \dot{\boldsymbol{E}})$ and defining the Helmholtz free energy $\psi := \rho_0(e - \Theta\eta)$ based on reference unit volume. For purely mechanical processes the free energy depends only on the temperature Θ and the strain, measured by $\boldsymbol{E}$ in the case of $(\boldsymbol{S}, \dot{\boldsymbol{E}})$. In the isothermal case we get

$$\boldsymbol{S} : \dot{\boldsymbol{E}} - \frac{\partial \psi}{\partial \boldsymbol{E}} : \dot{\boldsymbol{E}} \geq 0 \ , \quad \forall \ \boldsymbol{X} \in \mathcal{B}_0 \tag{2.66}$$

and this relation must be held for all imaginable processes. For reversible processes the unequal sign changes to an equal sign and we get the *constitutive equation* for the stresses

$$\boldsymbol{S} = \frac{\partial \psi}{\partial \boldsymbol{E}} = 2\frac{\partial \psi}{\partial \boldsymbol{C}} \ , \quad \text{with} \quad S^{AB} = \frac{\partial \psi}{\partial E_{AB}} = 2\frac{\partial \psi}{\partial C_{AB}} \ . \tag{2.67}$$

These relations causes a functional dependence between the stress quantity $\boldsymbol{S}$ and the strain quantity $\boldsymbol{E}$ or deformation quantity $\boldsymbol{C}$. For the later used linearization of the second Piola-Kirchhoff stress tensor we introduce the corresponding symmetric tangent moduli

$$\mathbb{C} := \frac{\partial \boldsymbol{S}}{\partial \boldsymbol{E}} = \frac{\partial^2 \psi}{\partial \boldsymbol{E} \partial \boldsymbol{E}} = 4\frac{\partial^2 \psi}{\partial \boldsymbol{C} \partial \boldsymbol{C}} \ , \quad \text{with} \quad \mathbb{C}^{ABCD} = 2\frac{\partial S^{AB}}{\partial C_{CD}} \ . \tag{2.68}$$

Analogously, we proceed for the work-conjugated pair $(\boldsymbol{P}, \dot{\boldsymbol{F}})$ and we achieve the material form of Equation (2.64)

$$\boldsymbol{P} : \dot{\boldsymbol{F}} - \dot{\psi} \geq 0 \quad \Rightarrow \quad \boldsymbol{P} : \dot{\boldsymbol{F}} - \frac{\partial \psi}{\partial \boldsymbol{F}} : \dot{\boldsymbol{F}} \geq 0 \ , \quad \forall \ \boldsymbol{X} \in \mathcal{B}_0 \tag{2.69}$$

with the restriction to isothermal processes and the free energy $\psi = \psi(\boldsymbol{F})$. Consequently, for a reversible process the constitutive equation for the first Piola-Kirchhoff stress tensor is given by

$$\boldsymbol{P} = \frac{\partial \psi}{\partial \boldsymbol{F}} \ , \quad \text{with} \quad P_a{}^A = \frac{\partial \psi}{\partial F^a{}_A} \ , \tag{2.70}$$

and the corresponding tangent moduli, also referred to as *nominal tangent*, is calculated by

$$\mathbb{A} := \frac{\partial \boldsymbol{P}}{\partial \boldsymbol{F}} = \frac{\partial^2 \psi}{\partial \boldsymbol{F} \partial \boldsymbol{F}} \ , \quad \text{with} \quad \mathbb{A}_a{}^A{}_b{}^B = \frac{\partial P^a{}_A}{\partial F^b{}_B} = \frac{\partial^2 \psi}{\partial F^b{}_B \partial F^a{}_A} \ . \tag{2.71}$$

2.5 Principles for the Design of Constitutive Material Models

In the previous sections we introduce the material independent balance principles of thermodynamics. As we are interested in the description of the behavior of individual materials, we have to regard several construction principles for the constitutive equations. This helpful advice preserves us from constructing a physically unreasonable material model. The precepts are namely:

principles of *causality*, *determinism*, *equipresence*, *objectivity*, *material invariance*, *neighborhood*, *memory*, *admissibility*, *dissipation*.

In the sequel we elaborate on the principles of objectivity and material invariance. For details on the other principles we refer to advanced textbooks, for the original development see NOLL [161], TRUESDELL AND NOLL [229] and for further remarks MARSDEN AND HUGHES [142], HOLZAPFEL [106]. The principle of admissibility claims that the constitutive equation for the desired material does not have to contradict the conservation and balance principles as well as the second law of thermodynamics. Material models, which fulfill these conditions, are called to be *thermodynamically consistent*.

Remarks on Observer Independent Physical Quantities. Obviously, description of the motion $\boldsymbol{x}$ of a body is directly connected to the position of the observer, i.e. to the choice of the reference coordinate system. For the further statements we consider the two observers B_1 and B_2 measuring with respect to the reference system $\mathcal{K}$ and $\mathcal{K}^+$, which are located at the origins O and O^+ with the base vectors $\{\boldsymbol{e}_i, \boldsymbol{e}_j, \boldsymbol{e}_k\}$ and $\{\boldsymbol{e}_i^+, \boldsymbol{e}_j^+, \boldsymbol{e}_k^+\}$, respectively. They must measure exactly the same deformation related to their respective reference system. The relation between the motion of the observers can be regarded as a rigid body motion. Thereby the mutual translation of the origins is described by the time dependent vector $\boldsymbol{c}(t)$. The mutual rotation of the reference systems are represented by a time dependent orthogonal tensor $\boldsymbol{Q}(t) \in \mathrm{SO}(3)$. Thereby $\mathrm{SO}(3)$ denotes the special orthogonal group, which represents the group of all arbitrary rigid body motions with $\det \boldsymbol{Q} = 1$ and $\boldsymbol{Q}^T = \boldsymbol{Q}^{-1}$. Furthermore, a time difference $t^+ = t - \Delta t$ with $\Delta t \in \mathbb{R}$ may exist. The time dependent description of the motion of the body with respect to both reference systems can be related to each other by the *Euclidean transformation*

$$\left.\begin{aligned} \boldsymbol{x}^+ &= \boldsymbol{Q}(t)\boldsymbol{x} + \boldsymbol{c}(t) \\ t^+ &= t - \Delta t \end{aligned}\right\} \quad \forall\, \boldsymbol{Q}(t) \in \mathrm{SO}(3)\,, \quad \text{with} \quad \boldsymbol{Q}(t) = \frac{\partial \boldsymbol{x}^+}{\partial \boldsymbol{x}}\,. \tag{2.72}$$

If we assume a time independent translation and rotation we achieve

$$\boldsymbol{x}^+ = \boldsymbol{Q}\boldsymbol{x} + \boldsymbol{c} \quad \text{with} \quad \boldsymbol{Q} = \boldsymbol{Q}(t) = \text{const.}\,,\ \boldsymbol{c} = \boldsymbol{c}(t) = \text{const.} \quad \forall\, \boldsymbol{Q} \in \mathrm{SO}(3)\,, \tag{2.73}$$

which is also referred to as *rigid transformation*. The Euclidean transformation enables the definition of specific transformation rules for physical quantities. If the quantities fulfill the conditions they are called observer independent or objective. For the objectivity of a scalar-valued quantity β, a vector-valued quantity $\boldsymbol{v}$ and a tensor-valued quantity $\boldsymbol{D}$ the transformations

$$\beta^+ = \beta\,, \quad \boldsymbol{v}^+ = \boldsymbol{Q}(t)\,\boldsymbol{v}\,, \quad \boldsymbol{D}^+ = \boldsymbol{Q}(t)\,\boldsymbol{D}\,\boldsymbol{Q}^T(t) \tag{2.74}$$

have to be held for the change of the reference system. For the deformation tensor $\boldsymbol{F}$ with its definition (2.8) the observer change yields

$$\boldsymbol{F}^+ = \operatorname{Grad} \boldsymbol{x}^+ = \frac{\partial \boldsymbol{x}^+}{\partial \boldsymbol{x}} \frac{\partial \boldsymbol{x}}{\partial \boldsymbol{X}} = \boldsymbol{Q}(t)\boldsymbol{F} \quad \neq \quad \boldsymbol{Q}(t)\,\boldsymbol{F}\,\boldsymbol{Q}^T(t) \tag{2.75}$$

and shows the non-objectivity of $\boldsymbol{F}$. Using the latter relation the right Cauchy-Green tensor (2.17) is transformed by

$$\boldsymbol{C}^+ = \boldsymbol{F}^{+T}\boldsymbol{F}^+ = \boldsymbol{F}^T\,\boldsymbol{Q}^T(t)\,\boldsymbol{Q}(t)\,\boldsymbol{F} = \boldsymbol{C} \tag{2.76}$$

and its invariance towards a change of the reference system is shown. The same property can be identified for the right stretch tensor $\boldsymbol{U}$ and the Green-Lagrange strain tensor $\boldsymbol{E}$.

2.5.1 Principle of Material Frame Indifference – Objectivity

The principle of material frame indifference specifies an essential requirement to material laws regarding the observer:

> The constitutive equations must be indifferent against a change of the reference system (observer).

Consequently, two observers B_1 and B_2 have to determine the same energy and stress state of the deformed body. Let both describe the position of the material point $\boldsymbol{X}$ in the deformed configurations by $\boldsymbol{x}(\boldsymbol{X}) \in \mathcal{B}_t$ and $\boldsymbol{x}^+(\boldsymbol{X}) \in \mathcal{B}_t{}^+$ each with respect to its reference systems $\mathcal{K}$ and $\mathcal{K}^+$. In the static case the mapping $\boldsymbol{x} \mapsto \boldsymbol{x}^+$ is achieved by the time independent form of the Euclidean transformation (2.73), i.e. rigid transformation, and the associated deformation gradient $\boldsymbol{F}$ is transformed by the Equation (2.75), see also Figure 2.3. Based on this the constitutive equations have to fulfill

$$\psi(\boldsymbol{F}^+) = \psi(\boldsymbol{Q}\boldsymbol{F}) = \psi(\boldsymbol{F}) \quad \text{and} \quad \boldsymbol{P}(\boldsymbol{Q}\boldsymbol{F}) = \boldsymbol{Q}\boldsymbol{P}(\boldsymbol{F}) \quad \forall\, \boldsymbol{Q} \in \mathrm{SO}(3) \tag{2.77}$$

to be observer independent (objective). But together with a priori objective strain measures, e.g. right Cauchy-Green tensor $\boldsymbol{C}^+ = \boldsymbol{C} = \boldsymbol{U}^2$, we achieve the reduced form of the constitutive equations

$$\psi(\boldsymbol{C}) = \psi(\boldsymbol{C}^+) \;, \quad \forall\, \boldsymbol{q} \in \mathrm{SO}(3) \;, \tag{2.78}$$

which a priori fulfills the principle of the material frame indifference. As a consequence of this property, we use formulations of the constitutive equations in the form of Equation (2.78) and use the corresponding second Piola-Kirchhoff stress tensor and the tangent modul in the forms

$$\boldsymbol{S} = 2\frac{\partial \psi(\boldsymbol{C})}{\partial \boldsymbol{C}} \quad \text{and} \quad \mathbb{C} = 4\frac{\partial^2 \psi(\boldsymbol{C})}{\partial \boldsymbol{C} \partial \boldsymbol{C}} \;. \tag{2.79}$$

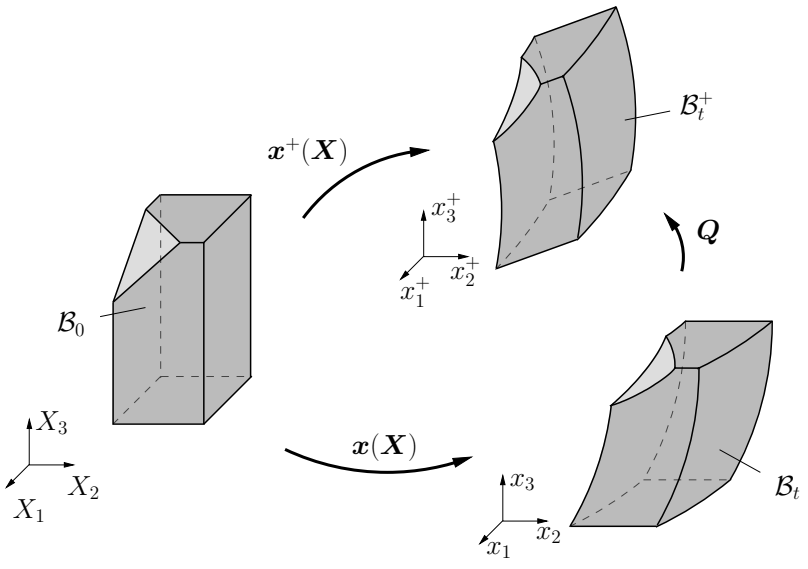

Figure 2.3: Objectivity: Euclidean transformation of spatial configuration.

2.5.2 Principle of Material Symmetry

The principle of material symmetry describes the influence of a change of the reference frame on the constitutive equations:

> The constitutive equations have to be invariant with respect to all transformations of the material coordinates, which belong to the symmetry group $\mathcal{G}$ of the underlying material.

The symmetry group $\mathcal{G}$ has to be specified regarding the physical symmetry properties of the individual material. A material with identical properties in all directions is labeled as *isotropic material* and an arbitrary reference configuration can be chosen. The corresponding symmetry group is the orthogonal group O(3), which includes all orthogonal tensors $\boldsymbol{Q}$, i.e. all proper and improper rotations, and represents the largest symmetry group. An essential subgroup of O(3) is the proper orthogonal group SO(3) excluding the improper rotations – also known as reflections and rotoinversions. If the symmetry group of a material is only a subgroup of the proper orthogonal group the material behavior is denoted as *anisotropic*.

For a change of the reference configuration $\mathcal{B}_0$ to an other reference configuration $\mathcal{B}_0{}^*$ the mapping $\boldsymbol{X} \mapsto \boldsymbol{X}^*$ of the material point positions is given by

$$\boldsymbol{X}^* = \boldsymbol{Q}\boldsymbol{X} \;, \quad \forall\, \boldsymbol{Q} \in \mathcal{G} \subset \mathrm{O}(3) \;, \tag{2.80}$$

where $\boldsymbol{Q}$ denotes the symmetry transformations included in the individual material symmetry group $\mathcal{G}$. Hence the transformation

$$\boldsymbol{F}^* = \frac{\partial \boldsymbol{x}}{\partial \boldsymbol{X}} \frac{\partial \boldsymbol{X}}{\partial \boldsymbol{X}^*} = \boldsymbol{F}\boldsymbol{Q}^T \tag{2.81}$$

pertains for the deformation gradient, see Figure 2.4. A scalar-valued quantity, e.g. the free energy ψ, must transform as follows

$$\psi(\boldsymbol{F}) = \psi(\boldsymbol{F}\boldsymbol{Q}^T) \;, \quad \forall\, \boldsymbol{Q} \in \mathcal{G} \subset \mathrm{O}(3) \tag{2.82}$$

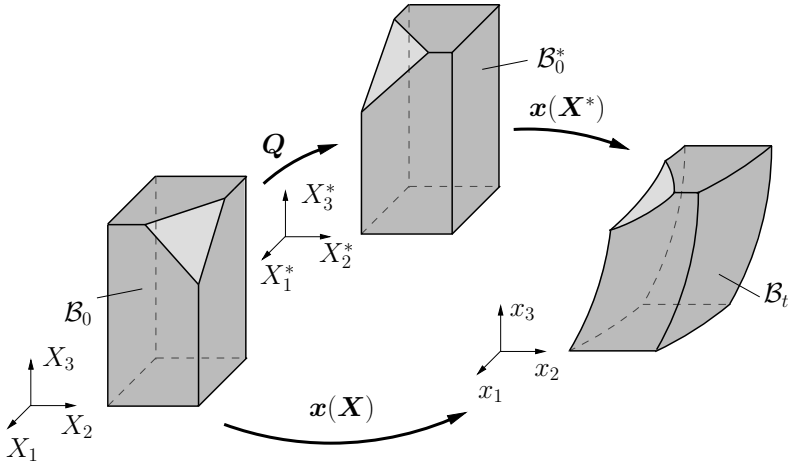

Figure 2.4: Material Symmetry: Change of Reference Frame.

to fulfill the principle of material symmetry. For the reduced constitutive equations $\psi(\boldsymbol{C})$ and $\boldsymbol{S}(\boldsymbol{C})$ – the form we prefer since it fulfills a priori the principle of objectivity – the requirement of material symmetry amounts to

$$\left.\begin{aligned} \psi(\boldsymbol{C}) &= \psi(\boldsymbol{Q}\boldsymbol{C}\boldsymbol{Q}^T) \\ \boldsymbol{Q}\boldsymbol{S}(\boldsymbol{C})\,\boldsymbol{Q}^T &= \boldsymbol{S}(\boldsymbol{Q}\boldsymbol{C}\boldsymbol{Q}^T) \end{aligned}\right\} \quad \forall\, \boldsymbol{Q} \in \mathcal{G} \subset \mathrm{O}(3)\ . \tag{2.83}$$

Note, that in contrast to the material frame indifference the principle of material symmetry is not generally satisfied.

2.5.3 Representation Theorems and Invariant Theory

In this section the framework of the invariant theory is provided and from that the representation theorems of tensor functions are introduced. They are essential concepts in many branches of modern continuum mechanics and in this thesis they offer a helpful tool for the modeling of the anisotropic material response, which we observe in the context of arterial walls in the sequel of this thesis.

For the classical invariant theory we refer to e.g. the classical treatise of Grace and Young [86], Gurevich [88], Weyl [248], Schur [199]. The evolution of the representation theorems for isotropic tensor functions were mainly influenced by the scientific papers of Wang [238; 239; 240] and Smith [212; 213], wherein the authors introduce different approaches. The conflict of opinion between Wang and Smith resulted in a critical paper by Smith [214], which in turn was the occasion for new representations by Wang [241; 242] and a corrigendum by Wang [243]. An analysis of Smith's and Wang's approaches is provided by Boehler [26] and ends up in *irreducible representations of isotropic scalar-valued functions*. Several scientific publications show applications of tensor representations in the field of continuum mechanics, in this context we refer to Truesdell and Noll [229], Spencer [217], Boehler [29], Betten [24; 25], Schröder [191] and Schröder and Neff [194] among many others. At this point we emphasize the concept of structural tensors, introduced in an attractive way by Boehler [27; 28], which is a helpful concept especially for the modeling of anisotropic response functions. Note, that some similar ideas might have been referred to earlier. An overview of the theory of the representations of tensor functions as well as a summary of important theorems can be found in Zheng [258]. In Ebbing [64] a comprehensive overview of isotropic tensor functions in the context of polyconvex energy functions for all anisotropy classes is given.

Note on Irreducible Sets of Invariants. In the previous section we state, that the principle of material symmetry is satisfied for the constitutive equations only under specific transformation, which belong to the material symmetry group. Thus, one of the main goals in the invariant theory is to find a set of basic invariants for a given set of tensor arguments under specified coordinate transformations from which all other invariants can be generated. The possibility of this is ensured by *Hilbert's Theorem*, which was published as well as proved in Hilbert [94; 95] and states in its original form:

> "*Ist ein System von Grundformen mit beliebig vielen Veränderlichenreihen gegeben, welche in vorgeschriebener Weise den nämlichen oder verschiedenen linearen Transformationen unterliegen, so giebt es für dasselbe stets eine e n d l i c h e Zahl von ganzen und rationalen Invarianten, durch welche sich jede andere ganze und rationale Invariante in ganzer und rationaler Weise ausdrücken lässt.*"
> HILBERT [94]

Thus may be stated, that for any finite set of tensor agencies of any order relative to an anisotropy group, there exists a finite number of invariants (an integrity basis). In this context the definitions of the terminology of invariant sets are important:

Integrity Basis: The set of invariants for a given set of tensor arguments relative to a fixed symmetry group $\mathcal{G}$ is called an *integrity basis* $\mathcal{I}$, if an arbitrary polynomial invariant of the same arguments can be expressed as a polynomial in the basic invariants. If no element of the considered set can be expressed as a polynomial in the remaining invariants of $\mathcal{I}$, it is called *irreducible*.

Functional Basis: The set of invariants is called a *functional basis* $\mathcal{F}$, if an arbitrary invariant in terms of the underlying arguments can be expressed as a function (not necessarily polynomial) in terms of the elements of $\mathcal{F}$. It is said to be *irreducible*, if none of the elements of the basic set $\mathcal{F}$ can be expressed as a function of the other invariants of $\mathcal{F}$, i.e., if all elements of $\mathcal{F}$ are functionally independent.

Isotropic Functions. A scalar-valued function h and a second-order tensor-valued function $\boldsymbol{H}$ are called *isotropic*, if for any argument the following conditions are satisfied

$$\left.\begin{aligned} y(\alpha, \boldsymbol{a}, \boldsymbol{A}) &= y(\alpha, \boldsymbol{Q}\boldsymbol{a}, \boldsymbol{Q}\boldsymbol{A}\boldsymbol{Q}^T) \\ \boldsymbol{Q}\,\boldsymbol{Y}(\alpha, \boldsymbol{a}, \boldsymbol{A})\,\boldsymbol{Q}^T &= \boldsymbol{Y}(\alpha, \boldsymbol{Q}\boldsymbol{a}, \boldsymbol{Q}\boldsymbol{A}\boldsymbol{Q}^T) \end{aligned}\right\} \quad \forall\, \boldsymbol{Q} \in \mathrm{O}(3)\ , \tag{2.84}$$

where $\alpha \in \mathbb{R}$, $\boldsymbol{a} \in \mathbb{R}^3$ and $\boldsymbol{A} \in \mathbb{R}^{3\times 3}$. An isotropic function is also referred to as a coordinate-invariant function. If the functions are invariant with respect to the proper orthogonal group SO(3), they are called hemitropic functions. In the following we do not differentiate between isotropic and hemitropic functions.

For the representation of an arbitrary isotropic tensor function $\boldsymbol{Y}(\boldsymbol{A})$ the *Cayley-Hamilton theorem*[2.)] is advantageous, because it says that an arbitrary quadratic tensor $\boldsymbol{A}$ satisfies its own characteristic equation. Considering the tensor $\boldsymbol{A} \in \mathbb{R}^{3\times 3}$ with its characteristic polynomial $p(\boldsymbol{A}) = \det(\boldsymbol{A} - \lambda\boldsymbol{1}) = 0$ the theorem leads to the final expression

$$p(\boldsymbol{A}) = -\boldsymbol{A}^3 + I_1\boldsymbol{A}^2 + I_2\boldsymbol{A} + I_3\boldsymbol{1} = \boldsymbol{0} \quad \Rightarrow \quad \boldsymbol{A}^3 = I_1\boldsymbol{A}^2 - I_2\boldsymbol{A} + I_3\boldsymbol{1} \tag{2.85}$$

with its non-trivial solution for the *principal invariants*

$$I_1 = \operatorname{tr}\boldsymbol{A}, \quad I_2 = \operatorname{tr}[\operatorname{Cof}\boldsymbol{A}], \quad I_3 = \det\boldsymbol{A}\ . \tag{2.86}$$

The resultant expression (2.85) of the Cayley-Hamilton theroem enables us to express every power of a tensor greater than three as a polynomial of order two. As an example we achieve

$$\begin{aligned} \boldsymbol{A}^4 &= (I_1^2 - I_2)\boldsymbol{A}^2 - (I_1 I_2 - I_3)\boldsymbol{A} + I_1 I_3 \boldsymbol{1} \\ \boldsymbol{A}^{-1} &= \frac{1}{I_3}(\boldsymbol{A}^2 - I_1\boldsymbol{A} + I_2\boldsymbol{1}) \end{aligned} \tag{2.87}$$

[2.)] Named for Arthur Cayley (1821–1895) and William Rowan Hamilton (1805–1865), who independently from each other initiated the theorem.

by multiplying (2.85) with $\boldsymbol{A}$ or $\boldsymbol{A}^{-1}$, respectively. The principal invariants meet the requirements (2.84) for a scalar-valued isotropic tensor function, i.e.

$$\operatorname{tr}\boldsymbol{A} = \operatorname{tr}[\boldsymbol{Q}\boldsymbol{A}\boldsymbol{Q}^T], \quad \operatorname{tr}[\operatorname{Cof}\boldsymbol{A}] = \operatorname{tr}\big[\operatorname{Cof}[\boldsymbol{Q}\boldsymbol{A}\boldsymbol{Q}^T]\big] , \quad \det\boldsymbol{A} = \det[\boldsymbol{Q}\boldsymbol{A}\boldsymbol{Q}^T] , \tag{2.88}$$

and consequently the representation

$$\boldsymbol{Y}(\boldsymbol{A}) = f_1\mathbf{1} + f_2\boldsymbol{A} + f_3\boldsymbol{A}^2 \tag{2.89}$$

for a polynomial tensor function $\boldsymbol{Y}(\boldsymbol{A})$ is isotropic if the coefficients f_1, f_2, f_3 are scalar-valued polynomial functions in terms of the principal invariants of $\boldsymbol{A}$, i.e.,

$$f_a = f_a[I_1(\boldsymbol{A}), I_2(\boldsymbol{A}), I_3(\boldsymbol{A})], \quad a = 1, 2, 3 . \tag{2.90}$$

Thus for the description of an isotropic material behavior we apply this representation theorem to the second Piola-Kirchhoff stress tensor $\boldsymbol{S}$ in terms of the right Cauchy-Green tensor $\boldsymbol{C}$, i.e.

$$\boldsymbol{S}(\boldsymbol{C}) = 2\frac{\partial\psi}{\partial\boldsymbol{C}} = f_1\mathbf{1} + f_2\boldsymbol{C} + f_3\boldsymbol{C}^2 , \tag{2.91}$$

where the coefficients f_1, f_2, f_3 are now expressed in terms of the principal invariants of $\boldsymbol{C}$

$$I_1 = \operatorname{tr}\boldsymbol{C}, \; I_2 = \operatorname{tr}[\operatorname{Cof}\boldsymbol{C}], \; I_3 = \det\boldsymbol{C} . \tag{2.92}$$

In the following we use the abbreviation I_1, I_2, I_3 in the sense of (2.92). For some applications it may be convenient to express the constitutive equations in terms of the so-called *main invariants*

$$J_1 = \operatorname{tr}\boldsymbol{C}, \quad J_2 = \operatorname{tr}[\boldsymbol{C}^2], \quad J_3 = \operatorname{tr}[\boldsymbol{C}^3] , \tag{2.93}$$

which yield the relations

$$I_1 = J_1, \quad I_2 = \tfrac{1}{2}(J_1^2 - J_2), \quad I_3 = \tfrac{1}{3}(J_3 - \tfrac{3}{2}J_1J_2 + \tfrac{1}{2}J_1^3) . \tag{2.94}$$

In regard to the free energy the function ψ must also be an isotropic scalar-valued function in terms of the whole set of principal invariants of $\boldsymbol{C}$, i.e.

$$\psi(\boldsymbol{C}) = \psi(I_1, I_2, I_3) . \tag{2.95}$$

Inserting the previous equation into the representation (2.91) enables the identification of the coefficients. By applying the alternative expression $\boldsymbol{C}^2 = I_1\boldsymbol{C} - I_2\mathbf{1} + I_3\boldsymbol{C}^{-1}$, deduced from Equation $(2.87)_2$, we achieve the tensor $\boldsymbol{S}$ in the form

$$\boldsymbol{S}^{\text{iso}} = 2\left[\left(\frac{\partial\psi}{\partial I_1} + \frac{\partial\psi}{\partial I_2}I_1\right)\mathbf{1} - \frac{\partial\psi}{\partial I_2}\boldsymbol{C} + \frac{\partial\psi}{\partial I_3}\operatorname{Cof}\boldsymbol{C}\right] . \tag{2.96}$$

Using Equation (2.68) and considering the symmetry $\frac{\partial^2\psi}{\partial I_i\partial I_j} = \frac{\partial^2\psi}{\partial I_j\partial I_i}$ the material tangent

moduli is computed by [3.)]

$$\begin{aligned}\mathbb{C}^{\text{iso}} = 4\Bigg[& \frac{\partial^2\psi}{\partial I_1 \partial I_1}\mathbf{1}\otimes\mathbf{1} + \frac{\partial^2\psi}{\partial I_2 \partial I_2}\{I_1\mathbf{1}-\boldsymbol{C}\}\otimes\{I_1\mathbf{1}-\boldsymbol{C}\} \\ & + \frac{\partial^2\psi}{\partial I_3 \partial I_3}\,\text{Cof}\,\boldsymbol{C}\otimes\text{Cof}\,\boldsymbol{C} \\ & + \frac{\partial^2\psi}{\partial I_2 \partial I_1}[\mathbf{1}\otimes\{I_1\mathbf{1}-\boldsymbol{C}\} + \{I_1\mathbf{1}-\boldsymbol{C}\}\otimes\mathbf{1}] \\ & + \frac{\partial^2\psi}{\partial I_3 \partial I_1}[\mathbf{1}\otimes\text{Cof}\,\boldsymbol{C} + \text{Cof}\,\boldsymbol{C}\otimes\mathbf{1}] \\ & + \frac{\partial^2\psi}{\partial I_3 \partial I_2}[\{I_1\mathbf{1}-\boldsymbol{C}\}\otimes\text{Cof}\,\boldsymbol{C} + \text{Cof}\,\boldsymbol{C}\otimes\{I_1\mathbf{1}-\boldsymbol{C}\}] \\ & + \frac{\partial\psi}{\partial I_2}[\mathbf{1}\otimes\mathbf{1} - \mathbf{1}\boxtimes\mathbf{1}] + \frac{\partial\psi}{\partial I_3}I_3[\boldsymbol{C}^{-1}\otimes\boldsymbol{C}^{-1} - \boldsymbol{C}^{-1}\boxtimes\boldsymbol{C}^{-1}]\Bigg] .\end{aligned} \tag{2.97}$$

Anisotropic Functions. A scalar-valued function h and a second-order tensor-valued function $\boldsymbol{H}$ are called *anisotropic*, if for any argument the following conditions are satisfied

$$\left.\begin{aligned} y(\alpha,\boldsymbol{a},\boldsymbol{A}) &= y(\alpha,\boldsymbol{Q}\boldsymbol{a},\boldsymbol{Q}\boldsymbol{A}\boldsymbol{Q}^T) \\ \boldsymbol{Q}\,\boldsymbol{Y}(\alpha,\boldsymbol{a},\boldsymbol{A})\,\boldsymbol{Q}^T &= \boldsymbol{Y}(\alpha,\boldsymbol{Q}\boldsymbol{a},\boldsymbol{Q}\boldsymbol{A}\boldsymbol{Q}^T)\end{aligned}\right\} \quad \forall\,\boldsymbol{Q}\in\mathcal{G}\subset\text{O}(3)\,, \tag{2.98}$$

where $\alpha\in\mathbb{R}$, $\boldsymbol{a}\in\mathbb{R}^3$ and $\boldsymbol{A}\in\mathbb{R}^{3\times3}$. An anisotropic function is also referred to as a $\mathcal{G}$-invariant function with respect to the whole argument list. Note that compared to definition (2.84) the group $\mathcal{G}$ is only a subset of O(3).

The list of arguments in Equation (2.98) can be extended straightforwardly to $(\alpha_1,\dots\alpha_l,\boldsymbol{a}_1,\dots\boldsymbol{a}_m,\boldsymbol{A}_1,\dots\boldsymbol{A}_n)$. Such an extension is used for the construction of the constitutive equations in Section 4.2.1, wherein the modeling of anisotropic material response of soft biological tissues is described under consideration of a coordinate-invariant representation. Taking up again the reduced form of the constitutive equations (2.83) and considering a material symmetry group $\mathcal{G}\subset\text{O}(3)$ we achieve anisotropic tensor functions for the free energy function ψ and the second Piola-Kirchhoff stress tensor $\boldsymbol{S}$

$$\left.\begin{aligned} \psi(\boldsymbol{C}) &= \psi(\boldsymbol{Q}\boldsymbol{C}\boldsymbol{Q}^T) \\ \boldsymbol{Q}\boldsymbol{S}(\boldsymbol{C})\boldsymbol{Q}^T &= \boldsymbol{S}(\boldsymbol{Q}\boldsymbol{C}\boldsymbol{Q}^T)\end{aligned}\right\} \quad \forall\,\boldsymbol{Q}\in\mathcal{G}\,. \tag{2.99}$$

We now enforce the above mentioned extension of the argument list by introducing the $\mathcal{G}$-invariant structural tensors $\boldsymbol{\Xi}$. They consist of the amount of first-order structural tensors $\boldsymbol{a}_1,\boldsymbol{a}_2,\dots$ and the second-order structural tensors $\boldsymbol{M}_1,\boldsymbol{M}_2,\dots$ collected as $\boldsymbol{\Xi}=\{\boldsymbol{a}_1,\boldsymbol{a}_2,\dots\boldsymbol{M}_1,\boldsymbol{M}_2,\dots\}$ with the corresponding transformation

$$\boldsymbol{Q}*\boldsymbol{\Xi} = \{\boldsymbol{Q}\boldsymbol{a}_1,\boldsymbol{Q}\boldsymbol{a}_2,\dots\boldsymbol{Q}\boldsymbol{M}_1\boldsymbol{Q}^T,\boldsymbol{Q}\boldsymbol{M}_2\boldsymbol{Q}^T,\dots\} \quad \forall\,\boldsymbol{Q}\in\text{O}(3)\,. \tag{2.100}$$

With the extension of the argument list and Equation (2.100) we obtain

$$\left.\begin{aligned} \psi(\boldsymbol{C},\boldsymbol{\Xi}) &= \psi(\boldsymbol{Q}\boldsymbol{C}\boldsymbol{Q}^T,\boldsymbol{Q}*\boldsymbol{\Xi}) \\ \boldsymbol{Q}\boldsymbol{S}(\boldsymbol{C},\boldsymbol{\Xi})\boldsymbol{Q}^T &= \boldsymbol{S}(\boldsymbol{Q}\boldsymbol{C}\boldsymbol{Q}^T,\boldsymbol{Q}*\boldsymbol{\Xi})\end{aligned}\right\} \quad \forall\,\boldsymbol{Q}\in\text{O}(3)\,, \tag{2.101}$$

[3.)] Note: $(\boldsymbol{A}\boxtimes\boldsymbol{B})(\boldsymbol{a}\otimes\boldsymbol{b}) := \boldsymbol{A}\boldsymbol{a}\otimes\boldsymbol{B}\boldsymbol{b}\quad\forall\boldsymbol{A},\boldsymbol{B}\in\mathbb{R}^{3\times3},\ \boldsymbol{a},\boldsymbol{b}\in\mathbb{R}^3$, cf. [56, 90]

which represents the definition of an isotropic tensor function in the complete list of arguments $(\boldsymbol{C}, \boldsymbol{\Xi})$. Therefore, the concept of structural tensors, presented with important applications in BOEHLER [27; 28], is also referred to as the isotropicization of anisotropic tensor functions. Thus, the principle of material symmetry is a priori satisfied, considering Equation (2.98) and using an extended argument list $(\boldsymbol{C}, \boldsymbol{\Xi})$.

Since we later deal with a transversely isotropic material behavior in the context of arterial walls, the application of the concept of structural tensors to this case is shown. For treatments of further material symmetry groups we refer to ZHENG AND SPENCER [259], XIAO [255], EBBING [64] and references therein. The transverse isotropy features a preferred direction $\boldsymbol{a}$, defined in the reference configuration, and a rotation-symmetry around this preferred direction. The corresponding material symmetry group $\mathcal{G}_{\text{ti}}$ is composed on

$$\mathcal{G}_{\text{ti}} := \{\pm\mathbf{1};\, \boldsymbol{Q}(\alpha, \boldsymbol{a}) \,|\, 0 < \alpha < 2\pi\} \tag{2.102}$$

where $\boldsymbol{Q}(\alpha, \boldsymbol{a})$ are all rotations about the $\boldsymbol{a}$-axis. For the extension of the argument list of the constitutive equations we introduce the structural tensor

$$\boldsymbol{M} = \boldsymbol{a} \otimes \boldsymbol{a} \quad \text{with } |\boldsymbol{a}| = 1 \;\Rightarrow\; \operatorname{tr} \boldsymbol{M} = 1 \,, \tag{2.103}$$

cf. BOEHLER [29], which preserves the material symmetry group $\mathcal{G}_{\text{ti}}$ of the transverse isotropy. For the derivation of the corresponding invariants, depending on two symmetric tensor $\boldsymbol{C}$ and $\boldsymbol{M}$, we refer to RIVLIN [182] and use the *mixed invariants*

$$J_4 = \operatorname{tr}[\boldsymbol{C}\boldsymbol{M}], \quad J_5 = \operatorname{tr}[\boldsymbol{C}^2\boldsymbol{M}], \quad \widetilde{J}_4 = \operatorname{tr}[\boldsymbol{C}\boldsymbol{M}^2], \quad \widetilde{J}_5 = \operatorname{tr}[\boldsymbol{C}^2\boldsymbol{M}^2] \,. \tag{2.104}$$

Note, that with the reformulation $J_4 = \boldsymbol{a} \cdot \boldsymbol{C}\boldsymbol{a}$ of the fourth invariant we achieve an alternative formulation, given by SPENCER [216; 217], from which J_4 can be interpreted as the square of the stretch in the direction $\boldsymbol{a}$, c.f.

$$J_4 = \boldsymbol{a} \cdot \boldsymbol{C}\boldsymbol{a} = \boldsymbol{F}\boldsymbol{a} \cdot \boldsymbol{F}\boldsymbol{a} = \left(\frac{|\widetilde{\boldsymbol{a}}|}{|\boldsymbol{a}|}\right)^2 \quad \text{with } \widetilde{\boldsymbol{a}} = \boldsymbol{F}\boldsymbol{a} \text{ and } |\boldsymbol{a}| = 1 \,. \tag{2.105}$$

Since we suppose the unit length of the preferred direction vector $\boldsymbol{a}$, the normalization condition $\|\boldsymbol{M}\| = 1$ holds and we obtain the identities $\widetilde{J}_4 \equiv J_4$ and $\widetilde{J}_5 \equiv J_5$. So we can omit the terms $\widetilde{J}_4$ and $\widetilde{J}_5$ and achieve the functional bases

$$\mathcal{I}^1_{\text{ti}} := \{I_1, I_2, I_3, J_4, J_5\} \quad \text{or} \quad \mathcal{I}^2_{\text{ti}} := \{J_1, J_2, J_3, J_4, J_5\} \quad , \tag{2.106}$$

which are invariant under all transformations with elements of $\mathcal{G}_{\text{ti}}$. Consequently, the polynomial functions in elements of the bases are also invariant under these transformations. Thus, the general form

$$\psi = \sum_k \psi^{\text{ti}}_k(L_i | L_i \in \mathcal{I}^{\text{ti}}_j) + c \quad \text{for} \quad j = 1 \quad \text{or} \quad j = 2 \tag{2.107}$$

for the free energy function ψ reflecting the material behavior of a transversely isotropic material is used. In order to fulfill the non-essential normalization condition $\psi(\mathbf{1}) = 0$ we introduce the constant $c \in \mathbb{R}$. In the sequel we restrict ourselves only to energy functions formulated in elements of the basis $\mathcal{I}^1_{\text{ti}}$. The corresponding second Piola-Kirchhoff stress tensor is calculated from

$$\boldsymbol{S}^{\text{ti}} = 2 \sum_i \left(\frac{\partial \psi}{\partial L_i} \frac{\partial L_i}{\partial \boldsymbol{C}}\right) \quad \text{with} \quad L_i \in \mathcal{I}^{\text{ti}}_1 \,, \tag{2.108}$$

which leads to

$$\boldsymbol{S}^{\text{ti}} = \boldsymbol{S}^{\text{iso}} + 2\left[\frac{\partial\psi}{\partial J_4}\boldsymbol{M} + \frac{\partial\psi}{\partial J_5}(\boldsymbol{C}\boldsymbol{M} + \boldsymbol{M}\boldsymbol{C})\right] \tag{2.109}$$

under consideration of the second Piola-Kirchhoff stress tensor $\boldsymbol{S}^{\text{iso}}$ (2.96) for the isotropic case. Using the material tangent moduli $\mathbb{C}^{\text{iso}}$ (2.97) we end up with the moduli for the transverse isotropy

$$\begin{aligned}
\mathbb{C}^{\text{ti}} = \mathbb{C}^{\text{iso}} + 4\Bigg[& \frac{\partial^2\psi}{\partial J_4\partial J_4}\boldsymbol{M}\otimes\boldsymbol{M} + \frac{\partial^2\psi}{\partial J_5\partial J_5}\{\boldsymbol{C}\boldsymbol{M}+\boldsymbol{M}\boldsymbol{C}\}\otimes\{\boldsymbol{C}\boldsymbol{M}+\boldsymbol{M}\boldsymbol{C}\} \\
& + \frac{\partial^2\psi}{\partial I_1\partial J_4}\big[\boldsymbol{1}\otimes\boldsymbol{M} + \boldsymbol{M}\otimes\boldsymbol{1}\big] \\
& + \frac{\partial^2\psi}{\partial I_1\partial J_5}\big[\boldsymbol{1}\otimes\{\boldsymbol{C}\boldsymbol{M}+\boldsymbol{M}\boldsymbol{C}\} + \{\boldsymbol{C}\boldsymbol{M}+\boldsymbol{M}\boldsymbol{C}\}\otimes\boldsymbol{1}\big] \\
& + \frac{\partial^2\psi}{\partial I_2\partial J_4}\big[\{I_1\boldsymbol{1}-\boldsymbol{C}\}\otimes\boldsymbol{M} + \boldsymbol{M}\otimes\{I_1\boldsymbol{1}-\boldsymbol{C}\}\big] \\
& + \frac{\partial^2\psi}{\partial I_2\partial J_5}\big[\{I_1\boldsymbol{1}-\boldsymbol{C}\}\otimes\{\boldsymbol{C}\boldsymbol{M}+\boldsymbol{M}\boldsymbol{C}\} + \{\boldsymbol{C}\boldsymbol{M}+\boldsymbol{M}\boldsymbol{C}\}\otimes\{I_1\boldsymbol{1}-\boldsymbol{C}\}\big] \\
& + \frac{\partial^2\psi}{\partial I_3\partial J_4}\big[\operatorname{Cof}\boldsymbol{C}\otimes\boldsymbol{M} + \boldsymbol{M}\otimes\operatorname{Cof}\boldsymbol{C}\big] \\
& + \frac{\partial^2\psi}{\partial I_3\partial J_5}\big[\operatorname{Cof}\boldsymbol{C}\otimes\{\boldsymbol{C}\boldsymbol{M}+\boldsymbol{M}\boldsymbol{C}\} + \{\boldsymbol{C}\boldsymbol{M}+\boldsymbol{M}\boldsymbol{C}\}\otimes\operatorname{Cof}\boldsymbol{C}\big] \\
& + \frac{\partial^2\psi}{\partial J_4\partial J_5}\big[\{\boldsymbol{C}\boldsymbol{M}+\boldsymbol{M}\boldsymbol{C}\}\otimes\boldsymbol{M} + \boldsymbol{M}\otimes\{\boldsymbol{C}\boldsymbol{M}+\boldsymbol{M}\boldsymbol{C}\}\big] \\
& + \frac{\partial\psi}{\partial J_5}\big[(\boldsymbol{1}\boxtimes\boldsymbol{M})^{\overset{34}{T}} + (\boldsymbol{M}\boxtimes\boldsymbol{1})^{\overset{34}{T}}\big]\Bigg] ,
\end{aligned} \tag{2.110}$$

where the symmetry $\frac{\partial^2\psi}{\partial I_k\partial I_j} = \frac{\partial^2\psi}{\partial I_j\partial I_k}$ is considered and the operation $(\bullet)^{\overset{34}{T}}$ appears in index notation as $\big[\{(\bullet)\}_{ijkl}\big]^{\overset{34}{T}} = \{(\bullet)\}_{ijlk}$.

Before we start with the introduction of several specific free energy functions in the next section we would shortly introduce the term *stress-free reference configuration* in the context of hyperelastic material. From the physical point of view it is obviously that the stresses in such a material are only induced by deformations. So in the unloaded state ($\boldsymbol{C} = \boldsymbol{1}$) the stresses in the body of interest must be zero. The mathematical formulation of the so-called *natural state condition* reads

$$\boldsymbol{S}(\boldsymbol{C} = \boldsymbol{1}) = \boldsymbol{0}\,. \tag{2.111}$$

To check the condition for a specific material model, the deformation state $\boldsymbol{C} = \boldsymbol{1}$ is inserted into the corresponding form of the second Piola-Kirchhoff stresses, here Equation (2.109) for a transversely isotropic material, i.e.

$$\left(\frac{\partial\psi}{\partial I_1} + 2\frac{\partial\psi}{\partial I_2} + \frac{\partial\psi}{\partial I_3}\right)\boldsymbol{1} + \left(\frac{\partial\psi}{\partial J_4} + 2\frac{\partial\psi}{\partial J_5}\right)\boldsymbol{M} = 0 \tag{2.112}$$

In general this condition leads to additional restrictions for the material parameters. On this account we introduce several polyconvex free energy functions in the following sections, which imply a stress-free reference configuration.

2.6 Hyperelasticity: Free Energy Function

For the description of a hyperelastic material behavior the existence of a Helmholtz free energy function ψ is postulated as a consequence of the second principle of thermodynamics, c.f. section 2.4.3. Afterwards we introduced several restrictions for the design of the constitutive equations, e.g. material symmetries, and give some concepts, e.g. structural tensors, to deal with them. All these conditions are formulated in order to obtain a physically reasonable material behavior. Further restrictions covering the form of the free energy function carry great weight especially for the constitutive modeling of the hyper elasticity. As a result of these considerations we prefer the usage of polyconvex energy functions. After a short introduction to the notion of polyconvexity in the sense of finite elasticity we give examples for polyconvex isotropic and anisotropic energy functions in the subsequent sections. A summary of the definition of convexity and its implications can be found in Appendix B. For deeper studies we refer to e. g. Ball [6; 7], Marsden and Hughes [142], Dacorogna [53] and Šilhavý [232].

The additional restrictions are not deduced from the condition, e.g. balance equations, which are introduced in the previous sections. They are rather a question of the mathematical treatment of boundary value problems by variational principles, since we are interested to achieve stable algorithms for our analyses. Mainly two aspects are important in this context: the material stability and the existence of deformations minimizing a given hyperelastic potential.

The first argument could be treated by the Legendre-Hadamard Inequality, which ensures the existence of real wave speeds at each material point of the considered body and in each direction, c.f. Marsden and Hughes [142], Truesdell and Noll [229]. This behavior is analyzed by the ellipticity of the corresponding acoustic tensor, which is strongly related to the notion of rank-one convexity. A material breaking this inequality is referred to as unstable. Applications in the context of ellipticity and material stability are presented in e.g. Merodio and Ogden [146], Merodio and Neff [145], Schröder et al. [196].

A sufficient condition for the existence of minimizers is the sequential weak lower semicontinuity (s.w.l.s.) of $\int_{\mathcal{B}} \psi(\boldsymbol{F})\, \mathrm{d}V$ and the coercivity of ψ. Details on the notion of s.w.l.s. can be found in advanced textbooks on variational methods. The restriction of s.w.l.s.

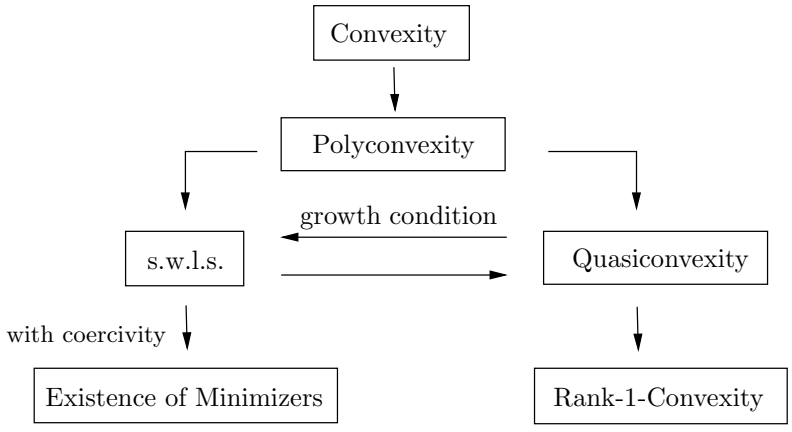

Figure 2.5: Implications of generalized convexity conditions, sequential-weak-lower-semicontinuity (s.w.l.s.) and existence of minimizers, taken from Schröder [192].

is fulfilled automatically in case of a free energy function, which is convex with respect to the deformation gradient. Convexity means in a rather simple description, that the straight connecting line between two arbitrary points of a convex function is located within the corresponding convex domain. But the convexity condition is too restrictive, since this property contradicts several physical requirements, see e. g. RIVLIN [183], HILL [98], COLEMAN AND NOLL [51], BALL [7]. A more suitable condition represents the *polyconvexity* in the sense of BALL [6; 7], see also MARSDEN AND HUGHES [142], CIARLET [47]. It states, that a function $\psi(\boldsymbol{F}) = \mathcal{P}(\boldsymbol{F}, \operatorname{Cof}\boldsymbol{F}, \det\boldsymbol{F})$ is polyconvex, if it is convex with respect to one of the arguments $\boldsymbol{F}$, $\operatorname{Cof}\boldsymbol{F}$ and $\det\boldsymbol{F}$. In contrast to the convexity condition the polyconvexity states a pointwise requirement on the free energy function.

Considering the implications of convexity conditions we show in Figure 2.5 the relations between convexity, existence of miminizeres and material stability (rank-one convexity/Legendre-Hadamard ellipticity). From this our preference of polyconvex energy function is founded. It implies one of two conditions for the existence of minimizers (s.w.l.s.) and the guarantee of material stability (rank-one convexity/Legendre-Hadamard ellipticity). Simultaneously, neither side conditions, except coercivity, has to be fulfilled like growth condition for quasiconvexity nor contradictions of physical requirements occur as mentioned for convexity. Note, that the converse implications are not true; for more information we refer to DACOROGNA [53], ŠILHAVÝ [232] and reference therein.

2.6.1 Isotropic Polyconvex Energies

In this section we summarize several isotropic energy functions which satisfy the polyconvexity condition. Here we restrict ourselves to the specification of the conditions among which the functions are polyconvex. Since we are only interested in the application of the material models we omit the proofs of polyconvexity and give the appropriate references.

For the construction of isotropic energy functions we introduce in Section 2.5.3 the set of principal invariants I_1, I_2 and I_3. Thus, the most obvious functions are the invariants themselves in a factorized and exponentiated form, i.e.

$$\psi_1^{\text{iso}} = \alpha_1 I_1^{\alpha_2}\,, \quad \psi_2^{\text{iso}} = \alpha_1 I_2^{\alpha_2}\,, \quad \psi_3^{\text{iso}} = \alpha_1 I_3^{\alpha_2} \quad \text{with} \quad \alpha_1 > 0\,, \quad \alpha_2 \geq 1\,. \tag{2.113}$$

The restriction of the material parameter α_1, α_2 is done due to the polyconvexity condition, see e.g. SCHRÖDER AND NEFF [193]. In some cases the energy function is decomposed into a volumetric part and an isochoric part. Thereby the deformation is split into a part driven by the volume change – also called volume dilatation – and the remaining distortional part. For that the additive split of the free energy function is suitable:

$$\psi(\boldsymbol{C}) = \psi^{\text{vol}}(J) + \psi^{\text{isoch}}(\tilde{\boldsymbol{C}})\,, \tag{2.114}$$

where $\tilde{\boldsymbol{C}} := J^{-2/3}\boldsymbol{C} = \det[\boldsymbol{C}]^{-1/3}\boldsymbol{C}$ denotes the isochoric part of the right Cauchy-Green tensor because $\det\tilde{\boldsymbol{C}} = 1$ holds, see e. g. WRIGGERS [254]. This strategy is even useful in case of modeling quasi-incompressible materials as we do in the sequel of this thesis. The isochoric counterpart $\tilde{I}_1$ of the first invariant leads to the polyconvex isochoric function

$$\psi_4^{\text{iso}} = \alpha_1 \frac{I_1^{\alpha_2}}{I_3^{\frac{\alpha_2}{3}}} = \alpha_1 \tilde{I}_1^{\alpha_2} \quad \text{with} \quad \alpha_1 > 0\,, \quad \alpha_2 \geq 1\,, \tag{2.115}$$

see Neff [158], Schröder and Neff [193]. The second invariant can be rewritten in its isochoric form

$$\psi_5^{\text{iso}} = \alpha_1 \frac{I_2^{\alpha_2}}{I_3^{\frac{2}{3}\alpha_2}} = \alpha_1 \tilde{I}_2^{\alpha_2} \quad \text{with} \quad \alpha_1 > 0\,, \quad \alpha_2 \geq 2\,, \tag{2.116}$$

and its polyconvexity is proved analogously to Equation (2.115). For volumetric polyconvex free energy functions $\psi^{\text{vol}}(J)$ possible formulations in terms of $I_3 = \det \boldsymbol{C}$ are

$$\psi_6^{\text{iso}} = \alpha_1 I_3^{\alpha_2}\,, \quad \psi_7^{\text{iso}} = -\alpha_1 \ln I_3 \quad \text{with} \quad \alpha_1 > 0\,, \quad \alpha_2 \geq 1\,. \tag{2.117}$$

All these functions are polyconvex considering the given restrictions towards the parameters but none of them satisfy the stress-free natural state, cf. Equation (2.111). To meet this requirement in Schröder and Neff [193] and Hartmann and Neff [92] several polyconvex functions are given and among other things proved with respect to polyconvexity. Some of them used in the sequel of this thesis are

$$\begin{aligned}
\psi_7^{\text{iso}} &= \alpha_1 \left(I_3 - \ln I_3\right) && \text{with} \quad \alpha_1 > 0\,, \\
\psi_8^{\text{iso}} &= \alpha_1 \left(\tilde{I}_1^{\alpha_2} - 3^{\alpha_2}\right)^{\alpha_3} && \text{with} \quad \alpha_1 > 0\,, \quad \alpha_2, \alpha_3 \geq 1\,, \\
\psi_9^{\text{iso}} &= \alpha_1 \left(I_3^{\alpha_2} + \frac{1}{I_3^{\alpha_2}} - 2\right)^{\alpha_3} && \text{with} \quad \alpha_1 > 0\,, \quad \alpha_2, \alpha_3 \geq 1\,.
\end{aligned} \tag{2.118}$$

Here, we remark a special characteristic of the third function in the latter equation regarding the incompressibility. The function can be used as a penalty term with respect to the deviation of the incompressibility condition $I_3 = \det \boldsymbol{C} = 1$. In this thesis this special feature is taken into account during the formulation of free energy functions representing the material behavior of soft tissues, cf. section 4.2.

Another important class is represented by the *Ogden-type materials* which contains several classical models describing an isotropic material behavior in finite elasticity. They hark back to the publications by Ogden in 1972 about "large deformation isotropic elasticity" concerning incompressible, cf. Ogden [165], and compressible rubberlike solids, cf. Ogden [166]. A general form in case of compressible materials in term of the principal invariants is given by

$$\begin{aligned}
\psi^{\text{Ogden}} &= \sum_{i=1}^{m} \alpha_i \|\boldsymbol{F}\|^{\gamma_i} && + \sum_{i=1}^{n} \beta_i \|\operatorname{Cof} \boldsymbol{F}\|^{\delta_i} && + \Gamma(\det \boldsymbol{F}) \\
&= \sum_{i=1}^{m} \alpha_i \operatorname{tr} \boldsymbol{C}^{\,\gamma_i/2} && + \sum_{i=1}^{n} \beta_i \operatorname{tr}[\operatorname{Cof} \boldsymbol{C}]^{\delta_i/2} && + \Gamma(\det \boldsymbol{F}) \\
&= \sum_{i=1}^{m} \alpha_i I_1^{\gamma_i/2} && + \sum_{i=1}^{n} \beta_i I_2^{\delta_i/2} && + \Gamma(\sqrt{I_3})\,,
\end{aligned} \tag{2.119}$$

where the relation $\|\boldsymbol{F}\|^2 = \operatorname{tr} \boldsymbol{C}$ is used. In Ciarlet [47] it is show, that such a function is polyconvex if the material parameters are restricted by α_i, $\beta_i > 0$ and γ_i, $\delta_i \geq 1$ as well as the third function $\Gamma(\det \boldsymbol{F})$ is convex with respect to its argument and shows the property $\Gamma(\det \boldsymbol{F}) \to +\infty$ as $\det \boldsymbol{F} \to 0^+$. Without the consideration of the third term $\Gamma(\det \boldsymbol{F})$ in Equation (2.119) we achieve a model for incompressible materials. One

example of an Ogden-type model is the *Mooney-Rivlin* model in case of compressibility in the form

$$\psi^{\text{MooRiv}} = \alpha_1 I_1 + \alpha_2 I_2 + \Gamma(I_3) \quad \text{with} \quad \Gamma(I_3) = \delta_1 I_3 - \delta_2 \ln(I_3) \,, \tag{2.120}$$

where the restrictions $\alpha_1, \alpha_2, \delta_1, \delta_2 > 0$ hold the polyconvexity condition, cf. Ciarlet and Geymonat [46]. The material model was originally introduced without the Γ-term by Mooney [152] and Rivlin [183] for the treatment of incompressible material. If we take a look at the corresponding second Piola-Kirchhoff stresses

$$\boldsymbol{S}^{\text{MooRiv}} = (2\alpha_1 + 2\alpha_2 I_1)\,\mathbf{1} - 2\alpha_2\,\boldsymbol{C} + \left(2\delta_1 - 2\frac{\delta_2}{I_3}\right) \operatorname{Cof}\boldsymbol{C} \,, \tag{2.121}$$

derived under consideration of Equation (2.96) , the stress-free reference configuration is not preserved a priori. The necessary material parameter dependence is ascertained by evaluating the natural state (2.111) of $\boldsymbol{S}^{\text{MooRiv}}$ under consideration of the principal invariants in the natural state ($\boldsymbol{C} = \mathbf{1}$)

$$I_1(\boldsymbol{C} = \mathbf{1}) = I_2(\boldsymbol{C} = \mathbf{1}) = 3, \quad I_3(\boldsymbol{C} = \mathbf{1}) = 1 \,. \tag{2.122}$$

This leads to the relations

$$\begin{aligned} \boldsymbol{S}^{\text{MooRiv}}(\boldsymbol{C} = \mathbf{1}) = \mathbf{0} \quad &\Rightarrow 2\,(\alpha_1 + 3\alpha_2 - \alpha_2 + \delta_1 - \delta_2)\;\mathbf{1} = \mathbf{0} \\ &\Rightarrow \delta_2 = \alpha_1 + 2\alpha_2 + \delta_1 \,, \end{aligned} \tag{2.123}$$

which restrict the choice of the material parameter δ_2 in addition to the ones, which ensure the polyconvexity of ψ^{MooRiv}.

2.6.2 Polyconvex Anisotropic Energies

In the sequel of this thesis we will focus on the transverse isotropy as one central anisotropic material behavior. Thus, we give here an overview of some free energy functions which are applicable in this context. For a wider range of the field dealing with the description of anisotropic materials by polyconvex functions we refer to e.g. Holzapfel [106], Schröder et al. [196], Balzani [8], Ebbing [64], Schröder [192] and the references given in the sequel.

In section 2.5.3 we introduce the framework of structural tensors and provide the functional basis $\mathcal{F}^1_{\text{ti}}$ $(2.106)_1$ for the construction of transversely isotropic energies. Therein the invariants J_4 and J_5 imply the anisotropy since they are based on the structural tensor. For a polyconvex function based on $J_4 = \operatorname{tr}[\boldsymbol{C}\boldsymbol{M}]$ we formulate

$$\psi_1^{\text{ti}} = \alpha_1 J_4^{\alpha_2} \,, \quad \psi_2^{\text{ti}} = \alpha_1 \frac{J_4^{\alpha_2}}{I_3^{\frac{1}{3}}} \quad \text{with} \quad \alpha_1 > 0 \,, \quad \alpha_2 \geq 1 \quad . \tag{2.124}$$

The proof of polyconvexity is given by Schröder and Neff [193]. However the analogous formulation in terms of $J_5 = \operatorname{tr}[\boldsymbol{C}^2\boldsymbol{M}]$ is not advisable because Merodio and Neff [145] show the non-polyconvexity of this invariant. To enable a formulation using this quantity in Schröder and Neff [193] the polyconvex function

$$K_3 := \operatorname{tr}[\operatorname{Cof}[\boldsymbol{C}]\,\boldsymbol{D}] = I_1 J_4 - J_5 = \| \operatorname{Cof}\boldsymbol{F}\|^2 - \| \operatorname{Cof}\boldsymbol{F}\,\boldsymbol{a}\|^2 \tag{2.125}$$

is introduced using an alternative structural tensor $\boldsymbol{D} := \mathbf{1} - \boldsymbol{M}$ with $\operatorname{tr}\boldsymbol{D} = 2$. This function is motivated by the physical interpretation, that $\sqrt{K_3}$ controls the deformation of an area element with a unit normal vector perpendicular to the preferred direction $\boldsymbol{a}$. Since we are interested in energy functions with a stress-free reference configuration we pass on the straightforward formulation based on Equation (2.125) and refer for that to the references given above.

A construction principle for polyconvex energy functions satisfying the natural state condition (2.111) was published by Balzani et al. [10]. Several functions suitable for the mechanical description of soft biological tissues are also given therein. One of these is the stress-free reference formulation based on J_4, i. e.

$$\psi_3^{\mathrm{ti}} = \begin{cases} \alpha_1 (J_4 - 1)^{\alpha_2} & \text{for} \quad J_4 \geq 1 \\ 0 & \text{for} \quad J_4 < 1 \,, \end{cases} \tag{2.126}$$

with $\alpha_1 \geq 0$ and $\alpha_2 > 1$. The same form using the isochoric counterpart $\tilde{J}_4 = J_4 / I_3^{1/3}$ is also a suitable polyconvex free energy function describing transversely isotropic material behavior. A polyconvex energy function in terms of K_3, which satisfy the stress-free reference configuration, also results from the application of the aforementioned construction principle and is given in the associated reference. Based on the knowledge of the incompressibility of such a material and the already mentioned physical meaning of K_3, it can be seen that this quantity is raised during a stretch in the preferred direction, here the embedded fibers. Hence this behavior is exploited to construct the free energy function

$$\psi_5^{\mathrm{ti}} = \begin{cases} \alpha_1 (K_3 - 2)^{\alpha_2} & \text{for} \quad K_3 \geq 2 \\ 0 & \text{for} \quad K_3 < 2 \,, \end{cases} \tag{2.127}$$

which generates stresses when the fibers are elongated. The constraints $\alpha_1 \geq 0$ and $\alpha_2 > 1$ ensure the polyconvexity condition and the choice $\alpha_2 > 2$ leads to continuous tangent moduli. The following function was originally proposed by Holzapfel et al. [110] and results as a special case from the construction principles. It is formulated in terms of the mixed invariant $\tilde{J}_4$ and reads

$$\psi_4^{\mathrm{ti}} = \begin{cases} \frac{\alpha_1}{2\alpha_2} \left[\exp[\alpha_2 (\tilde{J}_4 - 1)^2] - 1 \right] & \text{for} \quad J_4 \geq 1 \\ 0 & \text{for} \quad J_4 < 1 \,, \end{cases} \tag{2.128}$$

with $\alpha_1 \geq 0$ and $\alpha_2 > 0$. Note, that the formulation using J_4 instead of its isochoric part $\tilde{J}_4$ was proposed in Holzapfel et al. [111]. Since soft biological tissues show an exponential-type stress-strain behavior this function is also a possible formulation to model the mechanical response of such a material.

3 Finite Element Method

The application of numerical methods has become an essential part of many developmental stages in field of engineering. In some fields they substitute completely the manual or experimental processing step. Beside the application of computer aided design (CAD) the Finite Element Method has been firmly established in the design and analysis of many structural elements. Since this method is a numerical tool for approximate solution of partial differential equations not least the increasing performance of computer hardware has been accelerated this growth process and furthermore does it. In most cases these equations describe boundary value problems, which can have a linear or nonlinear character. Typical fields of application can be found in the automotive and metalworking industry as well as in the aircraft construction and shipbuilding, to name but a few. But in the last years the sector of biomechanics arises as a new field of application for the Finite Element Method, e. g. design of implants or analysis of angiopathy (vessel diseases). In this thesis we use the method for the simulation of the deformation of heterogeneous materials and at first we treat arterial walls and afterwards advanced high strength steels (AHSS). Therefore we introduce in this chapter the basic concept of the Finite Element Method and the numerical treatment regarding the case of incompressible materials as well as the solution of problems represented by a large number of degrees of freedom. Further information can be found in classical textbook concerning this topic, e. g. Wriggers [254], Bathe [18] and Zienkiewicz and Taylor [260].

Starting from a set of differential equations the weak form of the boundary value problem is achieved as a single-field formulation by the application of variational principles. Since we later show several numerical results arising from two dimensional simulations approximating three dimensional problems, we introduce two standard cases for these assumptions. In general the solution of the weak form can not be obtained analytically and thus we discuss the steps of linearization and the approximation in the sense of the isoparametric concept. For the standard displacement approach we introduce two finite element types and their formulation. For the case of an incompressible material we give the theoretical framework of a three-field variational formulation based on the so-called Hu-Washizu principle. Finally we give a brief introduction to the main concept of a parallel solution strategy, the so-called Finite Element Tearing and Interconnecting - Dual Primal (FETI-DP), which is able to obtain the solution of large systems of equations in an efficient way.

3.1 Strong Form of the Boundary Value Problem

The solution of a nonlinear boundary value problem with isothermal and quasi-static, hyperelastic characteristics is achieved by a set of differential equations consisting of

$$\begin{array}{lll} \text{i)} \quad \text{kinematical relations} & (2.8) & \boldsymbol{F} := \operatorname{Grad} \boldsymbol{x} \ , \\ \text{ii)} \quad \text{local form of balance of linear momentum} & (2.52) & \operatorname{Div} \boldsymbol{P} + \rho_0 \boldsymbol{f} = \boldsymbol{0} \ , \\ \text{iii)} \quad \text{material law} & (2.70) & \boldsymbol{P} = \partial_{\boldsymbol{F}} \psi \ . \end{array} \tag{3.1}$$

Alternatively, the set of equations can be formulated in terms of the other kinematical quantities and stress measurements following the definition of work-conjugated pairs.

In the context of boundary value problems the local form of balance of linear momentum $(3.1)_2$ is also referred to as the *strong form of equilibrium*.

The boundary value problem is described fully by the declaration of stress and displacement conditions on the boundary of body $\mathcal{B}_0$. Therefore, the reference surface $\partial\mathcal{B}_0$ is divided into two non-overlapping parts $\partial\mathcal{B}_{0t}$ and $\partial\mathcal{B}_{0u}$, i.e. they satisfy

$$\partial\mathcal{B}_0 = \partial\mathcal{B}_{0t} \cup \partial\mathcal{B}_{0u} \quad \text{and} \quad \partial\mathcal{B}_{0t} \cap \partial\mathcal{B}_{0u} = \emptyset \, . \tag{3.2}$$

Thereby, the prescribed stresses act on the part $\partial\mathcal{B}_{0t}$ and are referred to as *Neumann boundary conditions*. However, for the part $\partial\mathcal{B}_{0u}$ the displacements are prescribed by *Dirichlet boundary conditions*. The boundary conditions in the form

$$\begin{aligned} &\text{Neumann boundary conditions:} && \boldsymbol{T} = \boldsymbol{P}\boldsymbol{N} = \bar{\boldsymbol{t}} && \text{on} \quad \partial\mathcal{B}_{0t} \, , \\ &\text{Dirichlet boundary conditions:} && \boldsymbol{u} = \boldsymbol{u}_0 && \text{on} \quad \partial\mathcal{B}_{0u} \, , \end{aligned} \tag{3.3}$$

are associated to the above system of equations (3.1).

3.2 Weak Form of the Boundary Value Problem

Only in a few cases, where simple boundary value problems are considered, the above mentioned system of differential equations are able to be solved analytically. For more complex problems a discretization method based on the direct methods of the calculus of variation is suitable for achieving a solution, whereby the *weak form of equilibrium* is obtained. As later shown, that form is the basis for the application of the Finite Element Method. For the derivation of the weak form in this section we only consider the displacement vector $\boldsymbol{u}$ as unknown field, which is referred to the standard displacement formulation. We also apply this *single-field variational principle* in the following sections until we introduce a 3-field variational approach in section 3.6. The starting point is the local strong form $(3.1)_2$ and the multiplication of that with a suitable vector-valued test function $\delta\boldsymbol{u} = \{\delta\boldsymbol{u} | \delta\boldsymbol{u} = \boldsymbol{0} \text{ on } \partial\mathcal{B}_u\}$, also refer to the virtual displacements. The integration of the resulting product over the volume of the body $\mathcal{B}_0$ yields

$$\int_{\mathcal{B}_0} [\operatorname{Div} \boldsymbol{P} + \rho_0 \boldsymbol{f}] \cdot \delta\boldsymbol{u} \, \mathrm{d}V = 0 \, , \tag{3.4}$$

considering the boundary conditions (3.3). The recourses to transformation (2.38) under consideration of a vector and a tensor as well as to the Gauss divergence theorem (2.40) obtain the weak form of equilibrium

$$G(\boldsymbol{u}, \delta\boldsymbol{u}) := \underbrace{\int_{\mathcal{B}_0} \boldsymbol{P} : \delta\boldsymbol{F} \, \mathrm{d}V}_{G^{\mathrm{int}}} - \underbrace{\left[\int_{\mathcal{B}_0} \rho_0 \boldsymbol{f} \cdot \delta\boldsymbol{u} \, \mathrm{d}V + \int_{\partial\mathcal{B}_{0t}} \bar{\boldsymbol{t}} \cdot \delta\boldsymbol{u} \, \mathrm{d}A \right]}_{G^{\mathrm{ext}}} = 0 \tag{3.5}$$

with the virtual counterpart $\delta\boldsymbol{F} = \operatorname{Grad}[\delta\boldsymbol{u}]$ of the deformation gradient. The principle of virtual work is formally equivalent to the weak form of equilibrium, since the test function is interpreted as the vector of virtual displacements as well as the terms G^{int} and G^{ext} as work of internal and external forces acting on body $\mathcal{B}_0$, respectively. Consequently, solving the boundary value problem is comparable with the determination of a stationary point $\boldsymbol{u}$ of a functional Π, referred to as the *total potential energy*,

$$\Pi(\boldsymbol{u}) = \Pi^{\mathrm{int}}(\boldsymbol{u}) + \Pi^{\mathrm{ext}}(\boldsymbol{u}) \quad \rightarrow \quad \text{stat.} \, , \tag{3.6}$$

with the internal and external potential energy

$$\begin{aligned} \Pi^{\text{int}}(\boldsymbol{u}) &= \int_{\mathcal{B}_0} \psi(\boldsymbol{F}(\boldsymbol{u}))\, \mathrm{d}V \ , \\ \Pi^{\text{ext}}(\boldsymbol{u}) &= -\int_{\mathcal{B}_0} \rho_0 \boldsymbol{f} \cdot \boldsymbol{u}\, \mathrm{d}V - \int_{\partial \mathcal{B}_{0t}} \bar{\boldsymbol{t}} \cdot \boldsymbol{u}\, \mathrm{d}A \ . \end{aligned} \tag{3.7}$$

An alternative formulation of the weak form of equilibrium in term of the symmetric first Piola-Kirchhoff stress tensor $\boldsymbol{S}$ reads

$$G(\boldsymbol{u}, \delta\boldsymbol{u}) := \int_{\mathcal{B}_0} \boldsymbol{S} : \frac{1}{2}\delta\boldsymbol{C}\, \mathrm{d}V - \int_{\mathcal{B}_0} \rho_0 \boldsymbol{f} \cdot \delta\boldsymbol{u}\, \mathrm{d}V - \int_{\partial \mathcal{B}_{0t}} \bar{\boldsymbol{t}} \cdot \delta\boldsymbol{u}\, \mathrm{d}A = 0 \ , \tag{3.8}$$

exploiting the relation $\boldsymbol{P} : \delta\boldsymbol{F} = \boldsymbol{S} : \boldsymbol{F}^T \delta\boldsymbol{F}$, the symmetry of $\boldsymbol{S}$ and the variation of the Green-Lagrange strain tensor

$$\delta\boldsymbol{E} = \delta\left[\frac{1}{2}(\boldsymbol{C} - \boldsymbol{1})\right] = \frac{1}{2}\delta\boldsymbol{C} = \frac{1}{2}(\boldsymbol{F}^T\delta\boldsymbol{F} + \delta\boldsymbol{F}^T\boldsymbol{F}) \ . \tag{3.9}$$

3.3 Plain Strain and Plain Stress Condition

In several cases a three dimensional boundary value problem can be approximated by special assumptions leading to a two dimensional finite element model. A classical prototype is a plain strain element, which can be used for problems, where a slice of a structural part is analyzed in which the strain components related to the third dimensions are assumed to be zero. It takes thick geometries that extend long distances away from the two dimensional plane. The assumption of the plane strain model also includes that there are no forces acting normal to the section plane. Typical applications are dams under water pressure loading, sheet rolling and tunnels under pressure, see Figure 3.1a. Its numerical treatment is straightforward, since in the finite element the relevant entries of the strain field are set to zero before evaluating an arbitrary three dimensional constitutive law. Thus the programming interface of the material must not be customized with respect to the particular element type.

Another type is represented by plane stress elements. This model can be applied to geometries that have no forces acting normal to the section plane like the plain strain model before. But now it assumes that a two dimensional stress situation exists in the considered section plane. Thus, all components related to the third dimension are assumed to be zero. Examples are thin geometries like e.g. plates, in-plane actions of a beam or membranes, see Figure 3.1b. In a linear framework this constraint could easily be enforced with simple algebraic manipulations of the associated stress-strain constitutive law matrix representations. From the programmer's point of view and to keep the modularity of a Finite Element Method code it is desirable to use an uniform interface to the subroutines of three dimensional constitutive laws without concern about the type of applied finite elements (2D/3D solid elements, plate or shell elements). Thus the zero-normal-stress condition must be enforced, yielding the thickness strains, see Dvorkin et al. [63] and Klinkel and Govindjee [128]. After the evaluation of a general nonlinear three-dimensional constitutive law, e.g. $\boldsymbol{S} = \partial_{\boldsymbol{E}}\psi$, we start with a vectorization of the second

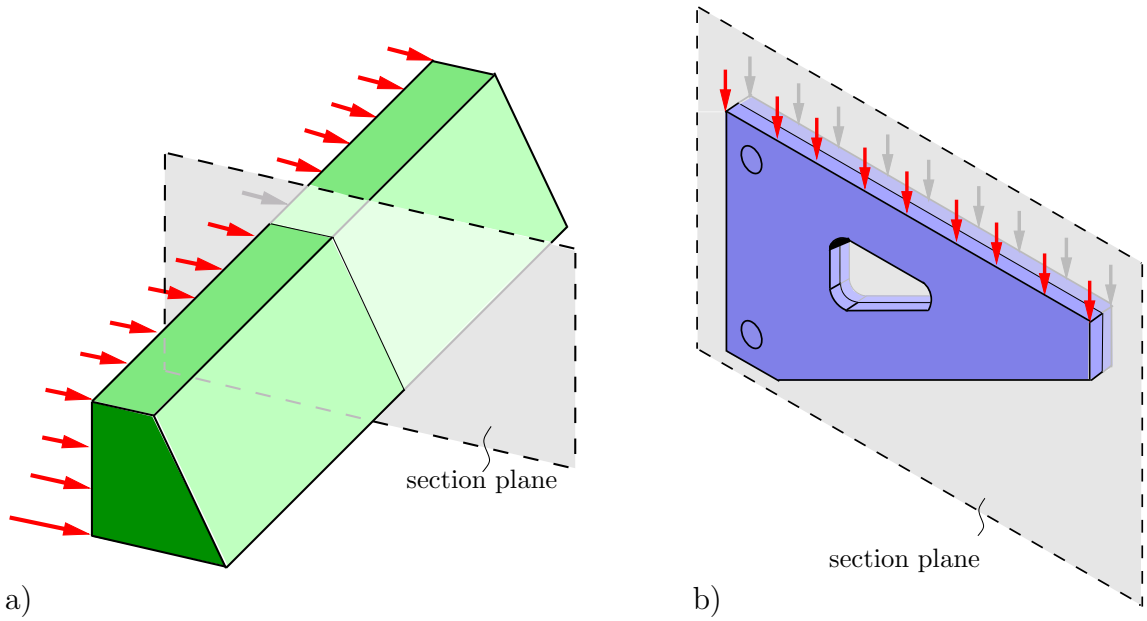

Figure 3.1: Examples of the application of two dimensional assumptions: section plane of a) dam under water pressure loading (plain strain) and b) plate with hole (plane stress).

Piola-Kirchhoff stress tensor considering its symmetry,

$$\widetilde{\boldsymbol{S}} = \begin{bmatrix} \widetilde{\boldsymbol{S}}^m \\ S^{33} \end{bmatrix} \quad \text{with} \quad \widetilde{\boldsymbol{S}}^m = \begin{bmatrix} S^{11} \\ S^{22} \\ S^{12} \\ S^{13} \\ S^{23} \end{bmatrix} . \tag{3.10}$$

But for the numerical treatment of the plane stress state we only use the resulting values of the stress tensor $\boldsymbol{S}$, which are organized in $\widetilde{\boldsymbol{S}}^m$. The zero-normal-stress condition $S^{33}(E_{33}) = 0$ is iteratively enforced and the required increment of the second Piola-Kirchhoff stress tensor is reformulated in matrix notation

$$\mathrm{d}\widetilde{\boldsymbol{S}} = \begin{bmatrix} \mathrm{d}\widetilde{\boldsymbol{S}}^m \\ \mathrm{d}S^{33} \end{bmatrix} = \begin{bmatrix} \underline{\underline{\widetilde{\mathbb{C}}}}^{mm} & \underline{\widetilde{\mathbb{C}}}^{m3} \\ \underline{\widetilde{\mathbb{C}}}^{3m} & \widetilde{\mathbb{C}}^{33} \end{bmatrix} \begin{bmatrix} \mathrm{d}\widetilde{\boldsymbol{E}}_m \\ \mathrm{d}E_{33} \end{bmatrix} = \widetilde{\mathbb{C}}\, \mathrm{d}\widetilde{\boldsymbol{E}} \, . \tag{3.11}$$

Therein $\widetilde{\mathbb{C}}$ is given by the obvious rearrangement of $\mathbb{C} = \partial_{\boldsymbol{E}} \boldsymbol{S}$, which is determined by a three dimensional stress analysis in the specific structural element and is arranged in the matrix notation given in Appendix A. In order to avoid confusions we denote the dimension type of the entries of $\widetilde{\mathbb{C}}$ by a single and double underline, respectively, i.e. $\underline{\underline{\widetilde{\mathbb{C}}}}^{mm} \in \mathbb{R}^{5\times5}$, $\underline{\widetilde{\mathbb{C}}}^{3m} \in \mathbb{R}^{5\times1}$ and $\underline{\widetilde{\mathbb{C}}}^{m3} \in \mathbb{R}^{1\times5}$. The Taylor series of the zero-normal-stress condition is truncated after the linear term and set to zero; therefore, we obtain

$$S^{33}(E_{33}^{(i)} + \Delta E_{33}^{(i)}) = S^{33(i)} + \widehat{\mathbb{C}}_{33}^{(i)}\, \Delta E_{33}^{(i)} = 0 \quad \text{with} \quad \widehat{\mathbb{C}}_{33}^{(i)} = \frac{dS^{33(i)}}{dE_{33}^{(i)}} \, , \tag{3.12}$$

and using $\Delta E_{33}^{(i)} = E_{33}^{(i+1)} - E_{33}^{(i)}$ the resulting update formula reads

$$E_{33}^{(i+1)} = E_{33}^{(i)} - \frac{S^{33(i)}}{\widehat{\mathbb{C}}_{33}^{(i)}} \, , \tag{3.13}$$

where i denotes the iteration number. We use a Newton scheme for the solution of the nonlinear scalar equation $S^{33}(E_{33}) = 0$, which provides the unknown thickness strains. Following the procedure described by KLINKEL AND GOVINDJEE [128] we evaluate Equation (3.11) for $\mathrm{d}S^{33} = 0$, which follows the equations

$$\mathrm{d}\widetilde{\boldsymbol{S}}^m = \underline{\underline{\widetilde{\mathbb{C}}}}^{mm}\,\mathrm{d}\widetilde{\boldsymbol{E}}_m + \underline{\widetilde{\mathbb{C}}}^{m3}\,\mathrm{d}E_{33} \quad \text{and} \quad 0 = \underline{\widetilde{\mathbb{C}}}^{3m}\,\mathrm{d}\widetilde{\boldsymbol{E}}_m + \widetilde{\mathbb{C}}^{33}\,\mathrm{d}E_{33}\,. \tag{3.14}$$

From the second equation we achieve the increment of the thickness strains

$$\mathrm{d}E_{33} = -\frac{1}{\widetilde{\mathbb{C}}^{33}}\,\underline{\widetilde{\mathbb{C}}}^{3m}\,\mathrm{d}\widetilde{\boldsymbol{E}}_m\,. \tag{3.15}$$

We insert this result into Equation $(3.14)_1$ and arrive after some reorganizations a formulation of the incremental stresses

$$\mathrm{d}\widetilde{\boldsymbol{S}}^m = \left(\underline{\underline{\widetilde{\mathbb{C}}}}^{mm} - \frac{1}{\widetilde{\mathbb{C}}^{33}}\,\underline{\widetilde{\mathbb{C}}}^{m3}\underline{\widetilde{\mathbb{C}}}^{3m}\right)\,\mathrm{d}\widetilde{\boldsymbol{E}}_m = \widehat{\mathbb{C}}\,\mathrm{d}\widetilde{\boldsymbol{E}}_m\,, \tag{3.16}$$

where $\widehat{\mathbb{C}}$ is the modified tangent modulus. Recapitulating, the procedure provides the plane stress condition using the standard outputs $\widetilde{\boldsymbol{S}}$ and $\widetilde{\mathbb{C}}$ of an arbitrary three dimensional constitutive law. Hence no modifications regarding the interface of a material subroutine are necessary and the programming effort is reduced.

3.4 Linearization and FE-Approximation

With a view at the variational formulations, as we introduce in Section 3.2, the nonlinear characteristic of them is obvious, considering nonlinear strain measures, e.g. Green-Lagrange strain tensor $\boldsymbol{E}$, and/or nonlinear constitutive equations for the description of e.g. elasto-plastic or visco-plastic effects. From this point the weak form $G(\boldsymbol{u}, \delta\boldsymbol{u}) = 0$ is a nonlinear function in term of the variable $\boldsymbol{u}$ and in general an analytical solution is not possible. Therefore, an iterative method, here the *Newton-Raphson iteration scheme*, is applied and that requires the linearization of the weak form of equilibrium. The linearization of $G(\boldsymbol{u}, \delta\boldsymbol{u})$ is done at $\boldsymbol{u} = \bar{\boldsymbol{u}}$ in the form

$$\mathrm{Lin}\,G(\bar{\boldsymbol{u}}, \delta\boldsymbol{u}, \Delta\boldsymbol{u}) := G(\bar{\boldsymbol{u}}, \delta\boldsymbol{u}) + \Delta G(\bar{\boldsymbol{u}}, \delta\boldsymbol{u}, \Delta\boldsymbol{u})\,, \tag{3.17}$$

where the linear increment $\Delta G(\bar{\boldsymbol{u}}, \delta\boldsymbol{u}, \Delta\boldsymbol{u})$ is calculated by the directional derivative of G at $\bar{\boldsymbol{u}}$ in the direction of $\Delta\boldsymbol{u}$, i.e.

$$\Delta G(\bar{\boldsymbol{u}}, \delta\boldsymbol{u}, \Delta\boldsymbol{u}) = \frac{\mathrm{d}}{\mathrm{d}\epsilon}[G(\bar{\boldsymbol{u}} + \epsilon\Delta\boldsymbol{u}, \delta\boldsymbol{u})]\Big|_{\epsilon=0} = \mathrm{D}G(\bar{\boldsymbol{u}}, \delta\boldsymbol{u}) \cdot \Delta\boldsymbol{u}\,, \tag{3.18}$$

with the incremental displacements $\Delta\boldsymbol{u}$. In the directional derivative of the weak form (3.8) the external parts vanish since we consider displacement-independent, so-called conservative, loads $\rho_0\boldsymbol{f}$ and $\bar{\boldsymbol{t}}$. Thus, the increment of G is reduced to the directional derivative $\mathrm{D}G^{\mathrm{int}}$ of the internal parts of the weak form and reads

$$\Delta G(\bar{\boldsymbol{u}}, \delta\boldsymbol{u}, \Delta\boldsymbol{u}) = \mathrm{D}G^{\mathrm{int}}(\bar{\boldsymbol{u}}, \delta\boldsymbol{u}) \cdot \Delta\boldsymbol{u} = \int_{\mathcal{B}_0} \Delta\boldsymbol{S} : \frac{1}{2}\delta\boldsymbol{C}\,\mathrm{d}V + \int_{\mathcal{B}_0} \boldsymbol{S} : \frac{1}{2}\Delta\delta\boldsymbol{C}\,\mathrm{d}V\,, \tag{3.19}$$

with the increment of the second Piola-Kirchhoff stresses $\Delta \boldsymbol{S}$ as well as the increment of the right Cauchy-Green tensor $\Delta \boldsymbol{C}$ and of its variation, c.f. Equation (3.9),

$$\begin{aligned} \Delta \boldsymbol{S} &= \mathbb{C} : \tfrac{1}{2} \Delta \boldsymbol{C} \quad \text{with} \quad \mathbb{C} = 2 \frac{\partial \boldsymbol{S}}{\partial \boldsymbol{C}} = 4 \frac{\partial^2 \psi}{\partial \boldsymbol{C} \partial \boldsymbol{C}} \, , \\ \Delta \boldsymbol{C} &= \Delta \boldsymbol{F}^T \boldsymbol{F} + \boldsymbol{F}^T \Delta \boldsymbol{F} \, , \\ \Delta \delta \boldsymbol{C} &= \delta \boldsymbol{F}^T \Delta \boldsymbol{F} + \Delta \boldsymbol{F}^T \delta \boldsymbol{F} \, . \end{aligned} \tag{3.20}$$

Note, that the material tangent modulus $\mathbb{C}$ is defined as a fourth-order tensor in Equation (2.68). The complete linearization term of the weak form,

$$\begin{aligned} \operatorname{Lin} G(\bar{\boldsymbol{u}}, \delta \boldsymbol{u}, \Delta \boldsymbol{u}) = & \int_{\mathcal{B}_0} \boldsymbol{S} : \frac{1}{2} \delta \boldsymbol{C} \, \mathrm{d}V - \int_{\mathcal{B}_0} \rho_0 \boldsymbol{f} \cdot \delta \boldsymbol{u} \, \mathrm{d}V - \int_{\partial \mathcal{B}_{0t}} \bar{\boldsymbol{t}} \cdot \delta \boldsymbol{u} \, \mathrm{d}A \\ & + \int_{\mathcal{B}_0} \frac{1}{2} \delta \boldsymbol{C} : \mathbb{C} : \frac{1}{2} \Delta \boldsymbol{C} \, \mathrm{d}V + \int_{\mathcal{B}_0} \boldsymbol{S} : \frac{1}{2} \Delta \delta \boldsymbol{C} \, \mathrm{d}V \, , \end{aligned} \tag{3.21}$$

is built from Equation (3.8) under consideration of the increments (3.19) and $(3.20)_1$. The main task in each iteration step is the computation of the incremental displacements $\Delta \boldsymbol{u}_{n+1}$ in such a way that the condition $\operatorname{Lin} G = 0$ holds, where n denotes the n^{th} iteration step. Along with the update of the displacements, i.e. $\bar{\boldsymbol{u}}_{n+1} = \bar{\boldsymbol{u}} + \Delta \boldsymbol{u}_{n+1}$, this procedure is done until the residuum $G(\bar{\boldsymbol{u}}, \delta \boldsymbol{u})$ is smaller than a given tolerance.

Since the analytical solution of $\operatorname{Lin} G = 0$ is not possible in most cases, the *Finite Element Method* is used to achieve a numerical solution. Thereby several approximations are applied like the discretization of the considered body by finite elements, the approximation of the primary variable inside the elements by ansatz functions and the calculation of integrals by a numerical integration procedure. The first mentioned approximation, which gives the method its name, describes the discretization of the physical domain $\mathcal{B}_0$ by n_{ele}-elements, where their union $\mathcal{B}_0^h$ approximates $\mathcal{B}_0$, i.e.

$$\mathcal{B}_0 \approx \mathcal{B}_0^h = \bigcup_{e=1}^{n_{\text{ele}}} \mathcal{B}_0^e \, . \tag{3.22}$$

In the Finite Element Method *ansatz functions* are used for the interpolation of both the geometry and the field of unknowns. For that reason the *isoparametric concept* was developed, which states, that the geometry as well as the displacement field $\boldsymbol{u}$ are aproximated by the same ansatz functions. The transformation mapping between the isoparametric subspace, the reference configuration and the actual configuration are introduced in the following and are illustrated in Figure 3.2. For that and the further notes on the Finite Element Method in this section we consider the general three-dimensional case. Special element formulations are given in the next sections. Based on the basic idea of the isoparametric concept the geometry in the reference and current configuration is approximated by the same ansatz function $N_I(\boldsymbol{\xi})$,

$$\boldsymbol{X} = \boldsymbol{X}(\boldsymbol{\xi}) = \sum_{I=1}^{n_{\text{node}}} N_I(\boldsymbol{\xi}) \boldsymbol{X}_I \quad \text{and} \quad \boldsymbol{x} = \boldsymbol{x}(\boldsymbol{\xi}) = \sum_{I_1}^{n_{\text{node}}} N_I(\boldsymbol{\xi}) \boldsymbol{x}_I \, . \tag{3.23}$$

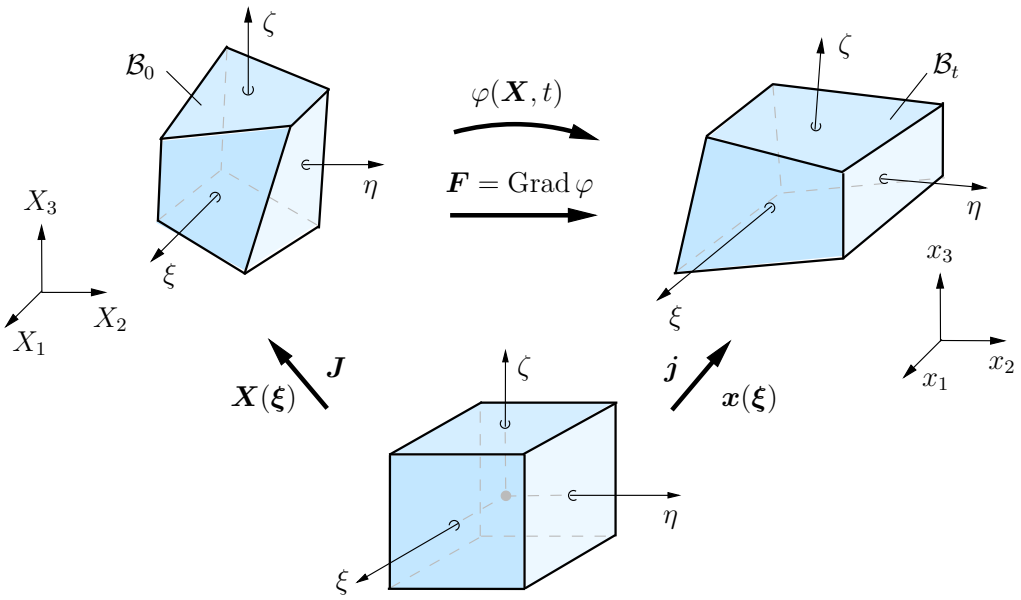

Figure 3.2: Isoparametric concept: Mapping between the configurations

Here, n_{node} denotes the number of nodes per element and I the local node number. In the three-dimensional case the vector of the natural coordinates $\boldsymbol{\xi}$ is arranged as $\boldsymbol{\xi} := [\,\xi, \eta, \zeta\,]^T$.

The discrete nodal displacement $\boldsymbol{d}_I$ enables the computation of the current geometry

$$\boldsymbol{x}_I = \boldsymbol{X}_I + \boldsymbol{d}_I \,. \tag{3.24}$$

For the mapping from the isoparametric space to the reference and the current space, shown in Figure 3.2, the so-called *Jacobian* of the transformation are introduced with

$$\boldsymbol{J} = \frac{\partial \boldsymbol{X}}{\partial \boldsymbol{\xi}} \quad \text{and} \quad \boldsymbol{j} = \frac{\partial \boldsymbol{x}}{\partial \boldsymbol{\xi}}\,, \quad \text{with} \quad \boldsymbol{j} = \boldsymbol{F}\boldsymbol{J} \,. \tag{3.25}$$

According to the isoparametric concept and Equation (3.23) we approximate the physical, virtual and incremental displacement field using the same ansatz functions N_I,

$$\boldsymbol{u} = \sum_{I=1}^{n_{\text{node}}} N_I(\boldsymbol{\xi})\boldsymbol{d}_I\,, \quad \delta\boldsymbol{u} = \sum_{I=1}^{n_{\text{node}}} N_I(\boldsymbol{\xi})\delta\boldsymbol{d}_I\,, \quad \Delta\boldsymbol{u} = \sum_{I=1}^{n_{\text{node}}} N_I(\boldsymbol{\xi})\Delta\boldsymbol{d}_I \,. \tag{3.26}$$

Based on previous equations the virtual and incremental deformation gradient is given by

$$\begin{aligned} \delta\boldsymbol{F} = \mathrm{Grad}[\delta\boldsymbol{u}] \;&= \sum_{I=1}^{n_{\text{node}}} \delta\boldsymbol{d}_I \otimes \mathrm{Grad}\, N_I(\boldsymbol{\xi}) \quad \text{with} \quad \delta F^a{}_A = \sum_{I=1}^{n_{\text{node}}} N_{I,A}\delta d_I^a \,, \\ \Delta\boldsymbol{F} = \mathrm{Grad}[\Delta\boldsymbol{u}] \;&= \sum_{I=1}^{n_{\text{node}}} \Delta\boldsymbol{d}_I \otimes \mathrm{Grad}\, N_I(\boldsymbol{\xi}) \quad \text{with} \quad \Delta F^a{}_A = \sum_{I=1}^{n_{\text{node}}} N_{I,A}\Delta d_I^a \,, \end{aligned} \tag{3.27}$$

where $N_{I,A}$ denotes the derivative of the ansatz function with respect to the referential coordinate X_A. The derivatives of the ansatz function with respect to the reference coordinates are calculated by

$$\mathrm{Grad}\, N_I(\boldsymbol{\xi}) = \frac{\partial N_I}{\partial \boldsymbol{\xi}}\frac{\partial \boldsymbol{\xi}}{\partial \boldsymbol{X}} = \boldsymbol{J}^{-T}\frac{\partial N_I}{\partial \boldsymbol{\xi}} \,. \tag{3.28}$$

The implementation of the Finite Element Method is usually based on a matrix notation of the tensorial quantities, since a compact formulation is achieved. Also that is a reasonable step taking into account the numerical implementation due to the fact that most programming languages are optimized for vector and matrix array handling. Thus, the coefficients of a second-order tensor are presented in vectors and the components of fourth-order tensors by matrices, see therefore the Appendix A. Under consideration of this arrangement the virtual and incremental right Cauchy-Green deformation tensor, introduced in Equations (3.9) and (3.20), are computed approximately by

$$\frac{1}{2}\delta\boldsymbol{C} = \sum_{I=1}^{n_{\text{node}}} \boldsymbol{B}_I \delta\boldsymbol{d}_I \ , \quad \frac{1}{2}\Delta\boldsymbol{C} = \sum_{I=1}^{n_{\text{node}}} \boldsymbol{B}_I \Delta\boldsymbol{d}_I \ , \tag{3.29}$$

with the so-called *B-Matrix* $\boldsymbol{B}_I$, which in the three-dimensional case is given by

$$\boldsymbol{B}_I = \begin{bmatrix} F_{11}N_{I,1} & F_{21}N_{I,1} & F_{31}N_{I,1} \\ F_{12}N_{I,2} & F_{22}N_{I,2} & F_{32}N_{I,2} \\ F_{13}N_{I,3} & F_{23}N_{I,3} & F_{33}N_{I,3} \\ F_{11}N_{I,2} + F_{12}N_{I,1} & F_{21}N_{I,2} + F_{22}N_{I,1} & F_{31}N_{I,2} + F_{32}N_{I,1} \\ F_{12}N_{I,3} + F_{13}N_{I,2} & F_{22}N_{I,3} + F_{23}N_{I,2} & F_{32}N_{I,3} + F_{33}N_{I,2} \\ F_{11}N_{I,3} + F_{13}N_{I,1} & F_{21}N_{I,3} + F_{23}N_{I,1} & F_{31}N_{I,3} + F_{33}N_{I,1} \end{bmatrix} . \tag{3.30}$$

Herein, $N_{I,A}$ denotes the derivative of the ansatz function with respect to the referential coordinate X_A. Note that due to a better clarity we neglect until now the specification of the arguments of the ansatz functions N_I. Now that we have all quantities appearing in Equation (3.5) in their discrete form, we can formulate the discrete weak form of equilibrium for a typical finite element $\mathcal{B}_0^e$ in the reference setting

$$\begin{aligned} G^e(\boldsymbol{d}^e, \delta\boldsymbol{d}^e) &= \sum_{I=1}^{n_{\text{node}}} (\delta\boldsymbol{d}_I)^T \left(\int_{\mathcal{B}_0^e} \boldsymbol{B}_I^T \boldsymbol{S} \, \mathrm{d}V - \int_{\mathcal{B}_0^e} N_I \rho_o \boldsymbol{f} \, \mathrm{d}V - \int_{\partial\mathcal{B}_{0t}^e} N_I \bar{\boldsymbol{t}} \, \mathrm{d}A \right) = 0 \\ &=: \sum_{I=1}^{n_{\text{node}}} (\delta\boldsymbol{d}_I)^T \boldsymbol{r}_I = (\delta\boldsymbol{d}^e)^T \boldsymbol{r}^e \ . \end{aligned} \tag{3.31}$$

The integration part in the previous equation is summed up to the nodal residual vector $\boldsymbol{r}_I$. Glancing at the finite element the nodal quantities are arranged in the elemental vector of virtual nodal displacement $(\delta\boldsymbol{d}^e)^T$ and the elemental residual vector $\boldsymbol{r}^e$ in the form

$$(\delta\boldsymbol{d}^e)^T = \left[\, \delta\boldsymbol{d}_1^T \, | \, \delta\boldsymbol{d}_2^T \, | \, \dots \, | \, \delta\boldsymbol{d}_{n_{\text{node}}}^T \, \right] \ , \quad \boldsymbol{r}^e = \left[\, \boldsymbol{r}_1^T \, | \, \boldsymbol{r}_2^T \, | \, \dots \, | \, \boldsymbol{r}_{n_{\text{node}}}^T \, \right]^T \ . \tag{3.32}$$

To complete the discrete formulation of the linearized weak form (3.21) we now need the approximation of the incremental terms therein. These terms are often referred to as the material part ΔG^{mat} and the geometrical part ΔG^{geo}, i.e.

$$\Delta G^{\text{mat}} = \int_{\mathcal{B}_0} \frac{1}{2}\delta\boldsymbol{C} : \mathbb{C} : \frac{1}{2}\Delta\boldsymbol{C} \, \mathrm{d}V \ , \quad \Delta G^{\text{geo}} = \int_{\mathcal{B}_0} \boldsymbol{S} : \frac{1}{2}\Delta\delta\boldsymbol{C} \, \mathrm{d}V \ . \tag{3.33}$$

The first mentioned integrand is transformed under consideration of Equation (3.29). Hence, the discrete form of the material part for $\mathcal{B}_0^e$ is obtained by

$$\Delta G^{e,\text{mat}} = \sum_{I=1}^{n_{\text{node}}} \sum_{J=1}^{n_{\text{node}}} (\delta\boldsymbol{d}_I)^T \boldsymbol{K}_{IJ}^{e,\text{mat}} \Delta\boldsymbol{d}_J \quad \text{with} \quad \boldsymbol{K}_{IJ}^{e,\text{mat}} := \int_{\mathcal{B}_0^e} \boldsymbol{B}_I^T \mathbb{C}^e \boldsymbol{B}_J \, \mathrm{d}V \ , \tag{3.34}$$

where $\boldsymbol{K}_{IJ}^{e,\mathrm{mat}}$ denotes the material part of the element stiffness matrix K_{IJ}^{e}. According to the already mentioned matrix notation, $\mathbb{C}^e$ is the matrix representation of the material tangent modulus $\mathbb{C} := 2\partial_C \boldsymbol{S}$, cf. Appendix A. The geometric part (3.33) contains the linearized virtual right Cauchy-Green tensor, defined in Equation $(3.20)_3$. Its discrete form in index notation is obtained by using the approximation of the virtual and incremental deformation gradient (3.27) and finally reads

$$\begin{aligned}
\tfrac{1}{2}\Delta\delta C_{AB} &= \tfrac{1}{2}\left(\delta F^{a}{}_{A}\ \delta_{ab}\ \Delta F^{b}{}_{B} + \Delta F^{a}{}_{A}\ \delta_{ab}\ \delta F^{b}{}_{B}\right) \\
&= \tfrac{1}{2}\left(\sum_{I=1}^{n_{\mathrm{node}}} N_{I,A}\delta d_I^a\ \delta_{ab} \sum_{J=1}^{n_{\mathrm{node}}} N_{J,B}\Delta d_J^b + \sum_{I=1}^{n_{\mathrm{node}}} N_{I,A}\Delta d_I^a\ \delta_{ab} \sum_{J=1}^{n_{\mathrm{node}}} N_{J,B}\delta d_J^b\right) \\
&= \sum_{I=1}^{n_{\mathrm{node}}}\sum_{J=1}^{n_{\mathrm{node}}} N_{I,A}\delta d_I^a\ \delta_{ab}\ N_{J,B}\Delta d_J^b\ ,
\end{aligned} \tag{3.35}$$

where δ denotes the Kronecker operator, cf. Equation $(2.3)_1$. Thus, for a typical finite element the geometric part is approximated by

$$\Delta G^{e,\mathrm{geo}} = \sum_{I=1}^{n_{\mathrm{node}}}\sum_{J=1}^{n_{\mathrm{node}}} (\delta\boldsymbol{d}_I)^T \boldsymbol{K}_{IJ}^{e,\mathrm{geo}} \Delta\boldsymbol{d}_J \quad \text{with} \quad \boldsymbol{K}_{IJ}^{e,\mathrm{geo}} := \int_{\mathcal{B}_0^e} (N_{I,A}N_{J,B}) S^{AB}\,\mathrm{d}V\ , \tag{3.36}$$

with the geometric part $\boldsymbol{K}_{IJ}^{e,\mathrm{geo}}$ of the complete element stiffness matrix $\boldsymbol{K}_{IJ}^{e}$, which is calculated by the sum of the material and the geometric part, i.e.

$$\boldsymbol{K}_{IJ}^{e} = \boldsymbol{K}_{IJ}^{e,\mathrm{mat}} + \boldsymbol{K}_{IJ}^{e,\mathrm{geo}}\ . \tag{3.37}$$

Summarizing the discrete parts of the linearized weak form of equilibrium for a typical finite element accordingly to Equation (3.17) we obtain

$$\mathrm{Lin}\, G^e = \underbrace{\sum_{I=1}^{n_{\mathrm{node}}} (\delta\boldsymbol{d}_I)^T \boldsymbol{r}_I}_{G^e(\boldsymbol{d}^e,\delta\boldsymbol{d}^e)} + \underbrace{\sum_{I=1}^{n_{\mathrm{node}}}\sum_{J=1}^{n_{\mathrm{node}}} (\delta\boldsymbol{d}_I)^T \boldsymbol{K}_{IJ}^{e} \Delta\boldsymbol{d}_J = 0}_{\Delta G^e(\boldsymbol{d}^e,\delta\boldsymbol{d}^e,\Delta\boldsymbol{d}^e)}\ . \tag{3.38}$$

For the overall formulation of the system of equation the elemental virtual and incremental displacements are arranged in the form

$$\begin{aligned}
\delta\boldsymbol{d} &= \left[\,(\delta\boldsymbol{d}^1)^T \,|\, (\delta\boldsymbol{d}^2)^T \,|\, \ldots \,|\, (\delta\boldsymbol{d}^{n_{\mathrm{ele}}})^T\,\right]^T\ , \\
\Delta\boldsymbol{d} &= \left[\,(\Delta\boldsymbol{d}^1)^T \,|\, (\Delta\boldsymbol{d}^2)^T \,|\, \ldots \,|\, (\Delta\boldsymbol{d}^{n_{\mathrm{ele}}})^T\,\right]^T\ .
\end{aligned} \tag{3.39}$$

Then the global stiffness matrix $\boldsymbol{K}$ and global residual vector $\boldsymbol{R}$ are the result of the standard assembling procedure of all element stiffness matrices and elemental residual vectors, i.e.

$$\boldsymbol{K} = \bigwedge_{e=1}^{n_{\mathrm{ele}}} \boldsymbol{K}^e \quad \text{and} \quad \boldsymbol{R} = \bigwedge_{e=1}^{n_{\mathrm{ele}}} \boldsymbol{r}^e\ . \tag{3.40}$$

Finally, we achieve the overall system of equation for the domain $\mathcal{B}_0$ in the discrete form

$$\delta\boldsymbol{D}^T(\boldsymbol{K}\Delta\boldsymbol{D} + \boldsymbol{R}) = 0 \quad \Rightarrow \quad \Delta\boldsymbol{D} = -\boldsymbol{K}^{-1}\boldsymbol{R}\,, \tag{3.41}$$

where the global nodal displacement field $\boldsymbol{D}$ is updated $\boldsymbol{D} \Leftarrow \boldsymbol{D} + \Delta\boldsymbol{D}$ during the Newton-Raphson iteration scheme, until the residual vector $\boldsymbol{R}$ is smaller than a given tolerance.

In the underlying equations for the element stiffness matrix and the elemental residual vector the integrands are generally rational functions. Therefore in most cases an analytical solution is not possible and a numerical integration scheme must be applied. Here we use the *Gauss integration procedure* – also called *Gauss quadrature* – which is an approximation of the considered integral by a weighted sum of function values at specified points within the domain of integration. Further details can be found in classical handbooks of mathematics and the Finite Element Method.

3.5 Standard Displacement Method

In the previous sections we introduce the general framework for the implementation of finite elements in the context of a pure displacement formulation. For two specific element types we give the essential relations and parameters in the following subsections and refer for more types to the classical textbooks treating the Finite Element Method.

3.5.1 10-noded Tetrahedral Element (T2)

In the course of this thesis we utilize several geometrically complex domains, e.g. biological tissue structure and microstructures of multiphase steels. For their discretization triangular elements – in 2D – and tetrahedral elements – in 3D – enable a sufficient geometrical approximation without using different element types. But the linear formulation of these finite elements exhibits a stiffening effect in many applications of structural mechanics. On this account we use 10-noded tetrahedral elements with quadratic ansatz functions, also referred to as T2 elements. In Figure 3.3 the isoparametric tetrahedral element is shown in the parameterized space Ω^e and the reference configuration $\mathcal{B}_0^e$. The corresponding ansatz functions in terms of the natural coordinates of the isoparametric space, i.e., $\xi \in [0,1]$, $\eta \in [0,1]$ and $\zeta \in [0,1]$, are given by

$$\begin{aligned} N_1 &= \lambda(2\lambda-1)\,, & N_6 &= 4\xi\eta\,, \\ N_2 &= \xi(2\xi-1)\,, & N_7 &= 4\eta\lambda\,, \\ N_3 &= \eta(2\eta-1)\,, & N_8 &= 4\zeta\lambda\,, \\ N_4 &= \zeta(2\zeta-1)\,, & N_9 &= 4\xi\zeta\,, \\ N_5 &= 4\xi\lambda\,, & N_{10} &= 4\eta\zeta\,, \end{aligned} \tag{3.42}$$

with the relation $\lambda = 1 - \xi - \eta - \zeta$.

For the requisite numerical integration

$$\begin{aligned} I &= \int_x \int_y \int_z f(x,y,z)\,\mathrm{d}z\,\mathrm{d}y\,\mathrm{d}x = \int_0^1 \int_0^{1-\xi} \int_0^{1-\xi-\eta} f(\xi,\eta,\zeta)\det(\boldsymbol{J})\,\mathrm{d}\xi\,\mathrm{d}\eta\,\mathrm{d}\zeta \\ &\approx \sum_{i=1}^{4} f(\xi_i,\eta_i,\zeta_i))\det[\boldsymbol{J}(\xi_i,\eta_i,\zeta_i)]\;\widetilde{w}_i \end{aligned} \tag{3.43}$$

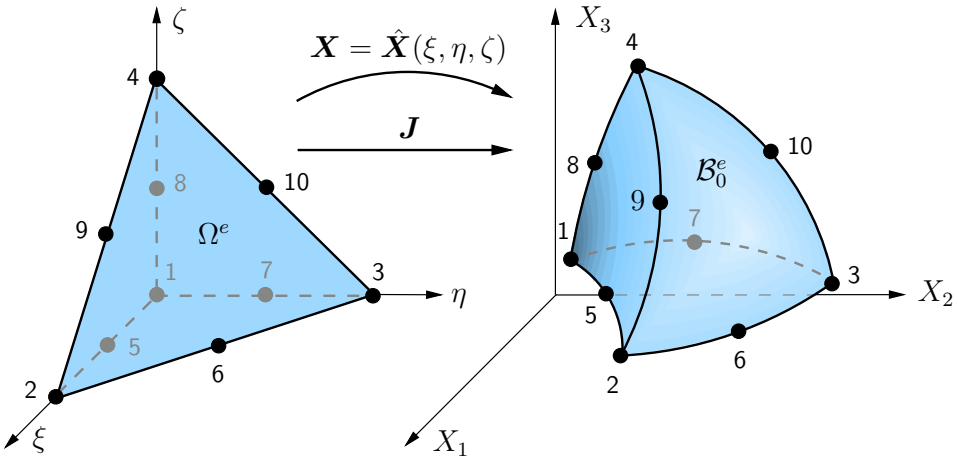

Figure 3.3: Isoparametric ten-noded tetrahedral finite element (left) in the parameterized space Ω^e and the mapping onto the reference configuration $\mathcal{B}_0^e$ (right).

we use four Gauss points per element with the natural coordinates

$$\begin{aligned}
\xi_1 &= \frac{5-\sqrt{5}}{20}, \quad \xi_2 = \frac{5-\sqrt{5}}{20}, \quad \xi_3 = \frac{5-\sqrt{5}}{20}, \quad \xi_4 = \frac{5+3\sqrt{5}}{20}, \\
\eta_1 &= \frac{5-\sqrt{5}}{20}, \quad \eta_2 = \frac{5-\sqrt{5}}{20}, \quad \eta_3 = \frac{5+3\sqrt{5}}{20}, \quad \eta_4 = \frac{5-\sqrt{5}}{20}, \\
\zeta_1 &= \frac{5-\sqrt{5}}{20}, \quad \zeta_2 = \frac{5+3\sqrt{5}}{20}, \quad \zeta_3 = \frac{5-\sqrt{5}}{20}, \quad \zeta_4 = \frac{5-\sqrt{5}}{20}
\end{aligned} \tag{3.44}$$

and the corresponding weight factors

$$w_1 = \frac{1}{24}, \quad w_2 = \frac{1}{24}, \quad w_3 = \frac{1}{24}, \quad w_4 = \frac{1}{24}, \tag{3.45}$$

cf. de Boer and Schröder [56].

3.5.2 3D Pressure Boundary Loading

In many fields of the deformation analysis of structural elements the application of pressure-dependent boundary conditions are required. The consideration of loadings onto components by hydrostatic pressure caused by fluids or wind can be mentioned as an example. The crucial aspect is that during the deformation process the related geometry change its shape. For this reason such a deformation dependent load is also refer to as pressure follower load. This condition pertains during the later shown simulation of human arteries, which are loaded by a pressure applied to the interior surface of the arterial wall. Detailed descriptions concerning deformation dependent loads can be found in Simo et al. [210], Wriggers [254] and references therein.

In general, we have to consider an element for the application of the boundary loading, whose dimension is $m-1$ considering a boundary value problem with the dimension m. Since we consider 3D problems discretized by 10-noded elements, we introduce a surface boundary element based on a quadratic triangular element. The loading is represented

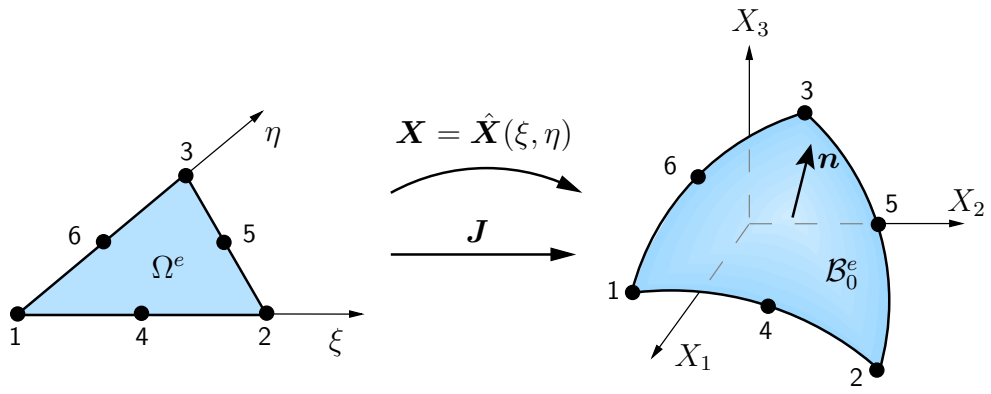

Figure 3.4: 6-noded triangular element for pressure boundary loading

by a hydrostatic pressure. Therefore the underlying continuum mechanical formulation is represented by the second term of the external work appearing in the weak form of equilibrium (3.5), which reads

$$G^{\text{ext}_2} = \int_{\partial \mathcal{B}_{0t}} \bar{\boldsymbol{t}} \cdot \delta \boldsymbol{u} \, \mathrm{d}A \; = \int_{\partial \mathcal{B}_{0t}} p \boldsymbol{n} \cdot \delta \boldsymbol{u} \, \mathrm{d}A \; , \tag{3.46}$$

with the hydrostatic pressure p and the normal $\boldsymbol{n}$ to the surface. As shown in Figure 3.4 we consider a 6-noded triangular finite element. The approximation is based on the quadratic ansatz functions

$$\begin{aligned} &N_1(\xi,\eta) = \lambda(2\lambda - 1) \, , \quad N_2(\xi,\eta) = \xi(2\xi - 1) \, , \quad N_3(\xi,\eta) = \eta(2\eta - 1) \\ &N_4(\xi,\eta) = 4\lambda\xi \, , \qquad\quad N_5(\xi,\eta) = 4\eta\xi \, , \qquad\quad N_6(\xi,\eta) = 4\lambda\eta \, , \end{aligned} \tag{3.47}$$

with the isoparametric subspace Ω^e, i.e. $\xi \in [0,1]$ and $\eta \in [0,1]$. Hence for one finite element we achieve the discretization of Equation (3.46)

$$G^{e,\text{ext}_2} = \sum_{I=1}^{6} (\delta \boldsymbol{d}_I)^T \int_{\partial \mathcal{B}_{0t}^e} N_I \, p \, \boldsymbol{n} \, \mathrm{d}A \; , \tag{3.48}$$

For the required numerical integration

$$I = \int_0^1 \int_0^{1-\xi} f(\xi,\eta) \det(\boldsymbol{J}) \, \mathrm{d}\xi \, \mathrm{d}\eta \approx \sum_{i=1}^{3} f(\xi_i,\eta_i) \det[\boldsymbol{J}(\xi_i,\eta_i)] \, w_i \tag{3.49}$$

we use three Gauss points per element with the natural coordinates ξ_i, η_i and the corresponding weight factors w_i

$$\begin{aligned} &\xi_1 = 0.5 \, , \quad \xi_2 = 0.0 \, , \quad \xi_3 = 0.5 \, , \\ &\eta_1 = 0.5 \, , \quad \eta_2 = 0.5 \, , \quad \eta_3 = 0.0 \, , \\ &w_1 = \frac{1}{6} \, , \quad w_2 = \frac{1}{6} \, , \quad w_3 = \frac{1}{6} \, , \end{aligned} \tag{3.50}$$

cf. de Boer and Schröder [56]. Since the loading is depending on the deformation the term G^{ext_2} does not vanish in the linear increment ΔG during the linearization, cf. Equation (3.19). For the full description of the linearization we refer to the literature mentioned at the beginning of this subsection.

3.6 3-Field Finite-Element Formulation (T2P0)

In the previous section we discuss the framework of the standard displacement formulation for finite elements. Since we use the Finite Element Method for the simulation of materials with quasi-incompressible behavior in the course of this thesis, we have to take a look with respect to a well-known phenomenon, the volumetric locking of finite elements. This locking becomes apparent during the simulation of such a material by the an over-stiffening due to the mechanical response and no reliable results can be expected. In contrast to other locking phenomenae, which are caused by kinematic constraints and therefore called geometric lockings (e. g. shear or membrane locking), the volumetric type is connected to the choice of a material parameter. An increasing bulk modulus, i. e. $\kappa \to \infty$, describes the incompressibility constraint due to the volumetric deformation. Considering the relation $\kappa = E/(3-6\nu)$, where E denotes Young's modulus, leads to the constraint $\nu \to 0.5$ of Poission's ratio. In the limit case a purely isochoric deformation should be observed, which leads to the corresponding constraint $J = \det \boldsymbol{F} = 1$ of the Jacobian J. The adherence of this constraint cause a stiffening of the bending modes within the finite element. The treatment of the volumetric locking has been the topic of many publications and several developments concerning the element formulation has been made. Several development due to the volumetric locking has been done and we give here only a brief overview of the some formulations, but we raise no claim to completeness of this list. In Simo et al. [209] the so-called Q1/P0 element is introduced based on a three-field formulation with independent variational approximations for pressure and dilatation. The enhanced assumed strain (EAS) elements preserve the locking by the introduction of additional strain components, see Simo and Armero [207]. Both these techniques based on the Hu-Washizu principle, see the following subsection. Other approaches consider a side condition, e. g. $G(J) = J - 1 = 0$, which is embedded by the method of the Lagrangian multipliers to the constitutive equations. Further developments in the context of the augmented Lagrangian method are presented in Simo and Taylor [203] and Glowinski and Le Tallec [84]. Here we focus on the $\bar{\boldsymbol{F}}$-approach, wherein the standard deformation gradient $\boldsymbol{F}$ is replaced by a modified deformation gradient, which based on the assumption of a element-wise constant dilatation, see e. g. Simo [206], Zienkiewicz and Taylor [260] and Freischläger [74]. For the computation of this dilatation we used the approach proposed by Nagtegaal et al. [155]. Other publications taking into account different dilatation formulations are Moran et al. [153] and de Souza Neto et al. [58].

3.6.1 Hu-Washizu Functional

In section 3.2 we introduce the variational principle due to a single-field formulation. An extension to this method is the so-called *Hu-Washizu* principle, see Hu [113] and Washizu [244; 245], where additional constraint equations are considered during the formulation of the weak form. These constraints can be written in terms of the kinematics and/or the constitutive equations. In its original form the potential was written in terms of the deformations, strains and stresses as independent variables, i. e. $\Pi = \Pi(\boldsymbol{u}, \boldsymbol{F}, \boldsymbol{P})$. For the treatment of quasi-incompressible material behavior Simo et al. [209] introduced a three-field functional, which is motivated by the Hu-Washizu functional. The kinematics of such materials are bounded by the constraint $J = \det \boldsymbol{F} = 1$ and use the additive split (2.114) of the energy function $\psi(\boldsymbol{C})$ in an isochoric part $\psi^{\text{isoch}}(\tilde{\boldsymbol{C}})$ and a volumetric

part $\psi^{\text{vol}}(J)$. Hence a functional $\Pi = \Pi(\boldsymbol{u}, p, \theta)$ arises containing the deformation $\boldsymbol{u}$, the pressure p and a strain variable θ equal to J as independent variables. But the necessary split of the energy function could be adversely in some cases of the chosen function. A more general formulation, which does not require any special modification towards the material model, is the $\bar{\boldsymbol{F}}$-approach discussed in Simo [206], Zienkiewicz and Taylor [260] and Freischläger [74]. We follow the derivation given in the latter reference and start on the multiplicative split of the standard deformation gradient

$$\boldsymbol{F} = \underbrace{(\det \boldsymbol{F})^{-1/3} \boldsymbol{F}}_{\boldsymbol{F}_{\text{iso}}} \; \underbrace{(\det \boldsymbol{F})^{1/3} \mathbf{1}}_{\boldsymbol{F}_{\text{vol}}} \tag{3.51}$$

into its volumetric part $\boldsymbol{F}_{\text{vol}}$ and its isochoric part $\boldsymbol{F}_{\text{iso}}$ with $\det[\boldsymbol{F}_{\text{iso}}] = 1$. In order to avoid possible locking effects that would arise when enforcing the quasi-incompressibility constraint point-wise, i. e. evaluation of $J = \det \boldsymbol{F}$, an additional variable Θ is introduced. It describes the dilatation and represents an element-wise constant quantity. By the replacement of J by the new quantity Θ in the volumetric part of Equation (3.51) we achieve the modified deformation gradient

$$\bar{\boldsymbol{F}} = \underbrace{J^{-1/3} \boldsymbol{F}}_{\boldsymbol{F}_{\text{iso}}} \; \underbrace{\Theta^{1/3} \mathbf{1}}_{\bar{\boldsymbol{F}}_{\text{vol}}} = \left(\frac{\Theta}{J} \right)^{1/3} \boldsymbol{F} \; . \tag{3.52}$$

The $\bar{\boldsymbol{F}}$-approach requires the evaluation of the constitutive equations of the considered material using the new operator $\bar{\boldsymbol{F}}$. Since we focus on constitutive equations in terms of the right Cauchy-Green tensor $\boldsymbol{C}$, we formulate the associated counterpart in terms of the $\bar{\boldsymbol{F}}$-operator

$$\bar{\boldsymbol{C}} = \bar{\boldsymbol{F}}^T \bar{\boldsymbol{F}} = \left(\frac{\Theta}{J} \right)^{2/3} \boldsymbol{F}^T \boldsymbol{F}. \tag{3.53}$$

With respect to the Hu-Washizu functional the potential is written as $\Pi = \Pi(\boldsymbol{u}, J, \Theta)$. Following Equation (3.8) we can now write the weak from of the three-field variational formulation of the $\bar{\boldsymbol{F}}$-approach as

$$G(\boldsymbol{u}, J, \Theta) := \underbrace{\int_{\mathcal{B}_0} \bar{\boldsymbol{S}} : \frac{1}{2} \delta \bar{\boldsymbol{C}} \, \mathrm{d}V}_{G^{\text{int}}} - \underbrace{\left[\int_{\mathcal{B}_0} \rho_0 \boldsymbol{f} \cdot \delta \boldsymbol{u} \, \mathrm{d}V + \int_{\partial \mathcal{B}_{0t}} \bar{\boldsymbol{t}} \cdot \delta \boldsymbol{u} \, \mathrm{d}A \right]}_{G^{\text{ext}}} \; . \tag{3.54}$$

Therein we use the symbol $\bar{\boldsymbol{S}}$ as abbreviation for the second Piola-Kirchhoff stresses $\boldsymbol{S}(\bar{\boldsymbol{C}})$, which are obtained by the evaluation of the constitutive equation using $\bar{\boldsymbol{C}} = \bar{\boldsymbol{F}}^T \bar{\boldsymbol{F}}$. In Equation (3.54) it is observable, that only the internal part G^{int} is modified by using the new $\bar{\boldsymbol{F}}$-operator. Consequently, we discuss only the modifications of this term in the sequel. First, we need the variation of the operator $\bar{\boldsymbol{C}}$

$$\delta \bar{\boldsymbol{C}} = \delta_{\boldsymbol{u}} \bar{\boldsymbol{C}} + \delta_J \bar{\boldsymbol{C}} + \delta_\Theta \bar{\boldsymbol{C}} \; , \tag{3.55}$$

where the detailed expression of the summands can be found the Appendix C. This enables us to reformulate the internal part G^{int} of the weak form to

$$G^{\text{int}} = \int_{\mathcal{B}_0} \left\{ \frac{1}{2} \delta \boldsymbol{C} \left(\frac{\Theta}{J} \right)^{2/3} + \frac{1}{3} \boldsymbol{C} \left(\frac{\Theta}{J} \right)^{2/3} \left(\frac{\delta \Theta}{\Theta} - \frac{\delta J}{J} \right) \right\} : \bar{\boldsymbol{S}} \, \mathrm{d}V \; . \tag{3.56}$$

Exploiting the symmetry of the Kirchoff stress tensor $\bar{\boldsymbol{\tau}}$, which is evaluated using the modified operator $\bar{\boldsymbol{C}}$, the latter equation can be reformulated to

$$G^{\text{int}} = \int_{\mathcal{B}_0} \left\{ \operatorname{grad} \delta\boldsymbol{u} + \frac{1}{3} \left(\frac{\delta\Theta}{\Theta} - \frac{\delta J}{J} \right) \right\} : \bar{\boldsymbol{\tau}} \, \mathrm{d}V \tag{3.57}$$

with $\delta\boldsymbol{F}\boldsymbol{F}^{-1} = \operatorname{grad} \delta\boldsymbol{u}$. Note, that $\operatorname{grad}(\bullet)$ denotes the partial derivative of the quantity $(\bullet)$ with respect to the spatial coordinates. The variation of the determinant J is calculated by

$$\frac{\delta J}{J} = \mathbf{1} : \operatorname{grad} \delta\boldsymbol{u} \; . \tag{3.58}$$

The variation of the dilatation Θ depends of the used ansatz. On this account we choose here the method proposed by Nagtegaal et al. [155], where the dilatation is chosen as its mean value over the element

$$\Theta = \frac{v}{V} = \frac{1}{V} \int_{\mathcal{B}_0} J \, \mathrm{d}V \; . \tag{3.59}$$

The associated variation is given by

$$\frac{\delta\Theta}{\Theta} = \frac{1}{v} \int_{\mathcal{B}_t} J(\mathbf{1} : \operatorname{grad} \delta\boldsymbol{u}) \, \mathrm{d}V = \frac{1}{v} \int_{\mathcal{B}_t} \mathbf{1} : \operatorname{grad} \delta\boldsymbol{u} \, \mathrm{d}v \tag{3.60}$$

and we use in the following the abbreviation

$$\langle (\bullet) \rangle := \frac{1}{v} \int_{\mathcal{B}_t} (\bullet) \, \mathrm{d}v \tag{3.61}$$

for the representation of the mean value of the quantity $(\bullet)$. Finally we achieve the following internal part of the weak form

$$G^{\text{int}} = \int_{\mathcal{B}_0} \left\{ \operatorname{grad} \delta\boldsymbol{u} + \frac{1}{3} \left(\langle \mathbf{1} : \operatorname{grad} \delta\boldsymbol{u} \rangle - \mathbf{1} : \operatorname{grad} \delta\boldsymbol{u} \right) \right\} : \bar{\boldsymbol{\tau}} \, \mathrm{d}V \; . \tag{3.62}$$

An alternative approach for the approximation of the dilatation is formulated by Moran et al. [153], where they use the dilatation at the element center, and de Souza Neto et al. [58] did a slight modification to this approach.

3.6.2 FE-Approximation and Linearization

As already outlined in section 3.4 we need the linearization of the weak form of equilibrium for the application of the Newton-Raphson iteration scheme. The increment of G^{int} yields

$$\Delta G^{\text{int}} = \underbrace{\int_{\mathcal{B}_0} \tfrac{1}{2} \delta\bar{\boldsymbol{C}} : \bar{\mathbb{C}} : \tfrac{1}{2} \Delta\bar{\boldsymbol{C}} \, \mathrm{d}V}_{\Delta G^{\text{mat}}} + \underbrace{\int_{\mathcal{B}_0} \bar{\boldsymbol{S}} : \tfrac{1}{2} \Delta\delta\bar{\boldsymbol{C}} \, \mathrm{d}V}_{\Delta G^{\text{geo}}} \; , \tag{3.63}$$

where $\bar{\mathbb{C}}$ denotes the material modulus evaluating by $\bar{\boldsymbol{C}}$. Note, that $\bar{\boldsymbol{S}}$ again denotes second Piola-Kirchhoff stresses $\boldsymbol{S}(\bar{\boldsymbol{C}})$, which are obtained by the evaluation of the constitutive equation using $\bar{\boldsymbol{C}} = \bar{\boldsymbol{F}}^T \bar{\boldsymbol{F}}$. We again distinguish between the material and geometrical part, cf. Equation (3.33). The variation of $\bar{\boldsymbol{C}}$ has been already derived in the previous

section and the increment $\Delta\bar{\boldsymbol{C}}$ can be formulated analogously. The increment of the variation of the operator $\bar{\boldsymbol{C}}$ appearing in the geometrical part is composed as follows

$$\begin{aligned}\Delta\delta\bar{\boldsymbol{C}} = &\Delta_{\boldsymbol{u}}\delta_{\boldsymbol{u}}\bar{\boldsymbol{C}} + \Delta_J\delta_{\boldsymbol{u}}\bar{\boldsymbol{C}} + \Delta_\Theta\delta_{\boldsymbol{u}}\bar{\boldsymbol{C}} \\ &+ \Delta_{\boldsymbol{u}}\delta_J\bar{\boldsymbol{C}} + \Delta_J\delta_J\bar{\boldsymbol{C}} + \Delta_\Theta\delta_J\bar{\boldsymbol{C}} \\ &+ \Delta_{\boldsymbol{u}}\delta_\Theta\bar{\boldsymbol{C}} + \Delta_J\delta_\Theta\bar{\boldsymbol{C}} + \Delta_\Theta\delta_\Theta\bar{\boldsymbol{C}}\,,\end{aligned} \tag{3.64}$$

where the detailed expression of the individual components can be found in the Appendix C. After some algebraic manipulations we achieve the material part

$$\begin{aligned}\Delta G^{\mathrm{mat}} = \int_{\mathcal{B}_0} &\left\{\frac{1}{2}\delta\boldsymbol{C}\left(\frac{\Theta}{J}\right)^{2/3} + \frac{1}{3}\boldsymbol{C}\left(\frac{\Theta}{J}\right)^{2/3}\left(\frac{\delta\Theta}{\Theta} - \frac{\delta J}{J}\right)\right\} : \bar{\mathbb{C}} \\ &: \left\{\frac{1}{2}\Delta\boldsymbol{C}\left(\frac{\Theta}{J}\right)^{2/3} + \frac{1}{3}\boldsymbol{C}\left(\frac{\Theta}{J}\right)^{2/3}\left(\frac{\Delta\Theta}{\Theta} - \frac{\Delta J}{J}\right)\right\}\,\mathrm{d}V\end{aligned} \tag{3.65}$$

and the geometrical part

$$\begin{aligned}\Delta G^{\mathrm{geo}} = &\int_{\mathcal{B}_0} \bar{\boldsymbol{S}} : \frac{1}{2}\boldsymbol{C} \quad \frac{2}{3}\left(\frac{\Theta}{J}\right)^{2/3}\left\{\frac{2}{3}\left(\frac{\Delta\Theta}{\Theta} - \frac{\Delta J}{J}\right)\left(\frac{\delta\Theta}{\Theta} - \frac{\delta J}{J}\right)\right. \\ &\left. + \left(\frac{\Delta J\delta J}{J^2} - \frac{\Delta\Theta\delta\Theta}{\Theta^2}\right) + \left(\frac{\Delta\delta\Theta}{\Theta} - \frac{\Delta\delta J}{J}\right)\right\}\,\mathrm{d}V \\ &+ \int_{\mathcal{B}_0} \bar{\boldsymbol{S}} : \frac{1}{2}\delta\boldsymbol{C} \quad \frac{2}{3}\left(\frac{\Theta}{J}\right)^{2/3}\left(\frac{\Delta\Theta}{\Theta} - \frac{\Delta J}{J}\right)\,\mathrm{d}V \\ &+ \int_{\mathcal{B}_0} \bar{\boldsymbol{S}} : \frac{1}{2}\Delta\boldsymbol{C} \quad \frac{2}{3}\left(\frac{\Theta}{J}\right)^{2/3}\left(\frac{\delta\Theta}{\Theta} - \frac{\delta J}{J}\right)\,\mathrm{d}V \\ &+ \int_{\mathcal{B}_0} \bar{\boldsymbol{S}} : \frac{1}{2}\Delta\delta\boldsymbol{C} \quad \left(\frac{\Theta}{J}\right)^{2/3}\,\mathrm{d}V\,.\end{aligned} \tag{3.66}$$

Using the relation $\delta\boldsymbol{F}\boldsymbol{F}^{-1} = \operatorname{grad}\delta\boldsymbol{u}$ the material part can be reformulated to

$$\begin{aligned}\Delta G^{\mathrm{mat}} = \int_{\mathcal{B}_0} &\left\{\operatorname{grad}\delta\boldsymbol{u} + \frac{1}{3}\left(\frac{\delta\Theta}{\Theta} - \frac{\delta J}{J}\right)\right\} : \bar{\mathbb{c}} \\ &: \left\{\operatorname{grad}\Delta\boldsymbol{u} + \frac{1}{3}\left(\frac{\Delta\Theta}{\Theta} - \frac{\Delta J}{J}\right)\right\}\,\mathrm{d}V\,,\end{aligned} \tag{3.67}$$

where $\bar{\mathbb{c}}$ denotes the spatial tangent modulus with $\bar{\mathbb{c}}_{iklm} = \bar{F}_{iA}\bar{F}_{lC}\bar{F}_{mD}\bar{F}_{kB}\bar{\mathbb{C}}_{ABCD}$. Analogously, the geometrical part is rewritten taking into account the symmetry of the Kirchoff stress tensor $\bar{\boldsymbol{\tau}}$

$$\begin{aligned}
\Delta G^{\text{geo}} = \int_{\mathcal{B}_0} \bar{\boldsymbol{\tau}} : \mathbf{1} \quad & \frac{1}{3}\left\{\frac{2}{3}\left(\frac{\Delta\Theta}{\Theta} - \frac{\Delta J}{J}\right)\left(\frac{\delta\Theta}{\Theta} - \frac{\delta J}{J}\right)\right. \\
& \left. + \left(\frac{\Delta J \delta J}{J^2} - \frac{\Delta\Theta\delta\Theta}{\Theta^2}\right) + \left(\frac{\Delta\delta\Theta}{\Theta} - \frac{\Delta\delta J}{J}\right)\right\} \, \mathrm{d}V \\
+ \int_{\mathcal{B}_0} \bar{\boldsymbol{\tau}} : \operatorname{grad}\delta\boldsymbol{u} \quad & \frac{2}{3}\left(\frac{\Delta\Theta}{\Theta} - \frac{\Delta J}{J}\right) \, \mathrm{d}V \\
+ \int_{\mathcal{B}_0} \bar{\boldsymbol{\tau}} : \operatorname{grad}\Delta\boldsymbol{u} \quad & \frac{2}{3}\left(\frac{\delta\Theta}{\Theta} - \frac{\delta J}{J}\right) \, \mathrm{d}V \\
+ \int_{\mathcal{B}_0} \bar{\boldsymbol{\tau}} : \operatorname{grad}^T\Delta\boldsymbol{u} \; & \operatorname{grad}\delta\boldsymbol{u} \, \mathrm{d}V \, .
\end{aligned} \tag{3.68}$$

For details on the reformulation concerning both the last equations we refer to Freischläger [74]. In the latter relations of the increments ΔG^{mat} and ΔG^{geo} of the weak form the incremental forms of J and Θ as well as of their variations appear. Considering the specific approach (3.59) for the calculation of the dilatation Θ, the increments can be written as

$$\begin{aligned}
\frac{\Delta J}{J} &= \mathbf{1} : \operatorname{grad}\Delta\boldsymbol{u} \, , \\
\frac{\Delta\delta J}{J} &= (\mathbf{1} : \operatorname{grad}\delta\boldsymbol{u})\,(\mathbf{1} : \operatorname{grad}\Delta\boldsymbol{u}) - \mathbf{1} : (\operatorname{grad}\delta\boldsymbol{u} \; \operatorname{grad}\Delta\boldsymbol{u}) \, , \\
\frac{\Delta\Theta}{\Theta} &= \langle \mathbf{1} : \operatorname{grad}\Delta\boldsymbol{u} \rangle \, , \\
\frac{\Delta\delta\Theta}{\Theta} &= \langle (\mathbf{1} : \operatorname{grad}\delta\boldsymbol{u})\,(\mathbf{1} : \operatorname{grad}\Delta\boldsymbol{u}) \rangle - \langle \mathbf{1} : (\operatorname{grad}\delta\boldsymbol{u} \; \operatorname{grad}\Delta\boldsymbol{u}) \rangle \, .
\end{aligned} \tag{3.69}$$

Taking into account these relations and the variations of J (3.58) and Θ (3.58) we achieve the formulations

$$\begin{aligned}
\Delta G^{\text{mat}} = \int_{\mathcal{B}_0} & \left\{\operatorname{grad}\delta\boldsymbol{u} + \frac{1}{3}\left(\langle \mathbf{1} : \operatorname{grad}\delta\boldsymbol{u} \rangle - \mathbf{1} : \operatorname{grad}\delta\boldsymbol{u}\right)\right\} : \bar{\mathbb{c}} \\
& : \left\{\operatorname{grad}\Delta\boldsymbol{u} + \frac{1}{3}\left(\langle \mathbf{1} : \operatorname{grad}\Delta\boldsymbol{u} \rangle - \mathbf{1} : \operatorname{grad}\Delta\boldsymbol{u}\right)\right\} \, \mathrm{d}V
\end{aligned} \tag{3.70}$$

and

$$
\begin{aligned}
\Delta G^{\text{geo}} = & \int_{\mathcal{B}_0} \bar{\boldsymbol{\tau}} : \operatorname{grad}^T \Delta \boldsymbol{u} \ \operatorname{grad} \delta \boldsymbol{u} \, \mathrm{d}V \\
& + \frac{2}{3} \int_{\mathcal{B}_0} \bar{\boldsymbol{\tau}} : \operatorname{grad} \delta \boldsymbol{u} \left\{ \langle \mathbf{1} : \operatorname{grad} \Delta \boldsymbol{u} \rangle - (\mathbf{1} : \operatorname{grad} \Delta \boldsymbol{u}) \right\} \mathrm{d}V \\
& + \frac{2}{3} \int_{\mathcal{B}_0} \bar{\boldsymbol{\tau}} : \operatorname{grad} \Delta \boldsymbol{u} \left\{ \langle \mathbf{1} : \operatorname{grad} \delta \boldsymbol{u} \rangle - (\mathbf{1} : \operatorname{grad} \delta \boldsymbol{u}) \right\} \mathrm{d}V \\
& + \frac{2}{9} \int_{\mathcal{B}_0} \bar{\boldsymbol{\tau}} : \mathbf{1} \Big[\left\{ \langle \mathbf{1} : \operatorname{grad} \Delta \boldsymbol{u} \rangle - (\mathbf{1} : \operatorname{grad} \Delta \boldsymbol{u}) \right\} \\
& \qquad \left\{ \langle \mathbf{1} : \operatorname{grad} \delta \boldsymbol{u} \rangle - (\mathbf{1} : \operatorname{grad} \delta \boldsymbol{u}) \right\} \Big] \mathrm{d}V \\
& + \frac{1}{3} \int_{\mathcal{B}_0} \bar{\boldsymbol{\tau}} : \mathbf{1} \left\{ \langle (\mathbf{1} : \operatorname{grad} \delta \boldsymbol{u}) \, (\mathbf{1} : \operatorname{grad} \Delta \boldsymbol{u}) \rangle \right. \\
& \qquad \left. - \langle \mathbf{1} : \operatorname{grad} \Delta \boldsymbol{u} \rangle \langle \mathbf{1} : \operatorname{grad} \delta \boldsymbol{u} \rangle \right\} \mathrm{d}V \\
& + \frac{1}{3} \int_{\mathcal{B}_0} \bar{\boldsymbol{\tau}} : \mathbf{1} \left\{ \mathbf{1} : (\operatorname{grad} \delta \boldsymbol{u} \ \operatorname{grad} \Delta \boldsymbol{u}) \right. \\
& \qquad \left. - \langle \mathbf{1} : (\operatorname{grad} \delta \boldsymbol{u} \ \operatorname{grad} \Delta \boldsymbol{u}) \rangle \right\} \mathrm{d}V \, .
\end{aligned}
\tag{3.71}
$$

Following the idea of the isoparametric concept we use the ansatz function $N(\boldsymbol{\xi})$ for the approximation of the gradients

$$
\begin{aligned}
\operatorname{grad} \delta \boldsymbol{u} &= \sum_{I=1}^{n_{\text{node}}} \delta \boldsymbol{d}_I \otimes \operatorname{grad} N_I \quad \text{with} \quad \{\operatorname{grad} \delta \boldsymbol{u}\}_{ab} = \sum_{I=1}^{n_{\text{node}}} N_{I,a} \, \delta d_I^b \, , \\
\operatorname{grad} \Delta \boldsymbol{u} &= \sum_{I=1}^{n_{\text{node}}} \Delta \boldsymbol{d}_I \otimes \operatorname{grad} N_I \quad \text{with} \quad \{\operatorname{grad} \Delta \boldsymbol{u}\}_{ab} = \sum_{I=1}^{n_{\text{node}}} N_{I,a} \, \Delta d_I^b \, ,
\end{aligned}
\tag{3.72}
$$

where here $N_{I,a}$ denotes the partial derivative N_I with respect to the coordinate $\boldsymbol{x}_a$ in the current configuration, i. e. $\partial N_I / \partial \boldsymbol{x}_a$. Note, that due to avoid confusions with the partial derivative $N_{I,A}$ with respect to the reference coordinates, see cf. Equation (3.27), we use a lowercased subscript a indicating the relation to the current configuration. Now we are able to formulate the discrete forms of the internal part (3.62) as well as of the incremental terms, the material part (3.70) and the geometrical part (3.71). Beginning with the internal part of the weak form we achieve

$$
G^{e,\text{int}} = \sum_{I=1}^{n_{\text{node}}} (\delta \boldsymbol{d}_I)^T \int_{\mathcal{B}_0^e} \left\{ \boldsymbol{B}_{t\,I}^T + \bar{\boldsymbol{B}}_{t\,I}^T \right\} \bar{\boldsymbol{\tau}} \, \mathrm{d}V \tag{3.73}
$$

with the matrix

$$
\boldsymbol{B}_{t\,I} = \begin{bmatrix}
N_{I,1} & 0 & 0 \\
0 & N_{I,2} & 0 \\
0 & 0 & N_{I,3} \\
N_{I,2} & N_{I,1} & 0 \\
0 & N_{I,3} & N_{I,2} \\
N_{I,3} & 0 & N_{I,1}
\end{bmatrix} \, , \tag{3.74}
$$

which is well-known from the standard displacement formulation in the current setting, cf. WRIGGERS [254], and the additional part arising from the $\bar{\boldsymbol{F}}$-approach

$$\bar{\boldsymbol{B}}_{t\,I} = \frac{1}{3}\begin{bmatrix} \langle N_{I,1}\rangle - N_{I,1} & \langle N_{I,2}\rangle - N_{I,2} & \langle N_{I,3}\rangle - N_{I,3} \\ \langle N_{I,1}\rangle - N_{I,1} & \langle N_{I,2}\rangle - N_{I,2} & \langle N_{I,3}\rangle - N_{I,3} \\ \langle N_{I,1}\rangle - N_{I,1} & \langle N_{I,2}\rangle - N_{I,2} & \langle N_{I,3}\rangle - N_{I,3} \\ 0 & 0 & 0 \\ 0 & 0 & 0 \\ 0 & 0 & 0 \end{bmatrix} . \tag{3.75}$$

The subscript t of both the matrices should indicate that the appearing partial derivatives of the ansatz functions must be done with respect to the current coordinates $\boldsymbol{x}_a$ with $a = 1, 2, 3$. The geometrical part of the increment ΔG is approximated by

$$\Delta G^{e,\mathrm{mat}} = \sum_{I=1}^{n_{\mathrm{node}}} \sum_{J=1}^{n_{\mathrm{node}}} (\delta \boldsymbol{d}_I)^T \left\{ \boldsymbol{K}^{e,\mathrm{mat}}_{t\,IJ} + \bar{\boldsymbol{K}}^{e,\mathrm{mat}}_{t\,IJ} \right\} \Delta \boldsymbol{d}_J \tag{3.76}$$

with the stiffness matrices

$$\boldsymbol{K}^{e,\mathrm{mat}}_{t\,IJ} := \int_{\mathcal{B}^e_0} \boldsymbol{B}^T_{t\,I}\, \bar{\mathbb{C}}^e\, \boldsymbol{B}_{t\,J}\, \mathrm{d}V \quad \text{and} \quad \bar{\boldsymbol{K}}^{e,\mathrm{mat}}_{t\,IJ} := \int_{\mathcal{B}^e_0} \bar{\boldsymbol{B}}^T_{t\,I}\, \bar{\mathbb{C}}^e\, \bar{\boldsymbol{B}}_{t\,J}\, \mathrm{d}V \quad , \tag{3.77}$$

where again the first matrix is well-known from the standard displacement formulation. Finally, we derive the discrete form of the geometrical part

$$\Delta G^{e,\mathrm{geo}} = \sum_{I=1}^{n_{\mathrm{node}}} \sum_{J=1}^{n_{\mathrm{node}}} (\delta \boldsymbol{d}_I)^T \left\{ \boldsymbol{K}^{e,\mathrm{geo}}_{t\,IJ} + \bar{\boldsymbol{K}}^{e,\mathrm{geo}}_{t\,IJ} \right\} \Delta \boldsymbol{d}_J \tag{3.78}$$

with the matrix also arising from the standard displacement formulation

$$\boldsymbol{K}^{e,\mathrm{geo}}_{t\,IJ} := \int_{\mathcal{B}^e_0} (N_{I,a} N_{J,b}) \bar{\tau}^{ab}\, \mathrm{d}V \ , \tag{3.79}$$

where $N_{I,a}$ and $N_{J,b}$ denotes the partial derivative of the ansatz functions with respect to the actual coordinates $\boldsymbol{x}_a$ and $\boldsymbol{x}_b$. The second matrix in the geometrical part reads

$$\begin{aligned} \bar{\boldsymbol{K}}^{e,\mathrm{geo}}_{t\,IJ} := \frac{2}{3} \int_{\mathcal{B}^e_0} \left\{ (\boldsymbol{B}^T_{t\,I} \bar{\boldsymbol{\tau}}) \otimes \widetilde{\boldsymbol{n}}_{J,\boldsymbol{x}} + \widetilde{\boldsymbol{n}}_{I,\boldsymbol{x}} \otimes (\boldsymbol{B}^T_{t\,J} \bar{\boldsymbol{\tau}}) \right\} \mathrm{d}V \\ + \frac{2}{9} \int_{\mathcal{B}^e_0} \mathrm{tr}\, \bar{\boldsymbol{\tau}}\, (\widetilde{\boldsymbol{n}}_{I,\boldsymbol{x}} \otimes \widetilde{\boldsymbol{n}}_{J,\boldsymbol{x}})\, \mathrm{d}V \\ + \frac{1}{3} \int_{\mathcal{B}^e_0} \mathrm{tr}\, \bar{\boldsymbol{\tau}}\, \left\{ \widetilde{\boldsymbol{N}}^{\mathrm{diag}}_{IJ,\boldsymbol{x}} + \widetilde{\boldsymbol{N}}^{\mathrm{full}}_{IJ,\boldsymbol{x}} \right\} \mathrm{d}V \end{aligned} \tag{3.80}$$

using the vector with its components

$$\{\widetilde{\boldsymbol{n}}_{I,\boldsymbol{x}}\}_a := \langle N_{I,a} \rangle - N_{I,a} \tag{3.81}$$

and the matrices build from

$$\begin{aligned} \{\widetilde{\boldsymbol{N}}^{\mathrm{diag}}_{IJ,\boldsymbol{x}}\}_{ab} &:= \delta_{ab} \left[\langle N_{I,a} N_{J,b} \rangle - \langle N_{I,a} \rangle \langle N_{J,b} \rangle \right] , \\ \{\widetilde{\boldsymbol{N}}^{\mathrm{full}}_{IJ,\boldsymbol{x}}\}_{ab} &:= N_{I,a} N_{J,b} - \langle N_{I,a} N_{J,b} \rangle \ , \end{aligned} \tag{3.82}$$

where $N_{I,a}$ denotes the partial derivative of the ansatz function with respect to the actual coordinates $\boldsymbol{x}_a$. From here the further steps, e. g. assembling and solving procedures, are the same than we discussed during the formulation of the standard displacement approach and we refer to section 3.4.

3.7 Finite Element Tearing and Interconnecting (FETI)

In the previous sections we show that the finite element method provides a suitable tool to achieve the solution of boundary value problems starting from the strong form of equilibrium given in Equation $(3.1)_2$. In this context the equations have to be discretized and linearized in order to obtain a system of equations

$$\boldsymbol{K}\Delta\boldsymbol{D} = -\boldsymbol{R}\,, \tag{3.83}$$

with the global stiffness matrix $\boldsymbol{K}$, the incremental nodal displacement vector $\Delta\boldsymbol{D}$ and the global residual vector $\boldsymbol{R}$, cf. Section 3.4. Obviously, an increasing number of finite elements arising from the discretization of the considered physical body means an increasing of the number of degrees of freedom. Since the dimension of the vector $\Delta\boldsymbol{D}$ mainly depends on the number of degrees of freedom, the solution time for Equation (3.83) increases along the number of finite elements. For adequate discretizations of complex geometrical structures this number often grows to a large amount and consequently the solution time is going up. Indeed the performance of computer hardware has been improved all the time since their invention, but a large system of equation still means a certain solution time. Additionally such systems requires an allocation of much computer memory for the system matrices as well as for index arrays during the assembling process and for history variables. In this context the application of parallel solution strategies enables on the one hand a more efficient solution process, since it arrange the calculation duties to several processor units. On the other hand the distribution increases the total amount of available computer memory.

For the parallelization of the solution process we focus on domain decomposition methods. Such methods decompose the global boundary value problem into several, possibly many, smaller boundary value problems on subdomains. To obtain numerical scalability often a coarse global problem is solved in addition to the local subdomain problems. Considering overlapping or non-overlapping subdomains is the main distinction of the different domain decomposition method. As methods attributed to the former type are the Schwarz methods and details on this can be found in Toselli and Widlund [228] and Quarteroni and Valli [177]. Here, we focus on the non-overlapping domain decomposition and outline in the sequel the main idea and concept of one specific method, the Finite Element Tearing and Interconnecting - Dual Primal (FETI-DP). For reader with a deeper interest

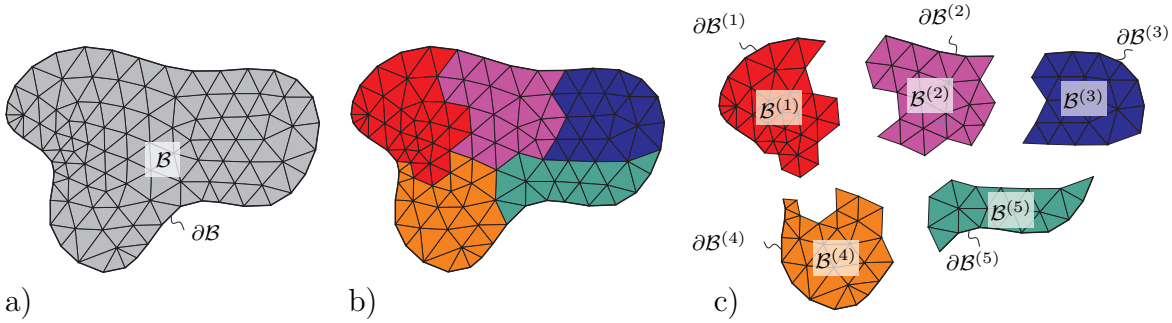

Figure 3.5: Decomposition of a discretized body: a) whole domain $\mathcal{B}$ with its boundary $\partial\mathcal{B}$, b) 5 subdomains and c) the exploded view. $\mathcal{B}^{(i)}$ denotes the i-th subdomain with its boundary $\partial\mathcal{B}^{(i)}$.

in the theory we refer to e. g. Farhat et al. [69], Klawonn and Widlund [125], Klawonn and Rheinbach [122; 123], Klawonn [121] and Rheinbach [179; 180]. Algorithms of the FETI-DP family have been shown to be highly scalable for more than 10^5 processor cores, see, e.g, Klawonn and Rheinbach [124].

The decomposition procedure the computational domain into many subdomains $\mathcal{B}^{(i)}$, $i = 1, \ldots, N$ is shown in Figure 3.5. We always have matching nodes across the subdomain interface. Consequently, every finite element e belongs to exactly one subdomain $\mathcal{B}^{(i)}$, i. e. $e \in \mathcal{B}^{(i)}$. In order to define the decomposition of the body into subdomains a graph partitioner is used, see Karypis et al. [119]. The assembling procedure on each subdomain i over the associated ${n_{\text{ele}}}^{(i)}$ finite elements results in the local stiffness matrices $\boldsymbol{K}^{(i)}$ and the local residual vectors $\boldsymbol{R}^{(i)}$, i. e.

$$\boldsymbol{K}^{(i)} = \mathop{\mathsf{A}}_{e=1}^{n_{\text{ele}}} \boldsymbol{K}^e \,, \quad \boldsymbol{R}^{(i)} = \mathop{\mathsf{A}}_{e=1}^{n_{\text{ele}}} \boldsymbol{r}^e \,, \quad \text{with} \quad i = 1, \ldots, n_{\text{subd}} \,, \tag{3.84}$$

where n_{subd} denotes the number of subdomains defined by a given decomposition of the global problem. The local problems read

$$\boldsymbol{K}^{(i)} \Delta \boldsymbol{D}^{(i)} = -\boldsymbol{R}^{(i)} \quad \text{with} \quad i = 1, \ldots, n_{\text{subd}} \,, \tag{3.85}$$

and in this form they are independent from each other. But such independent solutions of each subdomain would result in discontinuous deformations of the boundaries of the subdomains. Additionally, since a subdomain do not exhibit an intersection with the Dirichlet boundary conditions defining the global boundary value problem the associated local stiffness matrix is not invertible. To overcome these problems in the FETI method a continuity constraint $\boldsymbol{d}^{(i)} - \boldsymbol{d}^{(j)} = 0$ is introduced assuming on the interface $\Gamma := \bigcup_{i \neq j} \partial\mathcal{B}_{(i)} \cap \partial\mathcal{B}_{(j)}$ of the neighboring subdomains $\mathcal{B}^{(i)}$ and $\mathcal{B}^{(j)}$ matching finite element nodes. Over all subdomains this constraint can be written as

$$\sum_{i=1}^{n_{\text{subd}}} \boldsymbol{G}^{(i)} \Delta \boldsymbol{D}^{(i)} = \boldsymbol{0} \,, \tag{3.86}$$

where the matrix $\boldsymbol{G}^{(i)}$ is also called jump operator and offers a simple form due to its entries, which arise only to be 0, 1 and -1. By the introduction of the dual Lagrange multipliers $\boldsymbol{\lambda}$ as additional unknown variable we end up with the formulation

$$\begin{bmatrix} \boldsymbol{K} & \boldsymbol{G}^T \\ \boldsymbol{G} & \boldsymbol{0} \end{bmatrix} \begin{bmatrix} \Delta \boldsymbol{D} \\ \boldsymbol{\lambda} \end{bmatrix} = \begin{bmatrix} -\boldsymbol{R} \\ \boldsymbol{0} \end{bmatrix} \tag{3.87}$$

for the global problem. Note, that the global matrices and vectors are defined by

$$\begin{aligned} \boldsymbol{K} &= \begin{bmatrix} \boldsymbol{K}^{(1)} & \cdots & \boldsymbol{0} \\ \vdots & \ddots & \vdots \\ \boldsymbol{0} & \cdots & \boldsymbol{K}^{(n_{\text{subd}})} \end{bmatrix} \,, \quad \Delta \boldsymbol{D} = \begin{bmatrix} \Delta \boldsymbol{D}^{(1)} \\ \vdots \\ \Delta \boldsymbol{D}^{(n_{\text{subd}})} \end{bmatrix} \,, \\ \boldsymbol{R} &= \begin{bmatrix} \boldsymbol{R}^{(1)} \\ \vdots \\ \boldsymbol{R}^{(n_{\text{subd}})} \end{bmatrix} \,, \qquad \boldsymbol{G} = \begin{bmatrix} \boldsymbol{G}^{(1)} & \ldots & \boldsymbol{G}^{(n_{\text{subd}})} \end{bmatrix} \end{aligned} \,. \tag{3.88}$$

Additionally, in the FETI-DP algorithm a small subset of the continuity constraints in Equation (3.86) is fulfill exactly using a subassembly strategy, a global elimination,

instead of the multipliers. The set of interface variables, where the continuity constraint is fulfilled exactly is called *primal* and all other interface variables are called *dual*. Therefore, this variant of the FETI method is called "dual-primal" (DP). The remaining constraints are enforced by the Lagrange multipliers $\boldsymbol{\lambda}$, which are determined by an iterative procedure. Here, a parallel, preconditioned Generalized Minimal Residual (GMRES) method is applied. For details on the FETI-DP implementation, see, e.g. Klawonn and Rheinbach [122; 124], where the preconditioner is also described. Consequently, the local problems on the subdomains can be solved in parallel in each iteration step. Finally, with a suitable Lagrange multipliers $\boldsymbol{\lambda}$, which is obtained by the iterative process, the solution vector $\Delta \boldsymbol{D}$ is computed and the update within the global Newton iteration is performed. For details on this we also refer to the here given references regarding the FETI-DP method.

For the parallel computations presented in the sequel of this thesis we use an environment consisting of the Finite Element Program FEAP, see Taylor [224] and the implementation of the FETI-DP method shown in e.g. Klawonn and Rheinbach [122; 124]. The used FETI-DP algorithms are developed and provided by the group of Prof. Dr. A. Klawonn at the Universität Duisburg-Essen and this support is greatly acknowledged. Main tasks of FEAP are the pre- and postprocessing of the computation and it provides the element and material technology for the FE-discretization. Therefore existing FEAP libraries can be used for the novel environment. Using a common interface the relevant element data are exchanged between FEAP and the solver. The implementation of the domain decomposition method computes the solution solely based on this information. The domain is decomposed into subdomains and the systems of equations are assembled for all subdomains. The parallel algorithm solves the problem using MPI, PETSc Balay et al. [3; 4; 5], and UMFPACK Davis [55]. The workflow of a parallel computations consists of the following steps:

1. FEAP: initialization of the global boundary value problem,
2. FEAP: load step control, stops at final load
3. FEAP: convergence check of the global Newton iteration, in case of convergence go to step 2
4. FEAP: calculation of the element stiffness matrices and the element residual vectors and their transfer to the FETI-DP solver
5. FETI-DP: data reception and decomposition into subdomains
6. FETI-DP: parallel computation of the solution and transfer of solution vector to FEAP
7. FEAP: data reception and update of the global displacement vector
8. FEAP: go to step 3.

Note, that the communications between FEAP and the FETI-DP solver is done over the network using the Transmission Control Protocol (TCP) sockets.

4 Arterial Walls: Histology and Material Modeling

The diseases regarding the vascular system have become the most diagnosed illness responsible for mortality. Thereby, atherosclerotic degenerated arteries represented such a typical diseases, which is characterized by a change of the innermost arterial wall layer and is mostly followed by the reduction of the inner diameter of the vessel. Consequently, the attention studying the mechanical behavior of soft biological tissues and especially of the arterial walls has increased in the last years. This fact is certainly observable in the amount of publications coming from groups belonging to medical and biological research groups as well as groups related to engineering research fields. Beside the development and improvement of the treatments of vascular diseases several mathematical models for the description of the mechanical behavior have been introduced. These models represent an essential part, which is necessary for the analysis of the arteries and the treatment of their diseases using the Finite Element Method. On that account we first introduce general information of arteries with respect to their composition and wall structure as well as the typical diseases and their treatments. Since we later are focus on the reconstruction of a patient specific arterial geometry we are also interested in the medical imaging. Consequently, we give a brief introduction to the standard imaging techniques and explain in more detail the intravascular ultrasound (IVUS) method, which we use for the reconstruction in the sequel of this thesis. Afterwards we discuss the different mechanical properties of the artery, which offer the complex characteristics of soft biological tissues. Finally, we provide the constitutive modeling for the description of the mechanical behavior of arterial walls and adjust the parameter of the used models to experimental data.

4.1 Basics on Arteries

The arteries are an essential transport system in the human body as well as in many animal ones. In general their transport direction is away from the heart. Several types of arteries occur in the body. The first distinguishing feature is the affinity to the two circulation systems: the *pulmonary* circulation establishes the bidirectional connection between heart and lung and the *systemic* circulation delivers the blood from the heart to the periphery and back. When in pulmonary arteries the deoxygenated blood flows to the lung in systemic arteries blood is delivered. It is enriched with oxygen and flows to the capillaries where the actual exchange of oxygen and carbon dioxide occurs. The capillaries then deliver the deoxygenated blood to the veins for transport back to the lung and heart. Besides the oxygen supply the arteries among others is responsible for the nutrient transport. There exists a further subdivision criterion regarding the systemic arteries. They are divided into *elastic* and *muscular* arteries according to the relative compositions of elastic and muscle tissue in their medial layer as well as their size and the makeup of the internal and external elastic lamina, see Section 4.1.1. The elastic arteries are located near to the heart and have larger diameters ($> 10\,\text{mm}$), e.g. aorta, carotid and iliac ones. However muscular ones have diameters in the range $0.1 - 10\,\text{mm}$ and a much higher amount of muscle cells. The elastic arteries are responsible for the transformation of the pulsatile blood flow caused by the heart beat in a quasi-continuous flow and protect the periphery from blood pressure minima and maxima. Hence this artery type undergoes much larger deformations than the muscular arteries and for that reason we concentrate on the elastic arteries in this thesis. In

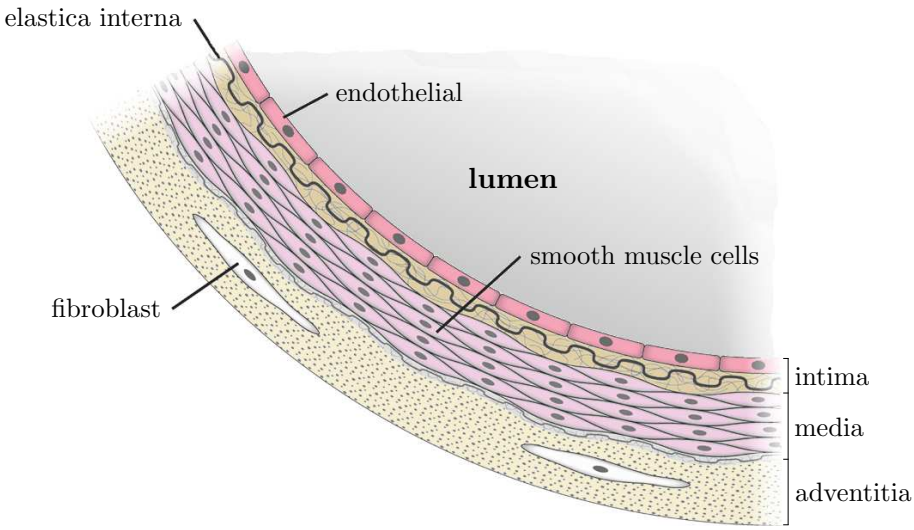

Figure 4.1: Schematic cross sectional view of a segment of a healthy elastic artery with its three distinct layers: adventitia, media and intima, adapted from Ghesquiere [82].

the following subsections we give brief introductions towards several aspects concerning arterial walls and their medical treatment to provide essential information regarding the applications in the sequel of this thesis. In addition to the references given in the subsections we refer to the classical publications in the field of medicine and biomechanics, e.g. Rhodin [181], Silver et al. [202], Junqueira and Carneiro [117], Holzapfel and Ogden [107; 108; 109] and Humphrey [116].

4.1.1 Histology: Adventitia, Media, Intima

Healthy arterial walls consist of three nearly concentric layers:

- the innermost layer tunica *intima* (intima),
- the middle layer tunica *media* (media),
- the outermost layer tunica *adventitia* (adventitia, tunica externa),

where each layer can be more or less marked regarding its thickness or appearance. The arrangement of the three layers in a healthy artery are schematically illustrated in Figure 4.1.

Intima In a healthy artery the innermost arterial layer, the tunica intima, consists essentially of the endothelium, a monolayer of endothelial cells (thickness $\approx 0.2-0.5\,\mu m$), and the underlying basal membrane (thickness $\approx 1\,\mu m$) composed of interlacing collagen, elastic fibrils and longitudinally arranged bundles of smooth muscle cells (Krstić [137]). At this point we remark, that the thickness of the intima varies according to the age of the patient and his/her anamnesis, see section 4.1.2. The functional background is the exchange of molecules between bloodstream and the surrounding tissues. The intima is surrounded by the internal elastic lamina, which represents the boundary to the next distinct layer: the media. For more information about the intimal composition see Rhodin [181].

Media The medial layer delimited by the internal elastic lamina at the interior and the external elastic lamina at the exterior. Both are fenestrated sheets of elastin and allow the transmitting of water, nutrients and electrolytes between the adjacent arterial layers as well as cellular communication. Note, that the external lamina is more distinct in walls

of elastic arteries than in the muscular counterparts and in cerebral arteries there are only a few elastic fibers instead of it. Independently from the type of artery (elastic/muscular) concentric pattern smooth muscle cells and elastic fibers compose the soft tissue between the bordering laminae. But the structure of the pattern differs between these types. Thus, in elastic ones the pattern is built from lamellar units – also called musculo-elastic fascicle – , which consists of layer-like packaged elastin, smooth muscle cells and collagen fiber bundles. The packages are bundled by thin (3 µm) fenestrated elastin sheets forming a continuous fibrous helix, see also Schultze-Jena [198], Staubesand [219]. The helix has a small pitch and consequently this structured arrangement gives the media an ability to resist high loads in the circumferential direction. The number of layers (up to 70) and their thickness ($5 - 20\,\mu m$) depends on the diameter of the vessel and therefore on the distance regarding the heart. In contrast to this in muscular arteries the media appears as a single thick layer of smooth muscle cells with a reduced fraction of collagenous fibers. Shekhonin et al. [201] shows, that the distribution of collagen in healthy and diseased (atherosclerotic) arteries does not significantly differ from each other. Beside the given references in the introduction of this chapter we refer especially regarding the medial layer of elastic arteries to Clark and Glagov [48; 49] and to 3D micro- and nanostructural analysis by O'Connell et al. [163].

Adventitia The adventitia appears as the outmost layer of the wall and has following constituents: fibroblasts, fibrocytes, histological ground substance – also called groundmatrix – and collagen fibers organized in thick bundles. While the adventitia is clearly delimited inwards to the media by the external elastic lamina, the outer boundary to the surrounding tissue (loose connective tissue) does not exist in such a distinct layer. It also serves as a layer that carries nutrients to the smooth muscle cells of the media. The adventitia's thickness depends on the type (elastic or muscular) of artery as well as on the physiological function and the location in the vascular tree. It increases from $\sim$10% of the wall thickness in elastic arteries to $\sim$50% in muscular ones and cerebral blood vessels almost entirely lack an adventitia. The structure of the collagen shows two opposed helical fiber arrangements but in contrast to the fibers in the media their individual orientations show larger deviations from the mean orientation, see Canham et al. [39], Finlay et al. [71]. Since the collagen fibers in the adventitial tissue have a wavelike character in the unstressed state, the adventitia shows a lower stiffness than the media. But at a certain strain level the fibers are straight and cause a much stiffer mechanical response. This behavior is protective mechanism from overstretch and rupture. The fact concerning the fewer differences in the collagen distribution of healthy and diseased arteries, already mentioned in the section "media", also applies to the adventitia (Shekhonin et al. [201]).

4.1.2 Arterial Wall Diseases and Their Treatments

The World Health Organization (WHO) published in WHO [249] that 16.3 % of deaths during year 2004 in high-income countries were classified as coronary heart disease and thereby the number one of the top ten causes of death. The second position was occupied by strokes and other cerebrovascular diseases with a fraction of 9.3 % of deaths for comparison only. In low-income and middle-income countries the amount was comparable, 11.2 % and 14.2 % respectively, but it holds "only" the second position. The Statistisches Bundesamt Deutschland (German federal agency of statistics) observed a similar result

for the year 2009, in which 8.6 % of deaths in Germany were caused by chronic ischaemic heart disease, see DESTATIS [61]. Thus, the interest in research for analysis methods and methods of treatment to improve these alarming data is obviously given. The main underlying reason for these diseases is *atherosclerosis*. Note, that the similarly pronounced word arteriosclerosis describes the broader term for several arterial diseases in addition to the atherosclerosis and means a hardening or stiffening of the arterial wall with loss of elasticity. The most important subgroup is the atherosclerosis and is completed by two other ones: Mönckeberg's medical calcific sclerosis and the arteriolosclerosis.

In this thesis we focus on the atherosclerotic disease since it represents the main reason for cardiac and vascular diseases and we refer for details regarding the other subgroups to classical medical literature, e.g. Baretton et al. [15]. The WHO gives the definition "Atherosclerosis is a variable combination of changes of the intima of arteries (as distinguished from arterioles) consisting of the focal accumulation of lipids, complex carbohydrates, blood and blood products, fibrous tissue and calcium deposits, and associated with medical changes.", cf. de Brux et al. [57]. In other words atherosclerosis is where plaque builds up and sticks to the walls of the arteries. The plaque is made up of cholesterol and fatty substances found in blood as well as other particles found in blood. Nowadays a long list of risk factors with different importance supporting atherosclerosis are known. The primary risk factors are hypertension (high blood pressure), metabolic disorder accompanied by high cholesterol level, tobacco smoking, diabetes melitus and age as well as sex. Secondarily are adiposity, hyperuricemia (high uric acid level in blood), stress, physical inactivity and hormonal factors.

As the direct causes for atherosclerosis are not known yet, there are two different hypotheses for the pathogenesis of atherosclerosis:

- The *"response-to-injury"* hypothesis, whereby an injury of the endothelium, including hypercholesterolemia, immunologic injury, injury from toxins or viruses and mechanical injury, causes an alteration in the functional and morphologic capacities of the endothelial cells. These alterations are followed by interaction with two cells from the blood, the platelet and the monocyte, which may enter the arterial wall. Platelet derived growth factors stimulate the smooth muscle cells to migrate from the media into the intima, and, to take up increased quantities of low density lipoprotein, the principal cholesterol carrying lipoprotein present in the plasma, see Ross [186]. The monocyte becomes a macrophage which takes up large quantities of lipid (fat) in the form of oxidized low-density lipoprotein (OxLDL) and then becomes a so-called foam cell, with large intracellular lipid deposits, being the earliest detectable lesions in atherosclerosis, also known as "fatty streaks". The foam cells also play a role in evolution around the area of atherosclerosis.

- The *"lipoprotein-induced atherosclerosis"* hypothesis, wherein the activator of the atherosclerosis is not an injury, but rather it starts with the oxidative modification of the low density lipoprotein when contacting with an arterial wall and then follows the same way as the "response-to-injury" hypothesis.

In the vasculature, the preferred sites of atherosclerosis are those of complex geometry, most often the atherosclerotic plaques occur in the abdominal aorta, iliacs, coronaries, femorals, popliteals, carotids, and cerebrals, cf. Humphrey [116]. In the early states of

disease the atherosclerosis does not cause any clinical symptoms and only after several decades the process comes to a state of a clinical syndrome having either a slow or an acute development. But in common the arterial wall loses its ability to balance the pressure and consequently the periphery of the vascular system is effected more and more by the pulsatile blood flow. In the larger elastic vessels and the aorta following complications can occur: *plaque rupture* or *abdominal aorta aneurysms* and *infrarenal aneurysms*. A thrombus causing an organ infarct is the result of a plaque rupture and the decreasing stability of the wall caused by a diffusion disorder leads to an aneurysm. Aneurysms represent critical disorders since they lead to spontaneous and often lethal hemorrhages. In the mid-size and small arteries a decreased lumen is the most frequent form of symptom and referred to as stenosis, which not uncommonly causes lethal complications like arterial occlusions. The definite detection of atherosclerotic diseases can only be done by medical imaging techniques like ultrasound and catheter-based examinations. Since in this thesis one focus is on the patient specific reconstruction of arteries, we separately treat the topic of medical imaging of arteries in section 4.1.3.

The healing of atherosclerosis is very difficult and the methods of treatment have different starting points. The medicamentous methods aim at the therapy of the basic diseases like hypertension or diabetes instead at the reversion of the decreased lumen since no suitable and authorized medicaments are available. But these treatments are only effective in an early state and slow down the disease process. In an advanced state of the atherosclerosis the treatment is done by invasive procedure: bypass surgery or catheter-based invasive techniques. During the bypass method the surgeon place a body's own vessel segment or artificial vascular implant going past the blood flow of the diseased arterial part. But because of less effort as well as the risk of complication several minimal invasive surgery methods are developed which are referred to catheter-based invasive techniques. All procedures start with a catheterization where the surgeon guides a thin flexible tube (catheter) into the narrowed arteries to open them using special tools and to improve the blood flow. Mostly, the access for the catheter is done through the femoral artery in the groin and sometimes the radial artery in the wrist is used. The two common types of catheter-based procedures are:

- *Balloon angioplasty with or without stenting.* The balloon angioplasty is done by attaching an empty and collapsed balloon to the catheter guided by a wire. Such a balloon catheter, shown in Figure 4.2a, is passed into the narrowed location and inflated to a fixed size using water pressure (75 to 500 times with 6 to 20 kPa). The pressure from the inflated balloon presses the plaque against the wall of the artery and damage effects in the arterial layers occur. They lead to remanent deformations and the increase lumen provides for an improvement of the previously diminished blood flow. If the angioplasty is combined with stenting a small expandable wire tube called a stent is inserted into the artery to ensure the increase lumen after the balloon deflation. Reclosure of the artery is less likely to occur after angioplasty followed by stenting than after angioplasty alone. A schematic illustration of the angioplasty is shown in Figure 4.2b.

- *Atherectomy.* During the catheterization a cutting device, is guided through the catheter to the narrowed portion of the artery. To remove the plaque different cutting devices are developed which grind or cut away the narrowing parts. The devices are often equipped with a unit for the storage of the removed particles, because these

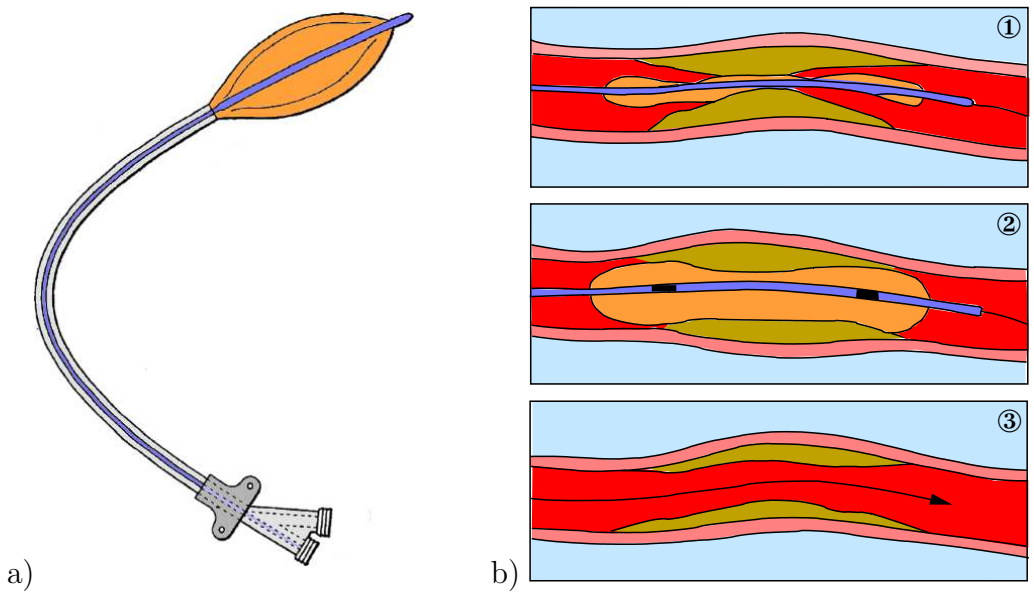

Figure 4.2: Balloon angioplasty of atherosclerotic arteries: a) balloon catheter, adapted from Schock [189]; b) essential steps: ① balloon-tipped catheter positioned across narrowed segment, ② balloon is inflated, stretching the wall and flattening the plaque, ③ catheter is pulled out and larger lumen allows improved blood flow.

particles can occur a closure in the following vascular tree. Some techniques use a balloon inflation to push the device towards the plaque. A newer method applies a laser beam instead of a cutting device to vaporize the plaque with the advantage of no more required storage.

Beside the advantages of this method to be a minimal invasive surgery there exist two non-neglectable disadvantages. The first one is the risk that during or after the procedure plaque particles from the treated part can cause an occlusion in the smaller arteries. On the one hand the particles can originate from a plaque rupture caused by ill-conditioned balloon pressure and resulting stress concentration across the arterial wall. On the other hand the particles can arise during the cutting process of the atherectomy. A further problem is the reoccurrence of stenosis, also called *restenosis*, which means a narrowing of the blood vessel again and has become a more relevant topic in the field of biomechanics in the last years. "Overstretching" of the arterial wall can fragment the internal elastic lamina, damage smooth muscle cells, disrupt cell-to-cell connections and tear medial elastin and collagen fibers. But a restenosis can be observed in arteries which have been furnished with a stent. For reducing the rate of restenosis the stent design and material have been developed permanently and the stent coating with drugs has been established. So stents have become a "hightech" product and for further information about their development see Wienecke et al. [250].

4.1.3 Medical Imaging

The discovery of the X-rays – the "invisible ray" – by Wilhelm Conrad Röntgen in 1895 was the beginning of a new era in the clinical diagnostics. It was the first method enabling "the look into the body" using a non-invasive technique. So painful and dangerous surgeries could be avoided. This investigation was the source of a new research field, the medical

imaging. For nearly 75 years the basic technique of Röntgen's discovery had not changed. The X-rays pass through the body and afterwards impinge on a radiation-sensitive material, e.g. a film or a screen. A geometric pattern is produced on this medium by the structures in the beam path. The development was confined to the improvement of the environment like fluoroscopic imaging and coupling with television. After World War II a new process of development in the medical imaging was started, which still lasts. It provides new diagnostic techniques like e.g. the magnetic resonance imaging (MRI), positron emission tomography (PET) and the ultrasound. All these medical imaging techniques base on the influence of the body's interior, namely atoms and molecules, to the change of properties of the transmitted waves. Whereby ultrasound uses high frequency sound waves instead of electromagnetic waves, which are produced during a X-ray, MRI or PET examinations. The answer to the question, which technique should be preferred for the different fields of application regarding the diagnostic of the human body can not be stated clearly. Since the development of medical imaging is a rapidly growing field every new investigation can change the criteria of decision. But also the economic view has to be considered as well as the side-effects including long-term effects to the health occurring from the application are crucial points. An interest discourse with respect to this topic is given in chapter 8 of Guy and ffytche [89]. For more details on the different methods of medical imaging regarding the theory as well as technique of application we refer in addition to the latter reference to the textbook by Robb [185]. Here we focus in the sequel on the ultrasound technique since it provides the feasibility to produce further information concerning the histology of arteries and their wall. Note that also the MRI technique can be used for the imaging of atherosclerotically degenerated arteries as shown in e.g. Choudhury and Fayad [43] and Desai and Lima [60]. But the MRI scanning is a more expensive diagnosis compared to the ultrasound because of the investment for purchase and operating. Since the X-ray radiograph provides extremely good contrast between bone and all soft tissue but low contrast regarding different tissue types it does not come into consideration for the determination of the distinct layers of the arterial wall. But as shown in section 5.1 the X-ray radiograph in combination with a radiocontrast agent can be used to visualize the geometry of the vessel's lumen.

The ultrasound describes sound waves, which are longitudinal and have a frequency range from 0.5 to 15 MHz. In the medical application one utilizes the effect that these waves describe the mechanical disturbance located occurring interior the body. Thereby the various tissues have different mechanical properties which influence the change towards the sound velocity. At their boundaries the waves are scattered and the reflection, also called echo signal, can be recorded by a receiver to form an image. The principle of a medical ultrasound procedure is illustrated schematically in Figure 4.3a. A piezoelectric transducer emits a pulse of ultrasound into the body of interest and inside the body it is partially reflected by the boundaries, the internal surfaces, of the different tissues. The receiver, mostly implemented in the transducer, detects these reflections. From the signal a monitor can display the amplitude and from the round trip time the type of tissue can be identified. The typical ranges of velocities of sound in various substances are shown in Figure 4.3b. The resulting image is a single line through the body and this scan method is referred to the amplitude or A-mode scan. Another type is the brightness or B-mode scan, which combines many differently orientated A-scans to a two-dimensional image transforming the echo amplitude into a greyscale map. The motion or M-mode scan is used where rapid motion monitoring is required.

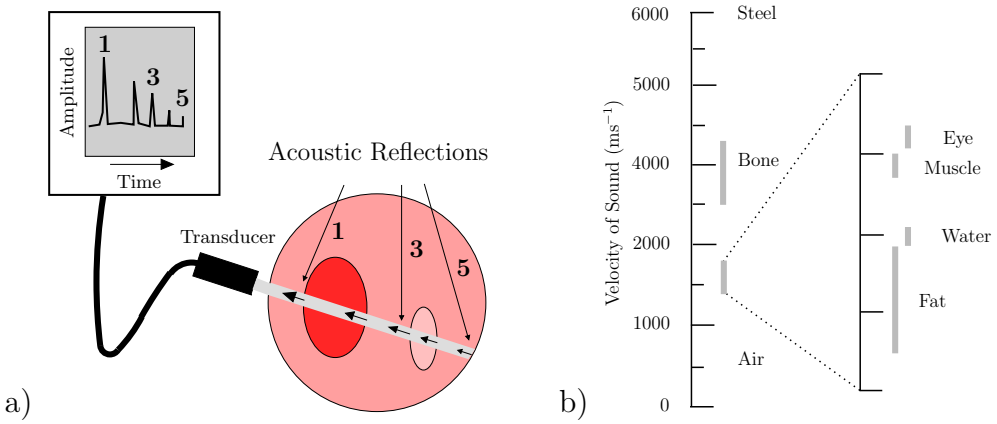

Figure 4.3: a) Principle of the "simplest" form of medical ultrasound scan (A-mode scan) and b) velocity of sound in a range of different substances. (Both adapted from Guy and ffytche [89]).

The most well-known application of ultrasound is the imaging of pregnancy but it has been also found its way into the diagnosis of e.g. liver, kidneys, pancreas and prostate glands. Additionally in both last decades the ultrasound becomes the so-called "gold standard" in the vascular diagnosis, see e.g. Görge et al. [85] and Erbel et al. [66]. The catheter-based intravascular ultrasound (IVUS) is used routinely in clinical practice for the realtime estimation of a vessels' degree of disease and represents a valuable tool helping to decide suitably if and how the affected artery should be medically treated, see also Böse et al. [30]. At the beginning of an IVUS treatment a plastic introducer sheath is inserted in the groin (Arteria femoralis) or the upper arm (Arteria brachialis) to provide an access to the vessel system. Afterwards the catheter is inserted through the sheath and threaded to the artery of interest, cf. Figure 4.4a. This catheter represents the guideway of wire with the ultrasound transducer at its tip. During the treatment the tip is pulled back by a motor unit due to better imaging results. IVUS provides a series of cross sectional grey scale images, see e.g. Figure 4.4b, wherein the grey-scale value represents the amplitude of the ultrasound signal.

The different echo lucencies of the various arterial tissues enable acoustically distinctive features and, consequently, their differentiation based on IVUS images. Figure 4.4b shows the identification of the media-lumen-interface and the external elastic membrane, which describes the interface between adventitia and media. The internal elastic membrane

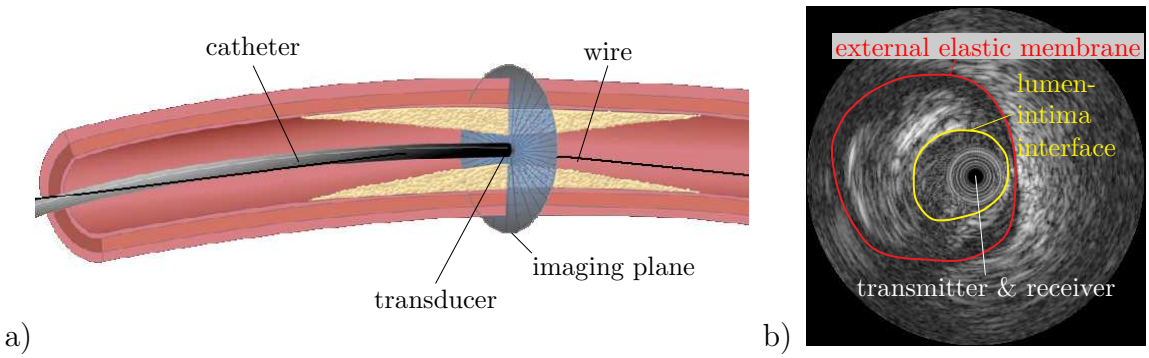

Figure 4.4: a) Schematic illustration of an IVUS examination, adapted from Bersch [22], and b) resulting greyscale IVUS-image with identification of layer interfaces.

can not be located based on the grey-scale images due to its low thickness. From these results the cross sectional area of the plaque can be estimated and e. g. the studies by Waller et al. [237], and Nissen and Yock [160] state these aspects. In addition to that, IVUS measurements are relatively insensitive compared to CT-scans with respect to movements of the thorax e.g. due to breathing of the patient. This represents an important information regarding the assessment of the disease severity. If the decision for a balloon-angioplasty is positive, the value of the applied balloon pressure plays an important role, since it happens in a non-negligible number of cases that a certain pressure causes fracture in the plaque possibly leading to severe complications for the patient. Therefore, information regarding the plaque composition which has a strong influence on the initialization of plaque rupture is also profitable. Unfortunately, IVUS does not provide the ability to identify between individual plaque components, since calcareous and strongly fibrotic tissue lead to similar ultrasound reflections. The same problem occurs for lipid-rich and normal fibrotic tissue.

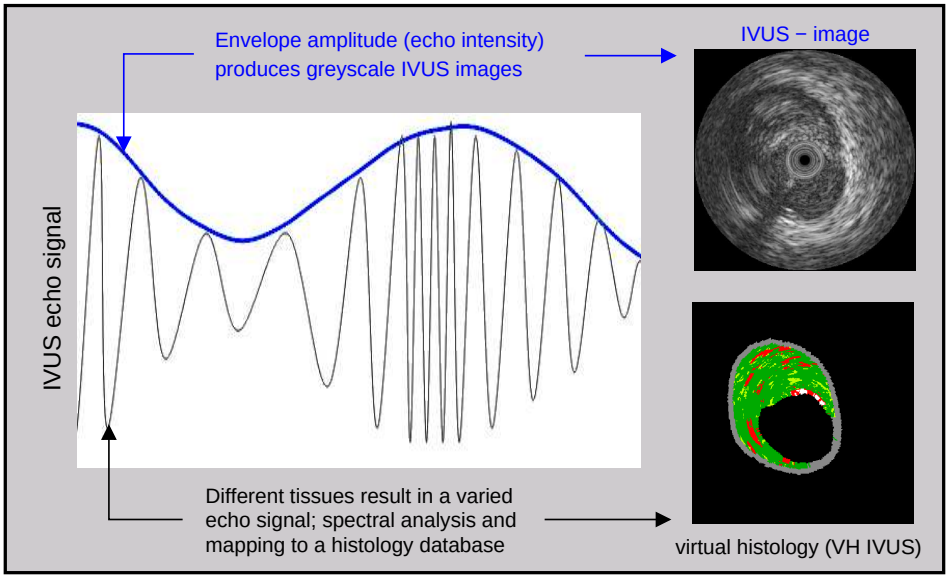

Figure 4.5: Comparison of functional principle of standard intravascular ultrasound imaging and the Virtual Histology. (Taken from Brands et al. [32])

For overcoming of these difficulties the Virtual Histology (VH IVUS[4.)]) was developed. In contrast to IVUS, which only uses the envelope amplitude (echo intensity) of the ultrasound echo signal, this technology makes use of an additional radio frequency analysis. Thereby not only the amplitudes but also the frequencies of the ultrasound data are investigated. Using a knowledge-based approach various plaque components are then classified and color coded as fibrotic tissue (dark green), fibrofatty tissue (green), necrotic core (red) and dense calcium (white). In Figure 4.5 the functional principle of the VH IVUS compared to the standard IVUS is shown along with the resulting cross-sectional images. The knowledge-based approach goes back to the study by Sonka et al. [215]. To the best of our knowledge in Nair et al. [156] association between the plaque composition and the analysis of the IVUS radiofrequency data was arisen firstly. For more details on this method we refer to Böse et al. [30], König and Klauss [130] and the references therein.

[4.)] VH® is registered trademark of Volcano Corporation, California, USA, see `www.volcanocorp.com`

Often, the cross sectional ultrasound images are then arranged in a sequence, possibly in virtual 3D space, and are thus presented to the physician as a pseudo 3D configuration, or a 2D cut thereof. Clearly, a realistic 3D configuration of an artery cannot be constructed without considering the position and path of the catheter's imaging sensor in space.

4.1.4 Mechanical Behavior

The knowledge of the mechanical characteristics of the arterial wall is a fundamental aspect during the modeling of constitutive material models as well as the simulation of arterial deformations using the Finite Element Method. If we look back at the complex structure of the arterial walls discussed in Section 4.1.1 and its constituents it is obvious that there exist many factors influencing the mechanical behavior of the wall. Thus, in the field of biomechanical research a variety of publications covering this topic and so the given references in this thesis raise no claim to completeness. Humphrey [116] describes in his classical textbook the general characteristics in an extensive manner and also connect it with several historical developments in the field of the arterial biomechanics. Additionally, we refer to the review by Gasser et al. [78], because it gives an appreciated overview of the mechanical properties. From this publication we adopt the Table 4.1, which contains a summary of references dealing with different characteristic properties of arterial walls. Without any contempt of the original work covering the table we adopt it to give the interested reader directly the possibility of a literature survey. In addition to the original content we emphasize the mechanical aspects taking into account for the constitutive modeling in this thesis.

Table 4.1: Some properties of the arterial wall and associated references (adopted from Gasser et al. [78])

properties change along the arterial tree†	Roy [187]
cylindrical orthotropy†	Patel and Fry [172]
	Weizsacker and Pinto [247]
incompressibility†	Carew et al. [40]
	Choung and Fung [44]
nonlinear stress strain response†	Roy [187]
highly deformable†	Roy [187]
axial *in situ* pre-strain	Fuchs [76]
residual stress in the load-free configuration	Bergel [20]
	Chuong and Fung [45]
	Greenwald et al. [87]
	Holzapfel and Ogden [102]
viscoelasticity	Fung [77]
pre-conditioning phenomena	Fung [77]
damage based softening and residual overstretch	Oktay et al. [169]

† Properties taking into account in this thesis.

The main characteristic is the variation of the properties along the arterial tree, which we have already mentioned in section 4.1 and its first subsection treating the arterial histology. Since we concentrate on the elastic arteries the following facts are primarily relevant to this type. Generally the mechanical behavior is related to the following material characteristics: non-linearity, anisotropy, (nearly) incompressibility and (in)elasticity. In the healthy state arteries are highly deformable and show a nonlinear stress-strain response. The non-linearity results from the different mechanical behaviors of the main

constituents, elastin and collagen. During low tension the main contribution to the overall response is given by the elastin since the collagen bundles remain mostly in a wavelike structure. But with increasing loading the collagen becomes more and more straight and causes a stiffening of the tissue. This statement is also established by the studies published in Roach and Burton [184], where the response due to low loadings is similar to that of elastin and during high loadings a stiffening comparable to that of collagen is observed. The stiffening of the arterial stress-strain response already arises at around the physiological strain level, see e.g. Abè et al. [1]. Since we have already mentioned the structural arrangement of the fibers in the arterial layers, the overall anisotropic behavior is obvious and in Patel and Fry [172] it was addressed to "cylindrical orthotropy". Based on the layered structure of the wall and the different compositions of each layer we consider the wall as not materially homogeneous. There are two possible assumptions of heterogeneity: a three layered wall with homogeneous mechanical properties within each layer, but varying from layer to layer, or a gradient in the wall constituents across the wall. For the mechanical modeling described in section 4.2 we restrict ourselves to the former mentioned assumption. If we regard the whole constituents of the wall the artery can be mechanically separated into two parts. A solid part consisting of cells and connective tissue and a fluid part, which is mainly comprised by intracellular and extracellular water (∼70% to 80% of wet weight). From this Humphrey [116] calls it a "mixture-composite". For the analysis of the constitutive behavior or/and stress distributions in many problems the fluid part can be neglected since the influence of the stress-induced movement of the fluid is very low and the wall can be treated as a homogenized solid. But the high amount of water inside the layers of the wall cannot be totally neglected since it is held accountable for the nearly isochoric deformation behavior of the artery under many loading conditions.

All characteristics mentioned by now are addressed to basic arterial properties and we consider them during our mechanical modeling in the sequel of this thesis. Beside them other features regarding the mechanical behavior of the wall are well-known, but not considered within the scope of our studies. Note, that the discussion of the limitations due to the validity regarding the numerical results in this thesis are given in section 5.4. But to give the reader an overview of the variety of mechanical properties we briefly introduce these features and refer to the literature for more detailed studies. There are mainly two pre-loading phenomena known under which the vessels are embedded in the body and they depend on the location, age and disease. The first one is the axial prestrain, which become apparent by a shortening of the vessels after the removal from the body. For example in animal aortas an axial stretch is also observed and measured from 1.2 near the aortic arch to 1.6 near the iliac bifurcation, see Han and Fung [91]. The fundamental role of the axial stress in compensatory adaptations by arteries has been reported by Humphrey et al. [115]. The article also gives an appreciated overview in its introduction, which can be used for further studies regarding this topic. The other preloading characteristic is the existence of residual stresses in the unloaded configuration. They were firstly reported by Bergel [20]: *"When an artery is split open longitudinally it will unroll itself. This surely indicates some degree of stress even when there is no distending pressure."* A layerwise analysis with respect to the residual stresses shows different so-called opening angles for each layer and enables the conclusion, that the layers are differently stressed in the unloaded configuration, see e.g. Greenwald et al. [87]. The most common assumption towards the existence of residual stresses is, that they smooth the strain and stress level through the wall at in vivo loading conditions.

Further mechanical properties are associated to inelastic effects, which mostly occur under non-in vivo loadings. Thus, it shows that in dynamical tests the arterial tissue exhibits several viscoelastic responses: hysteresis under cyclic loading, stress relaxation under constant extension and creep under constant load, see e.g. FUNG [77]. As a common assumption for this time-dependent deformation behavior is considered a dissipative mechanism of smooth muscle cell deformation and intraarterial fluid movement. Closely related to the viscous effect is the stress softening – also called pre-conditioning – which is recognizable after a few load cycles by a nearly repeatable stress-strain curve. Experiments show that the viscoelastic effect is more pronounced in muscular arteries than in the elastic type, while it increases along the arterial tree. Under consideration of the extremely slight dynamical components during an inflation of an artery and the lower importance of viscoelastic properties in the elastic arterial type we will neglect this property in the sequel of this work. Other important inelastic effects are the damage and failure in the arterial wall during a loading level above the physiological range. Such loads appear during treatments like the balloon-angioplasty and the stenting and result in significant changes in the mechanical behavior of the arterial tissue, see e. g. GASSER AND HOLZAPFEL [79]. These changes were the principles for the functionality of the treatments because they provide an increased lumen of the artery.

The variety and complexity of the mechanical properties of soft biological tissues, e.g. arterial walls, show the reader the reason for intensive research in the fields of biomechanics by many groups during the last years. These groups are founded by mechanics and mathematicians as well as biologists, chemists and medical scientists.

4.2 Continuum Mechanical Modeling

Since in the next chapter we analyze arteries using the Finite Element Method here we introduce several free energy functions, which can be used to describe the mechanical behavior of arterial walls. Lots of continuum mechanically motivated material laws for the description of the mechanical behavior of soft biological tissues have already been published. For a detailed overview of the variety of models we refer to the exhaustive reviews HUMPHREY [114], VITO AND DIXON [230],KALITA AND SCHAEFER [118] and HOLZAPFEL AND OGDEN [103] as well as to the classical textbooks HUMPHREY [116] and HOLZAPFEL AND OGDEN [107; 109]. For our treatment we consider two mechanical characteristics, the anisotropy and nearly incompressibility, which are outlined in section 4.1.4. As the mechanical influence of the healthy intima in atherosclerotically degenerated arteries is negligible we do not consider it in our modeling. This is in contrast to non-atherosclerotic intimal thickening in hyperplasia; see HOLZAPFEL [100]. The anisotropy is mainly governed by the structure of both external arterial layers, i.e. adventitia and media, where each one can be assumed as a composition of a matrix substance with embedded collagen fibers. The arrangement of these fibers can be characterized by two preferred directions following the mean orientation of the fibers. They are crosswire helically wound along the artery and symmetrically disposed with respect to the axial direction. For the parameterization of the fiber orientation we use the angle which is enclosed by the fibers and the circumferential direction of the artery. In the following we consider the angles $\beta_{\mathrm{A}} = 49.0^{\circ}$ and $\beta_{\mathrm{M}} = 43.39^{\circ}$ for the fiber orientation in the adventitia and media, respectively, which are proposed by BALZANI [8]. Consequently, the material behavior of the collagen fiber bundles can be represented by the superposition of two

transversely isotropic models, see HOLZAPFEL ET AL. [110]. Then the general form of the free energy function for the mechanical behavior of arterial walls is formulated by

$$\psi = \psi^{\text{iso}}(\boldsymbol{C}) + \psi^{\text{ti}(1)}(\boldsymbol{C}, \boldsymbol{M}^{(1)}) + \psi^{\text{ti}(2)}(\boldsymbol{C}, \boldsymbol{M}^{(2)}) \,. \tag{4.1}$$

The structural tensors $\boldsymbol{M}^{(1)}$ and $\boldsymbol{M}^{(2)}$ are calculated as given by Equation (2.103) and the preferred directions $a^{(1)}$ and $a^{(2)}$ are identified by the two assumed fiber directions. The incompressibility of the arterial tissue is treated by an penalty term in the isotropic part ψ^{iso} of the free energy function, cf. Equation (2.118).

In BRANDS ET AL. [31] several energy functions for the description of the mechanical behavior of arterial walls are adjusted to experimental data and also their influences on the numerical behavior are discussed. Here, we focus on two of therein considered functions, which were conclusively preferred by the authors. For an overview of all these functions and the related numerical results we refer to the latter reference.

4.2.1 Polyconvex Energies for Soft Biological Tissues

Since polyconvex functions guarantee the existence of minimizers, see section 2.6, we use such functions for the construction of the free energies. Based on the general form (4.1) we consider two different material models ψ_{A} and ψ_{B} obtained by using different choices for the isotropic and anisotropic terms. For that we hark back to the functions, which has been already introduced in section 2.6. The isotropic term ψ^{iso} in both energy functions is set up by ψ_8^{iso} and ψ_9^{iso} in Equation (2.118). Both parts satisfy the stress-free natural state, cf. Equation (2.111), and additionally the second one penalizes the volumetric deformations to achieve the satisfaction of the quasi-compressibility constraint. The first model ψ_{A} uses the polyconvex function (2.127) in the anisotropic parts $\psi^{\text{ti}(1)}$ and $\psi^{\text{ti}(2)}$, which was already proposed in BALZANI [8] and BALZANI ET AL. [10]. Thus, the free energy functions and the corresponding second Piola-Kirchhoff stress tensors $\boldsymbol{S} = \partial_{\boldsymbol{C}}\psi$, considered in this work, are

$$\psi_{\text{A}} = c_1 \left(\frac{I_1}{I_3^{1/3}} - 3 \right) + \varepsilon_1 \left(I_3^{\varepsilon_2} + \frac{1}{I_3^{\varepsilon_2}} - 2 \right) + \sum_{a=1}^{2} \alpha_1 \left\langle I_1 J_4^{(a)} - J_5^{(a)} - 2 \right\rangle^{\alpha_2} \,, \tag{4.2}$$

$$\begin{aligned} \boldsymbol{S}_{\text{A}} = {} & 2 \left\{ \frac{c_1}{I_3^{1/3}} + \sum_{a=1}^{2} \alpha_1 \alpha_2 \left\langle I_1 J_4^{(a)} - J_5^{(a)} - 2 \right\rangle^{\alpha_2 - 1} J_4^{(a)} \right\} \boldsymbol{I} \\ & + 2 \left\{ -\frac{c_1}{3} \frac{I_1}{I_3^{4/3}} + \frac{\varepsilon_1 \varepsilon_2}{I_3} \left(I_3^{\varepsilon_2} - \frac{1}{I_3^{\varepsilon_2}} \right) \right\} \det(\boldsymbol{C}) \boldsymbol{C}^{-1} \\ & + 2 \sum_{a=1}^{2} \alpha_1 \alpha_2 \left\langle I_1 J_4^{(a)} - J_5^{(a)} - 2 \right\rangle^{\alpha_2 - 1} I_1 \, \boldsymbol{M}^{(a)} \\ & - 2 \sum_{a=1}^{2} \alpha_1 \alpha_2 \left\langle I_1 J_4^{(a)} - J_5^{(a)} - 2 \right\rangle^{\alpha_2 - 1} (\boldsymbol{C}\boldsymbol{M}^{(a)} + \boldsymbol{M}^{(a)}\boldsymbol{C}) \,. \end{aligned} \tag{4.3}$$

Here $\langle(\bullet)\rangle$ denotes the Macauley brackets defined by $\langle(\bullet)\rangle = [|(\bullet)| + (\bullet)]/2$, with $(\bullet) \in \mathbb{R}$. They are used instead of a case differentiation to get a more compact formulation. This differentiation is necessary since the fibers are able to receive only tensile loading.

Consequently, the responsible energy term must be only take into account if its value is positive, cf. Equation (2.127). Furthermore, the anisotropic behavior in the second model ψ_{B} is described by the function (2.128) taken from HOLZAPFEL ET AL. [110]. The energy functions and corresponding second Piola-Kirchhoff stress tensors are

$$\psi_{\mathrm{B}} = c_1\left(\frac{I_1}{I_3^{1/3}} - 3\right) + \varepsilon_1\left(I_3^{\varepsilon_2} + \frac{1}{I_3^{\varepsilon_2}} - 2\right)^{\alpha_3} \tag{4.4}$$

$$+ \sum_{a=1}^{2} \frac{k_1}{2k_2}\left\{\exp\left(k_2\left\langle\frac{J_4^{(a)}}{I_3^{1/3}} - 1\right\rangle^2\right) - 1\right\}\,, \tag{4.5}$$

$$\begin{aligned}\boldsymbol{S}_{\mathrm{B}} = 2\frac{c_1}{I_3^{1/3}}\boldsymbol{I} + 2\Bigg\{ &-\frac{c_1}{3}\frac{I_1}{I_3^{4/3}} + \frac{\varepsilon_1\varepsilon_2\alpha_3}{I_3}\left(I_3^{\varepsilon_2} + \frac{1}{I_3^{\varepsilon_2}} - 2\right)^{\alpha_3-1}\left(I_3^{\varepsilon_2} - \frac{1}{I_3^{\varepsilon_2}}\right)\\ &- \sum_{a=1}^{2}\frac{k_1}{3}\exp\left(k_2\left\langle\frac{J_4^{(a)}}{I_3^{1/3}} - 1\right\rangle^2\right)\left\langle\frac{J_4^{(a)}}{I_3^{1/3}} - 1\right\rangle\frac{J_4^{(a)}}{I_3^{4/3}}\Bigg\}\det(\boldsymbol{C})\boldsymbol{C}^{-1}\\ &+ 2\sum_{a=1}^{2}\frac{k_1}{I_3^{1/3}}\exp\left(k_2\left\langle\frac{J_4^{(a)}}{I_3^{1/3}} - 1\right\rangle^2\right)\left\langle\frac{J_4^{(a)}}{I_3^{1/3}} - 1\right\rangle\boldsymbol{M}^{(a)}\,,\end{aligned} \tag{4.6}$$

Again, the Macauley brackets are used to take into account the loading condition of the fibers as discussed for the model ψ_{A}. To guarantee the polyconvexity of both functions we have to consider several restrictions to the material parameter, which were already given in section 2.6 beside the definition of each functional part. These restrictions on the material parameters in the isotropic parts and anisotropic parts are

$$\begin{aligned} &c_1 > 0\,, \quad \varepsilon_1 > 0\,, \quad \varepsilon_2 > 1\,, \quad \alpha_3 > 2 \quad \text{and}\\ &\alpha_1 > 0\,, \quad \alpha_2 > 2\,, \quad k_1 > 0\,, \quad k_2 > 0\,, \end{aligned} \tag{4.7}$$

respectively. Due to the lack of data regarding the material behavior of the individual diseased arterial tissues detected by the VH IVUS-technique we assume the plaque to be homogeneous as a first step. However, more sophisticated plaque compositions can be constructed from the proposed method described in section 5.1. For the plaque we apply the Mooney-Rivlin model

$$\psi_{\mathrm{C}} = \beta_1 I_1 + \eta_1 I_2 + \delta_1 I_3 - \delta_2 \ln(I_3) \tag{4.8}$$

by following its definition (2.120). The polyconvexity condition is hold by the restrictions $\beta_1 > 0$, $\eta_1 > 0$, $\delta_1 > 0$, and a stress-free reference configuration is achieved by $\delta_2 = \beta_1 + 2\,\eta_1 + \delta_1$, cf. Equation (2.123). In the next section we adjust the parameter of the functions to the behavior of the biological material to apply them in simulations treating the deformations of arterial walls.

4.2.2 Parameter Fitting to Experimental Data

(Parts of the subsequent results are first published in BRANDS ET AL. [31])

Here, we describe the adjustment of the parameter for the different energy function, given in section 4.2.1, to cover the mechanical behavior of soft tissue in the arterial wall. For

that task we perform numerical parameter fittings and acquire experimental data, which were originally published in HOLZAPFEL [100]. In these experiments the separated layers of an artery, i.e., intima, media and adventitia, were studied in uniaxial tension tests. For each layer the experiments were done with strips, which were originally orientated circumferentially and axially in the arterial walls. At this point we emphasize again, that we do not consider the healthy intima because of its less mechanical influence in atherosclerotically degenerated arteries.

In the used parameter fitting algorithm we adjust the Cauchy stresses $\boldsymbol{\sigma} = \boldsymbol{F}\boldsymbol{S}\boldsymbol{F}^T$ from the material models to the Cauchy stresses σ_{exp} from the experiments. We minimize the error $e_{\text{a}} + e_{\text{c}}$, where

$$\begin{aligned} e_{\text{a}} &= \sum_{i=1}^{n_{\text{a}}} \left[\frac{(\sigma_{\text{a,exp}}^{(i)} - \sigma_{\text{a}}^{(i)})^2}{(\sigma_{\text{a,exp}}^{(n_a)})^2} + \omega(\det \boldsymbol{C}_{\text{a}}^{(i)} - 1)^2 \right] , \\ e_{\text{c}} &= \sum_{i=1}^{n_{\text{c}}} \left[\frac{(\sigma_{\text{c,exp}}^{(i)} - \sigma_{\text{c}}^{(i)})^2}{(\sigma_{\text{c,exp}}^{(n_c)})^2} + \omega(\det \boldsymbol{C}_{\text{c}}^{(i)} - 1)^2 \right] , \end{aligned} \tag{4.9}$$

are the errors for axial (a) and circumferential (c) experiments, respectively. In order to enforce the quasi-incompressibility condition with numerically suitable parameters ε_1 and ε_2 acting on the pure volumetric parts of the free energy, the geometric constraint $\det \boldsymbol{C} = 1$ is added to the least square functional (4.9). The parameter ω is chosen as 10^{-4}, such that $\det \boldsymbol{C} = 1$ is violated by only a few percent in the uniaxial tension tests. The least-square functional is minimized by using an evolution strategy; see SCHWEFEL [200]. This strategy was already applied in BALZANI [8] and we use the same procedure published therein. In Equation (4.9) $\sigma^{(i)}$ are the stress components in tension direction computed at the deformation state $C_{11}^{(i)}$. The constraint conditions $\sigma_{ij} = 0$ for $i \neq j$ and $\sigma_{22} = \sigma_{33} = 0$ arising from the consideration of a uniaxial tension test are enforced iteratively, before evaluating the error functions (4.9).

Table 4.2: Material parameters for the representation of adventitia (adv.) and media (med.).

Model	Layer	Fig.	c_1 [kPa]	ε_1 [kPa]	ε_2 [-]	α_1 [kPa]	α_2 [-]	α_3 [-]	k_1 [kPa]	k_2 [-]
ψ_{A}	adv.	4.6a.2	6.6	23.9	10.0	1503.0	6.3	–	–	–
	med.	4.6a.1	17.5	499.8	2.4	30001.9	5.1	–	–	–
ψ_{B}	adv.	4.6b.2	6.2	101.0	10.0	–	–	3.0	6.0	20.0
	med.	4.6b.1	10.7	207.1	9.7	–	–	10.0	1018.8	20.0

The results of the parameter adjustment for the material models are summarized in Table 4.2. They are bounded from below as defined in Equation (4.7) regarding the polyconvexity of the energy functions. Additionally, the range of the parameters is bounded from above for multiplicative factors (c_1, ε_1, ε_2, α_1, k_1, k_2) by 5×10^5 and for exponents (α_2, α_3) to 10. This decision is made to avoid possible numerical problems like arithmetic overflows or cancellations. For exemplary effects of these aspects on the numerical behavior, especially in application to a parallel computation using FETI-DP, we refer

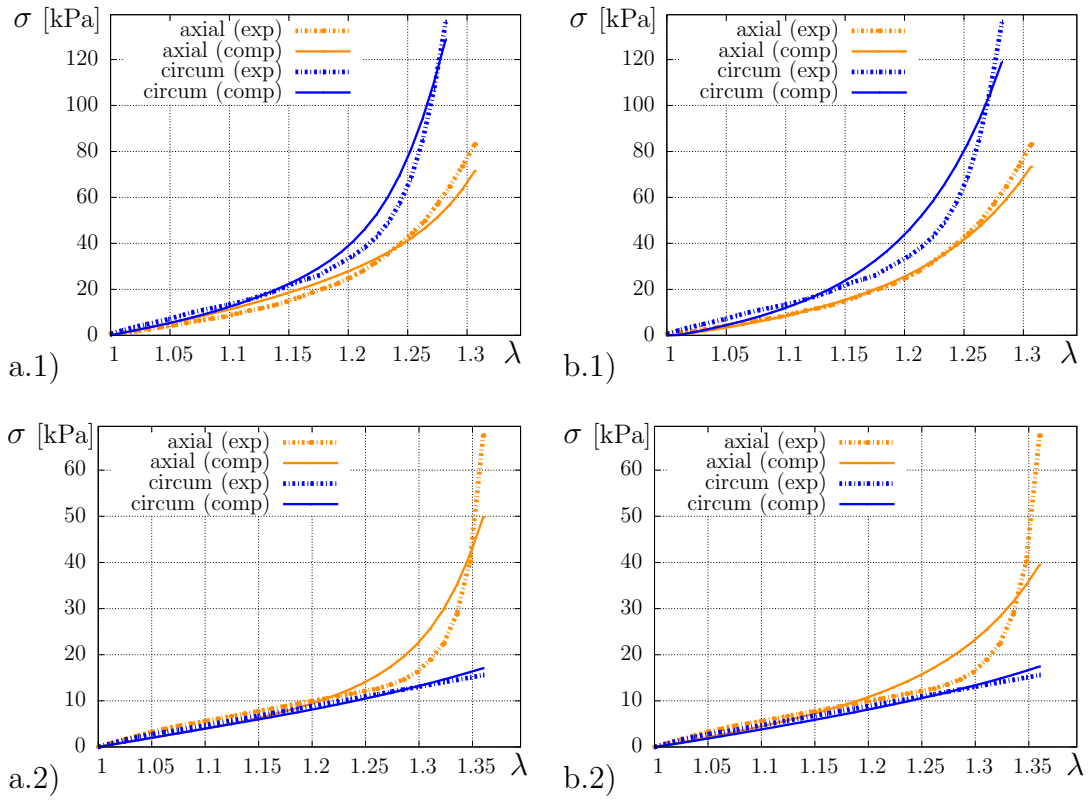

Figure 4.6: Cauchy stress σ [kPa] vs. stretch λ of 1) media and 2) adventitia computed by material model a) ψ_{A} and b) ψ_{B} using associated parameters from Table 4.2 (comp) and compared to the experimental data (exp) Holzapfel et al. [110]. (Taken from Brands et al. [31])

to Brands et al. [31]. There is a further parameter set considered, which violates the upper bounds and shows different results regarding the number of iterations and residual norms in a finite element simulation of an arterial wall. The comparisons between the experimental data and the numerical results using the presented functions are visualized in Figure 4.6 for both considered layers of an arterial wall.

As already mentioned the lack of data regarding the material behavior of the individual plaque components let us feel compelled to assume the plaque to be homogeneous. For this reason we take the parameter for the related energy function ψ_C from Brands et al. [31] and list them in Table 4.3. Note, that this consideration represents a restriction to the comparability of the simulations with the real material behavior. On this aspect we also refer to the discussion of the limitations given in section 5.4.

Table 4.3: Material parameters of energy function ψ_{C} applied to the plaque (assumed to be homogeneous), taken from Brands et al. [31]. Parameter δ_2 is computed by the other ones due to a stress-free reference configuration, cf. Equation (2.123).

β_1 [kPa]	η_1 [kPa]	δ_1 [kPa]	$\delta_2 = \beta_1 + 2\,\eta_1 + \delta_1$ [kPa]
80.0	250.0	2000.0	2580.0

5 FE-Analysis of Arterial Walls

In the following subsections we elaborate the numerical simulation of atherosclerotically degenerated arteries where an internal pressure follower load is applied to the interior wall, the luminal surface. Within the framework of such analysis the reconstruction of a three dimensional patient-specific arterial geometry plays an essential role. For this reason one focus of this thesis is on the geometrical modeling and the FE-discretization of a real artery based on medical imaging data. Afterwards we use the developed two- and three dimensional geometries for the simulation of an artery under internal pressure loading. Here, we emphasize that the shown numerical results represent only examples rather than providing realistic results, because we do not consider all mechanical characteristics in the material modeling, cf. section 4.1.4. On this account we close this chapter with a discussion of the limitations regarding the proposed reconstruction method and the numerical results.

5.1 Patient Specific Arterial Geometries

(Subsequent results are first published partly in Brands et al. [32] and Balzani et al. [14].)

The visualization of patient-specific arterial geometries would be helpful and sometimes necessary in the context of atherosclerotic degenerated arteries. On the one hand for the diagnosis of such diseases and the choice of their treatment detailed medical examinations are necessary. On the other hand representative geometrical model of real arteries are essential for the development of new treatment techniques and for the enhancement of the actual methods. Especially, the second aspect is part of the research of several groups related to different fields, e. g. medicine, biology, materials engineering, computer engineering and mechanics. As we introduced in Section 4.1.3 several medical imaging techniques, e. g. X-ray, magnetic resonance imaging (MRI), intravascular ultrasound (IVUS) and computer tomography (CT), are available for "a look into the body". The combination of angiograms obtained from MRI was used by Fessler and Macovski [70] to reconstruct arterial trees. Wahle et al. [234] pursued the same goal based on biplane X-ray angiograms and extended it by a volume model based on generalized elliptical conic sections. An optimized method for an online 3D reconstruction was presented by Chen and Carrol [42], where coronary arterial trees based on two angiographical images are visualized without any calibrating technique. The crucial part in the visualization of vessels is the segmentation of the arterial wall into the layer structure. This is an essential task especially for a mechanical analysis of the artery, since the different layers offer different material behaviors. All mentioned standard imaging techniques only provide little information about the wall structure. But some publications are available, wherein the authors present new strategies and approaches to overcome this problem. In Auer et al. [2] and Holzapfel et al. [104] 3D reconstructions of several tissue components from diseased arteries are done based on images from high resolution MRI. Thereby the presented segmentation tool is used to get 2D contours from the slice images and reconstruct a 3D geometrical model. In contrast to the beforehand mentioned references these authors used this technique for further studies of patient-specific geometries based on the Finite Element Method in several publication, e. g. Holzapfel et al. [105], Kiousis et al. [120] and Holzapfel and Kiousis [101]. Also in the field of the fluid-structure-simulations of abdominal aortic aneurysms several reconstruction methods are developed based on standard medical imaging techniques, e. g. Wolters et al. [251] and Leung et al. [139].

In contrast on the aforementioned references Nair et al. [156] use IVUS data and classify the plaque composition based on a spectral analysis applied to the radio-frequency echo signal. The same group enhance and validate their method by an ex-vivo study, cf. Nair et al. [157]. Based on this development and studies the standard IVUS treatment was enhance to the VH IVUS, details see Section 4.1.3. In the context of this treatment we also mentioned the study by Klingensmith et al. [126], wherein a border detection technique for the analysis of the lumen and medial-adventitial interfaces from the IVUS images.

Here, we focus on the VH IVUS imaging technique and use the resulting data for the construction of the patient-specific geometry. The procedure to achieve a finite element discretization of a patient-specific artery is shown in the following subsections We start from the geometrical data provided by the VH IVUS imaging of a patient-specific artery and go through the steps of treatment, e.g. separation of layers, image correction, three-dimensional path reconstruction and meshing. The reconstruction of the spatial catheter path shown in the sequel was developed and provided by the group of Prof. Dr. A. Klawonn, Universität Duisburg-Essen and proposed by Kownatzki [135]. These patient-specific data including the IVUS and VH IVUS images as well as the angiographic X-ray images of a real artery were provided by Prof. Dr. med. R. Erbel and Dr. med. D. Böse from the "Westdeutsches Herzzentrum Essen", Germany and this support is greatly appreciated.

5.1.1 Construction of Virtual Geometry

The construction of a virtual 3D geometry for a patient-specific vessel is described in this section. On that account we fuse the IVUS virtual histology (VH IVUS) data and the output of angiographic X-ray imaging and visualize the vessel geometry based on the resulting geometric data. The necessary processing steps are programmed in MATLAB[5.)], which provides a variety of useful enhancements like e.g. the Spline Toolbox™ or Image Processing Toolbox™. These data represent the prestage for the buildup of finite element discretizations of the arteries, which are shown in section 5.2 and 5.3. During the following remarks we discuss several potential difficulties which might occur either from the execution of the medical treatment or the data preprocessing by the VH IVUS technique. We analyze their relevance regarding our procedures and where necessary we provide a solution or treatment. For details on the used medical imaging techniques we refer to section 4.1.3.

The first step is the extraction of the 2D cross-sectional information which are given in terms of the color coded VH IVUS images. Although they provide significantly more information regarding the composition of arteries, the processed IVUS images as seen in Figure 4.5 usually contain a certain level of noise, i.e. small inclusions that only appear on single VH IVUS frames or small structures that are too tiny for the construction of 3D geometries. We assume that these structures can be considered as artefacts and thus, we remove these structures from the images before proceeding with the construction of the geometric models. For the construction of the 2D geometrical models we first construct a geometrical description of the two-dimensional VH IVUS images by polygonal contour lines. As the boundary of every inclusion is then described as a polygon, the area of every

[5.)] MATLAB® is registered trademark of MathWorks, Inc, see `www.mathworks.com`

inclusion can be computed using the formula of Gauss for polygons, i.e.,

$$A = \sum_{i=1}^{n} \frac{x_i y_{i+1} - y_i x_{i+1}}{2},$$

wherein x_i and y_i represent the coordinates in the two-dimensional VH IVUS image and n denotes the number of points of the individual polygon. Then, all inclusions with an area below a certain threshold ($A < A_{\text{filter}}$) are removed by filling the area from the outside with the colors in the neighborhood. In Figure 5.1 the result of such a filtering process is shown for a threshold of $A_{\text{filter}} = 50$ pixels.

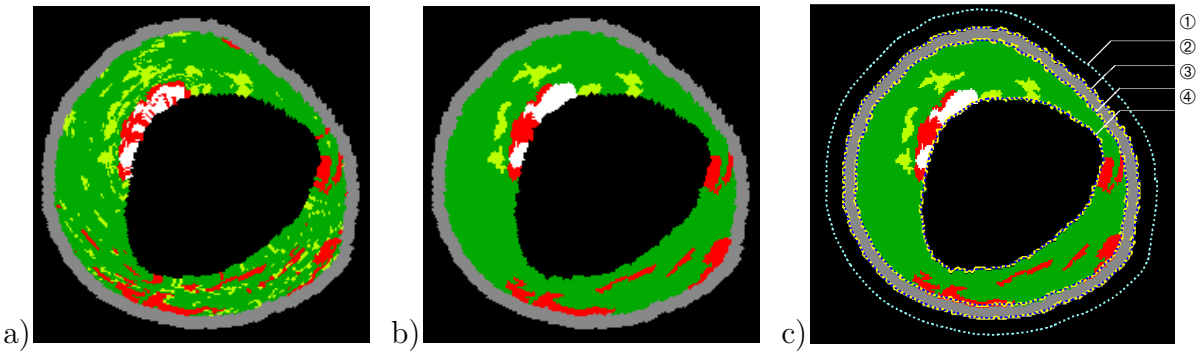

Figure 5.1: Image of VH IVUS with 207×207 pixels a) before filtering and b) after filtering with $A_{\text{filter}} = 50$ pixels and c) detected interface lines separating the arterial layers: ① adventitia from outer connective tissue, ② media from adventitia, ③ plaque from media, and ④ lumen from media. (Taken from Balzani et al. [14])

The preprocessing results in the two-dimensional image shown in Figure 5.1b. Before the segmentation can be started an additional task regarding the interface between adventitia and the surrounding connective tissue has to been done. Since this outer boundary of the arterial tissue can not be captured by neither the IVUS nor the VH IVUS analysis, we have to assume it. However, since the adventitia has a much lower stiffness than the media in the physiological loading regime and since it therefore does only contribute partially to the overall mechanical behavior in the vicinity of the media and not so much at the outer part, we conclude that its thickness is of minor importance. Hence, an associated interface line is generated for convenience such that the adventitia has the same thickness as the media, cf. Figure 5.1c. The contour lines separating the other main components from each other are approximated by the polygonal curves that separate the different color regions. Here, we focus on the interfaces separating the adventitia from the outer connective tissue (1), the media from the adventitia (2), the plaque from the media (3), and the lumen from the media (4), cf. Figure 5.1c. Since these polygonal lines are not sufficiently smooth, which is addressed to the noise of the echo signal, we apply a moving average to smoothen them. Although VH IVUS provides more information regarding the 2D composition of the plaque, we consider the plaques as a single component for the construction of the geometrical models used in this thesis. This is founded on the fact that the spatial resolution in the axial dimension, i.e., tangential to the catheter, is much smaller than the resolution in the tangential plane. In fact, the resolution in axial direction depends strongly on the speed of the automatic catheter pull-back and is typical about 2 data points per millimeter. This is in contrast to the resolution in the tangential plane

which is about 100 data points per millimeter and mainly influenced by the resolution level of the IVUS image. Since the resolution in axial direction of 2 data points per millimeter is not sufficient for a reliable segmentation of three-dimensional structures that are characterized by a comparable size in this direction, we do not take into account the individual plaque components here. Of course such analysis needs to be done in the future if more data points per millimeter can be achieved by an adapted pull-back speed of the catheter. Now, finite element meshes can be constructed based on the two dimensional data, which may serve for computational analysis of e. g. stress distributions inside arterial walls in cross sections as shown in Section 5.2.

Previously, we describe the processing of the patient-specific data regarding single cross sections of an artery. But for more descriptive studies we have to provide patient-specific arterial geometries in 3D. Unfortunately, the simple assembly of the single cross section images, which means stringing them together based on the image coordinate system, is not realistic. The ultrasound sensor is much smaller than the lumen to avoid an obstruction of the blood flow and thus can move within the lumen during the pull-back. Since the position of the ultrasound sensor is always in the center of the frame, the center of gravity of the arterial cross section seems to move slightly from frame to frame, see Figure 5.2. This would lead to bumpy outer surfaces of the artery using the aforementioned method.

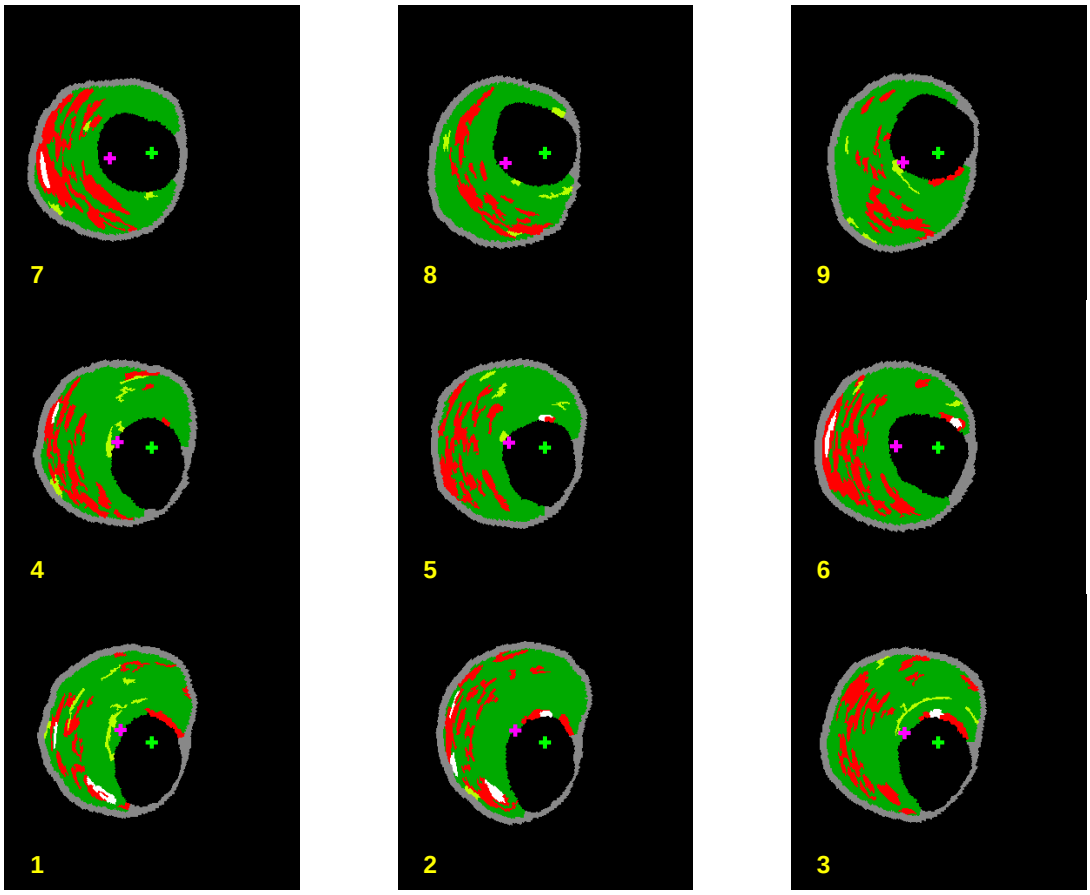

Figure 5.2: Stack of subsequent VH IVUS images with the position of the ultrasound sensor $\tilde{\boldsymbol{X}}_{IC}$ (green cross) and of the center of gravity of the contour $\tilde{\boldsymbol{X}}_{CG}$ of the arterial cross section (violet cross); the position of the ultrasound sensor is always in the center of the image. (Taken from Balzani et al. [14])

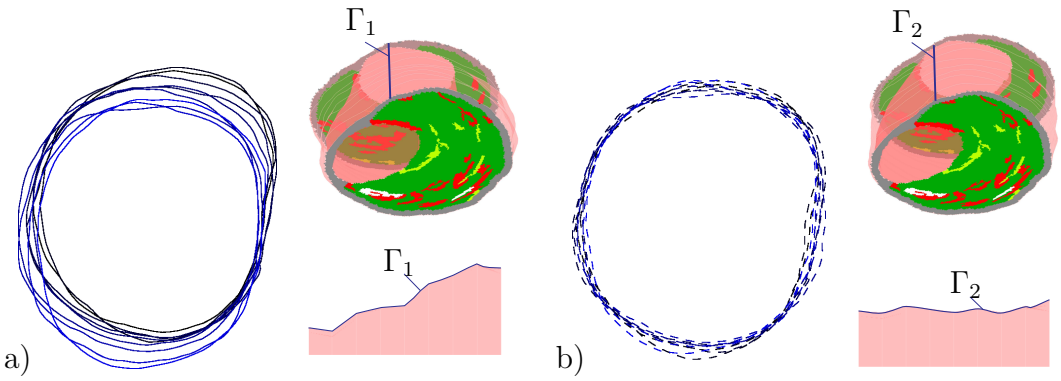

Figure 5.3: Comparison of the outer surface of a reconstructed arterial segment a) without and b) with the position correction using the center of gravity of the complete arterial cross section. Subframes: Overlay of 9 subsequent contour lines of the external elastic membrane (left), surface lines Γ_i (top right), visualization of regarding arterial segment (bottom right).

Different approaches can be found in the literature to solve this problem, e.g., Wahle et al. [235; 236], all of which are approximations. Here, we assume that the center of gravity of the contour of the arterial cross section can be treated as origin of the reference frame than the catheter position. Then, the individual offset of the image center (IC) and the center of gravity (CG) serve to apply an associated translation vector $\boldsymbol{r} := \tilde{\boldsymbol{X}}_{IC} - \tilde{\boldsymbol{X}}_{CG}$, where $\tilde{\boldsymbol{X}}_{IC}$ and $\tilde{\boldsymbol{X}}_{CG}$ denote the individual two-dimensional position vectors in the cross section plane. Thereby, a transition of the image is obtained such that the center of gravity becomes the center of each image and thus represents the axial coordinate axis. Figure 5.3 shows the influence of this correction on the outer boundary of the artery.

Obviously, the wire including the ultrasound sensor is able to rotate inside the catheter with respect to its axial direction during the treatment. To overcome this aspect, we face to an additional catheter wire inside the artery, which is usually therein due to surgery requirements, and should serve as reference in the following consideration. The second wire causes an artifact in the ultrasound images that is visible in the raw ultrasound images behind the second wire, see Figure 5.4. However, these artefacts are generally invisible in the VH IVUS. Therefore both, the raw ultrasound images and the VH IVUS images have to be available. Ideally, only one synchronization point is necessary to determine the collective orientation of the VH IVUS frames but in practice severals may serve to reduce potential error. Still, although the process can theoretically be automatic for numerical simulations it is essential that the result of the reconstruction is verified in an interactive process. In Figure 5.4 a sequence of four subsequent ultrasound images show the position of the second catheter. From each image we estimate the similar angular location of the reference wire with respect to the ultrasound sensor (image center) and, consequently, no correction regarding the rotation has to be done. It is emphasized that although only four IVUS images are depicted here, the complete sequence of 65 images does not show a significant rotation as well. This can be interpreted as the result of the automated pull-back of the ultrasound sensor. If no second catheter is available the moments of inertia of the lumen can be computed to analyze the angular relation between the frames.

In the human body most arteries are curved in the axial direction and, consequently, this fact has to be analyzed and checked for relevance with respect to our study. A possible treatment are angiographic X-ray images, since they clearly resolve the catheter path as

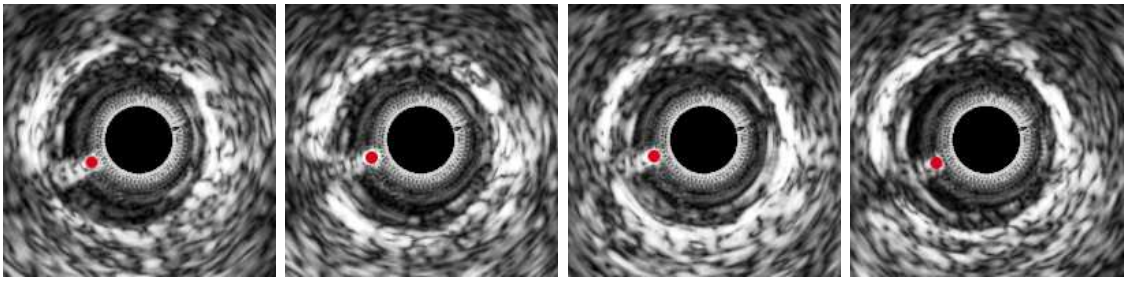

Figure 5.4: Series of subsequent IVUS images showing the artefact caused by the second catheter which is marked by red dots. The rotation of the sensor seems not to be significant. (Taken from Balzani et al. [14])

well as the current position of the ultrasound transducer, see Figure 5.5a,b. Additionally, the application of a contrast agent enable the possibility to visualize the lumen of the vessel. Biplane angiography helps to perceive the 3D configuration without moving or rotating the hardware. The resulting data are provided in DICOM (Digital Imaging and Communications in Medicine) format, which is standardized exchange format in medical imaging. Beside the whole set of angiographic images, which are captured during the examination, it contains information like e. g. the angle of projection, personal information of the patient, date and time. Using a DICOM viewer the images exemplarily shown in Figure 5.5a,b can be exported and used for the reconstruction of the catheter path in form of a 1D spline function. Note that projections of a point on three planes are necessary to identify the point's position in the three-dimensional space. On the contrary, in order to reconstruct a 1D path in 3D in many cases two projections are sufficient. A third projection is only needed to resolve remaining ambiguities, e.g., if double points in one of the projections exist. This is rarely the case with respect to the problem at hand since the surgeon will rotate the X-ray devices in order to avoid double points.

The detailed description of the three-dimensional path reconstruction is given by Kownatzki [135] and we only outline the main tasks here. First, the silhouette of the catheter, which is almost identical with the arterial axis, is marked by a set of points in the two angiographic images, cf. Figure 5.5a,b. Afterwards two points in each angiographic image that belong to the same position is identified. This step is manually done by someone, who has experience with interpreting the 22D angiographic images. Based on this reference the combination of the two sets of points leads to the three-dimensional arrangement of them. Then, a smooth piecewise polynomial function, e.g. a cubic spline function, is constructed from the 3D point set that defines the three-dimensional catheter path, see Figure 5.5c. The resulting spline function serves now as the "guiding wire" for the stacking of the cross-sectional VH IVUS images. But for the stacking additional information regarding the orientation and the position of the image plane with respect to the arterial path are necessary. In this context the relative distance between the VH IVUS images are given by the meta data, which are recorded during the medical examination. Note, that the exposure of the images is pulse triggered. Although the position and angle of the VH IVUS frames are well defined the frames may still be collectively rotated around the catheter path. But if an orientation is chosen for one VH IVUS image the Frenet-Serret formulas describe how the coordinate frame is transported on the spline curve, see Prause et al. [176] for a robust discrete version. In our case, the catheter path is indeed relatively simple, see Figure 5.5c, i.e. the curvature of the region of interest

is very moderate and the curvature remains in one plane. In this case the transport of an initial orientation along the path is straight forward. Still, an initial orientation has to be chosen. It can be viewed as a collective orientation for all frames that is transported along the spline curve. The stack of VH IVUS frames is manually or automatically rotated around the spline function until it best fits the appearance on the angiography. In principle, the collective orientation may also be determined automatically by choosing the orientation that "best fits" the VH IVUS lumen to its reconstruction from angiography in a certain sense, e.g. Wahle et al. [236]. For this, first the lumen has to be reconstructed from biplane angiography, see Wahle [233], Wahle et al. [235]. Unfortunately, even if the lumen cross section is assumed to be of elliptical shape - which obviously is an idealization - the reconstruction of the lumen is not uniquely determined from two projections. Therefore additional assumptions have to be made, such as minimal ellipticity: the lumen cross section is then reconstructed with the smallest ellipticity that is compatible with the given data, for related ideas see also Wahle et al. [235; 236]. Then, following Wahle et al. [235], for the VH IVUS images as well as for the lumen reconstruction so called out-of-center vectors are computed as the difference between the center of gravity of the lumen and the catheter position. A least square fit between the two gives the desired collective orientation, see also Wahle et al. [236].

Now we have two separated data sets concerning the same segment of a diseased artery: on the one hand the segmentation of the different layers in each VH IVUS image, on the other hand the three dimensional path of the vessel. The summary of the preparation of

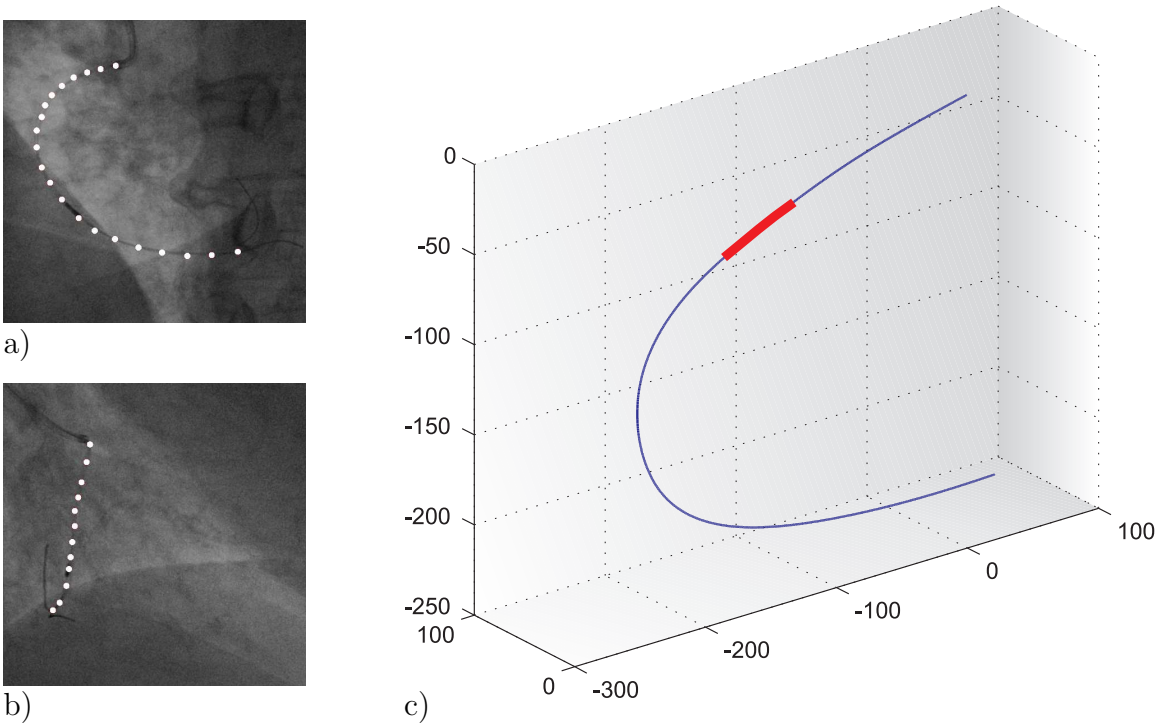

Figure 5.5: Angiographic X-ray images of the catheter wire from a) perspective 1 and b) perspective 2 (the path of the wire is marked by white circles), and c) reconstructed path of the catheter wire and the arterial segment of interest, cf. Kownatzki [135]. (Taken from Balzani et al. [14])

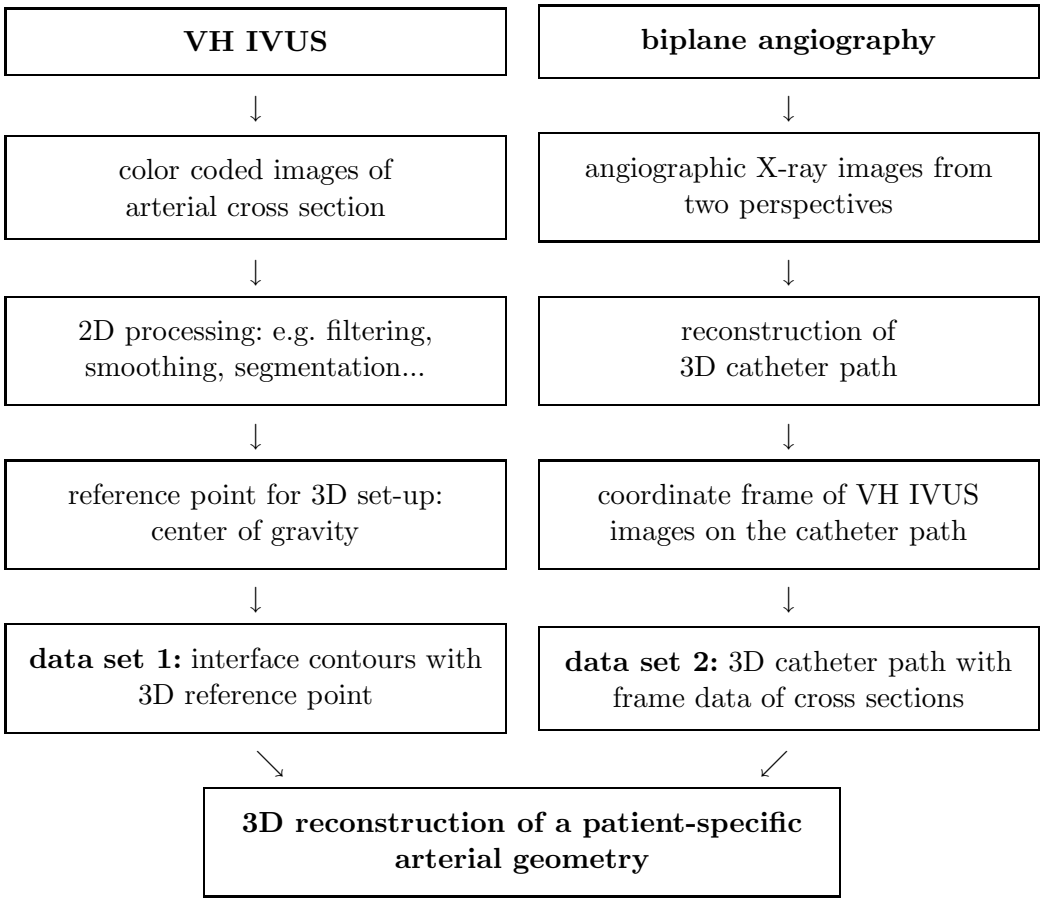

Figure 5.6: Workflow of the processing from medical imaging data to a virtual 3D geometry

these data, which is discussed aforementioned, is given as a flow chart in Figure 5.6. First we extracted from the VH IVUS images the information concerning the cross section, which is available as separated interface contours with the appropriated reference point for the three-dimensional set-up. The second data set contains the three-dimensional path of the catheter and the frame orientation and position of the VH IVUS images on this path. These data are combined in two steps: 1) rotation of the interface contours to match the cross-sectional orientation with the related frame on the catheter path, 2) translation of the rotated interface contours with respect to their reference point onto the center of the related frame on the catheter path. The result of these procedures is visualized in Figure 5.7. For an analysis of this arterial geometry using the Finite Element Method we need its discretization by finite elements, which is the topic of the next section.

5.1.2 Discretization of Real Arterial Geometries

In the previous section we outline the treatment from the medical imaging data to a visualization of the arterial geometry. The results are represented by a data stack of contours, which describe the interface between the arterial layers in each examined arterial cross section provided by VH IVUS. In this section we want to outline the process from these geometrical data to a finite element discretization. Note, that all steps described in this section are performed by using GAMBIT[6.)], whereby complex geometries can be

[6.)] GAMBIT is registered trademark of ANSYS, Inc., see `www.ansys.com`

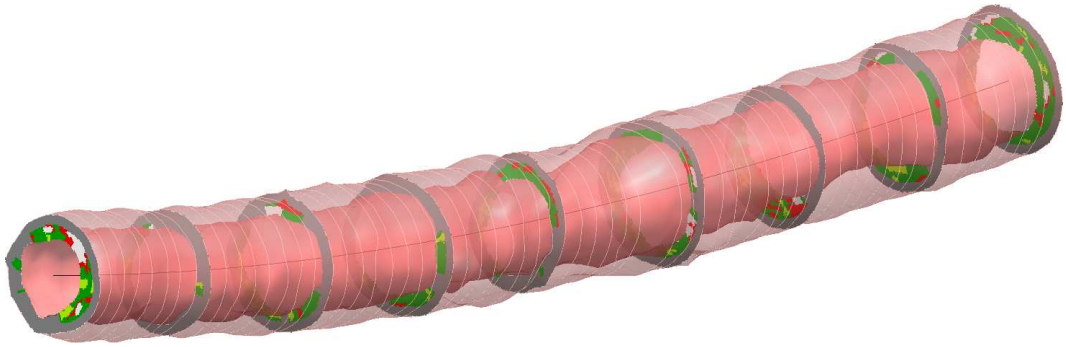

Figure 5.7: Arterial model including the plaque; every eighth VH IVUS image is shown. (Taken from Brands et al. [32])

generated and meshed by finite elements. Each set of contours out of data set 1 (in Figure 5.6) related to one single VH IVUS image can be used to build a two dimensional finite element model of this cross section. Since our focus is on the three dimensional modeling we give only a brief description on the two-dimensional modeling. Obviously, for this task the information provided by data set 2 regarding the three dimensional orientation of the cross section are not necessary. A data stack consisting of the sampling points of the polygonal lines describing the arterial interfaces is calculated. Based on these points areas for the different arterial constituents are defined and afterwards meshed by 6-noded triangular finite elements. As an example of two dimensional discretizations based on VH IVUS images we refer to Figure 5.11.

For a better visibility we use only four representative cross sections to illustrate the procedure to achieve a three dimensional discretization of a patient-specific artery. Again, we start with the calculation of a data stack, which consists of the sampling points of the polygonal lines describing the arterial interfaces. Figure 5.8a shows this exemplarily for the outermost arterial boundary layer. The distance between the individual cross sections is amplified for reasons of clarity and comprehensibility. Then splines are generated based on these points and afterwards connected by a surface, see Figure 5.8b. Right up to the previous step the treatment is the same for all of the four interfaces: i) adventitia to outer connective tissue, ii) media to adventitia, iii) plaque to media and iv) lumen to media. Now, the resulting surfaces of the first and last mentioned interfaces representing the outer- and innermost most arterial boundaries are used to define two individual vol-

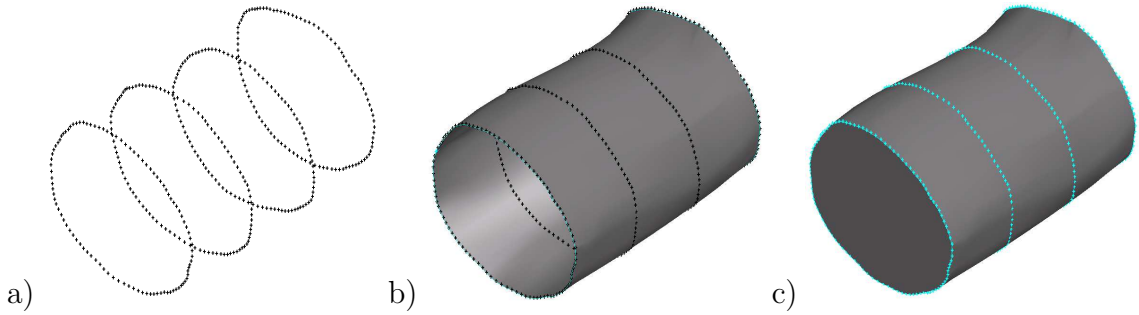

Figure 5.8: Construction of surfaces and resulting three dimensional volume models. a) series of interface line points obtained from VH IVUS analysis, b) constructed surface and c) resulting volume. The distance of the VH IVUS frames is amplified. (Taken from Balzani et al. [14])

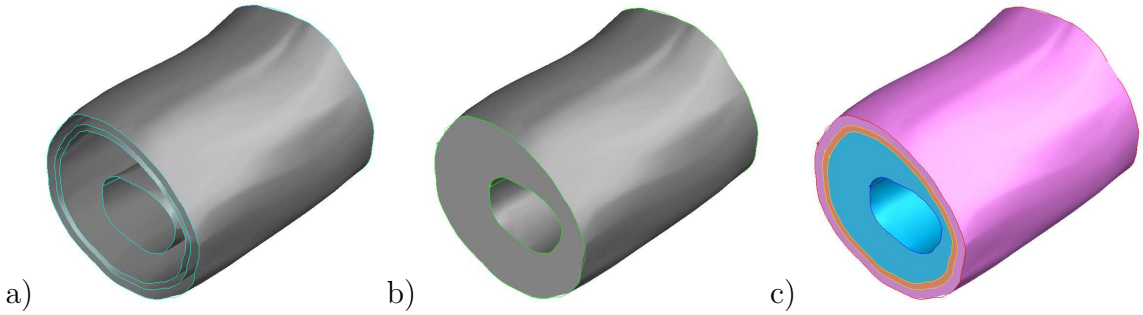

Figure 5.9: Construction of three-dimensional arterial geometries. a) surfaces separating the individual layers, b) complete arterial volume, and c) arterial model including the volumes of the individual layers. Again, the distance of the VH IVUS frames is amplified. (Taken from Balzani et al. [14])

umes. Thereby a plane surface is considered to close the both open ends of the tubelike geometries. The first volume describes the whole arterial geometry including the lumen, shown in Figure 5.8c. The second one can be identified as the thereof extracted partial luminal volume.

In Figure 5.9a the resulting three-dimensional surfaces of the four interfaces separating the arterial layers are depicted. To build up the geometry of the complete arterial volume we perform a Boolean volume subtraction using the previously generated volumes. In this process we use the whole arterial volume including the lumen as minuend and the luminal volume as subtrahend. The resulting geometry representing the complete volume of the wall is depicted in Figure 5.9b. Then the individual components of the artery (media, adventitia and plaque) are constructed by separating the complete volume into the particular layers based on the previously generated surfaces shown in Figure 5.9a. We obtain a volume model of the wall with separated geometries for each arterial layer, illustrated in color in Figure 5.9c. The final step is the discretization of the geometrical model by GAMBIT's mesh generator. At this point we abandon the finite element model for the simple geometry shown in Figure 5.9c. Instead we apply the proposed procedure to a segment 12 mm in length of the patient-specific artery from Figure 5.7, which is affected with pronounced atherosclerotic plaque.

Finally, Figure 5.10 shows the discretization of the considered arterial segment, 12 mm in length, using 10-noded tetrahedral elements. For the construction of the underlying

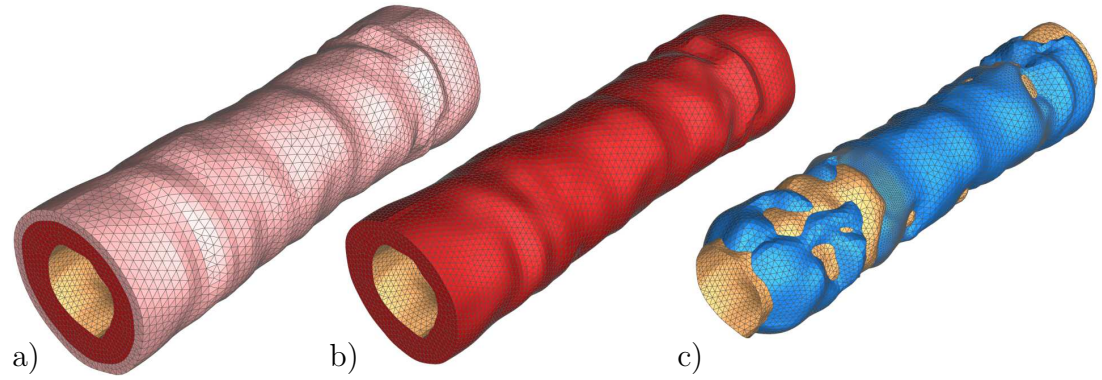

Figure 5.10: Finite element discretization by 305,033 elements (10-noded tetrahedral) with 434,517 nodes leading to roughly 1.3 million degrees of freedom: a) complete mesh, b) blanked adventitia and c) blanked adventitia and media showing only the plaque and the lumen interface. (Taken from Balzani et al. [14])

geometrical model the above presented method was applied. The mesh consists of 305,033 finite elements with 434,517 nodes leading to a total number of roughly 1.3 million degrees of freedom. This model is the arterial geometry, which is the subject matter of the analysis in the following sections

5.2 2D Simulation of Patient Specific Arteries

Before we analyze the three dimensional model of the atherosclerotic degenerated artery shown in Figure 5.10, we choose three cross sections of the whole set of VH IVUS images and perform a two dimensional FE-simulation. In the sequel these results will be taken for a comparison with cross-sectional results from the three dimensional simulation, outlined in the next section. The considered three cross-sectional images of the diseased artery and the finite element discretization are shown in Figure 5.11a-c and Figure 5.11d-f, respectively.

For the computation we consider the following boundary value problem. The finite element meshes based on 6-noded triangular elements assuming plain strain and approximating the displacements by quadratic ansatz functions. Compared to the three dimensional model in Figure 5.10 a lower number of degrees of freedom occurs within each two dimensional model, about 14,000 degrees of freedom. Therefore, the necessity for a complex parallel solution strategy as described in section 3.7 can be avoided and a single computation using FEAP's standard solution procedure is used. An internal hydrostatic pressure follower load is applied to the boundary of the interior wall using a 3-noded line element. The treatment of this element type is very similar to the three dimensional pressure bound-

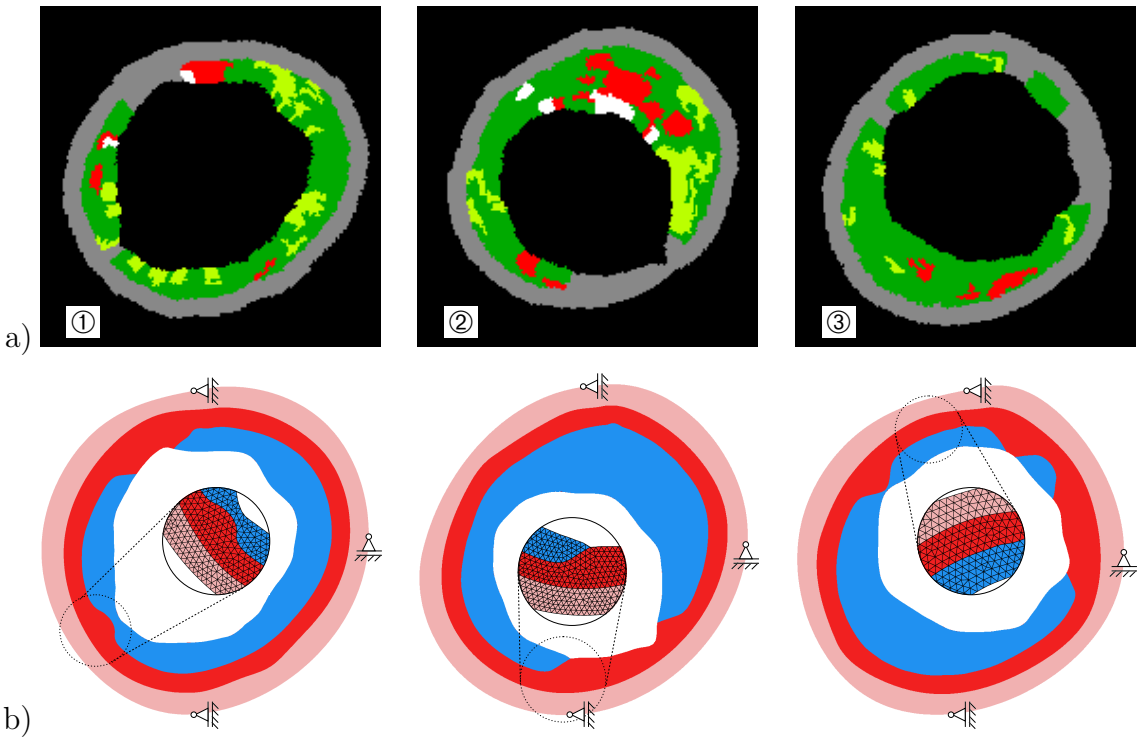

Figure 5.11: Considered cross sections for the two dimensional simulations with magnified parts of the discretization: a) VH IVUS images (for color coding see section 4.1.3) and b) discretizations by 6530 (①), 6888 (②) and 6552 (③) 6-noded triangular elements.

ary loading element in section 3.5.2. We abandon a discourse of the related theory of this element type as well as of the 6-noded triangles since they have become standard finite element types through the years. For that we refer to classical literature like e.g. Wriggers [254] and Bathe [18]. A statically determined system is achieved by applying Dirichlet boundary conditions to three outer boundary nodes such that they are only able to move radially, see Figure 5.11d-f. Finally, an internal hydrostatic pressure of 24 kPa representing a blood pressure of about 180 mmHg is applied stepwise by the aforementioned follower loading elements at the interior boundary. For the description of the mechanical behavior of the different materials, we apply the free energy function ψ_{A} and ψ_{C} with the corresponding material parameters from Table 4.2 and Table 4.3, respectively. The results of these simulations are shown in Figure 5.12, where the von Mises stresses are plotted based on the deformed configuration of the arterial cross section.

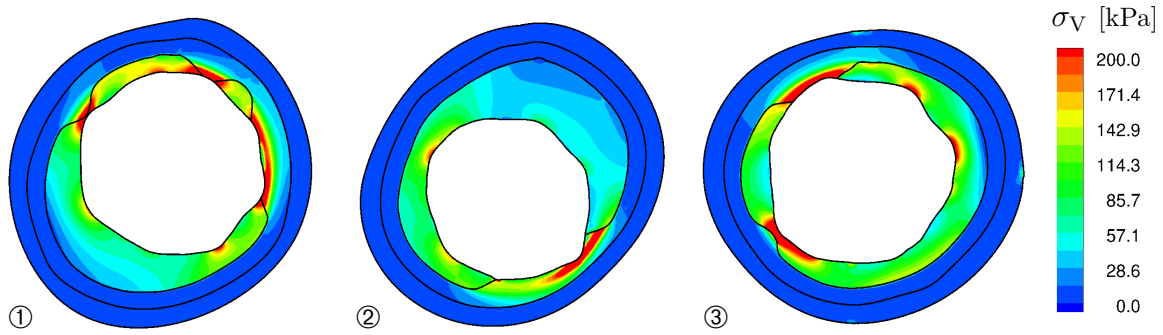

Figure 5.12: Distribution of the von Mises stresses σ_{V} in the three different arterial cross sections, shown in Figure 5.11. (Taken from Balzani et al. [14])

From the medical point of view the main focus on such simulations is on the localization of stress concentrations in the wall since these points are origins of material failures, e.g. plaque rupture or dissection. Especially in view of an angioplasty these aspects are essential if the risk of complications during the surgery should be minimized. In Figure 5.12 all stress distributions of such concentrations could be observed clearly. They appear mainly at the caps of the circumferential plaque boundaries and the region of the media between such adjacent caps. As already mentioned, the shown simulation results raise no claim to be realistic since we neglect several mechanical behaviors of arteries in the material models, e.g. residual stresses and homogenized plaque. But in this context we also emphasize that the foreground of this work is the reconstruction of real arterial geometries. Consequently, no quantitative analyses of the results are possible and from the qualitative point of view only on a limited scale is available. But for a comparison with three dimensional simulations the two dimensional results will be recovered in the next section.

5.3 3D Simulation of Patient Specific Arteries

Now we analyze the passive response of the patient-specific atherosclerotic artery, whose geometrical reconstruction and discretization were treated in section 5.1. Here, an axial segment, 12 mm in length, of the 3D artery model shown in Figure 5.7 is taken into account, where a pronounced atherosclerotic plaque is observable. The discretization has been already depicted in Figure 5.10 showing the finite element mesh of the individual

layers adventitia, media and the plaque. For the discretization we focus on 10-noded tetrahedral elements with quadratic ansatz functions for the displacements, cf. section 3.5.1. In order to overcome the locking phenomena arising from the incompressibility constraint we apply the $\bar{\boldsymbol{F}}$-approach, discussed in section 3.6. Since the discretization by 305,033 elements with 434,517 nodes leading to a total number of roughly 1.3 million degrees of freedom, we solve the boundary value problem by the FETI-DP domain decomposition method in order to end up in a fast simulation procedure. For this numerical computation we use the environment consisting of FEAP and the implementation of the FETI-DP method. Details on the parallel solution method and the environment are introduced in section 3.7. During the decomposition procedure the complete model is partitioned into 224 subdomains. Figure 5.13 depicts exploded views showing the individual subdomains.

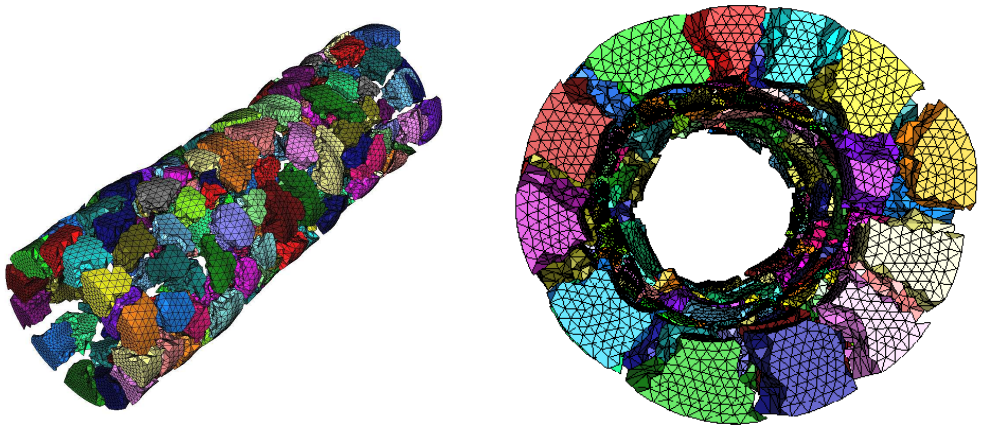

Figure 5.13: Exploded view of the complete geometrical model, which is decomposed into 224 subdomains. (Taken from Balzani et al. [14])

As Dirichlet boundary conditions we fix all nodes at the axial boundaries in axial direction, which can only be interpreted as an approximation for the real situation. However, it is assumed that the resulting boundary distortions flatten sufficiently in an adequate distance from the axial boundaries. In circumferential direction a statically determined system is introduced by fixing three outer boundary nodes such that they are able to move only in radial direction. Finally, an internal hydrostatic pressure follower load of 24 kPa representing a blood pressure of 180 mmHg is applied stepwise by surface elements described in section 3.5.2. In a first analysis we focus on the strain energy function ψ_{A} for the media and the adventitia and ψ_{C} for the plaque from Equations (4.2) and (4.8), respectively. The applied material parameters are given in Table 4.2 and 4.3. Finally, the resulting deformed configuration is depicted in upper images of Figure 5.14. There, the von Mises stresses σ_V are plotted in the artery-lumen interface in Figure 5.14a and in the plaque in Figure 5.14b. For a better visibility the media and adventitia are made translucent. The second analysis is performed using the strain energy function ψ_{B} from Equation (4.4) for the representation of the media and adventitia and ψ_{C} is kept for the plaque. The parameters given in Table 4.2 and 4.3 are used and the resulting von Mises stress distribution is depicted in the lower images of Figure 5.14 in the same manner as before.

The comparison of the results of both these simulations in Figure 5.14 leads to differences

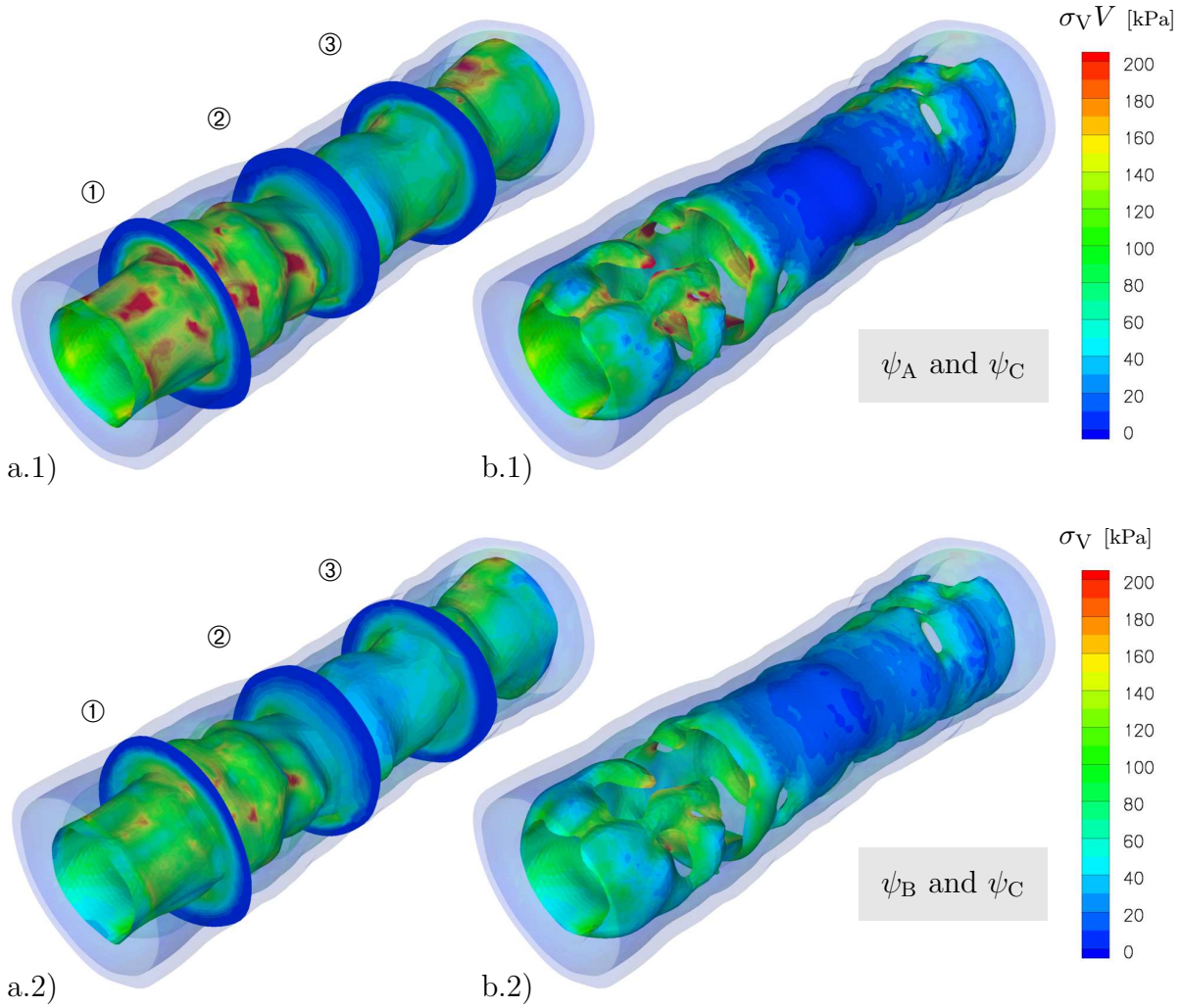

Figure 5.14: Distribution of the von Mises stresses σ_V a) in the artery-lumen interface with three exemplary cross sections ①, ②, ③, and b) in the plaque. The deformed configuration is shown, where the outer layers are depicted transparently. The upper figures a.1) and b.1) show the response due to the strain energy functions ψ_A and ψ_C and the lower ones a.2) and b.2) due to ψ_B and ψ_C. (Taken from Balzani et al. [14])

in the von Mises stress distribution throughout the artery. The stress-strain response of ψ_{A} and ψ_{B} are adjusted to the same experimental data and a quite similar response in the tension tests is obtained. Thus, the disagreements in the stress distributions should be due to the slight difference in the stiffness at higher loadings, cf. Figure 4.6. As mentioned before the positions of stress concentrations within the wall are important for medical applications, because these are strongly linked with failure initialization. Such concentrations could be observed in both resulting distributions. Although we have to emphasize again, that the here presented results raise no claim to be realistic.

In addition to that, we present the von Mises stress distribution of three distinct axial cross sections ①, ②, and ③ in Figure 5.15, which are provided by the results shown in Figure 5.14a. These cross sections were already considered as basis for the two dimensional simulations in the previous section, whose results are depicted in Figure 5.12. From these representations the transmural stress situations inside the plaque, the media, and the adventitia can be analyzed and compared with the two dimensional results from the

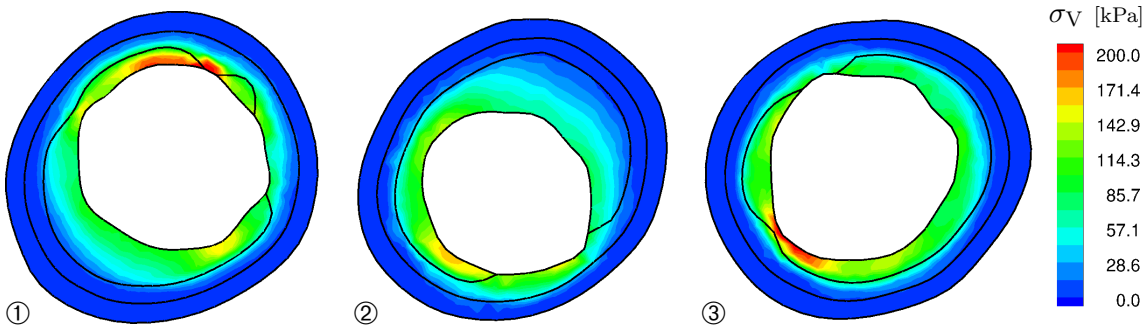

Figure 5.15: Distribution of von Mises stresses σ_V in the three different arterial cross sections extracted from Figure 5.14. The associated VH IVUS images are shown in Figure 5.11. (Taken from Balzani et al. [14])

previous section.

Although neither the results in the three-dimensional nor in the two-dimensional simulations can be interpreted as realistic, the difference is significant. Not only the qualitative distribution is completely different in the two-dimensional calculations, but also the positions of localized stress concentrations are different. This is obviously a result due to the neglected plaque heterogeneity in axial direction for the 2D simulations. In addition to that, the quantitative values of the stresses differ considerably. As an example, in cross section ① the stresses range from 0 to 240 kPa in the three-dimensional calculation and from 0 to 654 kPa in the two-dimensional one. This means an overestimation of the stresses if only the two-dimensional results are considered. Due to that further developments regarding the increase of accuracy of the computational results should be sought. Consequently, we discuss some starting points of possible improvements in the following section.

5.4 Limitations and Extensions

In the previous sections we showed several numerical results providing stress distributions of deformed arteries. We also mentioned several times that these results should rather be interpreted as qualitative examples since the modeling of living tissue is a complex issue and some assumptions were made. Although the focus of this thesis is on the construction of patient-specific three-dimensional geometric models of atherosclerotic arteries based on the VH IVUS-technique we try to consider some basic properties of the arterial wall, e.g. incompressibility, multi-layered material and anisotropy. But to obtain realistic numerical results more aspects have to be considered. Thus, in the following we discuss briefly the limitations regarding the presented numerical results. For more details on the individual properties commenting in the following we refer to section 4.1.4 and the references therein.

The first aspect covers the applied boundary conditions. In our modeling we assume a traction-free surface at the outer radial boundaries. Since the adventitia is usually not clearly separable from the outer connective tissue, this assumption leads to an radial extension of the arterial geometry without any back pressure from the surrounding tissue. But the stiffness of this connective tissue is relatively small compared to the tissue of the arterial wall and, consequently, the error is not very relevant.
Another aspect is the visco-elastic response of the tissue, which is not considered in the

material modeling in this thesis. But we only focus on elastic arteries and those ones exhibit a small number of smooth muscle cells. In contrast to the treatment of muscular arteries, thereby more sophisticated models for the smooth muscle cells, as e.g. Ståhlhand et al. [218], have to be taken into account.
If we look to the treatment of the atherosclerosis, the balloon-angioplasty, and essential behavior of the soft biological tissue is not considered in the shown simulations. During such a treatment the tissue undergo a distinct softening behavior due to the overstretching by the inflated balloon. Consequently, for meaningful simulations of a balloon-angioplasty a suitable material modeling should be applied. On that account the continuum damage approaches as e.g. proposed in Schröder et al. [195], Balzani et al. [11], Ehret and Itskov [65], Brinkhues et al. [35] or Peña and Doblaré [173] can be used. If more sophisticated constitutive laws are applied, the question remaining is how to determine the material parameters, since experiments are usually quite difficult and currently not available, e.g. for the individual plaque components. Therefore, in this thesis the plaque was assumed as a homogeneous isotropic material which is obviously only a first approximation. But we know from the sensitivity analysis of plaque components published by Brinkhues et al. [36] and Tielke [226], that the mechanical behavior of the plaque influences the overall mechanical behavior of the arterial wall. Nevertheless, the models for the media and adventitia are founded on experimental results given for the physiological loading regime in Balzani et al. [10].
In the present analysis no blood flow is considered and the quasistatic case is assumed. For a more realistic response of the artery in real-life circumstances the blood flow accompanied by dynamic influences could have a significant impact. Possible approaches for these coupling are published by e. g. Formaggia et al. [72], Formaggia et al. [73] and Passerini et al. [171]. Another aspect is the consideration of eigenstresses in the arterial wall. In section 4.1.4 we already mentioned the residual stress in the load-free configuration, which results in a spring open of the artery after a cut in radial direction. Possible treatments to get a prestressed artery in numerical simulations were published by e. g. Holzapfel et al. [110], Balzani et al. [11] and Balzani [8; 9], where an open geometry of the artery is numerically closed by different methods. A further method for obtaining a three-dimensional prestressed state of the arterial geometry was published by Gee et al. [80], where a physically meaningful stress-strain state is introduced and compared to a geometry from a patient-specific computer tomography.
The reinforcement by fibers in the arterial layers is another aspect, which should be discussed regarding the limitations. Here, we assume constant fiber orientations within the medial and adventitial layers, which are following the mean orientation of the fibers. But the arrangement of the fibers is an open question in particular for the plaque-media interface. Therefore, the issue of growth and remodeling needs to be investigated in detail in order to get more realistic fiber orientations. Also the fiber orientation in the adventitial layer is a further starting point for additional investigations. Since the individual orientations show larger deviations from the mean direction compared to those ones located in the media an dispersion of the fibers should be take into account in the material modeling. For example, in Gasser et al. [78] a possible treatment of this aspect is presented.

6 Micro Heterogenous Two-Phase Steels

In many fields of steel applications, e.g. automotive engineering or aircraft construction, the optimization of the material properties becomes one of the main challenges. Although the properties of steels was improved all over the years since the invention of their production, the main characteristic of the mechanical properties has been unchanged. The mechanical behavior of steels are called elasto-plastic and Figure 6.1 shows schematically the essential characteristic of the related stress-strain response.

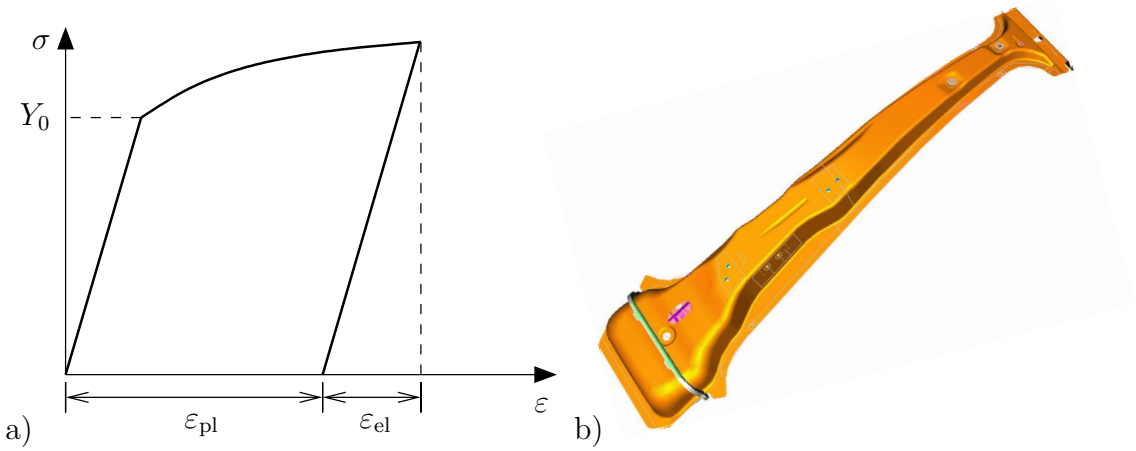

Figure 6.1: a) Schematical illustration of the stress-strain response of an material with an elasto-plastic behavior, which shows hardening effect after reaching the minimum or initial yield strength Y_0. The range of the elastic and plastic strains are denoted by ε_{el} and ε_{pl}, respectively. b) Typical application of advanced high strength steels in the automotive manufacturing: B-pillar of a car (`www.benteler.de`)

At the beginning of applying a load to an elasto-plastic material the stresses σ increase linear with respect to the strains ε. But from reaching a critical value Y_0 of the stresses the plastic flow of the material starts, consequently Y_0 is called initial yield strength or minimum yield strength. The resulting plastic deformations are irreversible and remain after unloading the material as plastic strains ε_{pl}. In steels and others metals these inelastic deformations are caused by dislocations of the crystal lattice spoiling each other during the further deformation process, from which the hardening of the material results. Especially, these plastic properties enables the formability of steels and consequently the application in many fields of engineering. Especially in the development of new car concepts like e. g. the UltraLight Steel Auto Body (ULSAB), cf. WorldAutoSteel [252], should be lightweight, safe and structurally sound. On that account in the last three decades several new steel types has been developed. These ones are represented by the group of advanced high strength steels (AHSS), in which the following steel types can be found: dual-phase (DP), transformation induced plasticity (TRIP), complex phase (CP) and martensitic (MS) steels. They exhibit on the one hand higher strength and enhanced formability and on the other hand a better energy absorbance with respect to a better crash energy management. At that point, one important contributor to these macroscopic (effective) properties is the micro-heterogeneity of the material. Their microstructures represents the main distinguishing characteristic compared to the group of conventional high strength steels (HSS). Since these ones are characterized as single phase ferritic steels, in AHSS other phases can be observed, e. g. martensite, bainite and/or austenite. In this

thesis we focus on steels consisting of two phases like e. g. DP steels and refer for general information regarding the manufacture of steel to the literature of the field of materials, e. g. Bargel and Schulze [16], Bergmann [21] and Hornbogen et al. [112]. In addition to these references the *AHSS application guidelines* WorldAutoSteel [253] provides a wide range of information regarding the properties as well as the applications of AHSS. It is a pooled knowledgebase of several experts from the WorldAutoSteel.

In the sequel of this thesis the analysis and modeling of the mechanical behavior of two-phase steels is an important item. Therefore, we give an overview of the properties of DP steels exemplifying a possible two-phase steel and discuss their microstructural morphology in addition to the mechanical features. Afterwards we give a brief introduction to some metallographical treatments providing information about the microstructure and composition of steels. Since in this thesis we perform several FE-simulations considering a two-phase steel as the underlying material we introduce a constitutive model, the finite J_2-plasticity, for the description of the mechanical behavior of the individual phases.

6.1 Morphology and Mechanical Properties of DP-Steels

In the 1970s the first developments of higher strength steels especially the dual-phase (DP) steels with greater formability than conventional steels were made, see e. g. Koo and Thomas [132] and Davies [54]. The process of investigation regarding the improvement of the manufacturing process and the mechanical properties has been produced numerous publications over the last forty years, e. g. Sarwar and Priestner [188], Tavares et al. [223], Fallahi [68], Chakraborti and Mitra [41] and references therein.

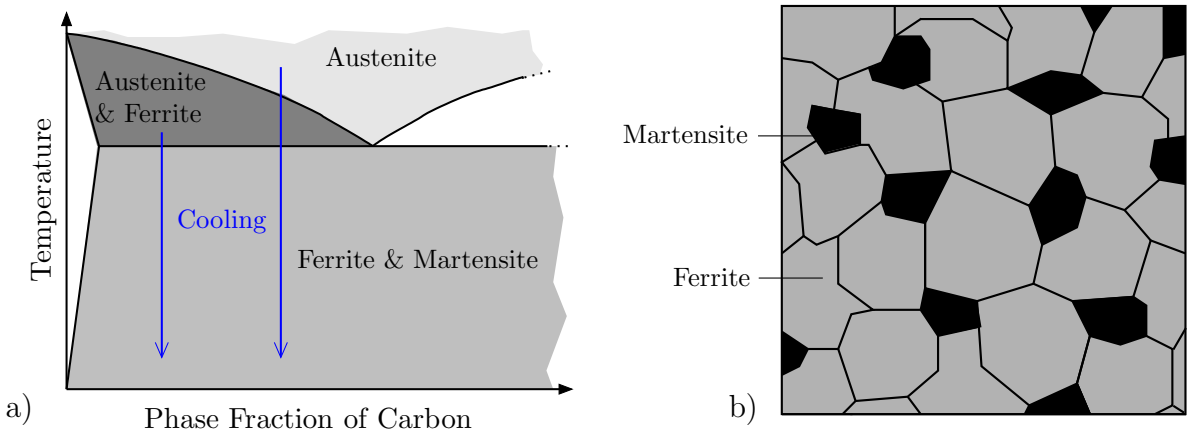

Figure 6.2: Schematical illustration of a) the essential section of the phase diagram for the production of dual-phase steels and the paths (blue arrows) for the cooling procedure and b) the resulting morphology of a dual-phase steel after the cooling process consisting of a ferritic matrix phase (grey) and a martensitic inclusion phase (black).

The DP steels are mainly characterized by the composition at the microscopic level, where a matrix/inclusion morphology is observed. For the evolution of such a morphology a controlled cooling rate of the steel from the austenite or austenite-ferrite phase is essential. Therefore, the steel is annealed and afterwards the transformation process from austenite to martensite is driven by a rapid cooling, cf. Figure 6.2a. Consequently, the matrix phase consist of ferrite and the inclusion phase contains martensite, which is harder than

the matrix phase. As shown schematically in Figure 6.2b the ferrite phase is generally continuous, which is accountable for the good ductility of the DP steels. For an additional improvement of this feature as well as the thoughness the application of controlled rolling processes has been developed, see e.g. Fallahi [68]. In common the mechanical properties of DP steels are distinguished with respect to those of conventional steels by higher ultimate tensile strengths while similar yield strength can be observed. This behavior is mainly governed by a high work-hardening rate and a good elongation characteristic. A further and essential tool for the modification of the mechanical properties is the addition of ingredients, like e. g. manganese, chromium, nickel and vanadium, and consequently the range of the yield strength and the tensile strength for typical DP steels is from 240 to 700 MPa and from 450 to 1000 MPa, respectively, cf. WorldAutoSteel [253].

Note that there are general differences between dual-phase steels and the also well-known duplex steels and both types should not be mixed up. In contrast to the ferritic-martensitic texture of dual-phase steels the duplex steels consists of a ferritic and an austenitic phase, whose volume fractions are divide equally.

6.2 Metallographical Treatments

In the previous subsection we discuss the properties of a typical two-phase steel and provide in Figure 6.2b a schematic representation of the microstructure. The visualization of the real microstructure of a metallic material and its characterization are the main tasks of a metallographical treatment. In this section we give a summary of two micro-

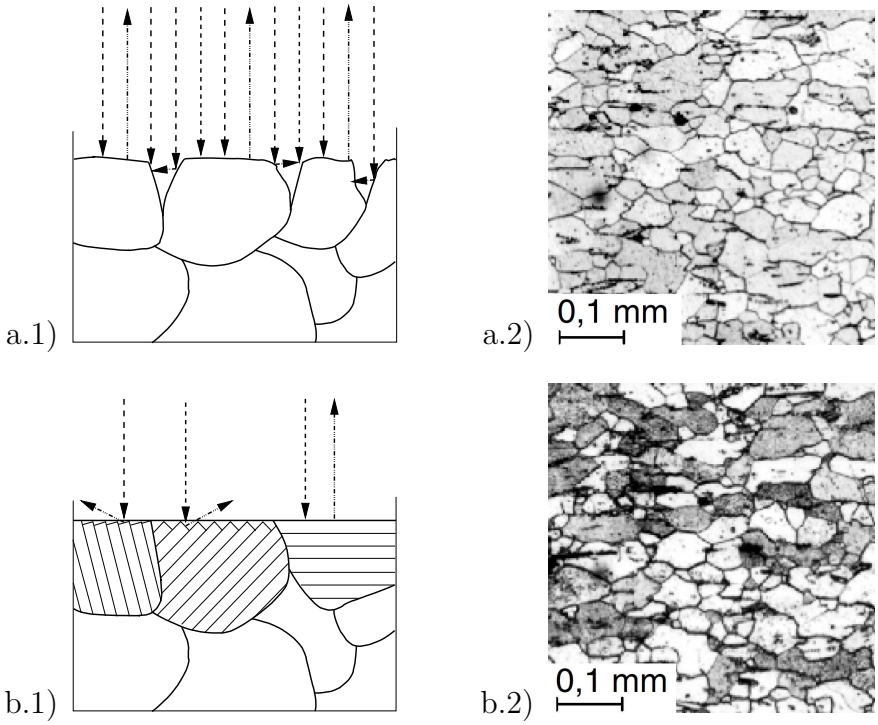

Figure 6.3: Light microscopies of an sample of aluminum prepared by etching of a) grain boundaries and of b) grain surfaces. a.1) & b.1) Schematical illustrations of the reflection of light rays and a.2) & b.2) visualizations of the resulting visualizations by the microscope. (Taken from Bargel and Schulze [16])

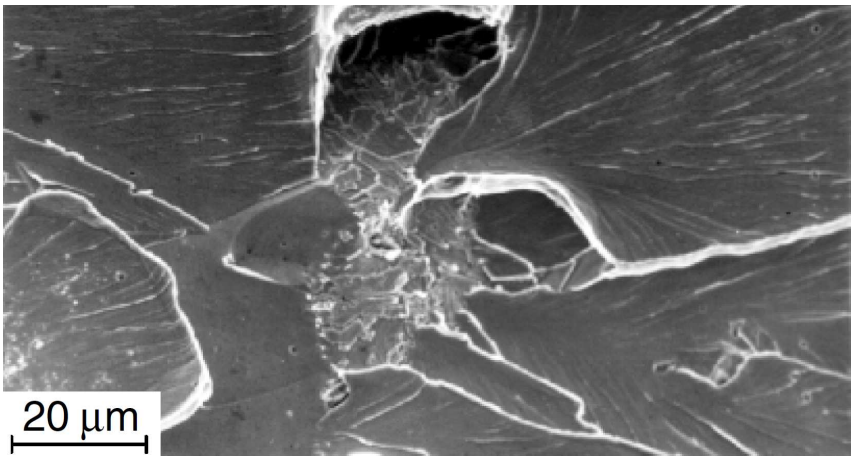

Figure 6.4: Visualization of the surface of a fraction by scanning electron microscope, taken from Bargel and Schulze [16]

scopical methods, the light microscopy and the electron microscopy. Note, that there are several other treatments available (e. g. X-ray diffraction) and, consequently, we refer to classical textbook concerning the metallography, e. g. Bargel and Schulze [16] and Oettel and Schumann [164].

The visualization of microstructures obtained by light microscopy has a maximum in-plane resolution of 0.3 µm and a focus depth of 0.01 µm. Before the sample could be analyzed using the microscope, it has to be prepared regarding the roughness of the surface to be studied. On that account the surface is mechanically and/or electrolytically polished. The second preparing method avoid the cold forming process and consequent microstructural disorders, which is observed by the mechanical treatment. For the enhancement of the contrast a chemical or electrolytic etching is applied to the surface. Thereby it is differed between two etching methods: one pits the grain boundaries and the other ones the grain surfaces. Consequently, the images resulting from the light microscopy shows different contrast levels, cf. Figure 6.3. The first etching method result in a visualization, which emphasizes the grain boundaries and shows only a low contrast regarding the different orientations of the grains. In contrast, the other method gives more information about these orientations, since visualization of the grains shows a wider greyscale range.

Another technique used for the analysis of the microstructure of different materials is the scanning electron microscope (SEM). This method enables a resolution up to 0.01 µm, a focus depth of about 35 µm and a magnification up to $200,000s$. Thereby, a beam of electrons with a diameter of about 0.01 µm is used to scan the surface of the sample. This electron beam dissolves out additional electrons from the surface of the sample, which are visualized on a screen after an amplification. The principle of a SEM based on the fact, that from protruding parts of the surface more electrons can be dissolved compared to lower located regions and, consequently, theses parts appear with a higher brightness on the screen. But in contrast to the light microscopy the observer must have more experiences in the interpretation of the results, cf. Figure 6.4.

6.3 Material Modeling: Finite J_2-Plasticity

In the sequel of this thesis we treat Finite Element Method simulations of boundary value problem where the material is considered as dual-phase steel. Since we distinguish in these problems between the two phases on the microscopic level we have to provide a constitutive law for the description of their elasto-plastic behavior. The research regarding the plasticity of materials has become an important field and is still in progress. Thus a wide range of publications at this field are done over the years and we give only an overview of several ones, which can be used for a deeper study regarding the plasticity in the continuum mechanical framework. The theory of the geometrical linear treatment is presented by e. g. Hill [96; 97], whereas in e. g. Miehe and Stein [148], Miehe [147], Simo and Hughes [208] and Oñate and Owen [162] the theoretical framework as well as the numerical implementation is discussed, particularly, the case of large strains.

In this thesis we consider an elasto-plasticity model for the description of the mechanical behavior of the individual metallic phases. This model takes into account an isotropic exponential-type hardening based on a von Mises flow criterion, also refer to the J_2-plasticity, which is documented in e. g. Simo [204; 205], Peric et al. [174] and Klinkel [127]. In the following subsections we summarize the results of the theoretical and numerical treatment and refer for more details to the given references.

6.3.1 Constitutive Modeling

The constitutive modeling takes the multiplicative decomposition of the deformation gradient as a starting point, cf. Kröner [136] and Lee [138], and provides

$$\boldsymbol{F} = \boldsymbol{F}^{\mathrm{e}}\,\boldsymbol{F}^{\mathrm{p}} \tag{6.1}$$

with the elastic $\boldsymbol{F}^{\mathrm{e}}$ and plastic $\boldsymbol{F}^{\mathrm{p}}$ parts. Thereby the elastic quantity $\boldsymbol{F}^{\mathrm{e}}$ describes the stress-driven deformations and the intermediate configuration represented by the plastic counterpart $\boldsymbol{F}^{\mathrm{p}} = (\boldsymbol{F}^{\mathrm{e}})^{-1}\boldsymbol{F}$ is stress free. For the kinematical description we use the left Cauchy-Green tensor, cf. Equation $(2.17)_2$,

$$\boldsymbol{b} = \boldsymbol{F}\,\boldsymbol{F}^T = \boldsymbol{F}^{\mathrm{e}}\,\boldsymbol{b}^{\mathrm{p}}\,(\boldsymbol{F}^{\mathrm{e}})^T\,, \quad \boldsymbol{b}^{\mathrm{p}} = \boldsymbol{F}^{\mathrm{p}}\,(\boldsymbol{F}^{\mathrm{p}})^T\,, \quad \boldsymbol{b}^{\mathrm{e}} = \boldsymbol{F}^{\mathrm{e}}\,(\boldsymbol{F}^{\mathrm{e}})^T\,, \tag{6.2}$$

and the associated spectral decomposition of the elastic deformation tensor

$$\boldsymbol{b}^{\mathrm{e}} = \sum_{A=1}^{3} (\lambda_A^{\mathrm{e}})^2 \boldsymbol{n}_A \otimes \boldsymbol{n}_A\,. \tag{6.3}$$

The spectral decomposition allows the representation of the tensor by a sum regarding the dyadic products of the eigenvectors $\boldsymbol{n}_A$, which are multiplied with the associated eigenvalues $(\lambda_A^{\mathrm{e}})^2$ of $\boldsymbol{b}^{\mathrm{e}}$. The quantities λ_A^{e} are identified as the elastic stretch and can be computed by the solution of the eigenvalue problem $[\boldsymbol{b}^{\mathrm{e}} - (\lambda_A^{\mathrm{e}})^2\mathbf{1}]\boldsymbol{n}_A = \mathbf{0}$, cf. Simo [205]. Analogously, the right Cauchy-Green tensor can written as

$$\boldsymbol{C} = \boldsymbol{F}^T\boldsymbol{F}\,, \quad \boldsymbol{C}^{\mathrm{p}} = \boldsymbol{F}^{\mathrm{p}T}\boldsymbol{F}^{\mathrm{p}}\,, \quad \boldsymbol{C}^{\mathrm{e}} = \boldsymbol{F}^{\mathrm{e}T}\boldsymbol{F}^{\mathrm{e}} \tag{6.4}$$

and the relations between both these strain tensors are

$$\boldsymbol{b}^{\mathrm{e}} = \boldsymbol{F}\boldsymbol{C}^{\mathrm{p}-1}\boldsymbol{F}^T \quad \text{and} \quad \boldsymbol{C}^{\mathrm{p}-1} = \boldsymbol{F}^{-1}\boldsymbol{b}^{\mathrm{e}}\boldsymbol{F}^{-T}\,. \tag{6.5}$$

For the structure of the free energy function we assume

$$\psi = \psi^{\mathrm{e}}(\boldsymbol{b}^{\mathrm{e}}) + \psi^{\mathrm{p}}(\alpha) \; , \tag{6.6}$$

wherein the elastic part depends only on the strain measure $\boldsymbol{b}^{\mathrm{e}}$ and the plastic counterpart is a function of the internal variable α. Starting from the local form of the Clausius-Duhem inequality (2.64) for isothermal processes

$$\mathcal{D} = \boldsymbol{\tau} : \boldsymbol{d} - \dot{\psi} \geq 0 \tag{6.7}$$

with the Cauchy stress tensor $\boldsymbol{\tau}$ and the stretching tensor $\boldsymbol{d}$, see sections 2.2 and 2.3, the constitutive equations as well as the flow rule is achieved. The equation for the stresses $\boldsymbol{\tau}$ and the conjugated stress-like variable β are given by

$$\boldsymbol{\tau} = 2\frac{\partial \psi^{\mathrm{e}}}{\partial \boldsymbol{b}^{\mathrm{e}}}\,\boldsymbol{b}^{\mathrm{e}} \quad \text{and} \quad \beta := -\frac{\partial \psi^{\mathrm{p}}}{\partial \alpha} \; . \tag{6.8}$$

The principle of maximum plastic dissipation states, that the thermodynamical equilibrium is achieved for the case of maximal entropy, cf. Simo and Hughes [208]. Considering this principle an optimization problem using the Lagrange multiplier γ can be formulated, which is solved iteratively. The well-known Kuhn-Tucker optimality conditions

$$\gamma \geq 0 \; , \quad \phi \leq 0 \; , \quad \gamma\phi = 0 \; , \tag{6.9}$$

ensure the fulfillment of the underlying Lagrange functional, see e. g. Bertsekas [23]. From the optimization problem the flow rule and the evolution of the internal variable arise as

$$-\gamma\frac{\partial \phi}{\partial \boldsymbol{\tau}} = \frac{1}{2}\mathcal{L}(\boldsymbol{b}^{\mathrm{e}})\boldsymbol{b}^{\mathrm{e}-1} \quad \text{and} \quad \dot{\alpha} = \gamma\frac{\partial \phi}{\partial \beta} \; . \tag{6.10}$$

Note, that $\mathcal{L}(\boldsymbol{b}^{\mathrm{e}})$ denotes the directional derivative, the so-called Lie-derivative, of the elastic finger tensor $\boldsymbol{b}^{\mathrm{e}}$, see e. g Marsden and Hughes [142], and is calculated by

$$\mathcal{L}(\boldsymbol{b}^{\mathrm{e}}) = \boldsymbol{F}\left\{\frac{\partial}{\partial t}\left[\boldsymbol{F}^{-1}\boldsymbol{b}^{\mathrm{e}}\boldsymbol{F}^{-T}\right]\right\}\boldsymbol{F}^{T} = \boldsymbol{F}\dot{\boldsymbol{C}}^{\mathrm{p}-1}\boldsymbol{F}^{T} \; . \tag{6.11}$$

Using the latter equation an alternative formulation of the flow rule (6.10) reads

$$\dot{\boldsymbol{C}}^{\mathrm{p}} = 2\gamma\,\boldsymbol{C}^{\mathrm{p}}\left(\boldsymbol{F}^{-1}\frac{\partial \phi}{\partial \boldsymbol{\tau}}\boldsymbol{F}\right) \tag{6.12}$$

Before considering a specific free energy function and a flow criterion we give a note to the aforementioned Kuhn-Tucker conditions due to their interpretation in the sense of loading/unloading conditions. The flow criterion $\phi < 0$ represents the purely elastic behavior because the stress state is located interior the domain defined by the yield surface. Also no plastic behavior is initiated since the condition $(6.9)_3$ forces $\gamma = 0$ and accordingly the evolution of the internal variable is zero. In contrast to that $\phi = 0$ represents the stress state on the yield surface and we differentiate between

$$\begin{array}{lllll} \text{elastic unloading:} & \dot{\phi} < 0 & \text{and} & \gamma = 0 \; , \\ \text{neutral loading:} & \dot{\phi} = 0 & \text{and} & \gamma = 0 \; , \\ \text{plastic loading:} & \dot{\phi} = 0 & \text{and} & \gamma > 0 \end{array}$$

and achieve the consistency condition

$$\gamma\dot{\phi} = 0\ . \tag{6.13}$$

Since we assume an isotropic mechanical behavior the elastic part of the free energy function can be formulated in terms of the main invariants according to section 2.5.3. In Simo [205] the energy function

$$\psi^{\mathrm{e}} = \frac{\lambda}{2}[\epsilon_1^{\mathrm{e}} + \epsilon_2^{\mathrm{e}} + \epsilon_3^{\mathrm{e}}]^2 + \mu[(\epsilon_1^{\mathrm{e}})^2 + (\epsilon_2^{\mathrm{e}})^2 + (\epsilon_3^{\mathrm{e}})^2] \tag{6.14}$$

is propose based on the logarithmic elastic strains $\epsilon_A^{\mathrm{e}} = \log \lambda_A^{\mathrm{e}}$ using the Lamé constants λ and μ. For the description of the plastic behavior we consider a von Mises flow criterion with isotropic, exponential-type hardening. The flow criterion reads

$$\phi = \| \operatorname{dev} \boldsymbol{\tau} \| - \sqrt{\tfrac{2}{3}}\, \beta \leq 0 \tag{6.15}$$

with the conjugated internal variable

$$\beta = y_\infty + (y_0 - y_\infty) \exp(-\eta\alpha) + h\ \alpha\ . \tag{6.16}$$

Herein, y_0 is the initial yield strength, y_∞ and η describe an exponential hardening behavior and h is the slope of a superimposed linear hardening. The resulting set of constitutive equations regarding the elastic free energy function (6.14) and the yield criterion (6.15) based on the specific conjugated internal variable (6.16) are summarized in Table 6.1.

Table 6.1: Equation box of the finite J_2-Plasticity model.

kinematics	$\boldsymbol{F} = \boldsymbol{F}^{\mathrm{e}}\boldsymbol{F}^{\mathrm{p}}, \quad \boldsymbol{b}^{\mathrm{e}} = \boldsymbol{F}^{\mathrm{e}}\boldsymbol{F}^{\mathrm{e}T}$
strain energy	$\psi = \psi^{\mathrm{e}}(\boldsymbol{b}^{\mathrm{e}}) + \psi^{\mathrm{p}}(\alpha)$
elastic part	$\psi^e = \frac{\lambda}{2}[\epsilon_1^{\mathrm{e}} + \epsilon_2^{\mathrm{e}} + \epsilon_3^{\mathrm{e}}]^2 + \mu[(\epsilon_1^{\mathrm{e}})^2 + (\epsilon_2^{\mathrm{e}})^2 + (\epsilon_3^{\mathrm{e}})^2]$ with $\epsilon_A^{\mathrm{e}} = \log(\lambda_A^{\mathrm{e}})$
plastic part	$\psi^{\mathrm{p}} = y_\infty\alpha - \frac{1}{\eta}(y_0 - y_\infty)\ \exp(-\eta\alpha) + \frac{1}{2}\ h\ \alpha^2$
stresses	$\boldsymbol{\tau} = \sum_{A=1}^{3} \tau_A\, \boldsymbol{n}_A \otimes \boldsymbol{n}_A \quad \text{with} \quad \tau_A = \frac{\partial \psi_{\mathrm{e}}}{\partial \epsilon_A^{\mathrm{e}}}$
conj. internal variable	$\beta = y_\infty + (y_0 - y_\infty)\ \exp(-\eta\alpha) + h\ \alpha$
yield criterion, yield rule	$\phi = \|\| \operatorname{dev} \boldsymbol{\tau} \|\| - \sqrt{\frac{2}{3}}\beta, \quad \frac{1}{2}\mathcal{L}(\boldsymbol{b}^{\mathrm{e}})\boldsymbol{b}^{\mathrm{e}-1} = -\lambda\frac{\partial \phi}{\partial \boldsymbol{\tau}}$
evolution of int. variable	$\dot{\alpha} = \sqrt{\frac{2}{3}}\gamma$
loading conditions	$\gamma \geq 0\,, \quad \phi \leq 0\,, \quad \lambda\phi = 0$

6.3.2 Consistent Algorithmic Treatment

Here we briefly outline the strategy for the numerical implementation and refer for further studies on the literature given in the preamble of this section. The constitutive equations given by Table 6.1 are solved applying a *return-mapping algorithm* to the time interval $[t_n, t_{n+1}]$ with the time step $\Delta t := t_{n+1} - t_n$, see e. g. Simo and Hughes [208]. The

flow rule for the plastic quantity is integrated using an implicit exponential update algorithm, which preserves plastic incompressibility (Weber and Anand [246], Simo [205], and Miehe and Stein [148]). The quantities at time t_n are denoted by $(\bullet)_n$ and are assumed to be known. Since we focus on the displacement driven formulation for finite elements, the deformation state $\boldsymbol{F}_{n+1}$ at time t_{n+1} is also known. Following the multiplicative decomposition the boundary value problem is divided in an elastic and a plastic subproblem. First, a trial elastic state is introduced, wherein the evolution of the plastic flow on the time step $[t_n, t_{n+1}]$ is "frozen", i. e.

$$\boldsymbol{C}^{\mathrm{p,trial}}_{n+1} = \boldsymbol{C}^{\mathrm{p}}_{n} \ , \quad \alpha^{\mathrm{trial}}_{n+1} = \alpha_n \ . \tag{6.17}$$

Based on this trial state the flow criterion

$$\phi^{\mathrm{trial}}_{n+1} \leq 0 \tag{6.18}$$

is checked. In the case of its fulfillment a purely elastic step is performed and the stresses are given by $\boldsymbol{\tau}_{n+1} = \boldsymbol{\tau}^{\mathrm{trial}}_{n+1}$. Otherwise, the trial stresses are projected on to the closest point of the yield surface. If the material is perfectly plastic, the yield surface is constant, but e. g. $h > 0$ in Equation (6.16) the yield surface expands during the plastic flow, and the stress is projected on the expanded yield surface. In the case of isotropic hardening as we consider here this task is also known as radial return algorithm. Due to the considered nonlinear hardening law the projection is done by a local Newton iteration. Therefore we follow the algorithmic formulation in a material setting as proposed in Klinkel [127].

7 Multiscale Computation of Two-Phase Steels

The application of two-phase steels, e. g. dual-phase (DP) steels, finds its way into many fields of engineering due to their high ductility and stiffness, cf. Chapter 6. This is due to the fact that the interplay between the individual constituents on the microscale yield outstanding strength and ductility properties. However, the complicated interactions of the individual phases of the micro-heterogeneous composite lead to complex local hardening effects and failures on the microscale. The usage of such complex materials in engineering applications like e. g. bending, deep-drawing and hydro-forming requires a sufficient number of experiments. Numerical simulations enable in addition to real investigations the possibility to reduce the number and costs of these tasks. But also the computational analysis gives the possibility to examine the material and the process from another point of view, e.g. the view inside the material during deformations or the estimation of necessary load conditions for the process. Thus, the mechanical properties of the material must be represented by the used numerical model. At that point, one important contributor to the macroscopic (effective) properties is the micro-heterogeneity of the material. One possible implementation is the consideration of the microstructure during the simulation by a two-scale modeling approach to capture the characteristic phenomena. Thereby a sufficient large section of the microstructure, approximated by a representative volume element (RVE), is attached to each point of the macroscale. This numerical treatment is known as the direct micro-macro-transition procedure or the FE^2-method and is discussed in the first subsection here. Originally, the main concept of this approach dates from papers by Suquet [222], Ghosh et al. [83], Terada and Kikuchi [225]. More developments and applications in this field of research are documented in publications by e.g. Smit et al. [211], Brekelmans et al. [33], Miehe et al. [149; 150], Schröder [191], Kouznetsova et al. [134], Miehe et al. [151], Kouznetsova [133] and Geers et al. [81].

The drawback of this approach is the high computational cost (high computation times and assignment of memory space), when we deal with large random microstructures. In order to circumvent these drawbacks we focus on the construction of statistically similar representative volume elements (SSRVEs) which are characterized by a much less complexity than the real random microstructures but represent the macroscopic mechanical response of the real (target) structure in an adequate manner. The framework for the construction of SSRVEs for two-phase microstructures is given in the second part and also analyzed in the subsequent sections. The chapter is closed with applications of the constructed SSRVEs to simulations using the FE^2-method.

7.1 Homogenization Method

In common we describe the material properties in a material point assuming a uniform distribution of the stress and strain fields in the immediate neighborhood. This means the assumption of a material which is homogeneous. But every real material is inhomogeneous if its structure is looked at on a certain scale. For example structural elements, e.g. a cross member of a car, seems to be a homogeneous material on the scale of its full dimension (centimeter to meter). However the view through a microscope on the microscale offers a heterogeneous structure. Consequently it is referred to as *micro-heterogeneous* and no uniform distribution is guaranteed. Especially the numerical treatment, a direct consideration

of the microstructure by a full-scale discretization, is not reasonable, except for simple geometries or for structures without very different lengthscales. At that point the field of micromechanics provides sustainable methods to incorporate microstructural information to the macroscale continuum. For detailed introduction into this topic we refer to the textbooks Zohdi and Wriggers [261], Torquato [227] and Buryachenko [38].

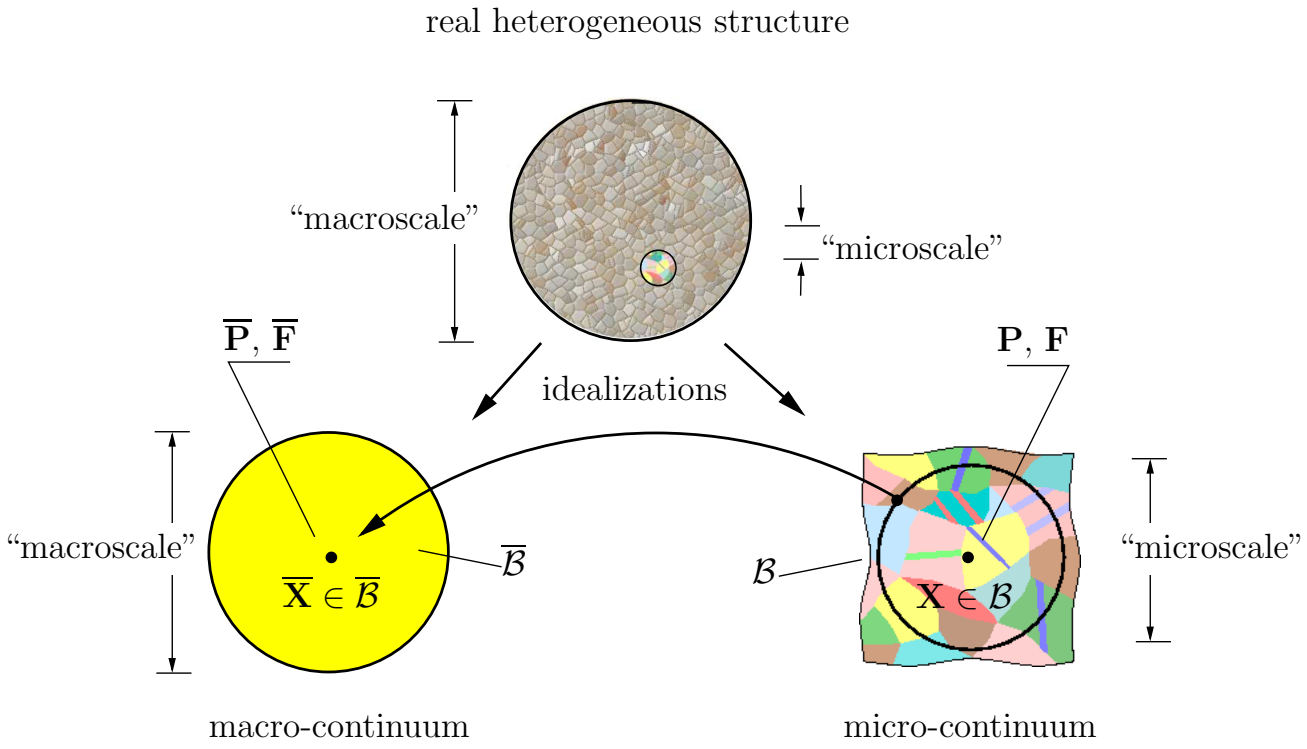

Figure 7.1: Concept of the direct micro-macro modeling. Macrocontinuum $\overline{\mathcal{B}}$ is described by the application of the associated microstructure $\mathcal{B}$ in each point $\overline{\boldsymbol{X}} \in \overline{\mathcal{B}}$ on the macroscale. Adapted from Schröder [191]

The main concept of the computational homogenization is illustrated in Figure 7.1, where the macroscopic quantities are estimated from the underlying microstructure. On that account the definition of the microstructural boundary value problem and the formulation of the equations for the direct micro-macro transition are essential aspects. This homogenization procedure can be subdivided into four subitems, adapted from Suquet [222]:

- definition of the representative volume element (RVE) accompanied by the conflict regarding the size of the RVE: "... small enough to distinguish the microscopic heterogeneities, yet large enough to represent the overall behavior of the heterogeneous medium,..." (Suquet [222]).
- transition "micro → macro": definition of the macroscopic field using microscopic ones by an averaging process.
- transition "macro → micro": this localization procedure provides relation for the microscopic quantities based on macroscopic ones,
- homogenization procedure itself: establishment of the relationship between the macroscopic input and output quantities.

The first item is discussed separately in the first subsection because of its general meaning in the field of homogenization. Afterwards we introduce the theoretical and numerical framework of the FE^2-method.

7.1.1 Concept of a Representative Volume Element (RVE)

The transition from ensemble average computations to more applicable approaches is enabled by further physical assumptions strongly associated with the ergodic hypothesis. In this context the ensemble average is replaced by simple volumetric averages over one RVE, see e.g. Hill [99] and Hashin [93]. A partial volume of the material, which is macroscopically considered to be statistically homogeneous, is defined as the representative volume element. This induces that the choice of a RVE is not unique and various definitions for a RVE exist. An important requirement for the application of the concept of representative volume elements is the existence of two length scales: the length scale of the macrostructure, which defines the infinitesimal vicinity, and the length scale of the microstructure, which is characterized by the smallest significant dimension of the micro-heterogeneities. In order to obtain a volume element, which has a representative character, the RVE is usually much larger than the characteristic size of an inclusion if segments of a real microstructure serve as a RVE. Otherwise RVEs could be assumed, which consist of pure matrix or inclusion material. But in contrast to this and with respect to the computational feasibility the size of RVE should only be as large as precisely necessary. Over the years of progress in this research field several definitions have been proposed regarding the requirements towards size of RVEs. Some of them, which are summarized in Zeman [257], are:

- Hill [99] (1963): RVE has to represent the typical representative structure with respect to the whole specimen and consists of enough inclusions to ensure the independency of the overall moduli from surface value of traction and displacement, as long as these values are "macroscopically uniform".
- Hashin [93] (1983): Based on the RVE the effective properties of the considered material are estimated. Although enough information should be captured by an appropriate size of it, it should still show a distinct smaller size compared to the macroscopic body.
- Drugan and Willis [62] (1996): RVE's size should be decreased as long as its effective modulus agrees sufficiently to represent the mean constitutive response.
- Ostoja-Starzewski [170] (2001): Two possible definitions: RVE i) is the unit cell of a periodic microstructure and/or ii) fulfills the requirements to be statistically homogeneous and ergodic
- Stroeven et al. [221] (2002): No unique definition can be given without consideration of the individual material as well as its structural sensitivity regarding the mechanical properties.

7.1.2 Direct Micro-Macro Transition

In this section we discuss the theoretical and numerical treatment of the FE^2-method according to the outline in Schröder [191] but also regard Miehe et al. [149; 150].

For the differentiation of the quantities with respect to the scales on which they are defined we mark the macroscopic ones by an overline ($\overline{\bullet}$). Note that the given remarks only take into account the special treatments regarding the FE^2-method since the standard framework of continuum mechanics and the Finite Element Method have already been introduced in chapter 2 and 3.

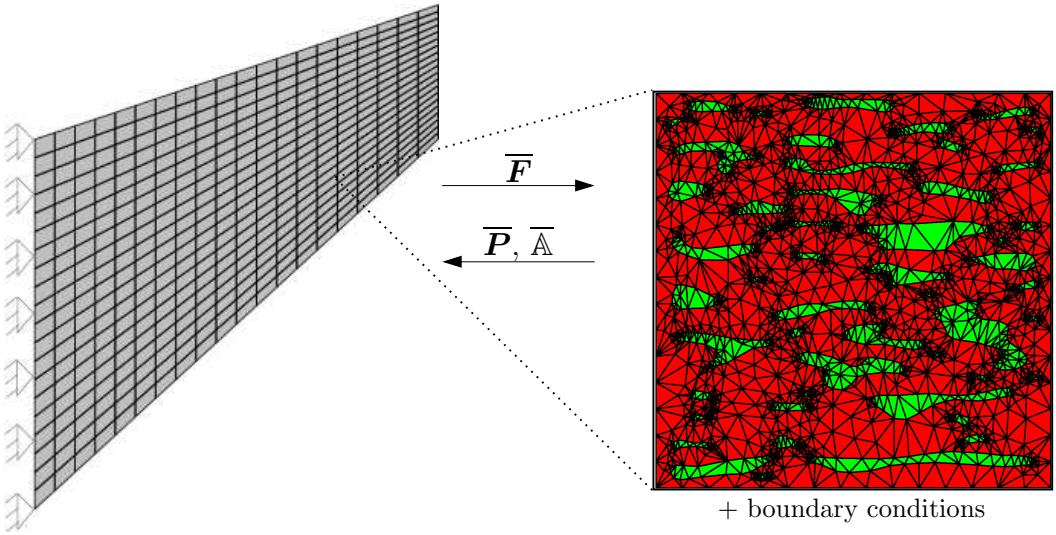

Figure 7.2: Basic idea of the FE^2-method: the macroscopic boundary value problem (left) considers at each integration (Gauss) point a microscopic boundary value problem (right).

The basic idea of the FE^2-method is that a microscopic boundary value problem is solved at each Gauss point of a macroscopic boundary value problem, see Figure 7.2.

Boundary Value Problems on Both Scales. The macroscopic deformation gradient $\overline{\boldsymbol{F}}$ is defined by

$$\overline{\boldsymbol{F}} := \operatorname{Grad} \overline{\boldsymbol{x}} = \frac{\partial \overline{\boldsymbol{x}}}{\partial \overline{\boldsymbol{X}}} \,, \tag{7.1}$$

cf. Equation (2.8), where $\overline{\boldsymbol{X}}$ and $\overline{\boldsymbol{x}}$ denote the material points of the considered body in its reference configuration $\overline{\mathcal{B}}_0$ and actual configuration $\overline{\mathcal{B}}_{0t}$ at the macroscale, respectively. The corresponding local form of the material balance of linear momentum reads

$$\operatorname{Div} \overline{\boldsymbol{P}} + \rho_0 \overline{\boldsymbol{f}} = \boldsymbol{0} \quad \forall\, \overline{\boldsymbol{X}} \in \overline{\mathcal{B}}_0 \tag{7.2}$$

cf. Equation (2.52), where we neglect inertia terms and use the macroscopic first Piola-Kirchhoff stresses $\overline{\boldsymbol{P}}$. For the full description of the macroscopic boundary value problem we give according to Equation (3.3) the boundary conditions

$$\overline{\boldsymbol{T}} = \overline{\boldsymbol{P}}\,\overline{\boldsymbol{N}} = \overline{\boldsymbol{t}} \quad \text{on} \quad \partial\overline{\mathcal{B}}_{0t} \qquad \text{and} \qquad \overline{\boldsymbol{u}} = \overline{\boldsymbol{u}}_0 \quad \text{on} \quad \partial\overline{\mathcal{B}}_{0u} \,, \tag{7.3}$$

with Neumann conditions on the surface part $\partial\overline{\mathcal{B}}_{0t}$ and with Dirichlet conditions on $\partial\overline{\mathcal{B}}_{0u}$.

Analogously the microscopic deformation gradient is defined by

$$\boldsymbol{F} := \operatorname{Grad} \boldsymbol{x} = \frac{\partial \boldsymbol{x}}{\partial \boldsymbol{X}} \,, \tag{7.4}$$

where $\boldsymbol{X}$ and $\boldsymbol{x}$ denote the material points of the considered body in its reference configuration $\mathcal{B}_0$ and actual configuration $\mathcal{B}_{0t}$ at the microscale, respectively. For the local form

of material balance of linear momentum we neglect the volume acceleration in addition to the inertia terms and end up with

$$\operatorname{Div} \boldsymbol{P} = \boldsymbol{0} \quad \forall\, \boldsymbol{X} \in \mathcal{B}_0 \,, \tag{7.5}$$

using the microscopic first Piola-Kirchhoff stress $\boldsymbol{P}$. For the complete description of the microscopic boundary value problem we need the corresponding boundary conditions, which are introduced after the relations regarding the micro-macro transition in the next paragraph.

Micro-Macro Coupling. For the transition between the scales the definition of the equations for the relevant quantities plays a crucial role. These relations are mainly based on adequate volume averaging expressions which were initially proposed in Hill [99]. A more useful and experimentally motivated description is also achieved by formulations based on terms on the boundary of the RVE. One argument is the measurement of loads and displacement in experiments which are commonly performed on the RVE's boundary. In this paragraph we give the functions for the macroscopic quantities dependent on the quantities on the microscale and refer for an illustrative derivation to Schröder [191].

We considered a RVE, parameterized in $\boldsymbol{X} \in \mathcal{B}_0$, and delimited by the boundary $\partial\mathcal{B}_0$. The definition of macroscopic deformation gradient as function of microscopic quantities reads

$$\overline{\boldsymbol{F}} := \frac{1}{V} \int_{\partial\mathcal{B}_0} \boldsymbol{x} \otimes \boldsymbol{N} \, \mathrm{d}A = \frac{1}{V} \left[\int_{\mathcal{B}_0} \boldsymbol{F} \, \mathrm{d}V - \int_{\mathcal{L}} \boldsymbol{x} \otimes \boldsymbol{N} \, \mathrm{d}A \right] \,, \tag{7.6}$$

where $\boldsymbol{x}$ are the points on $\mathcal{B}$ in the deformed state, $\boldsymbol{N}$ the normals on the undeformed boundary and $\mathcal{L}$ the boundaries of voids. Note that $\overline{\boldsymbol{F}}$ can only be calculated from the volume average of $\boldsymbol{F}$ if no voids or cracks exist. In contrast to that the macroscopic first Piola-Kirchhoff stress tensor is computed averaging the microscopic counterpart over the volume $\mathcal{B}$ of the RVE. Thus we obtain the definition

$$\overline{\boldsymbol{P}} := \frac{1}{V} \int_{\mathcal{B}_0} \boldsymbol{P} \, \mathrm{d}V \;\; = \frac{1}{V} \int_{\partial\mathcal{B}_0} \boldsymbol{t}_0 \otimes \boldsymbol{X} \, \mathrm{d}A \,, \tag{7.7}$$

wherein $\boldsymbol{t}_0$ are the traction vectors acting on the boundary $\partial\mathcal{B}_0$. Note that the averaging over the volume also pertains for the Kirchhoff stresses and the Cauchy stresses.

All extensive quantities can be considered for the transition "micro→macro" by proper averages. These quantities are state variables in a homogeneous body, which are proportional to the mass of the system, e.g. density, internal energy, entropy and dissipation. Consequently, intensive quantities are independent of the mass of the system.

Boundary Conditions of the Microscopic BVP. We already introduced the full description of the boundary value problem on the macroscale above as well as the balance equation of the microscopic counterpart. But we have omitted adequate conditions on the boundary $\partial\mathcal{B}$ yet. Here we consider the macro-homogeneity condition, also referred to as Hill–condition, see Hill [99], to derive three types of boundary conditions in this paragraph. That condition postulates that the macroscopic power is equal to the volumetric average of the microscopic powers, i. e.

$$\overline{\boldsymbol{P}} : \dot{\overline{\boldsymbol{F}}} = \frac{1}{V} \int_{\mathcal{B}_0} \boldsymbol{P} : \dot{\boldsymbol{F}} \, \mathrm{d}V \,. \tag{7.8}$$

An alternative representation of the latter Hill-condition is obtained after some mathematical manipulations,

$$\frac{1}{V}\int_{\mathcal{B}_0}(\boldsymbol{t}-\overline{\boldsymbol{P}}\boldsymbol{N})\cdot(\dot{\boldsymbol{x}}-\dot{\overline{\boldsymbol{F}}}\boldsymbol{X})\,\mathrm{d}V=0\,. \tag{7.9}$$

see e. g. Schröder [191]. Valid boundary conditions applied to the microscopic boundary problem $\mathrm{Div}\,\boldsymbol{P}=0$ must satisfy the latter equation. Obviously the boundary conditions

$$\boldsymbol{t}=\overline{\boldsymbol{P}}\boldsymbol{N}\quad\text{on}\quad\partial\mathcal{B}_0\quad\text{and}\quad\boldsymbol{x}=\overline{\boldsymbol{F}}\boldsymbol{X}\quad\text{on}\quad\partial\mathcal{B}_0 \tag{7.10}$$

are suitable but an additional type, the periodic boundary conditions, can be achieved through the following approach.

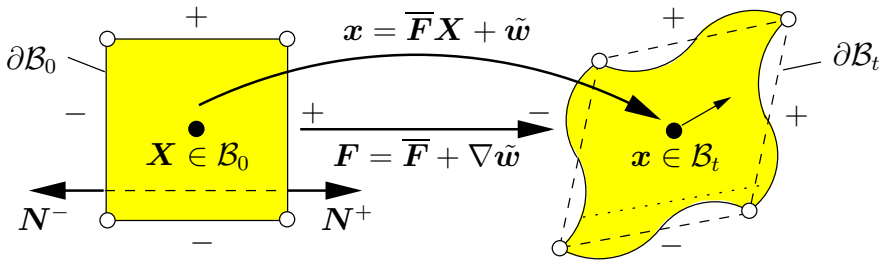

Figure 7.3: Deformation of the RVE $\mathcal{B}_0$ under consideration of periodic boundary conditions, adapted from Schröder [191].

In Figure 7.3 the application of periodic boundary condition to the RVE is shown, where the boundary $\partial\mathcal{B}$ is divided in $\partial\mathcal{B}^+$ and $\boldsymbol{P}^-$. Then it can be shown, that the approach

$$\boldsymbol{x}=\overline{\boldsymbol{F}}\boldsymbol{X}+\tilde{\boldsymbol{w}}\quad\text{with}\quad\tilde{\boldsymbol{w}}^+=\tilde{\boldsymbol{w}}^-\quad\text{and}\quad\boldsymbol{t}^+=-\boldsymbol{t}^-\quad\text{on}\quad\partial\mathcal{B}_0 \tag{7.11}$$

satisfy the Hill–condition, where $\tilde{\boldsymbol{w}}$ denotes fluctuations of the displacement field. The side conditions $(7.11)_{2,3}$ are applied to two appropriate points $\boldsymbol{X}^+\in\partial\mathcal{B}^+$ and $\boldsymbol{X}^-\in\partial\mathcal{B}^-$ on the opposite boundaries with the outer normal unit vectors $\boldsymbol{N}^+=-\boldsymbol{N}^-$. Consequently, the microscopic deformation gradient is calculated by

$$\boldsymbol{F}=\mathrm{Grad}\,\boldsymbol{x}=\overline{\boldsymbol{F}}+\mathrm{Grad}\,\tilde{\boldsymbol{w}}=:\overline{\boldsymbol{F}}+\tilde{\boldsymbol{F}}\,. \tag{7.12}$$

In addition to the derivation of the boundary conditions in Schröder [191], we refer to an alternative way in Miehe et al. [150].

Note, that the straightforward extension of the boundary conditions (7.10) leads to the well-known semi-analytical Reuss and Voigt assumptions respectively, see Reuss [178] and Voigt [231]. They represent the lower (Reuss) and upper (Voigt) bound for the overall material stiffness, where the first-mentioned one assumes constant stresses over the RVE and the second one constant deformations. But their character is very rough and does not take into account sufficiently the real structure on the microscale.

Numerical Implementation. For the numerical implementation we need the variational formulation and the approximation for the Finite Element Method. Therefor we follow again the description given by Miehe et al. [150] and Schröder [191]. The Finite Element Method was already introduced in section 3 and consequently we only discuss here the changes regarding the application to the used homogenization scheme.

The variational formulation of the macroscopic boundary value problem (7.2) results to the weak form of equilibrium

$$\overline{G} := \int_{\overline{\mathcal{B}}_0} (\delta\overline{\boldsymbol{F}} : \overline{\boldsymbol{P}} - \delta\overline{\boldsymbol{x}} \cdot \overline{\boldsymbol{f}}) \, \mathrm{d}V - \int_{\partial\overline{\mathcal{B}}_{0t}} \delta\overline{\boldsymbol{x}} \cdot \overline{\boldsymbol{t}} \, \mathrm{d}A = 0 \tag{7.13}$$

with $\delta\overline{\boldsymbol{F}} = \mathrm{Grad}[\delta\overline{\boldsymbol{x}}]$, cf. Equation (3.5). Since this system of equations has a non-linear character an iterative solution scheme is applied and we consider the linear increment

$$\Delta\overline{G} = \int_{\overline{\mathcal{B}}_0} \delta\overline{\boldsymbol{F}} : \overline{\mathbb{A}} : \Delta\overline{\boldsymbol{F}} \, \mathrm{d}V \quad \text{with} \quad \Delta\overline{\boldsymbol{F}} = \mathrm{Grad}[\Delta\overline{\boldsymbol{x}}] \tag{7.14}$$

for the linearization, cf. section 3.4. The definition of the macroscopic modul $\overline{\mathbb{A}} := \partial_{\overline{\boldsymbol{F}}}\overline{\boldsymbol{P}}$ is given by Equation (2.71). Considering a displacement-based Finite Element Method, introduced in section 3.4, we achieve the system of equations

$$\overline{G} + \Delta\overline{G} = \delta\overline{\boldsymbol{D}}^T(\overline{\boldsymbol{K}}\,\Delta\overline{\boldsymbol{D}} + \overline{\boldsymbol{R}}) = 0 \quad \Rightarrow \quad \overline{\boldsymbol{K}}\,\Delta\overline{\boldsymbol{D}} + \overline{\boldsymbol{R}} = \boldsymbol{0} \tag{7.15}$$

which has to be solved iteratively with respect to the global incremental displacement vector $\Delta\overline{\boldsymbol{D}}$. During the solution process of the macroscopic problem the calculation of the macroscopic moduli $\overline{\mathbb{A}}$ becomes the most decisive part. In contrast to the macroscopic stress tensor $\overline{\boldsymbol{P}}$, which can be calculated averaging the stresses on the microscale, the moduli $\overline{\mathbb{A}}$ can not be estimated by this "simple" procedure. In Miehe et al. [150] an attractive way is proposed starting from the local form of material balance of linear momentum (7.5). In the sequel we focus on periodic boundary condition on the microscale and consequently the deformations on the microscale are calculated from $\boldsymbol{x} = \overline{\boldsymbol{F}}\boldsymbol{X} + \tilde{\boldsymbol{w}}$. The application of the variational principles with the test function $\tilde{\boldsymbol{w}}$ and the following linearization leads to

$$G + \Delta G = \int_{\mathcal{B}_0} \delta\tilde{\boldsymbol{F}} : \boldsymbol{P} \, \mathrm{d}V + \int_{\mathcal{B}_0} \delta\tilde{\boldsymbol{F}} : \mathbb{A} : (\Delta\overline{\boldsymbol{F}} + \Delta\tilde{\boldsymbol{F}}) \, \mathrm{d}V = 0 \,, \tag{7.16}$$

with $\delta\tilde{\boldsymbol{F}} = \mathrm{Grad}[\delta\tilde{\boldsymbol{w}}]$ and $\Delta\tilde{\boldsymbol{F}} = \mathrm{Grad}[\Delta\tilde{\boldsymbol{w}}]$. The approximations of the actual fluctuations $\tilde{\boldsymbol{w}}$ and the associated gradients $\tilde{\boldsymbol{F}}$ for a typical element $\mathcal{B}^e$ result in

$$\tilde{\boldsymbol{w}} = \sum_{I=1}^{n_{\mathrm{node}}} N^I(\xi,\eta)\tilde{\boldsymbol{d}}_I \,, \quad \tilde{\boldsymbol{F}} = \boldsymbol{B}\tilde{\boldsymbol{d}} \,, \tag{7.17}$$

where the virtual and incremental counterparts $\delta\tilde{\boldsymbol{w}}$, $\Delta\tilde{\boldsymbol{w}}$ as well as $\delta\tilde{\boldsymbol{F}}$, $\Delta\tilde{\boldsymbol{F}}$ are built analogously. For suitable Ansatz functions $N_I(\xi,\eta)$ and for the so-called B-matrix we refer to section 3.4. Consequently, the discrete representation of the linearized weak form of equilibrium on the microscale reads

$$G + \Delta G = \delta\tilde{\boldsymbol{D}}^T(\boldsymbol{K}\Delta\tilde{\boldsymbol{D}} + \boldsymbol{L}\Delta\overline{\boldsymbol{F}} + \boldsymbol{R}) = 0 \quad \Rightarrow \quad \boldsymbol{K}\Delta\tilde{\boldsymbol{D}} + \boldsymbol{L}\Delta\overline{\boldsymbol{F}} + \boldsymbol{R} = 0 \,. \tag{7.18}$$

Therein the fluctuation matrices and the residual vector

$$\boldsymbol{K} = \mathop{\mathsf{A}}_{e=1}^{n_{\mathrm{ele}}} \int_{\mathcal{B}_0^e} \boldsymbol{B}^T\mathbb{A}\boldsymbol{B} \, \mathrm{d}V \,, \quad \boldsymbol{L} = \mathop{\mathsf{A}}_{e=1}^{n_{\mathrm{ele}}} \int_{\mathcal{B}_0^e} \boldsymbol{B}^T\mathbb{A} \, \mathrm{d}V \,, \quad \boldsymbol{R} = \mathop{\mathsf{A}}_{e=1}^{n_{\mathrm{ele}}} \int_{\mathcal{B}_0^e} \boldsymbol{B}^T\boldsymbol{P} \, \mathrm{d}V \tag{7.19}$$

are used. Now let us considered two steps on the microscale:

i) Since we perform a displacement driven formulation only the fluctuations $\tilde{\boldsymbol{w}}$ are unknown. The macroscopic deformation gradient is provided by the transition "macro→micro" and within the iterations of the microscopic iterative solution scheme it is constant, i. e. $\Delta\overline{\boldsymbol{F}} = 0$ in Equation (7.18). The resulting system

$$\boldsymbol{K}\Delta\tilde{\boldsymbol{D}} + \boldsymbol{R} = 0 \tag{7.20}$$

is solved using a Newton iteration scheme and we get the incremental discrete fluctuations $\Delta\tilde{\boldsymbol{D}}$ in the equilibrium state.

ii) Before the transition "micro→macro" can be done the macroscopic tangent moduli $\overline{\mathbb{A}}$ has to be calculated. Inserting Equation (7.7) into the incremental constitutive relation $\Delta\overline{\boldsymbol{P}} = \overline{\mathbb{A}} : \Delta\overline{\boldsymbol{F}}$ and considering $\boldsymbol{F} = \overline{\boldsymbol{F}} + \tilde{\boldsymbol{F}}$ we obtain

$$\Delta\overline{\boldsymbol{P}} = \frac{1}{V}\int_{\mathcal{B}_0} \Delta\boldsymbol{P}\, \mathrm{d}V = \frac{1}{V}\int_{\mathcal{B}_0} \mathbb{A} : (\Delta\overline{\boldsymbol{F}} + \Delta\tilde{\boldsymbol{F}})\, \mathrm{d}V\ . \tag{7.21}$$

Obviously the crucial part of this relation is the fluctuation term $\Delta\tilde{\boldsymbol{F}}$. On that account we consider again Equation (7.18) but now in the equilibrium state achieved in step i), i. e. $\boldsymbol{R} = 0$. In contrast to step i) $\Delta\overline{\boldsymbol{F}} := \overline{\boldsymbol{F}}_{n+1} - \overline{\boldsymbol{F}}_n$, where n denotes the macroscopic iteration counter. Then we achieve the increment of the fluctuation gradient

$$\Delta\tilde{\boldsymbol{F}} = \boldsymbol{B}\Delta\tilde{\boldsymbol{D}} = -\boldsymbol{B}\boldsymbol{K}^{-1}\boldsymbol{L}\Delta\overline{\boldsymbol{F}}\ , \tag{7.22}$$

using Equation $(7.17)_2$. Combining both latter equations we achieve

$$\Delta\overline{\boldsymbol{P}} = \frac{1}{V}\int_{\mathcal{B}_0} \mathbb{A} : (\Delta\overline{\boldsymbol{F}} - \boldsymbol{B}\boldsymbol{K}^{-1}\boldsymbol{L}\Delta\overline{\boldsymbol{F}})\, \mathrm{d}V \tag{7.23}$$

and with Equation (7.19) the macroscopic moduli can be calculated by

$$\overline{\mathbb{A}} = \frac{1}{V}\int_{\mathcal{B}_0} \mathbb{A}\, \mathrm{d}V - \frac{1}{V}\boldsymbol{L}^T\boldsymbol{K}^{-1}\boldsymbol{L} \tag{7.24}$$

at the macroscopic point $\overline{\boldsymbol{X}} \in \overline{\mathcal{B}_0}$ and time t_{n+1}. The first term denotes the classical Voigt bound and the second additive term represents a softening modulus necessary for the consistent linearization.

The workflow of the numerical implementation of the FE^2-method in a typical finite element is illustrated in Figure 7.4. Thereby in the finite element code the FE^2-environment is called instead of the evaluation a phenomenological material law during the macroscopic iteration process. As an input the macroscopic deformation gradient $\overline{\boldsymbol{F}}$ is submitted, which is calculated from the iterative nodal displacements of the macroscopic element. From this quantity and the microscopic fluctuations $\tilde{\boldsymbol{w}}$, which is restored from the history, the microscopic displacement field is computed. Note, that for every microscopic boundary value problem a separate history field has to be allocated, i. e. the number of macroscopic Gauss points is an indicator of the amount of memory requirements. Afterwards the iterative loop for the solution process on the microscale is entered. Therein a typical iteration scheme of the Finite Element Method is processed: i) assembling of stiffness matrix $\boldsymbol{K}$

and residual vector $\boldsymbol{R}$, ii) computing incremental vector, iii) update of solution vector and iv) convergence check. In the last step it is decided whether a further iteration step is needed ($\|\boldsymbol{R}\| > \text{tol}$) or the criterion is reached ($\|\boldsymbol{R}\| < \text{tol}$). In case of convergence the macroscopic quantities, stress tensor $\overline{\boldsymbol{P}}$ and moduli $\overline{\mathbb{A}}$, can be calculated. Before leaving the FE^2-environment the actual fluctuations $\tilde{\boldsymbol{w}}$ are written to the history. By returning the output quantities $\overline{\boldsymbol{P}}$ and $\overline{\mathbb{A}}$ the stiffness matrix and the residual vector of the calling macroscopic finite element can be computed. Hence the macroscopic boundary value problem can be established by a standard assembling procedure of the element stiffness matrix and residual vector.

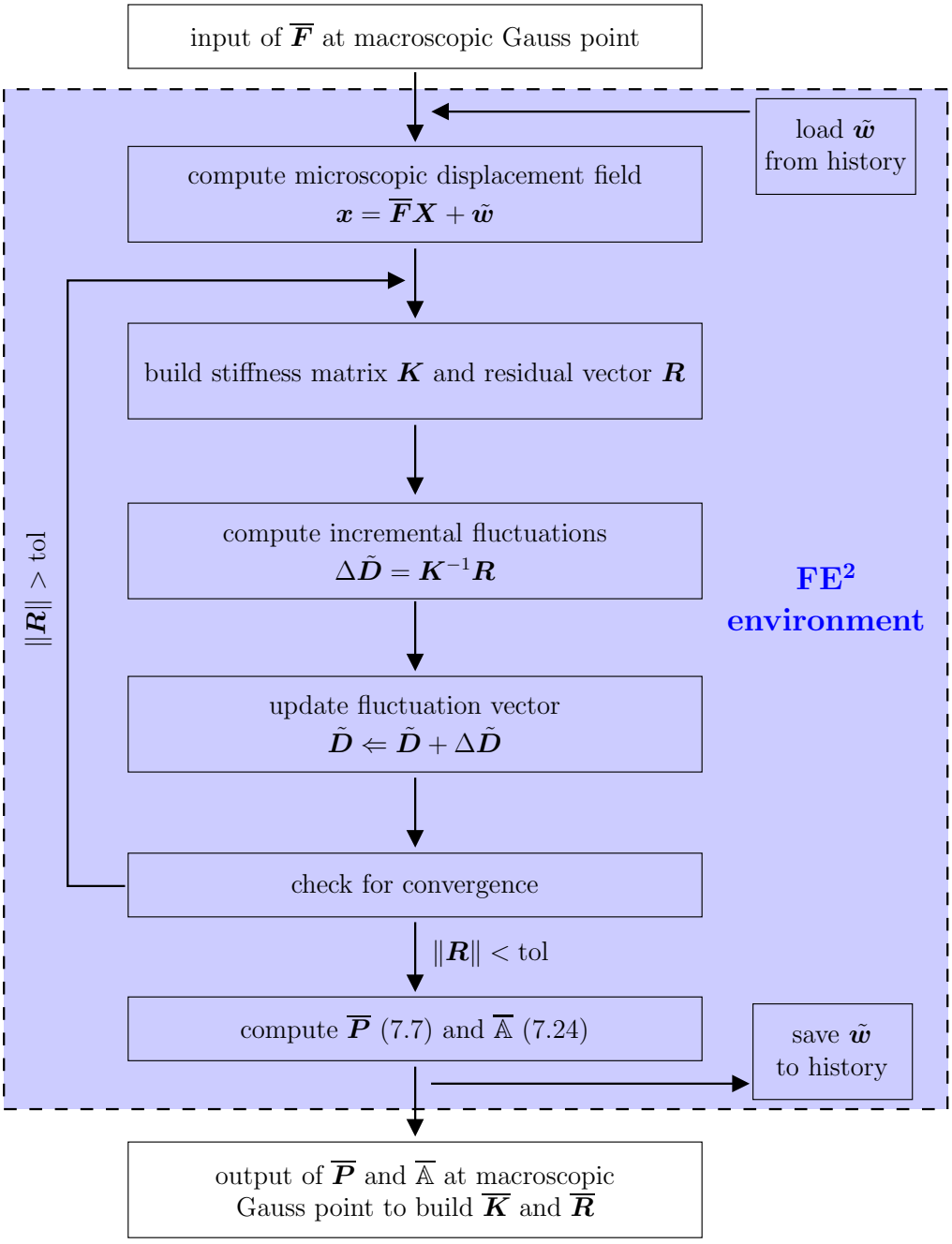

Figure 7.4: Workflow of the FE^2 implementation in a standard finite element code within the Gauss loop.

7.2 Statistically Similar Representative Volume Elements (SSRVEs)

In multiscale modeling the challenging tasks is that smaller scales must be well resolved over the range of the larger ones. Thereby, the estimation and identification of the statistical representative volume element (RVE) is a central task. In the literature several definitions regarding the size of the RVE has been made, cf. Section 7.1.1. In most cases a usual RVE for a random inclusion/matrix-microstructure is determined by the smallest possible sub-domain which is still able to represent the macroscopic material behavior in the context of direct micro-macro approaches. Although these RVEs are the smallest possible sub-structures, they could be too complex for efficient calculations. Thus, the construction of statistically similar RVEs, which are characterized by a lower complexity than the smallest possible random sub-structures, is proposed here for the reduction of computational costs, see also Balzani et al. [12; 13] and Schröder et al. [197].

Considering micro-heterogeneous materials the continuum mechanical properties at the macroscale are characterized by the morphology and by the properties of the particular constituents at the microscale. In this context the basic idea of our construction method is to replace a RVE with an arbitrary complex inclusion morphology by a periodic one composed of optimal periodically arranged unit cells, see Figure 7.5. These unit cells should have similar mechanical properties at the macroscale compared to the (real) microstructure but exhibit a lower complexity. Then the main effort is that in FE^2 calculations only the periodic unit cell needs to be considered as a RVE provided that periodic boundary conditions are applied. Additionally, the lower complexity of the unit cell leads to a lower number of degrees of freedom in the finite element discretization and reduces the computational cost.

7.2.1 Statistical Measures for Microstructural Characterization

For the statistical description of the microstructural morphology we discuss in this section several statistical measures. Starting from basic parameters we extend the list of parameters to statistical measures of higher order like the two-point probability functions, spectral density and the lineal-path function. Thereby, we restrict ourselves to the

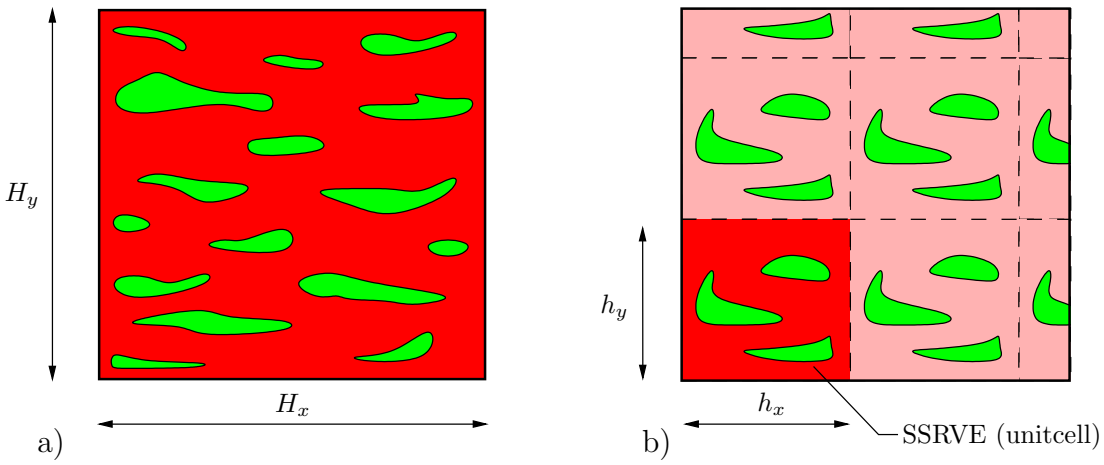

Figure 7.5: Schematic illustration of the basic concept: a) complex (non-periodic) RVE for a two-phase microstructure with arbitrary inclusion morphology and b) simplified periodic microstructure with SSRVE. (Taken from Schröder et al. [197])

mathematical formulation in terms of an ergodic microstructure, which means that all states available to an ensemble of microstructure samples are also available to every sample in the ensemble. An example illustrating the properties of the introduced measures closes the section.

Basic Parameters. In Ohser and Mücklich [168] for basic parameters are proposed for the description of microstructure morphology. The first one is the volume fraction (or phase fraction), defined by

$$\overset{3D^{(i)}}{\mathcal{P}_V} := \frac{V_{(i)}}{V} \quad \text{and} \quad \mathcal{P}_V^{(i)} := \frac{A_{(i)}}{A} \tag{7.25}$$

where $V_{(i)}$ and V denotes the volume of the phase i of the considered material segment, respectively. In the two-dimensional case $(7.25)_2$ we can calculate the phase fraction using the respective areas $A_{(i)}$ and A. It is emphasized that the phase fraction is an essential property which should be matched by all considered RVEs. Further measures given in the aforementioned reference are the specific internal surface density, the specific integral of mean curvature and the specific integral of total curvature. The first mentioned one provides information with respect to the aspect how fine an inclusion phase is distributed. Both the other basic parameters provide in some sense statistical information concerning the degree of curvature of the inclusion phase. Details regarding their calculation can be also found in the given reference.

Although these four parameters are widely used for the description of microstructures they are obviously not able to cover direction-dependent and periodic information since they are scalar-valued. But especially in the case of a macroscopic anisotropic response of the micro-heterogeneous material, which for example is caused by oriented inclusions, we need statistical measures of higher order. This aspect is shown in detail in Balzani et al. [13]. Thus, in the following we introduce several measures of higher order, which are able to gather such morphological information.

Two-Point Probability Functions. As a first statistical measure of higher order we consider the two-point probability function, which is the second order type of the n-point probability functions. These functions were introduced by Brown [37] and important applications with respect to effective elastic moduli are given in e.g. Beran [19]. During the calculation of these functions the indicator function,

$$\chi^{(i)}(\boldsymbol{x}, \alpha) = \begin{cases} 1, & \text{if } \boldsymbol{x} \in D^{(i)}(\alpha), \\ 0, & \text{otherwise}, \end{cases} \tag{7.26}$$

plays a fundamental role, where $D^{(i)}(\alpha)$ denote the domain occupied by the considered phase i in the particular sample α. Note, that $\sum_{i=1}^{n} \chi^{(i)}(\boldsymbol{x}, \alpha) = 1$ must hold for n phases and every point $\boldsymbol{x}$. Here we focus on the description for the inclusion phase of two-phase microstructures. For that case the general n-point probability function, which is also referred to as n-point correlation function, is defined by the ensemble average

$$\mathcal{S}_n^{\mathrm{I}}(\boldsymbol{x}_1, \dots \boldsymbol{x}_n) = \overline{\chi^{\mathrm{I}}(\boldsymbol{x}_1, \alpha)\chi^{\mathrm{I}}(\boldsymbol{x}_2, \alpha) \dots \chi^{\mathrm{I}}(\boldsymbol{x}_n, \alpha)}\,, \tag{7.27}$$

which represents the probability that the points $\boldsymbol{x}_1, \dots \boldsymbol{x}_n$ are located in the inclusion phase. Generally, the larger the set of probability functions taking into account, the more extensive is the description of the microstructure. This is of course impossible to be

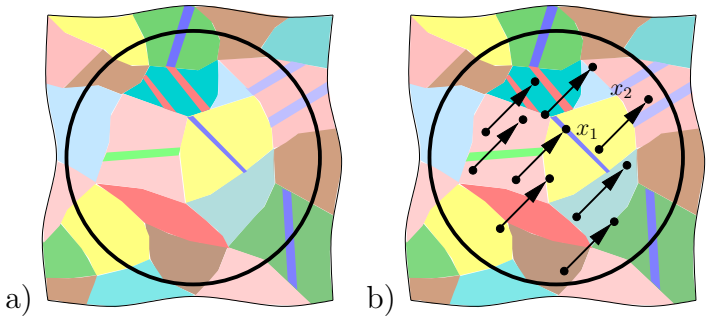

Figure 7.6: a) Multi-phase microstructure and illustration of the and b) of the two-point probability function. (Taken from SCHRÖDER ET AL. [197])

computed practically since it represents an infinite number of measures calculated for an infinite number of multiple positions. Consequently, we focus here on the two-point probability function ($n = 2$) for the statistical description of the inclusion morphology,

When evaluating the two-point probability function for the inclusion phase in a binary image of an ergodic two-phase microstructure with a number of $N = N_x \times N_y$ pixels, the discrete representation

$$\mathcal{S}_2^{\mathrm{I}}(r,s) = \frac{1}{(p_{\mathrm{U}} - p_{\mathrm{L}})(q_{\mathrm{U}} - q_{\mathrm{L}})} \sum_{p=p_{\mathrm{L}}}^{p_{\mathrm{U}}-1} \sum_{q=q_{\mathrm{L}}}^{q_{\mathrm{U}}-1} \chi^{\mathrm{I}}(p,q)\chi^{\mathrm{I}}(p+r,q+s) \tag{7.28}$$

can be applied, where the limits

$$\begin{aligned} p_{\mathrm{L}} &= \max[0,-r] \quad , \quad p_{\mathrm{U}} = \min[N_x, N_x - r] \\ q_{\mathrm{L}} &= \max[0,-s] \quad , \quad q_{\mathrm{U}} = \min[N_y, N_y - s] \end{aligned} \tag{7.29}$$

for the summations are used. For periodic microstructures it is sufficient to consider only the periodic unit cell, then the two-point probability function is computed by

$$\mathcal{S}_2^{\mathrm{I}}(r,s) = \frac{1}{N_x N_y} \sum_{p=1}^{N_x} \sum_{q=1}^{N_y} \chi^{\mathrm{I}}(p,q)\chi^{\mathrm{I}}(p+r,q+s)\,. \tag{7.30}$$

Note, for binarization with a high resolution in width and height the evaluation of the probability function requires a high computational cost. On that account, we introduce in the following paragraph a measure, which covers similar information but exhibits a lower computational cost.

Spectral Density. Here, we describe a statistical measure for the characterization of microstructures, which is strongly correlated to the two-point probability function. The (discrete) spectral density for the inclusion phase of a binary image also enables a statistical description of the morphology of a microstructure. For the calculation of the spectral density we consider the indicator function for the inclusion phase I following the definition Equation (7.26) and compute the (discrete) Fourier transform

$$\mathcal{F}^{\mathrm{I}}(r,s) = \sum_{p=1}^{N_x} \sum_{q=1}^{N_y} \exp\left(\frac{2\,\mathrm{i}\,\pi\,r\,p}{N_x}\right) \exp\left(\frac{2\,\mathrm{i}\,\pi\,s\,q}{N_y}\right) \chi^{\mathrm{I}}(p,q)\,. \tag{7.31}$$

The variables N_x and N_y describe the width and height of the considered binary image. Then the discrete spectral density is computed by the multiplication of the discrete Fourier-transform with its conjugate complex

$$\mathcal{P}_{SD}(r,s) := \frac{1}{2\pi\, N_x\, N_y} \left|\mathcal{F}(r,s)\right|^2 . \tag{7.32}$$

As previously mentioned, the strong correlation with the two-point probability function exists, since it can also be computed from the Fourier transform

$$\mathcal{S}_2^{\mathrm{I}}(r,s) = \frac{1}{N_x\, N_y} (\mathcal{F}^{\mathrm{I}})^{-1}[\mathcal{F}^{\mathrm{I}}[\chi^{\mathrm{I}}(r,s)]\overline{\mathcal{F}^{\mathrm{I}}[\chi^{\mathrm{I}}(r,s,\alpha)]}] , \tag{7.33}$$

cf. Zeman [257]. Herein, $\mathcal{F}^{\mathrm{I}}$ and $(\mathcal{F}^{\mathrm{I}})^{-1}$ denote the discrete- and the inverse discrete Fourier transform following Equation (7.31). Consequently, the spectral density covers information concerning the periodicity of a given microstructure as well as contains information associated to the two-point probability function. At once, there exist a variety of efficient algorithms for the computation of the discrete Fourier transform, see e. g. the "Fastest Fourier Transform in the West" (FFTW) library by Frigo and Johnson [75]. Based on these advantages the spectral density may be of particular interest when the challenge is to simplify a (in general non-periodic) real microstructure by a periodic one.

Lineal-Path Function. In Lu and Torquato [140] another statistical measure is proposed for the characterization of microstructures. It also exhibits a higher order compared to the basic parameters but a similar one compared to the two-point probability function and the spectral density. The main feature of this measure is the description of the probability that a complete line segment $\overrightarrow{\boldsymbol{x}_1\boldsymbol{x}_2}$ is located in the same phase. This is a rather practicable measure since its computation can be performed in an efficient way. For its mathematical description regarding the morphology of the inclusion I, we consider the modified indicator function

$$\chi^{\mathrm{I}}(\overrightarrow{\boldsymbol{x}_1\boldsymbol{x}_2},\alpha) = \begin{cases} 1, & \text{if } \overrightarrow{\boldsymbol{x}_1\boldsymbol{x}_2} \in D^{\mathrm{I}}(\alpha), \\ 0, & \text{otherwise}, \end{cases} \tag{7.34}$$

simply checking if a whole line segment is located in the domain D^{I} of the inclusion phase. Then the general definition of a lineal-path function demands the computation of the ensemble average and we get the definition

$$\mathcal{P}_{\mathrm{LP}}^{\mathrm{I}}(\overrightarrow{\boldsymbol{x}_1\boldsymbol{x}_2}) = \overline{\chi^{\mathrm{I}}(\overrightarrow{\boldsymbol{x}_1\boldsymbol{x}_2},\alpha)} , \tag{7.35}$$

see the illustration shown in 7.7a,b.

Considering an ergodic microstructure we only need to analyze one representative sample α and together with the discrete representation (binary image) of the microstructure the associated lineal-path function is defined by

$$\mathcal{P}_{\mathrm{LP}}^{\mathrm{I}}(r,s) = \frac{1}{(p_{\mathrm{U}}-p_{\mathrm{L}})(q_{\mathrm{U}}-q_{\mathrm{L}})} \sum_{p=p_{\mathrm{L}}}^{p_{\mathrm{U}}-1} \sum_{q=q_{\mathrm{L}}}^{q_{\mathrm{U}}-1} \chi^{\mathrm{I}}(\tilde{\boldsymbol{y}}) \tag{7.36}$$

with the difference vector $\tilde{\boldsymbol{y}} = [p+r, q+s]^T$ and the lower and upper limits for the summations

$$\begin{aligned} p_{\mathrm{L}} &= \max[0,-r] \quad , \quad p_{\mathrm{U}} = \min[N_x, N_x - r] \\ q_{\mathrm{L}} &= \max[0,-s] \quad , \quad q_{\mathrm{U}} = \min[N_y, N_y - s] . \end{aligned} \tag{7.37}$$

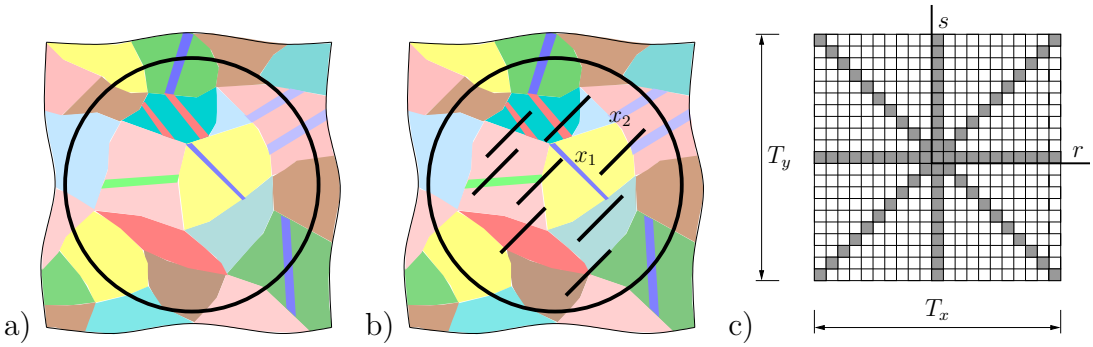

Figure 7.7: a) Multi-phase microstructure, b) illustration of some representative lineal path elements and c) a typical template for the analyzed line directions $\beta_L = 0°, 45°, 90°, 135°$. (Taken from Schröder et al. [197])

For periodic unit cells the lineal-path function is computed by

$$\mathcal{P}^{\mathrm{I}}_{\mathrm{LP}}(r,s) = \frac{1}{N_x N_y} \sum_{p=1}^{N_x} \sum_{q=1}^{N_y} \chi^{\mathrm{I}}(\tilde{\boldsymbol{y}}) \,. \tag{7.38}$$

Efficient procedures for the calculation of the lineal-path function can be obtained by defining suitable templates, cf. Zeman [257]. Such a template consists of $T_x \times T_y$ pixels, wherein each pixel characterized by the coordinate pair (r,s) has either the value one or zero. The value one means that the associated line segment defined by the difference vector which ends in this coordinate pair (r,s) is part of the analysis. One example for a template is shown in Figure 7.7c, where only the line segments in the horizontal-, vertical- and diagonal directions are analyzed. Then each line segment defined by the template is compared with the original image for each admissible position (p,q) to compute the value of the associated indicator function. For the case under investigation here, the lineal-path function is invariant with respect to reflections of line segments. Hence, the lower half of the template shown in Figure 7.7c is unnecessary. For binary images each line segment to be analyzed has to be defined in an integer manner, which means that by given difference vector $\boldsymbol{y}$ a unique discrete line segment has to be constructed in the template. For this purpose the classical Bresenham algorithm (Bresenham [34]) can be used. If the complete lineal-path function has to be computed, the template needs to have the double size of the original binary image, e.g.

$$T_x = 2\,N_x - 1 \quad , \quad T_y = N_y \,, \tag{7.39}$$

and each pixel in the template needs to have the value one. Then all possible line-segments are analyzed. For the example shown in Figure 7.7c the original binary image has to have a minimal size of 11×11 pixels. Of course in most cases it is not necessary to compute a complete lineal-path function. The first possibility to improve the efficiency of the algorithm is to reduce the size of the template according to a characteristic maximal inclusion size. A second possibility is to reduce the number of analyzed line segments; in most cases it will be sufficient to analyze only a certain set of line orientations.

Example of Different Statistical Measures. To provide an illustration of the different statistical measures we now consider the oversimplified academic microstructure whose binary image is shown in Figure 7.8a. The size of the image is 10×10 pixels and the phase fraction of the inclusion phase is $\mathcal{P}_V = 0.13$.

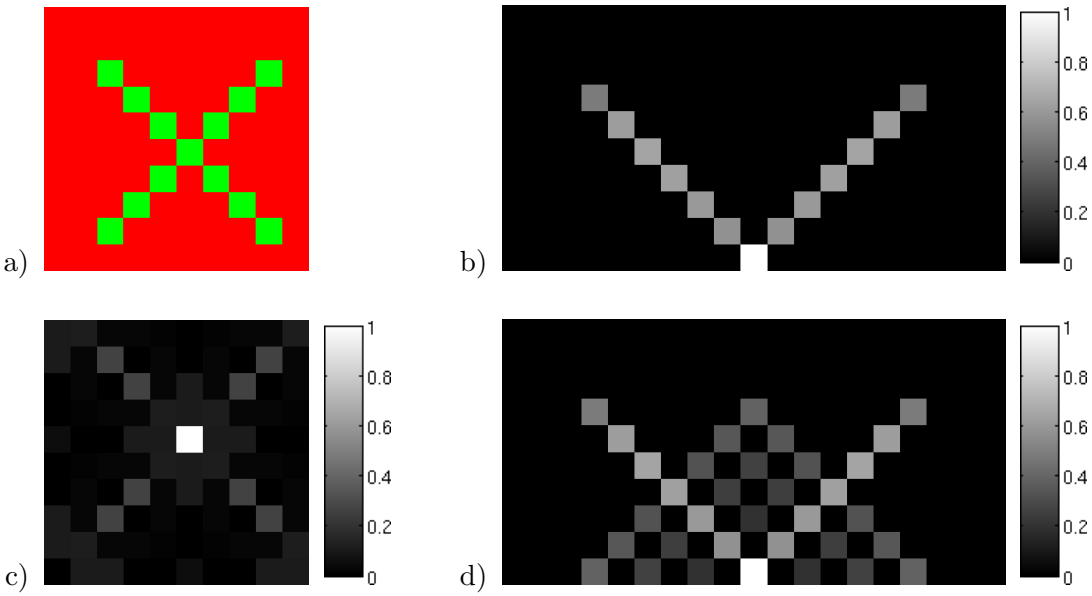

Figure 7.8: Example of statistical measures describing the inclusion phase morphology: a) Binary image and graphical illustrations of the normalized b) lineal-path function, c) spectral density and d) two-point probability function. For the lineal-path and the two-point probability function the absolute maximum value is located in the center and equal to the phase fraction $\mathcal{P}_V = 0.13$.

Then the spectral density, the complete two-point probability function and the complete lineal-path function are computed, which are shown in their normalized representations in Figure 7.8c,d,b. Please note that the horizontal and vertical axis in the pictures are associated with the index m and k. The origin of the coordinate system is located in the lower left corner for the spectral density and in the lower center for the two-point probability and lineal-path function. When analyzing the result for the lineal-path function (Figure 7.8b) we observe non-vanishing entries only in diagonal direction. This is obvious since connected line segments with a length larger than 2 pixels are only found in the original image (Figure 7.8a) in diagonal direction as well. When comparing this with the two-point probability function we observe that further non-vanishing entries also exist in directions differing from the diagonal one. This directly results from the fact that repeating pixels in different directions exist. For instance, the upper and lower two pixels of the inclusion in Figure 7.8 are the only two pairs of pixels that have a horizontal distance of 6 pixels. This oriented distance ($m = 6, k = 0$) is able to be detected a number of $4 \times 10 = 40$ times, hence, the probability of finding this distance in a microstructure of the dimension 10×10 pixels is $\mathcal{S}_2^{\mathrm{I}}(6,0) = 2/40 = 0.05$. It is noticed that the absolute maximum value computed for the two-point probability and the lineal-path function is always located in the origin of the graphical illustration and is equal to the phase fraction (here: $\mathcal{P}_V = 0.13$).

7.2.2 Construction Principles

The method for the generation of statistically similar representative volume elements (SSRVEs) is substantiated on the approach for the construction of periodic structures proposed in Povirk [175]. There, the position of circular inclusions with constant and equal diameters is optimized by the minimization of a least-square functional taking into

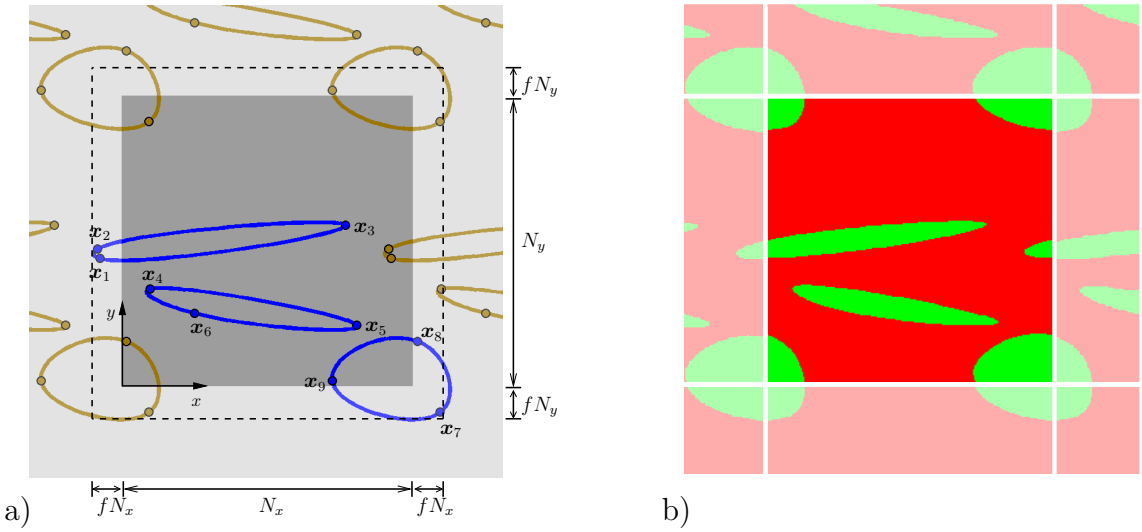

Figure 7.9: Periodic unit cell construction based on splines: a) required splines with the sampling points and b) resulting binary SSRVE image (center) with the periodic expansion (brightened). (Taken from Schröder et al. [197])

account the side condition that the spectral density of the periodic RVE should be as similar as possible to the one of the non-periodic microstructure. Motivated by this approach we consider the objective function

$$\mathcal{L}(\boldsymbol{\gamma}) = \sum_{L=1}^{n_{sm}} \omega_i \, \mathcal{L}_{\mathrm{SM}}^{(L)}(\boldsymbol{\gamma}) \quad \rightarrow \quad \min , \tag{7.40}$$

cf. Balzani et al. [12], which has to be minimized. A number of n_{sm} different statistical measures $\mathcal{L}_{\mathrm{SM}}^{(L)}$ describing the inclusion morphology is taken into account by incorporating suitable least-square functionals. These functionals take into account the squares of differences of the individual statistical measures $\mathcal{P}_{\mathrm{SM}}^{\mathrm{real}}$ and $\mathcal{P}_{\mathrm{SM}}^{\mathrm{SSRVE}}(\boldsymbol{\gamma})$ computed for a real (complex) microstructure, called target structure in the sequel, and for the SSRVE. The weighting factor ω levels the influence of the individual measures. Due to the discrete character of the statistical measures entering the minimization problem Equation (7.40), the energy surface is not smooth and therefore, no gradient-based optimization method can be applied. Therefore, in section 7.2.3 an alternative optimization method is proposed. For the description of a general inclusion phase morphology in the SSRVE we assume a suitable two-dimensional parameterization controlled by the vector $\boldsymbol{\gamma}$. In this work splines are used for the parameterization, thus, the coordinates of the sampling points enter the general vector $\boldsymbol{\gamma}$

$$\boldsymbol{\gamma} := [\hat{x}_1 \ , \ \hat{y}_1 \ , \ \hat{x}_2 \ , \ \hat{y}_2 \ , \ \ldots \ , \ \hat{x}_{n_{\mathrm{sp}}} \ , \ \hat{y}_{n_{\mathrm{sp}}}]^T \tag{7.41}$$

with the number of sampling points n_{sp}.

Due to the fact that periodic boundary conditions have to be applied the inclusions have to be constructed appropriately. For this purpose the construction procedure is as follows: first, the number of inclusions and the number of sampling points is defined. Then, random positions of the sampling points are computed in a specified space $[(N_x + 2\,f\,N_x) \times (N_y + 2\,f\,N_y)]$ where a certain spatial overlap factor f with respect to the SSRVE space of interest $(N_x \times N_y)$ is taken into account. This means that

the sampling point coordinates have to match

$$x_i \in [-fN_x, N_x + fN_x]\,, \quad y_i \in [-fN_y, N_y + fN_y] \quad \text{for} \quad i = 1 \ldots n_{\text{sp}}\,. \tag{7.42}$$

Here, we set the overlap factor to $f = 0.1$ and consider a SSRVE resolution of $N_x \times N_y = 60 \times 60$ pixels. The resulting splines are shown exemplarily in Figure 7.9a as dark (blue) splines. Then, the SSRVE is periodically expanded by inserting the generated splines at the periodic positions, cf. the lighter (brown) splines in Figure 7.9a. In order to preclude inclusions that intersect with themselves or with others, this construction procedure is repeated until a permitted unit cell is obtained and a resulting binary image of the SSRVE as shown in Figure 7.9b is constructed.

If intersections of splines with themselves are not excluded, an unreasonable inclusion morphology leading to degenerated finite-element discretizations is generated if one spline consists of more than three sampling points. Note, that convex inclusions are obtained if a spline has less than four sampling points.

7.2.3 Optimization Method

For an illustration of the main characteristics of the minimization problem (7.40) a simple test example is given in Balzani et al. [12], where the volume fraction and the spectral density is taken into account as the statistical measure. Therein an assumed real two-dimensional microstructure with one inclusion is considered as a target structure, which is generated by randomly distributing four sampling points, see Figure 7.10a.. Then a SSRVE is constructed by one spline with four sampling points as well, where three sampling points are set to the values used for the generation of the target structure.

Hence, we end up in a problem where only one sampling point is free to move in the optimization process and one is able to visually analyze the objective function plotted over the degrees of freedom. The target structure should be recovered by minimizing the objective function $\mathcal{L}$. In this example we start from the microstructure depicted in Figure 7.10b, where we fix three sampling points and let only one point free (point A), so we obtain two degrees of freedom. The objective function is plotted over the degrees of freedom, see Figure 7.11, and we notice by zooming into the minimum that the objective function is far away from being smooth.

Apparently, the computation of the discrete spectral density and the volume fraction takes into account a specific discrete image resolution. Hence, this leads to a non-smooth func-

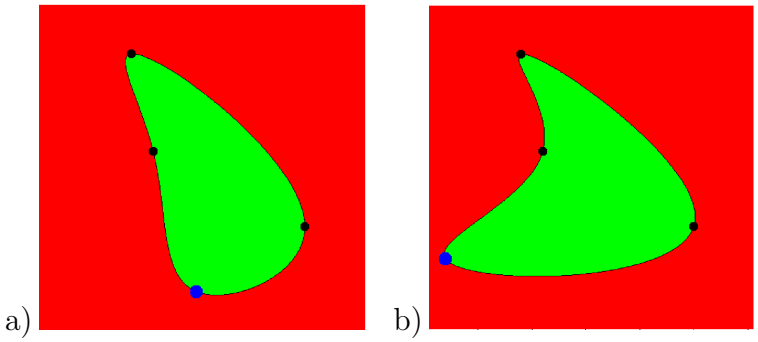

Figure 7.10: Simple test example: a) generated target structure and b) initial configuration in the optimization process for finding the SSRVE. (Balzani et al. [12])

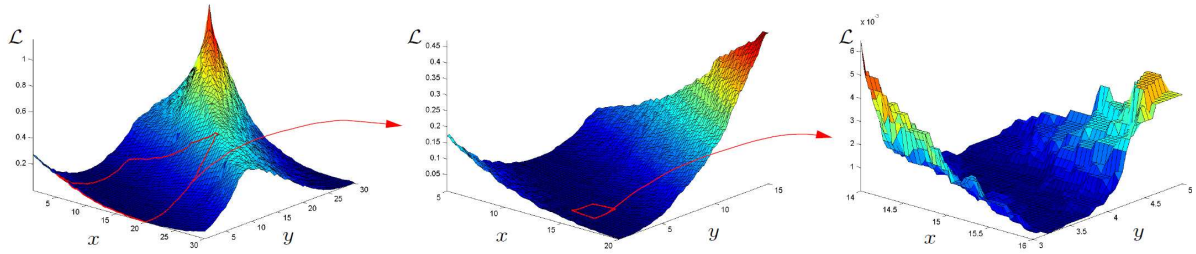

Figure 7.11: Visualization of the objective function for a simple test example with two magnifications of the minimum area. (Balzani et al. [12])

tion and precludes the application of standard gradient-based optimization procedures. This is a rather structural problem since most statistical measures are based on a discrete image characterized by a given resolution. In addition to this, the problem is non-convex and thus, we have to deal with many local minima when increasing the number of degrees of freedom.

To overcome the difficulties arising from the particular minimization problem in Balzani et al. [12] a moving frame algorithm is proposed. For this purpose random initial sampling point coordinates $x_{0,k}, y_{0,k}$ are generated first, which direct to the sampling point $M_{0,k}$. Then further n_{mov} random points $M_{j,k}(x_{j,k}, y_{j,k})$ with $j = 1 \dots n_{\text{mov}}$ in a frame of the size $2a \times 2a$ are generated, see Figure 7.12a, and the objective function is evaluated for each generated sampling point.

Then the initial sampling point moves to the sampling point $M_{0,k+1}$ defined by the lowest value of $\mathcal{L}$ and the iteration counter is initialized $l_{\text{iter}} = 0$, see Figure 7.12b . If the frame center remains unaltered, i.e. no lower value of $\mathcal{L}$ is found in this iteration step ($M_{0,k+1} = M_{0,k+2}$), we set $l_{\text{iter}} = l_{\text{iter}} + 1$, see Figure 7.12c. If $l_{\text{iter}} = l_{\text{itermax}}$ the stopping criterion is reached and the actual minimal value of $\mathcal{L}$ is interpreted as local minimum associated to the starting value. In addition, this procedure is repeated a predefined number of cycles with different random starting values. If a high fraction of minimizers of the individual optimization cycles leads to similar sampling point coordinates, then we choose this result as an appropriate solution. In order to improve the method the frame size a can be modified depending on the difference $|\boldsymbol{d}|$ and l_{iter}. Furthermore, a combination with a line-search algorithm is implemented, where $\mathcal{L}$ is also evaluated at a

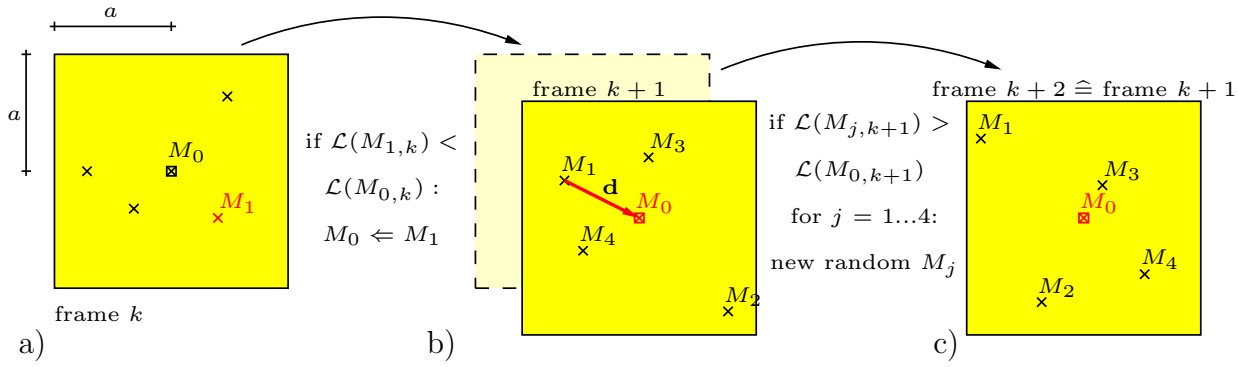

Figure 7.12: Schematic illustration of the moving frame algorithm. Optimization frames a) k, b) $k+1$ and c) $k+2$. (Balzani et al. [12])

number of n_{line} points interconnecting the frame center point M_0 with the random points $M_1, M_2, \ldots M_{n_{\text{mov}}}$.

The moving-frame algorithm used here is rather a statistical method for finding the minima. Further possibilities for the solution of non-smooth optimization problems can be found in e.g. Kolda et al. [129], Conn et al. [52] and Mäkelä and Neittaanmäki [141]. A possible improvement of the minimization algorithm may be obtained by filtering out structural oscillations associated to the non-smoothness in order to obtain at least locally smooth objective function approximations. In this case bundle methods where generalized gradient information is exploited (e.g. Schramm and Zowe [190]) could be used or the Nelder-Mead method (Nelder and Mead [159]), if only function evaluations are desirable.

7.3 Analysis of Combinations of Statistical Measures

(Subsequent results were first published in Schröder et al. [197].)

After introducing the framework for the construction of SSRVEs for two-phase microstructures we study in this section the applicability of different statistical measures describing the microstructural morphology. In Balzani et al. [13] the application of the basic parameters like specific internal surface and the specific integral of mean curvature are analyzed in addition to the spectral density and the overall important volume fraction. However, no improvement was observed when extending the objective function taking into account the spectral density and the volume fraction by one of the other basic parameters. In fact, even worse results were obtained when using the specific internal surface. So other statistical measures have to be taken into account for improving the results.

As already mentioned in section 7.2.1, for an nearly exact description of the microstructure one would need to take into account a large set of n-point probability functions. But even if "only" a three-point probability function is considered as an additional measure, then the procedure will likewise be very expensive to be computed since the three-point probability function has a much higher dimension of solution space than the two-point probability function. Therefore, the lineal-path function may be a further reasonable statistical measure since it has the same solution space as the two-point probability function and it covers further information with respect to the type of connectivity of points and therefore the connectedness of inclusions. This information is rather not covered by the spectral density. Conversely, information regarding relative distances between the inclusions can not be represented by the lineal-path function, but is one of the main features of the spectral density. In total, three different statistical measures are considered in this thesis leading to the three individual least-square functionals:

$$\begin{aligned}
\mathcal{L}_{\text{V}}(\boldsymbol{\gamma}) &:= \left(1 - \frac{\mathcal{P}_{\text{V}}^{\text{SSRVE}}(\boldsymbol{\gamma})}{\mathcal{P}_{\text{V}}^{\text{real}}}\right)^2 \quad , \\
\mathcal{L}_{\text{SD}}(\boldsymbol{\gamma}) &:= \frac{1}{N_x\, N_y} \sum_{m=1}^{N_x} \sum_{k=1}^{N_y} \left(\mathcal{P}_{\text{SD}}^{\text{real}}(m,k) - \mathcal{P}_{\text{SD}}^{\text{SSRVE}}(m,k,\boldsymbol{\gamma})\right)^2 , \\
\mathcal{L}_{\text{LP}}(\boldsymbol{\gamma}) &:= \frac{1}{N_x\, N_y} \sum_{m=1}^{N_x} \sum_{k=1}^{N_y} \left(\mathcal{P}_{\text{LP}}^{\text{real}}(m,k) - \mathcal{P}_{\text{LP}}^{\text{SSRVE}}(m,k,\boldsymbol{\gamma})\right)^2 ,
\end{aligned} \tag{7.43}$$

where the definitions of the statistical measures are given in section 7.2.1.

Note, that for the following analysis we use different software environments. The construction of the SSRVEs including the optimization is fully realized in MATLAB, whereby build-in functions are used as well as subroutines written by ourselves. The discretization of the resulting SSRVEs are performed by a combination of MATLAB and ANSYS[7.)]. Thereby in MATLAB the segmentation of the binary image is done including the semi-automatic mesh generation using the preprocessor of ANSYS and the converting of the resulting mesh data. For the application of periodic boundary condition to the resulting discretization we force a special generation of the finite element node at the outer boundaries. Therefore, the opposite outer boundaries are divided by the same arrangement of the nodes, respectively. Afterwards the FE^2-simulation is computed using FEAP including a self-written micro-macro transition environment. Thereby, the solution of the microscopic boundary value problem is achieved by the application of the direct solver SuperLU (Vers. 3.1), for details see Demmel et al. [59].

7.3.1 Setup of Analysis

In order to check the performance of the proposed method and to analyze the influence of the individual statistical measures, SSRVEs are constructed approximating a virtually generated target microstructure. Then, the mechanical response of the SSRVEs is compared in simple virtual experiments with the response of the target structure. To provide quantitative estimations for the accuracy of the individual considered least-square functionals, a mechanical error analysis is performed.

(Virtual) Target Structure. In addition to the general applicability of our method to two-phase microstructures we want to analyze the capturing feature of the SSRVEs with respect to the anisotropic behavior of the considered target structure. In order to provide a target structure with a pronounced anisotropy we generate a virtual structure. Thus, the virtual target microstructure is obtained by the Boolean method, where a certain two-dimensional space of interest is first completely filled with the inclusion phase. Then, ellipsoids with the semi-axis r_x and r_y of predefined aspect ratios, here $r_x/r_y = 14.3$, and random semi-axis $r_x \in [3, 6]\,\mu\text{m}$ are randomly placed in the space of interest. This process is stopped if a certain phase fraction of $\mathcal{P}_\text{V} = 0.1872$ is reached. The resulting

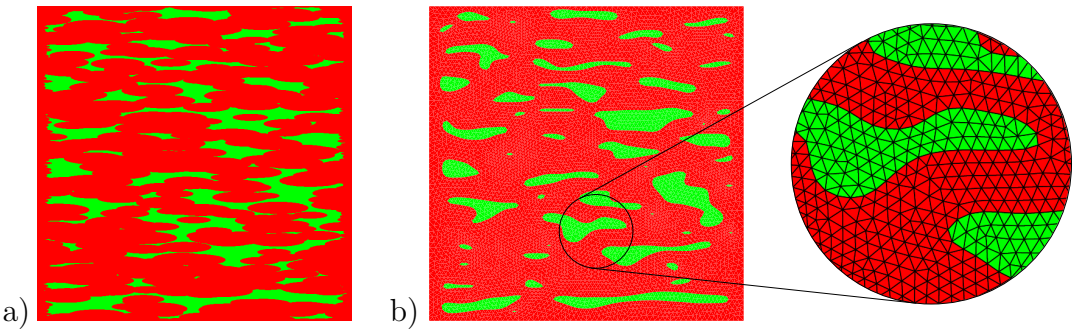

Figure 7.13: Steps for the generation of the target structure: a) result of the Boolean method and b) smoothened inclusion phase boundaries with a section of the FE-discretization. (Taken from Schröder et al. [197])

[7.)] ANSYS is registered trademark of ANSYS, Inc., see `www.ansys.com`

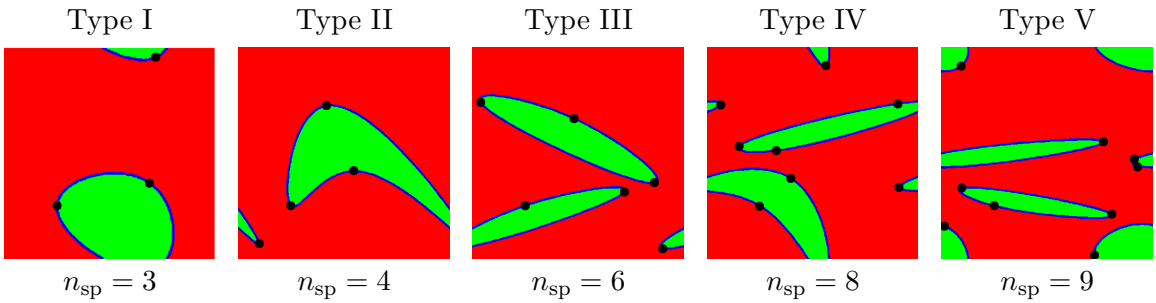

Figure 7.14: Illustration of the five considered SSRVE types, where n_{sp} denotes the number of sampling points. The dots mark the sampling points of the splines. (Schröder et al. [197])

binary image is shown in Figure 7.13a. Subsequently, the boundaries of the inclusion phase are smoothened and a finite-element discretization is automatically generated, see Figure 7.13b. Here, 14,982 triangular Finite Elements with quadratic ansatz functions for the displacements are taken into account.

SSRVE Types. One main goal is to construct suitable SSRVEs that are characterized by a much less complexity than the target structure and that lead to a very similar mechanical response. For the construction of the SSRVEs five different types are considered: Type I takes into account one inclusion with three sampling points, Type II one inclusion with four sampling points, Type III two inclusions with three sampling points each, Type IV two inclusions with four sampling points each and Type V three inclusions with three sampling points each, cf. Figure 7.14. Please note, that splines with three sampling points lead to convex inclusion morphologies.

Virtual Mechanical Experiments. For the mechanical error analysis three different simple macroscopic virtual experiments are considered: horizontal tension, vertical tension and simple shear, cf. Figure 7.15a-c. FE^2-simulations taking into account the target structure at the microscale are compared with FE^2-calculations focusing on the constructed SSRVEs. For this purpose microscopic boundary value problems where a discretization by triangular Finite Elements with quadratic ansatz functions for the displacements are considered. Furthermore, plain stress conditions and periodic boundary conditions are applied. The individual constituents at the microscale are modeled by the simple J_2-plasticity model using a von Mises type hardening law, which is described in section 6.3. The material parameters as given in Table 7.1 are used. In Figure 7.15d the macroscopic mechanical response of the three virtual experiments using the target structure at the microscale is shown. Especially, the results of the tension tests exhibit the macroscopic anisotropic behavior of the target structure, which we force during the generation of the target structure considering the predefined aspect ratio of the ellipsoids.

As comparative mechanical measures we consider the relative errors r_x, r_y and r_{xy} defined

Table 7.1: Material parameters of the single phases

phase	λ [MPa]	μ [MPa]	y_0 [MPa]	y_∞ [MPa]	η [-]	h [-]
matrix	118,846.2	79,230.77	260.0	580.0	9.0	70.0
inclusion	118,846.2	79,230.77	1000.0	2750.0	35.0	10.0

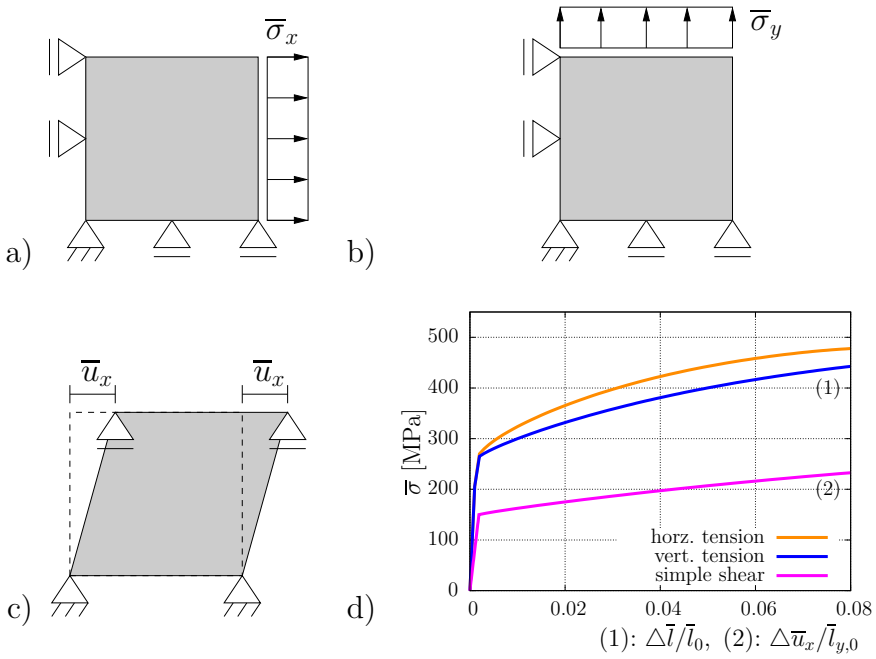

Figure 7.15: Virtual macroscopic experiments: a) horizontal tension, b) vertical tension and c) simple shear. d) Mechanical response using the target structure (Figure 7.13) and periodic boundary conditions at the microscale: Cauchy stresses versus strains.

as the deviation of the resulting macroscopic SSRVE stress response from the target structure response at each evaluation point i for the three virtual experiments:

$$r_x^{(i)} = \frac{\overline{\sigma}_{x,i}^{\text{real}} - \overline{\sigma}_{x,i}^{\text{SSRVE}}}{\overline{\sigma}_{x,i}^{\text{real}}}, \qquad r_y^{(i)} = \frac{\overline{\sigma}_{y,i}^{\text{real}} - \overline{\sigma}_{y,i}^{\text{SSRVE}}}{\overline{\sigma}_{y,i}^{\text{real}}}, \qquad r_{xy}^{(i)} = \frac{\overline{\sigma}_{xy,i}^{\text{real}} - \overline{\sigma}_{xy,i}^{\text{SSRVE}}}{\overline{\sigma}_{xy,i}^{\text{real}}}, \tag{7.44}$$

where only values with non-vanishing denominator are taken into account. In addition to that, the average errors for each experiment

$$\widetilde{r}_j = \sqrt{\frac{1}{n_{\text{ep}}} \sum_{i=1}^{n_{\text{ep}}} [r_j^{(i)}]^2} \quad \text{with} \quad r_j^{(i)} := r\left(\tfrac{i}{n} \triangle l_{\max}/l_0\right) \quad \text{and} \quad j = x, y, xy \tag{7.45}$$

and the overall comparative measure

$$\widetilde{r}_{\varnothing} = \sqrt{\tfrac{1}{3}(\widetilde{r}_x^2 + \widetilde{r}_y^2 + \widetilde{r}_{xy}^2)} \tag{7.46}$$

are taken into account for quantitative statements with respect to the performance of the individual SSRVEs. The total number of evaluation points i is denoted by n_{ep}.

Remarks Regarding the Limitations. In the considered boundary value problems we enforce plain stress conditions at each point of the microstructure. Furthermore, we assume that the individual phases can be described within the framework of the isotropic J_2-plasticity theory. Both assumptions are only approximations of the real material behavior. In a variety of micro-heterogeneous problems the three-dimensional nature of the inclusion morphology must be taken into account in order to capture the realistic macroscopic material behavior. However, from our experience with the analysis of thin steel plates the crucial plain stress assumption often leads to appropriate results when comparing with experimental data.

7.3.2 Optimization Results and Mechanical Verification

In the following subsections we present the resulting SSRVEs of the optimization based on two different objective functions. The first case represents the combination of the least-square functionals of the volume fraction and the spectral density. In addition to that the second case takes into account additionally the appropriated functional regarding the lineal-path function. The scenario without the lineal-path function should represent the results, which were already obtained in preceding investigations, Balzani et al. [12; 13]). Therein we state, that the spectral density seems to be a suitable measure covering information concerning as well as macroscopic anisotropy. Also in comparison with the results of the second objective function it will show in which manner the application of the lineal-path function improves the results.

Volume Fraction and Spectral Density. The first analysis considers the spectral density as the statistical measure describing the inclusion morphology, because it provides information regarding periodicity and the relative distances between the individual inclusions. Since also the phase fraction of the inclusions should reflect the one of the target structure, the associated least-square functional is additionally taken into account. This leads to the overall objective function

$$\mathcal{L}_1(\boldsymbol{\gamma}) = \omega_{\mathrm{V}}\, \mathcal{L}_{\mathrm{V}}(\boldsymbol{\gamma}) + \ \omega_{\mathrm{SD}}\, \mathcal{L}_{\mathrm{SD}}(\boldsymbol{\gamma}) \quad \text{with} \quad \omega_{\mathrm{V}} = \omega_{\mathrm{SD}} = 1\,, \tag{7.47}$$

wherein the individual least-square functionals are given by Equations $(7.43)_{1,2}$. The weighting factors ω_{V} and ω_{SD} are set to one. In order to end up in a more efficient optimization procedure a relevant area of the spectral density is defined. For this purpose the complete spectral density of the target structure is computed and normalized before optimization. Since the target structure consists of 200×200 pixels the number of entries

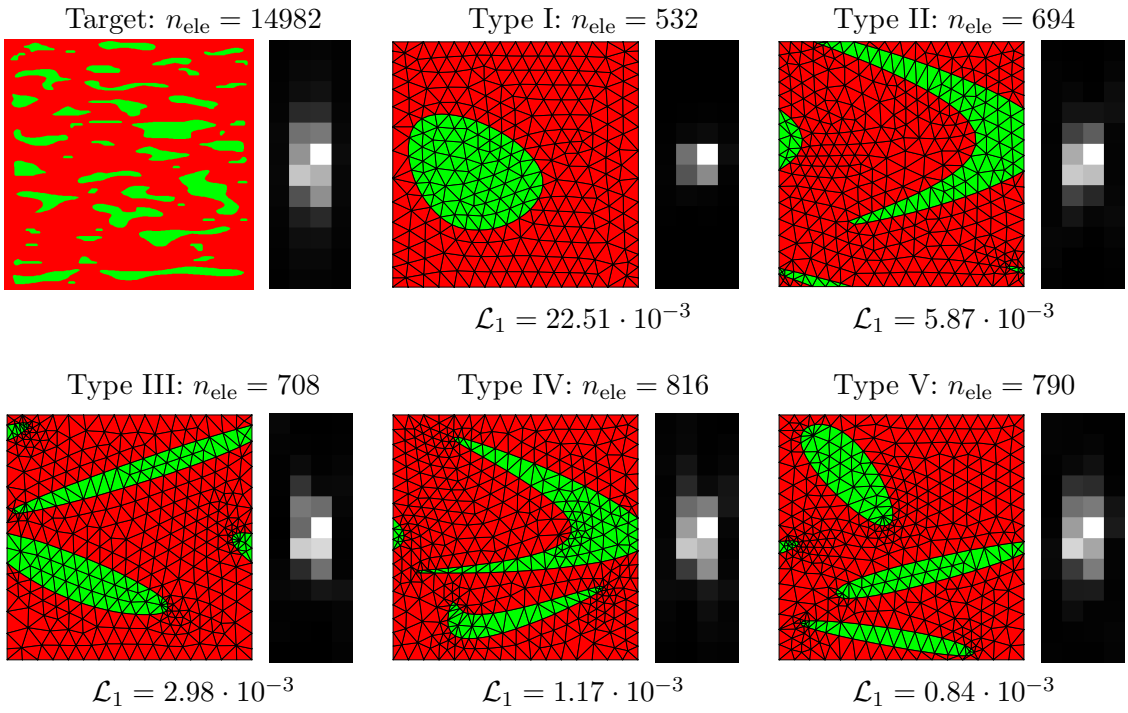

Figure 7.16: Target structure and discretization of SSRVEs with corresponding relevant area of the spectral density resulting from the minimization of $\mathcal{L}_1$. (Schröder et al. [197])

in the complete spectral density is 200×200. Then the spectral density is rebinned to the size 20×20, which seems to be reasonable because the important characteristics of the spectral density are maintained by rebinning. For a further enhancement of the numerical procedure, the minimal rectangular sub-area of the rebinned spectral density is identified, where no entry higher than a predefined threshold value of 0.02 is placed outside of the relevant area. Then only this rebinned relevant area of the spectral density with the size 4×12 enters the least-square functional. Finally, the objective function (7.47) is minimized with respect to the sampling point coordinates of the splines, which are assembled in $\boldsymbol{\gamma}$, by using the moving-frame algorithm introduced in section 7.2.3. The resulting SSRVEs are automatically discretized in terms of the Finite Element Method and the realizations shown in Figure 7.16 are obtained.

It can be observed that the number of finite elements n_{ele}, that is required for a suitable discretization, increases with increasing complexity of the SSRVE. Therefore, it seems that the number of required finite elements serves as some kind of estimation for the complexity of the inclusion morphology. In addition to that, the value of the computed minimum of the objective function is decreasing from $\mathcal{L}_1 = 22.51 \cdot 10^{-3}$ for Type I to $\mathcal{L}_1 = 0.84 \cdot 10^{-3}$ for Type V. This is kind of obvious since an increasing complexity of the inclusion morphology coincides more or less with an increase of the number of sampling points, which liberates the optimization problem given in Equation (7.40). For the visual comparison the rebinned relevant areas of the spectral density are provided on the right hand side of the microstructure images. The spectral density of Type V obviously matches the spectral density of the target structure more accurately than Type I. For the mechanical comparison of the SSRVEs with the target structure the three virtual homogeneous experiments are calculated using the FE^2-scheme and the stress-strain response shown in Figure 7.17 is obtained. There, also the distribution of the relative mechanical error versus the strain is given.

For a better quantitative comparative analysis, the average errors, together with their standard deviation, and the overall mechanical comparative measures are computed, cf. section 7.3.1, and given in Table 7.2. Note that we sort the results in the table primarily with respect to the number of sampling points per inclusion and then taking into account the number of degrees of freedom in the related optimization problem. Since both aspects are accountable for the complexity of the inclusion's geometry it seems to be an obvious arrangement. First, it is observed that the order of magnitude of the least-square function regarding the phase fraction $\mathcal{L}_{\text{V}}$ is twice to four times lower than the one regarding the spectral density $\mathcal{L}_{\text{SD}}$. Since we are interested in SSRVEs where the phase fraction matches very well with the phase fraction of the target structure the choice of $\omega_{\text{V}} = \omega_{\text{SD}} = 1$ seems to be reasonable. Second, it can be observed that with increasing complexity in each category (three and four sampling points based SSRVEs) the overall comparative error decreases in general and Type V turns out to yield the best mechanical correspondence to the response of the target structure. However, when analyzing the individual average errors for the three virtual experiments a relatively high value of $\widetilde{r}_{xy} = 3.08$ is obtained for the simple shear test. Although the other two experiments of SSRVE Type V fit rather well the response of the target structure, the simple shear test is only partly represented accurately. This is also shown by the significantly deviating stress-strain curve shown in Figure 7.17. In turn, the rather simple SSRVE Type I provides the best representation of the simple shear test, but the horizontal tension test is reflected less accurately such that the overall comparative measure is $\widetilde{r}_{\varnothing} = 4.92$.

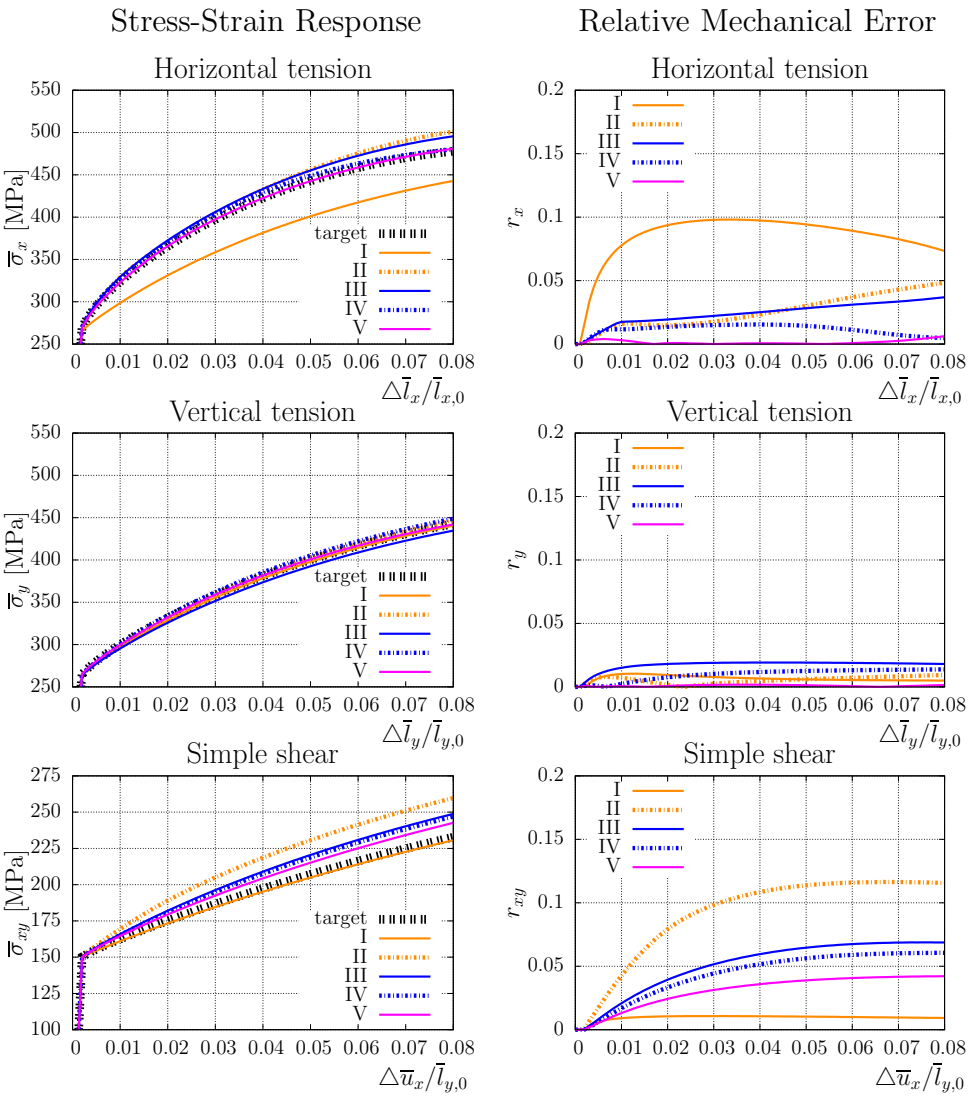

Figure 7.17: Results of the virtual experiments using the discretizations of the SSRVEs (Figure 7.16) based on $\mathcal{L}_1$. On the left hand side the Cauchy stresses are plotted versus strains, the right hand side shows the relative mechanical error. (Schröder et al. [197])

We conclude that possibly not enough statistical information is covered by the statistical measures considered in $\mathcal{L}_1$. Therefore, the subsequent section focuses on the additional incorporation of the lineal-path function.

Table 7.2: Values of the objective function $\mathcal{L}_1$ and the errors $\widetilde{r}$ using the SSRVEs shown in Figure 7.16, n_{dof} denotes the number of global degrees of freedom of the finite element discretization.

SSRVE	$\mathcal{L}_1$ $[10^{-3}]$	$\mathcal{L}_{\text{V}}$ $[10^{-6}]$	$\mathcal{L}_{\text{SD}}$ $[10^{-3}]$	n_{dof}	$\widetilde{r}_x$ [%]	$\widetilde{r}_y$ [%]	$\widetilde{r}_{xy}$ [%]	$\widetilde{r}_{\varnothing}$ [%]
I	22.51	0.80	22.50	2254	8.44 ± 1.96	0.66 ± 0.22	0.95 ± 0.22	4.92
III	2.98	0.30	2.98	2962	2.43 ± 0.86	1.72 ± 0.40	5.06 ± 2.07	3.39
V	0.84	39.76	0.80	3290	0.14 ± 0.15	0.09 ± 0.06	3.08 ± 1.24	1.78
II	5.87	27.16	5.84	2914	2.56 ± 1.29	0.54 ± 0.26	9.12 ± 3.40	5.48
IV	1.17	0.80	1.17	3402	1.14 ± 0.39	0.97 ± 0.44	4.38 ± 1.85	2.67

Incorporation of the Lineal-Path Function. By now we take into account statistical measures that cover information regarding the phase fraction and the frequency of two points. But they are not able to regard type of connectivity between two points in the structure. For this purpose, the objective function given in Equation (7.47) is extended by the lineal-path function in order to incorporate statistical measures of higher order. This leads to the objective function

$$\mathcal{L}_2(\boldsymbol{\gamma}) = \omega_{\mathrm{V}}\,\mathcal{L}_{\mathrm{V}}(\boldsymbol{\gamma}) + \omega_{\mathrm{SD}}\,\mathcal{L}_{\mathrm{SD}}(\boldsymbol{\gamma}) + \omega_{\mathrm{LP}}\,\mathcal{L}_{\mathrm{LP}}(\boldsymbol{\gamma}) \quad \text{with} \quad \omega_{\mathrm{V}} = \omega_{\mathrm{SD}} = 1,\ \omega_{\mathrm{LP}} = 10\,, \tag{7.48}$$

wherein the weighting factors are set such that the order of magnitude of the individual least-square function values are in a reasonable range. The individual least-square functionals $\mathcal{L}_{\mathrm{V}}$, $\mathcal{L}_{\mathrm{SD}}$ and $\mathcal{L}_{\mathrm{LP}}$ are given by in Equation (7.43). To end up in a more efficient optimization procedure again the definition of a relevant area as described above is taken into account when comparing the spectral density in $\mathcal{L}_{\mathrm{SD}}$.

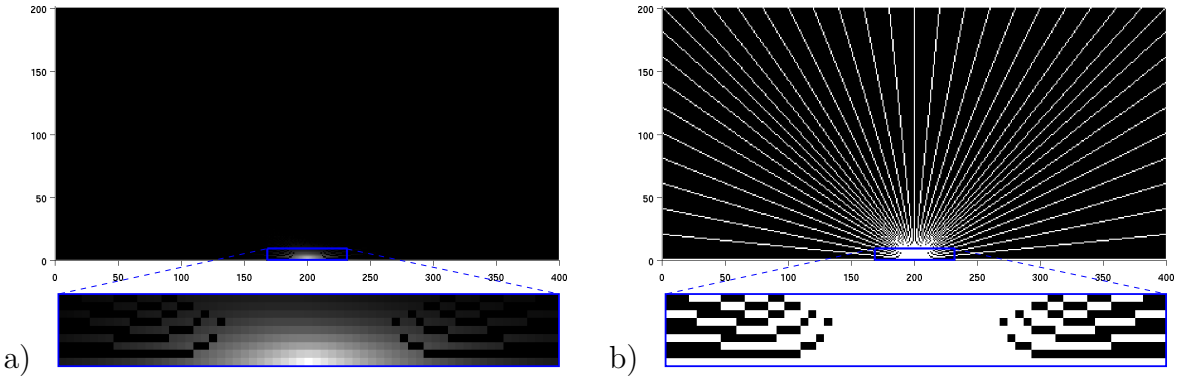

Figure 7.18: a) Lineal-path function of the target structure and b) the used template in order to improve the computational performance. The blue boxes mark the relevant region taking into account during the optimization procedure.

Due to the fact that computing the lineal-path function demands even more operations than computing the spectral density, an improved calculation method is required in this respect, too. Therefore, only a number of 40 line orientations distributed uniformly between the horizontal and the vertical direction is taken into account by an appropriate definition of the template, cf. Figure 7.18b. Furthermore, the size of the template which is considered for the computation of the lineal-path function of the SSRVEs can be significantly reduced by considering the typical length of inclusions in the target structure. For this purpose, the complete lineal-path function taking into account a template size $T_x \times T_y = 399 \times 200\,\mathrm{px}^2$ is computed for the target structure before optimization, shown in Figure 7.18a. Then, all values which are lower than a specified threshold value of 0.1 are set to zero. This defines the relevant template analogous to the way the relevant spectral density is identified. This leads to the fact that the size of the lineal-path function and the template size coincide and the specific size $T_x \times T_y = 63 \times 9\,\mathrm{px}^2$ is considered. In Figure 7.18 this aspect is reflected by the blue boxes, which mark the relevant regions of the lineal-path function and the template.

By using this improved procedure the objective function (7.48) is minimized with respect to $\boldsymbol{\gamma}$ and the SSRVEs as illustrated in Figure 7.19 are obtained. Again, a similar behavior of the objective function is observed. For increasing complexity of the SSRVE-type the value of the computed objective function minimum decreases from $\mathcal{L}_2 = 34.56 \cdot 10^{-3}$ for Type I

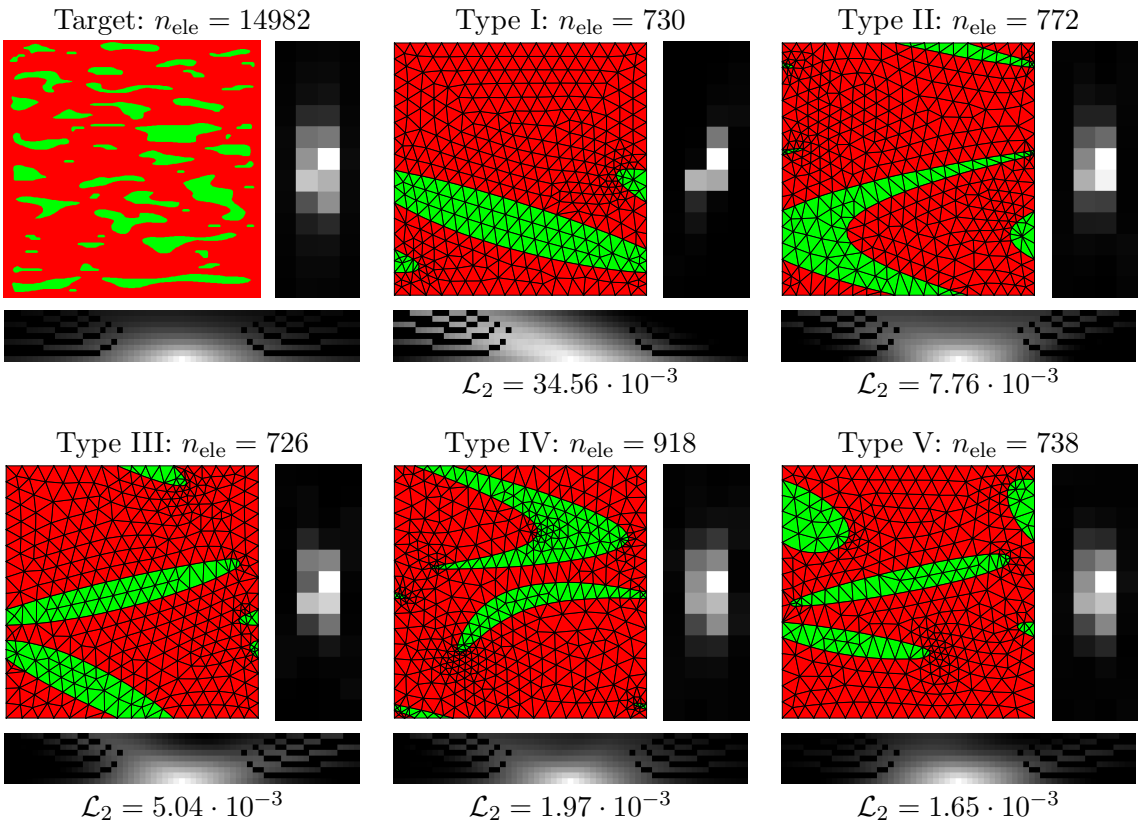

Figure 7.19: Target structure and discretization of SSRVEs with corresponding relevant area of the spectral density (right hand side) and the lineal-path function (beneath the microstructure images) resulting from the minimization of $\mathcal{L}_2$; n_{ele} denotes the number of finite elements. (Taken from Schröder et al. [197])

to $\mathcal{L}_2 = 1.65 \cdot 10^{-3}$ for Type V. Obviously, the absolute values of the minimized objective functions for the individual SSRVE types is now slightly higher than for $\mathcal{L}_1$, because an additional least-square functional is taken into account. However, the comparison of the mechanical response remains to be analyzed. Let us first investigate the stress-strain response which is shown in Figure 7.20.

There the distribution of the relative mechanical errors r_x, r_y and r_{xy} shows that SSRVE Type V seems to be the best SSRVE since the curve is below the curve of the other SSRVEs. In addition to that, the stresses obtained from SSRVE Type V are similar to the ones of the target structure for all three virtual experiments, also for the simple shear test, which is in contrast to the results obtained from minimizing $\mathcal{L}_2$. Hence, it seems that incorporating the lineal-path function additionally into the optimization problem leads to an improved overall mechanical representation of the target structure by the SSRVE. For a more detailed analysis the average mechanical errors as well as the overall comparative measures are given in Table 7.3, where we again prefer the ordering by the number of sampling points per spline and then the SSRVE type, cf. Table 7.2.

The most suitable SSRVE with the lowest overall comparative error is Type V. Although Type I also leads to a rather low value of $\widetilde{r}_{\varnothing}$, the average error for the horizontal tension test is rather high with $\widetilde{r}_x = 4.11$. In turn, SSRVE Type V yields low average errors for all three virtual experiments and yields the best approximation of the overall mechanical behavior of the target structure. Moreover it is observable, that the SSRVE types based on a

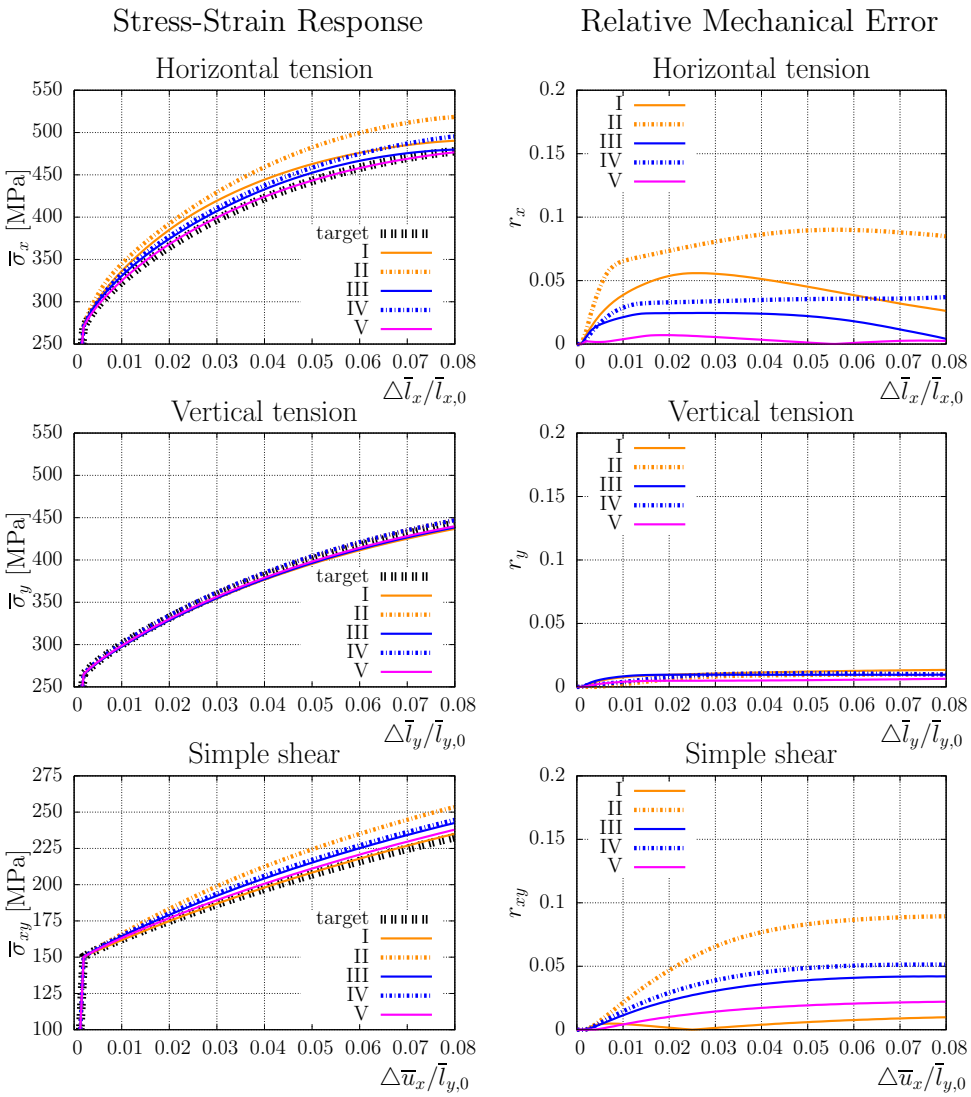

Figure 7.20: Results of the virtual experiments using the discretizations of the SSRVEs (Figure 7.19) based on $\mathcal{L}_2$. On the left hand side the Cauchy stresses are plotted versus strains, the right hand side shows the relative mechanical error. (Schröder et al. [197])

convex inclusion interface, i.e. 3 sampling points each spline, show better results compared to the corresponding SSRVE types with 4 sampling points each spline. Compared to the results obtained from minimizing $\mathcal{L}_1$, we can conclude that the incorporation of statistical measures of higher order seems to be promising, since the additional incorporation of the lineal-path function yields significantly improved SSRVEs.

Table 7.3: Values of the objective function $\mathcal{L}_2$ and the errors $\widetilde{r}$ using the SSRVEs shown in Figure 7.19, n_{dof} denotes the number of global degrees of freedom of the FE-discretization.

SSRVE	$\mathcal{L}_2$ [10^{-3}]	$\mathcal{L}_{\text{V}}$ [10^{-5}]	$\mathcal{L}_{\text{SD}}$ [10^{-4}]	$\mathcal{L}_{\text{LP}}$ [10^{-5}]	n_{dof}	$\widetilde{r}_x$ [%]	$\widetilde{r}_y$ [%]	$\widetilde{r}_{xy}$ [%]	$\widetilde{r}_{\varnothing}$ [%]
I	34.56	158.11	189.21	140.54	3054	4.11 ± 1.28	1.05 ± 0.30	0.49 ± 0.30	2.47
III	5.04	6.55	28.12	21.61	3042	1.87 ± 0.67	0.89 ± 0.20	3.03 ± 1.29	2.12
V	1.65	6.55	7.04	8.85	3082	0.32 ± 0.21	0.49 ± 0.13	1.47 ± 0.70	0.91
II	7.76	9.08	44.70	31.98	3238	7.74 ± 1.92	0.73 ± 0.32	6.39 ± 2.81	5.81
IV	1.97	0.54	9.01	10.53	3814	3.20 ± 0.78	0.86 ± 0.35	3.78 ± 1.58	2.90

7.4 Applications

In this section we apply the most suitable SSRVE, which was constructed in the previous section, to macroscopically inhomogeneous FE^2-simulations to show the reliability and applicability of the presented framework. These computations are performed using FEAP with an embedded self-written FE^2-environment, whereby the solution of the microscopic boundary value problem is achieved by the application of the direct solver SuperLU (Vers. 3.1), for details see Demmel et al. [59].

7.4.1 Radially Loaded Circular Disc

(Subsequent results were first published in Schröder et al. [197].)

Now, we compare the mechanical response of two macroscopically inhomogeneous FE^2-simulations, where the target structure and the most suitable SSRVE constructed in the previous section are considered at the microscale.

Figure 7.21a depicts the macroscopic boundary value problem of a radially expanded circular disk with a hole, the outer radius is $r_\mathrm{o} = 3.0\,\mathrm{cm}$ and the inner radius is $r_\mathrm{i} = 0.5\,\mathrm{cm}$. We discretize the disk with 244 triangular elements with quadratic ansatz functions and consider plain strain conditions. During the simulation the outer radius is driven by a radially orientated displacement condition from $\overline{u}(t=0) = 0\,\mathrm{mm}$ up to $\overline{u}(t=t_\mathrm{max}) = 1.725\,\mathrm{mm}$. At the microscale periodic boundary conditions are applied and at first the target structure is considered where a discretization with 5452 quadratic triangular elements (21930 degrees of freedom) is taken into account, see Fig. 7.21b. Second, the SSRVE Type V constructed by minimizing the objective function $\mathcal{L}_2$ is considered at the microscale, where a discretization with 738 quadratic triangular elements (3082 degrees of freedom) is addressed. In Fig. 7.21c the finite element mesh of the considered SSRVE (regular colors) with its periodic expansion (brightened colors) of comparable size is shown. It is emphasized that for the FE^2-simulation only the SSRVE (regular colors) is taken into account since periodic boundary conditions are used.

Let us first investigate the macroscopic response of both simulations. Therefore, Fig. 7.22 shows the stress distributions $\overline{\sigma}_{11}$, $\overline{\sigma}_{22}$ and $\overline{\sigma}_{33}$ in the radially expanded disk at the final load step. When comparing the response of the second simulation, where the SSRVE is considered at the microscale (second row), with the first one based on the target structure

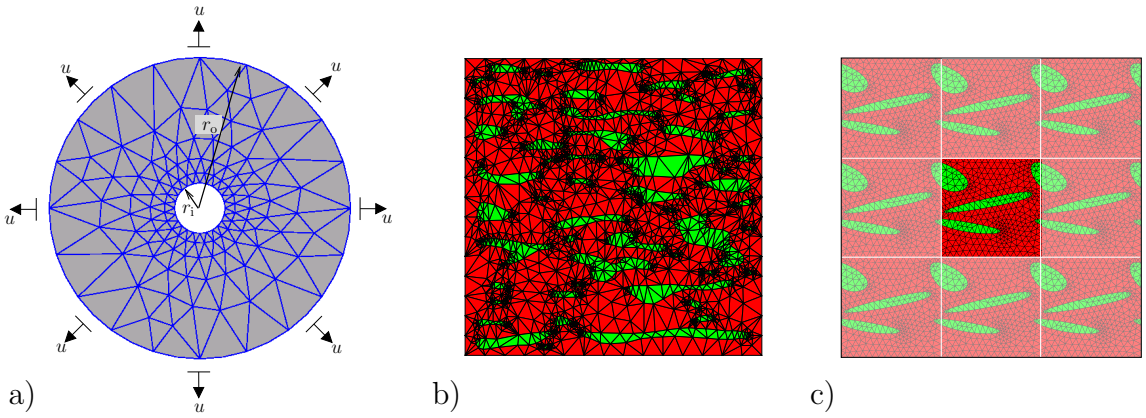

Figure 7.21: a) Macroscopic BVP: radially expanded circular disk with a hole ($r_\mathrm{i} = 0.5\,\mathrm{cm}$, $r_\mathrm{o} = 3.0\,\mathrm{cm}$) discretized with 244 quadratic triangular elements under plain strain conditions; discretization of b) target structure with a reduced number of $n_\mathrm{ele} = 5452$ finite elements and c) of SSRVE Type V based on $\mathcal{L}_2$ (with its periodic expansion). (Schröder et al. [197])

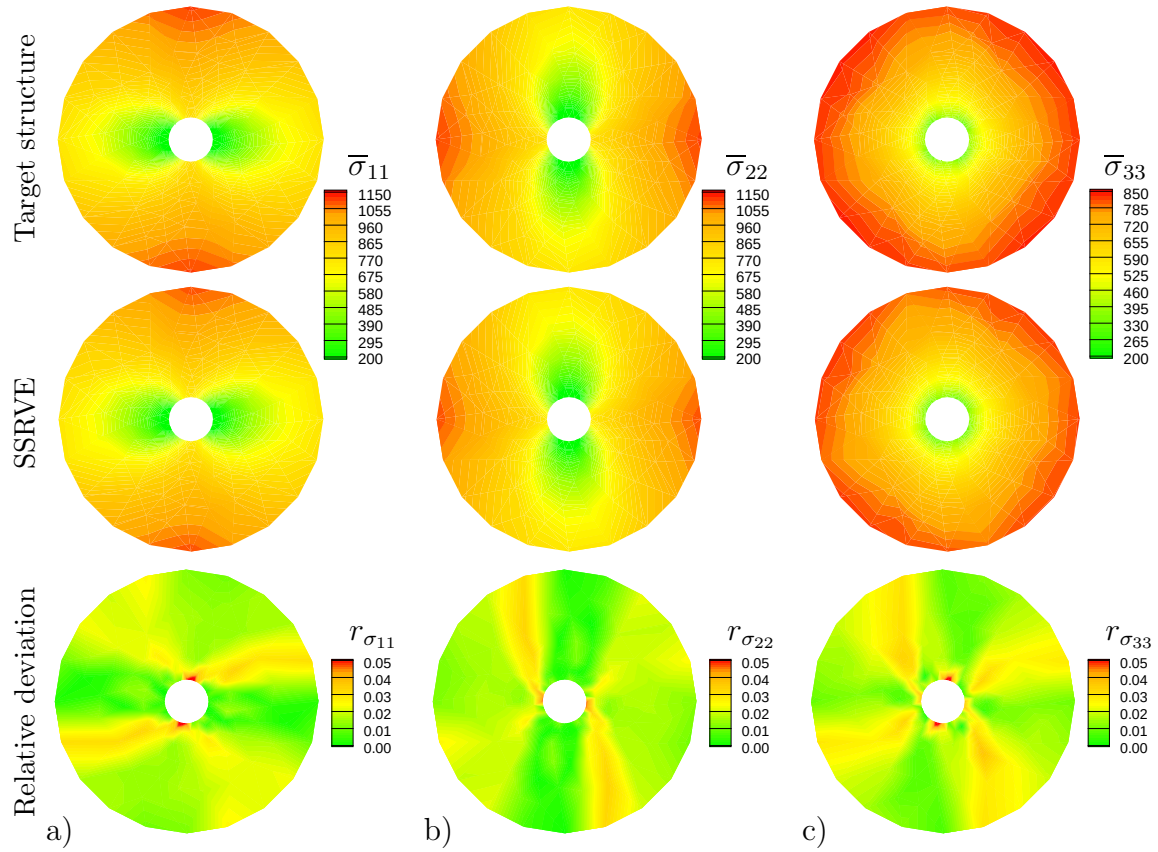

Figure 7.22: Macroscopic stress distribution for a) $\overline{\sigma}_{11}$, b) $\overline{\sigma}_{22}$ and c) $\overline{\sigma}_{33}$ of the FE^2-simulations based on the target structure (first row) and the SSRVE (second row), and the relative deviations a) $r_{\sigma_{11}}$, b) $r_{\sigma_{22}}$ and c) $r_{\sigma_{33}}$ comparing these two results (third row).

(first row), a qualitatively and quantitatively similar stress response is observed at the macroscale. To get a quantitative estimation of the accordance, the relative deviation

$$r_{\sigma_{ii}}(\overline{\boldsymbol{x}}) = \left| \left[\overline{\sigma}_{ii}^{\text{target}}(\overline{\boldsymbol{x}}) - \overline{\sigma}_{ii}^{\text{SSRVE}}(\overline{\boldsymbol{x}}) \right] \Big/ \max_{\overline{\boldsymbol{x}}} \left[\overline{\sigma}_{ii}^{\text{target}}(\overline{\boldsymbol{x}}) \right] \right| \quad \text{with} \quad i = 1,2,3 \tag{7.49}$$

is defined as a function of the position $\overline{\boldsymbol{x}}$ in the disk. This relative error describes the difference of the macroscopic stresses between both simulations relative to the maximal stress of the target structure at each macroscopic point. From the corresponding plots in the third row of Fig. 7.22 a relative deviation lower than 5% for all three stress components is observed. However, the maximum values of the relative deviation are rather localized, thus, a similar behavior of the macroscopic stress response can be concluded when comparing the response obtained for the SSRVE with the one based on the target structure. It is worthwhile mentioning that the macroscopic stress response shows a relatively low anisotropic character, although the virtual experiments in the last section show a significantly different behavior for the horizontal- and the vertical tension test. In Fig. 7.22c the contour plot of $\overline{\sigma}_{33}$ is quite close to a rotational-symmetric distribution. A more pronounced anisotropic response can be expected for larger expansions.

Nevertheless, when comparing the microscopic stress distributions at different positions in the disk, a rather strong anisotropic character may be observed. To show this, Fig. 7.23 provides the von Mises stress distribution at the final load step in the disk ($\overline{\sigma}_{vM}$) as well as in the microstructures (σ_{vM}) at different macroscopic positions. For this multiscale

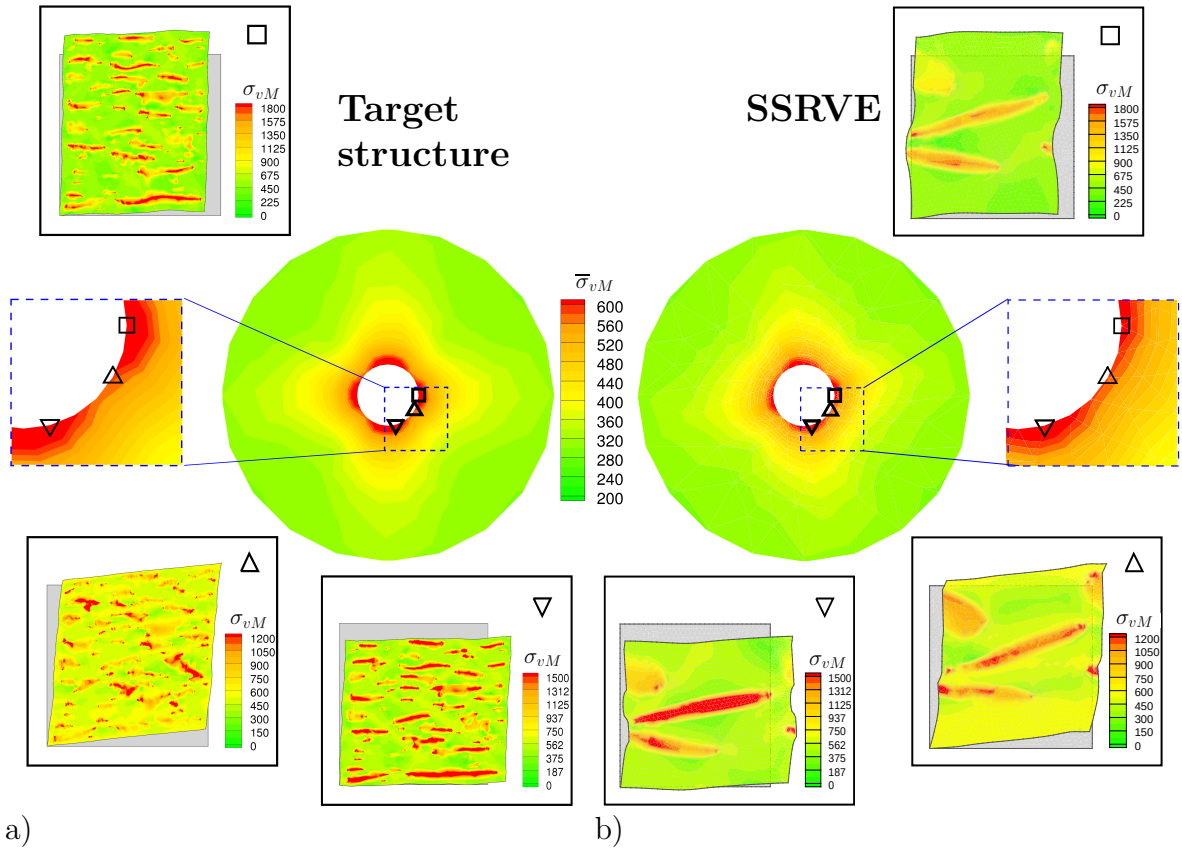

Figure 7.23: Results of the FE^2-simulations based on the a) the target structure and b) the SSRVE with the von Mises stress distributions in the deformed microstructures for three selected positions. The symbols in the upper right corner of the images for the microscopic response represent the link to the macroscopic position; the grey area behind the microstructure indicates the undeformed configuration.

comparison three different macroscopic points are considered, which are located at the same distance from the inner boundary close to the inner radius of the disk. The maximum stress levels at the analyzed microstructures differ at the individual macroscopic points significantly from approximately 1200 MPa to 1800 MPa due to the anisotropy of the RVEs. This represents a rather anisotropic character at the microscale although the macroscopic von Mises stress distribution is close to a rotational-symmetric one. In addition to that, the maximal stress levels at the microscales are significantly larger than at the macroscale. The latter two issues may play an important role with respect to failure initialization analysis, since the microscopically observable orders of magnitude and positions of maximum stress levels can not be observed in purely macroscopic simulations. If we compare the microscopic results related to the same macroscopic point of the simulation based on the SSRVE with the one based on the target structure, again similar stress levels are observed. Furthermore, the qualitative response at the microscale is similar, too. This accentuates the performance of the SSRVE and shows that it seems to be possible to approximate the response of random microstructures by much simpler SSRVEs. Finally, the profit with respect to the costs of data storage of the history variables is enormous when using SSRVEs compared with the chosen target structure. In the proposed approach the needed data storage capacity is approximately reduced about 95 %, for the considered coupled micro-macro boundary value problem and the computation time is significantly reduced. These are of course only rough estimates based on the considered discretizations.

7.4.2 Deep-Drawing

Since two-phase steels like the DP-steels are often used in many metal forming processes we consider the deep-drawing of a sheet metal as a further macroscopically inhomogeneous boundary value problem. During a deep-drawing process the sheet metal is stretched into the desired part shape by pushing a tool on the sheet and forcing it into a die cavity. The plastic deformations resulting from the tensile strain make sure that the desired shape remains after removing the tools. Structural components made by this method can be found in many fields, e. g. automotive bodies and fuel tanks as well as kitchen sinks, cans and cups.

In Figure 7.24 the setup of the deep-drawing process is schematically illustrated. Before the forming process starts the sheet metal is clamped by the blank holder over the drawing die. The die has a cavity representing the desired outer shape of the part. By pushing the punch into the sheet, the material is stretched, or drawn, into the die cavity. After reaching the final loading position the clamping is released by removing the blank holder and the punch is moved out of the sheet. In Figure 7.25 the loading and unloading is schematically shown including the aforementioned schedule for the releasing of the sheet metal.

In contrast to the multiscale analysis presented in the previous section we does not consider a FE^2-simulation of a deep-drawing process using the target structure for the microscopic boundary value problem. Although the number of integration points at the macroscopic boundary value problems does not differ strongly in the example of the deep-drawn sheet metal and the radially loaded circular disc, the first mentioned one exhibits higher complexity due to the application of the contact formulation. Much more, the shown example should emphasize the applicability of the presented method to multiscale simulation of sheet metal forming processes and the possibility to increase their efficiency.

For the computation we simplify the process to a macroscopic two-dimensional boundary value problem on the supposition of a plain strain condition. We also consider only one half of the problem because of the line symmetry. In Figure 7.26a the macroscopic

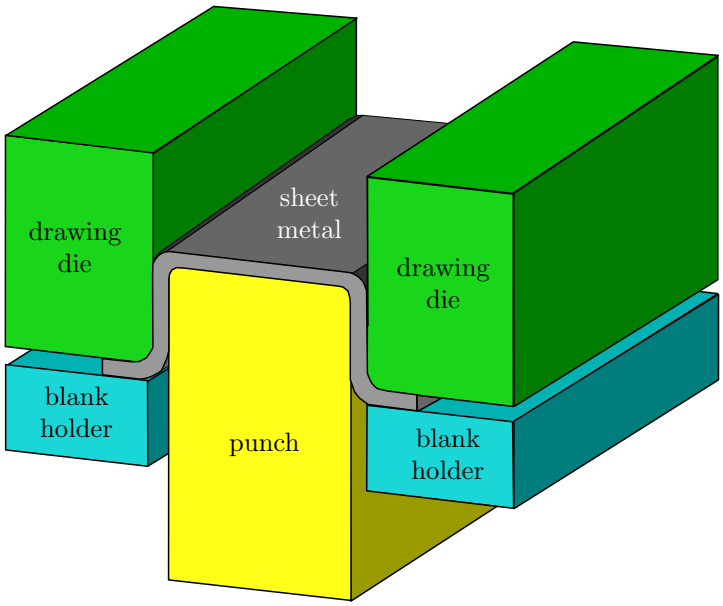

Figure 7.24: Illustration of the setup and tools of the deep-drawing in the loading state.

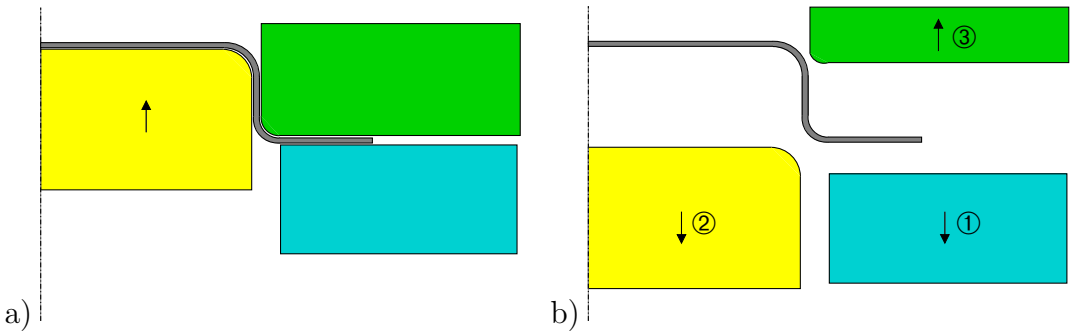

Figure 7.25: Process schedule in a cross-sectional half view of the forming process: a) deep-drawing and b) unloading steps. The numbers represents the order of tool releasing.

discretization of the sheet metal based on 165 linear quadrilateral elements using a 4-Gauss-point quadrature is depicted. Horizontal displacement boundaries are applied to the nodes at the left end of the sheet regarding for the symmetry condition. For a detailed view on the results of the microscale we consider three different locations along the sheet metal. In the final state they should be located near the punch radius (I), in the vertical section (II) and near the die radius (III), see Figure 7.26a. The tools are realized through a penalty contact. For the analyzed hat profile we consider a punch radius of 7 mm, a die radius of 6 mm and a drawing depth of 45.7 mm. The sheet has a half width of 100 mm and a thickness of 1.4 mm. In order to perform an efficient computation we use the most suitable SSRVE obtained in section 7.3.2 for a multiscale simulation of the deep-drawing process, since the application of the target structure will produce large computational costs due its number of degrees of freedom. The discretization of the SSRVE shown in Figure 7.26b consists of 738 quadratic triangular elements and 3082 degrees of freedom. Applying periodic displacement boundaries to its edges we achieve the boundary value problem at the microscale, which is solved at each macroscopic Gauss-point during the FE-simulation. On the microscale we use the Finite J_2-Plasticity material model described in Section 6.3 and the material parameters from Table 7.1 for the description of the mechanical behavior of the individual phases. In each of the aforementioned analysis locations along the sheet we monitor three points in the direction of the sheet thickness:

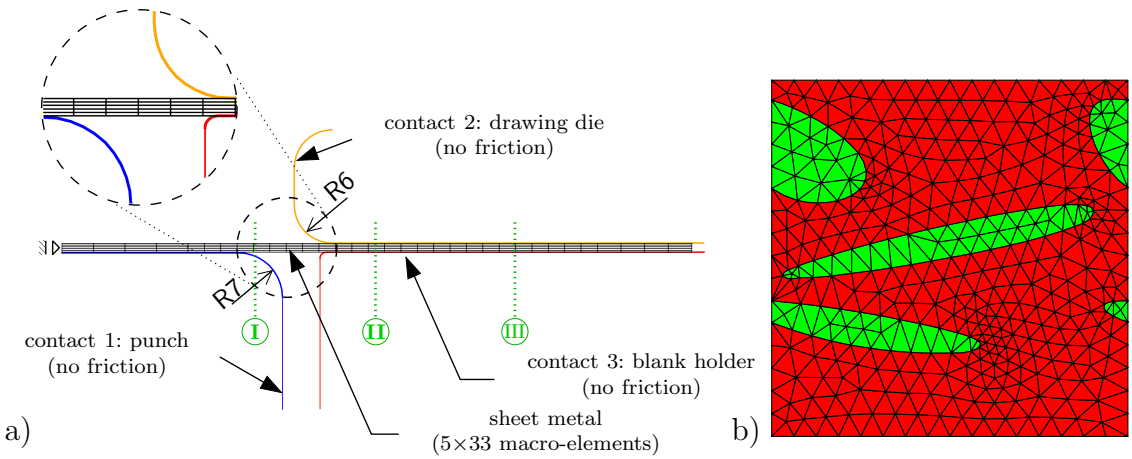

Figure 7.26: Discretization of a) the macroscopic BVP with 165 linear quadrilateral elements under plain strain condition and b) the SSRVE with 738 quadratic triangular elements used for the microscopic BVP in the multiscale simulation.

near the i) upside (□), ii) middle (◯) and iii) underside (△). For these overall nine macroscopic points we analyze the microscopic results at the final load and unload step.

After the deep-drawing is finished, see Figure 7.27, we observe a different stress distribution in the three microstructures at location I. This aspect can be addressed to the different loading states within the sheet in direction of thickness due to the bending by the punch radius. Consequently, near the underside a compression zone arises, which can be observed by a shortening of the horizontal edge length of the associated RVE (△). The opposite – a tension zone – can be observed near the upperside, since the edge of the RVE (◯) is longer in the deformed configuration. Since near the middle of the sheet the neutral axis should be appear, the RVE located near this location (◯) shows a lower stress maximum compared to both the other ones. At location II (Figure 7.28) we also observe different stress distribution in the related microstructures but all three RVEs show a similar elongation of the edges, which are orientated in longitudinal direction. The differences in the stresses may be result from the previous forming process by the die radius and the related plastic deformation. But in further progress the formed shape is rolled back to a straight sheet and, consequently, the differences in the length are removed. The final load state at location III and the associated results at the microscale are shown in Figure 7.29. Therein we observe qualitatively similar deformation and stress states at the different positions along the sheet thickness. Again we measure compression in the RVE associated to the position nearing the die radius and tension at the opposite of the sheet. One possible explanation can be a similar bending characteristic, which is applied to the sheet during the forming process by the die radius. But in common at all location we can observe a strong discrepancy between the maximal stress level at the microscale and the

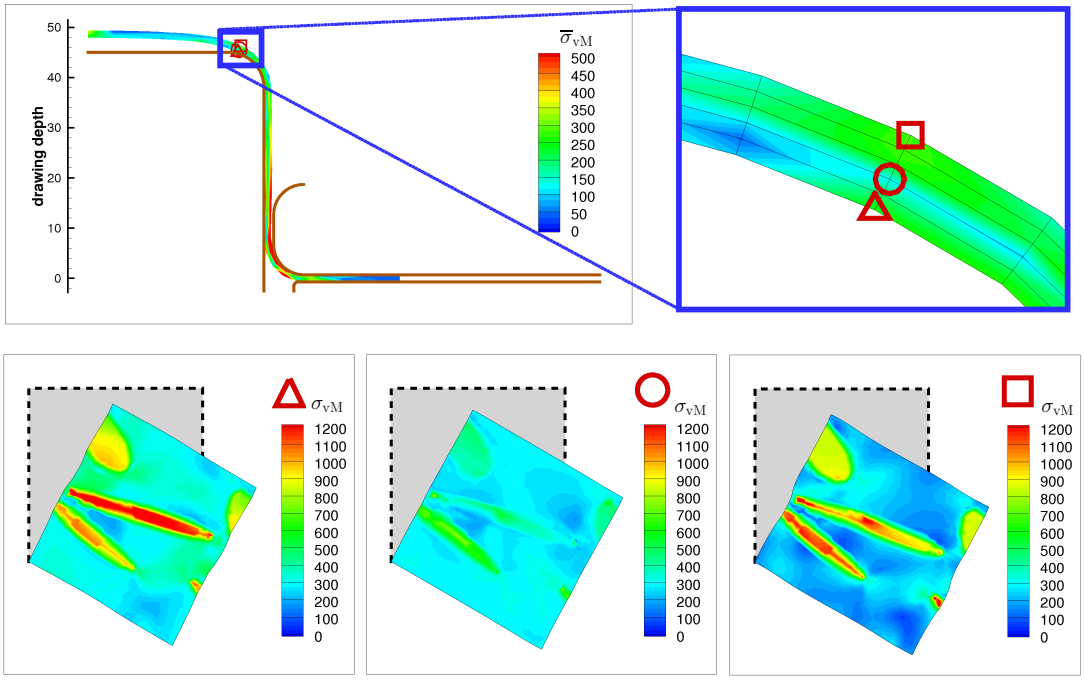

Figure 7.27: Location I: Final load step – von Mises stress distribution at the macroscopic and three microscopic boundary value problems. The symbol of the upper right corner of the images for the microscopic response represent the link to the macroscopic position; the grey area behind the microstructure indicates the undeformed configuration.

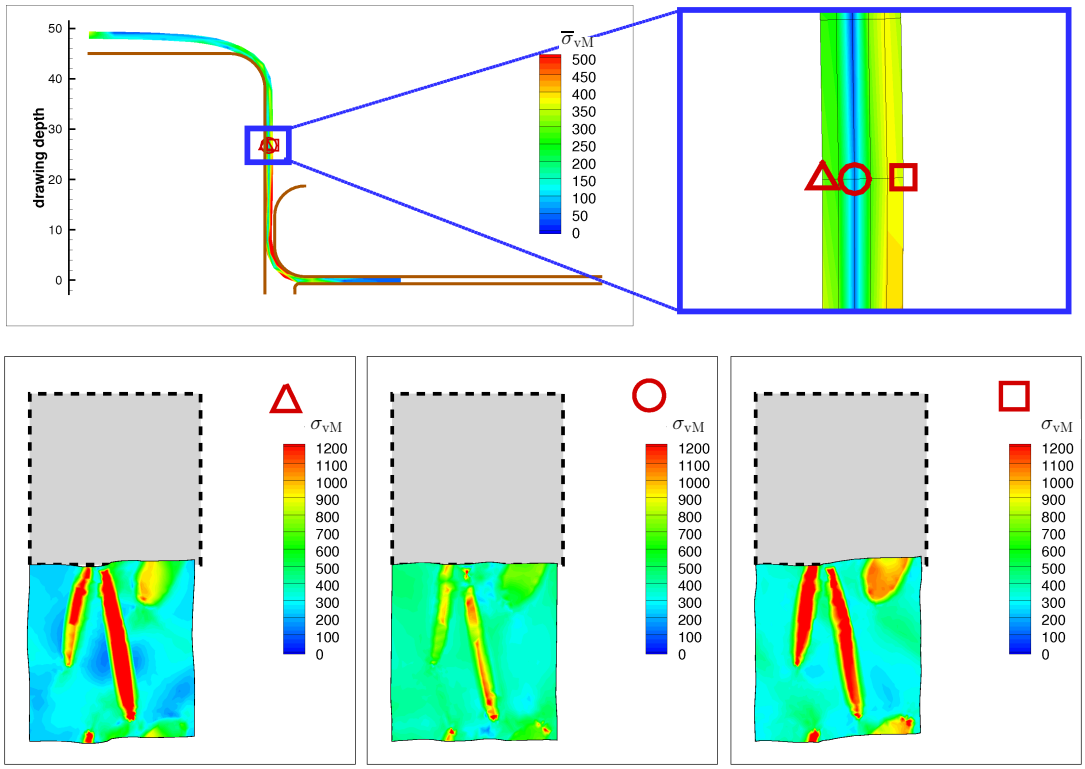

Figure 7.28: Location II: Final load step – von Mises stress distribution at the macroscopic and three microscopic boundary value problems. The symbol of the upper right corner of the images for the microscopic response represent the link to the macroscopic position; the grey area behind the microstructure indicates the undeformed configuration.

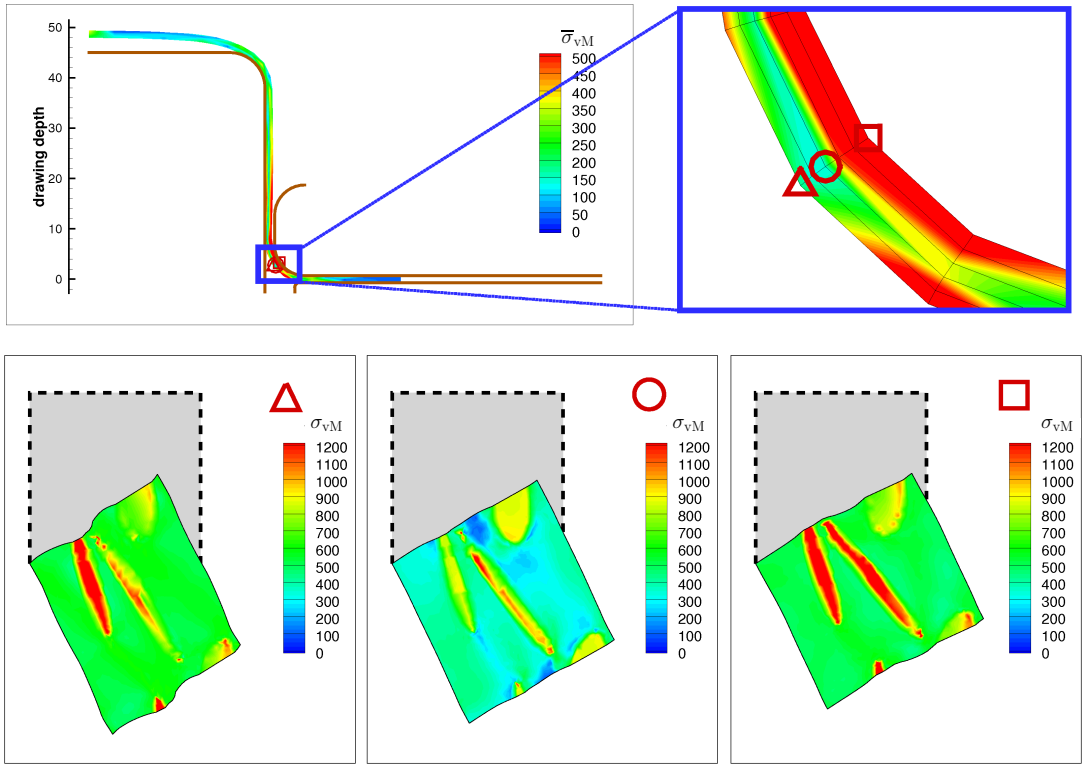

Figure 7.29: Location III: Final load step – von Mises stress distribution at the macroscopic and three microscopic boundary value problems. The symbol of the upper right corner of the images for the microscopic response represent the link to the macroscopic position; the grey area behind the microstructure indicates the undeformed configuration.

related macroscopic location. So this aspect is important if e.g. a failure analysis should be realized or a crack propagation for micro cracks should be incorporated.

In Figure 7.30, 7.31 and 7.32 the stress distribution in the released sheet and the related microstructures are shown. All stress state are relaxed compared to their counterpart at the final load step in Figure 7.27-7.29, but the discrepancy of the maximal stress levels between macro- and microscale still remains. From the deformation state of the macroscopic BVP we observe a typical phenomenon, the spring back, which occur typically in many metal forming processes after the releasing of the specimen. The right end of the sheet is moved up, cf. upper left subframe in Figure 7.29, compared to its deformed shape in the final load step, cf. upper left subframe in Figure 7.30. This behavior is explained by the release of the elastic deformations, which were stored in the sheet during the loading. In many research fields the spring back is a crucial topic, since the final shape of the deformed specimen is mainly influenced by this phenomenon. If we measure the deformations of the three microstructures at location I along their horizontal reference axis we again observe the aforementioned elongation of the RVE at the upside located structure, a nearly unchanged RVE at the middle and a compressed one at the underside. As also mentioned before, this behavior is addressed to the nearly pure bending at this location of the sheet. Whereas at the location II we observe a shear in the microstructure at the upside and underside of the sheet. In the middle the shear is only slightly observable. At location III similar states arises compared to those at location I. But a significantly higher stress level at the macrolevel and microlevel occur compared to the other locations. This could be caused by either the smaller die radius and/or the higher tensile force at this location in the sheet.

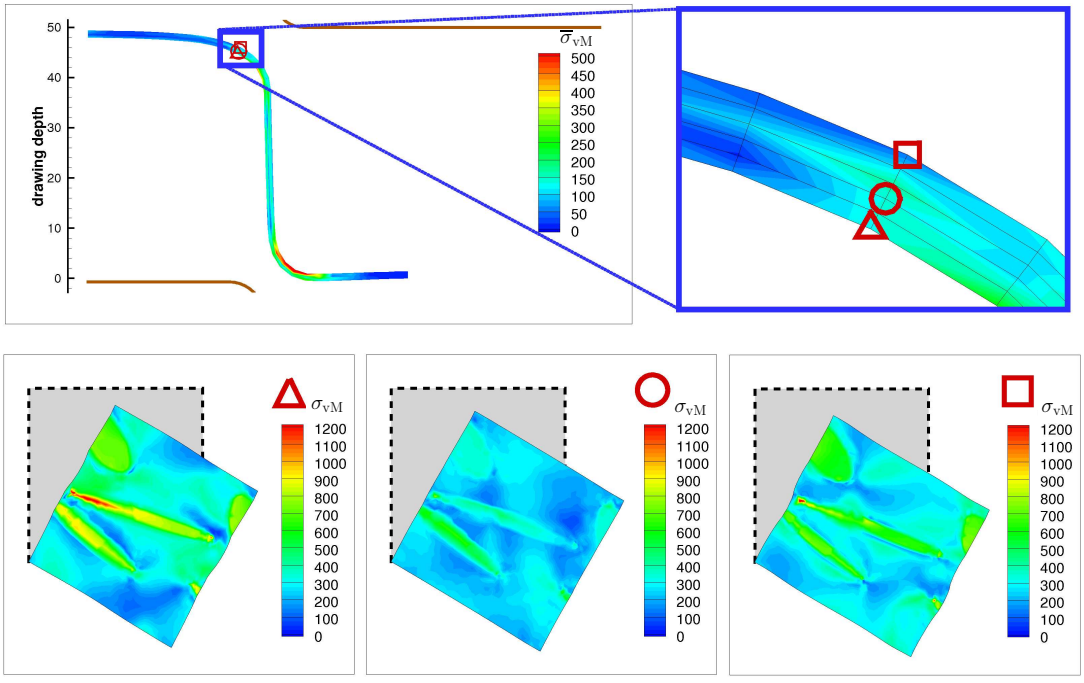

Figure 7.30: Location I: Final *un*load step – von Mises stress distribution at the macroscopic and three microscopic boundary value problems. The symbol of the upper right corner of the images for the microscopic response represent the link to the macroscopic position; the grey area behind the microstructure indicates the undeformed configuration.

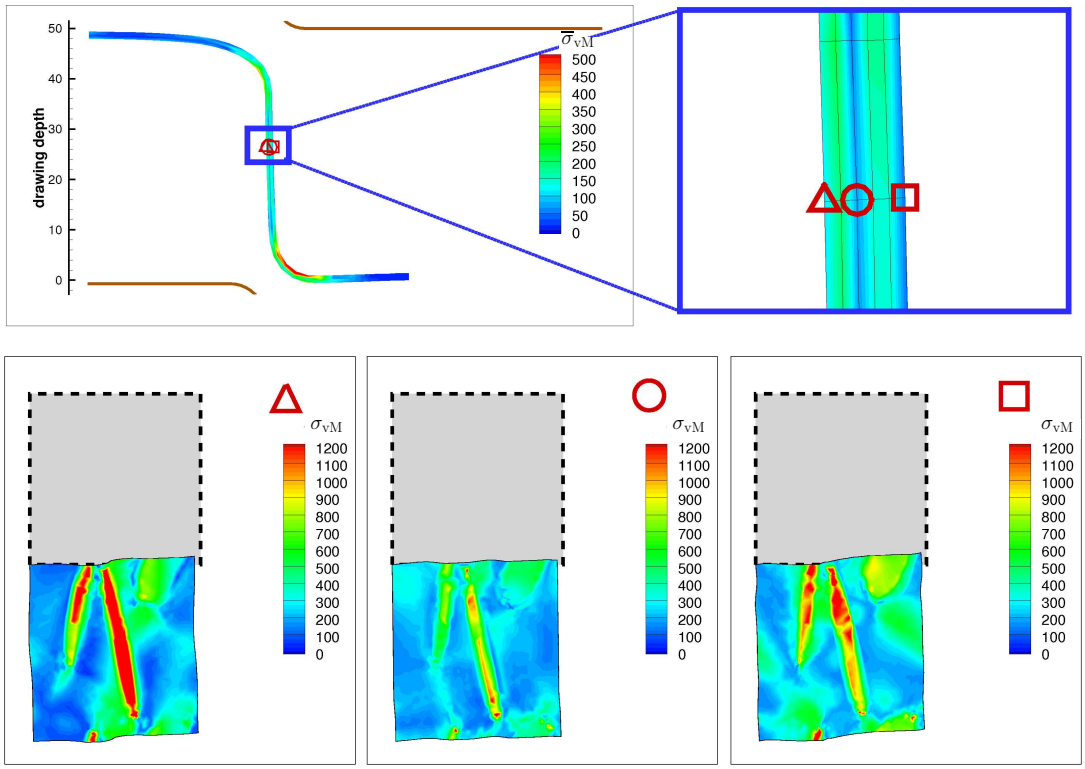

Figure 7.31: Location II: Final *un*load step – von Mises stress distribution at the macroscopic and three microscopic boundary value problems. The symbol of the upper right corner of the images for the microscopic response represent the link to the macroscopic position; the grey area behind the microstructure indicates the undeformed configuration

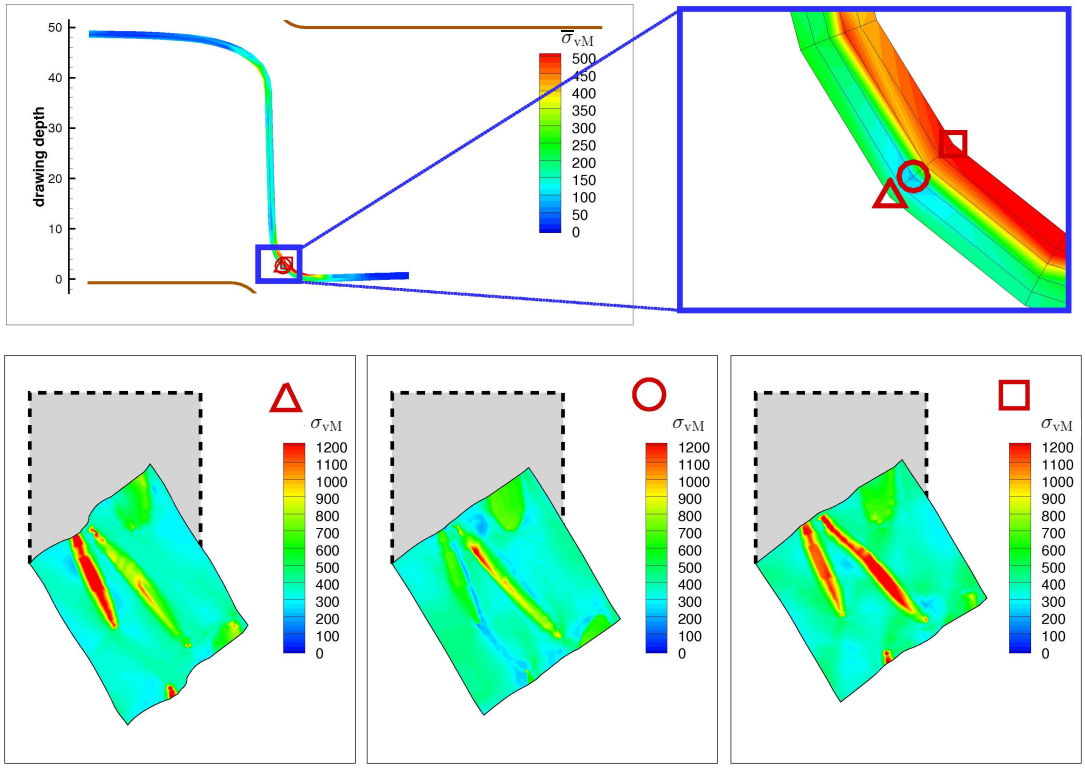

Figure 7.32: Location III: Final *un*load step – von Mises stress distribution at the macroscopic and three microscopic boundary value problems. The symbol of the upper right corner of the images for the microscopic response represent the link to the macroscopic position; the grey area behind the microstructure indicates the undeformed configuration.

7.5 Towards the Application to 3D Microstructures

In the previous sections we show, that our proposed method for the construction of SSRVEs is a suitable technique to reduce the computational effort in two-dimensional multiscale simulations of micro-heterogeneous materials. The next step should be the extension of this method to three-dimensional microstructures. At that account we discuss the aspects, which should arise as necessary steps in the development process of the 3D SSRVE method, and give some suggestions towards the solution of possible problems.

At first, the established statistical measures have to be modified to be applicable to three-dimensional structures. These steps are very straightforward and should not produce any problems. But in the framework of the SSRVE construction, the used statistical measures should capture enough geometrical informations of the morphology to describe their main characteristics. Thus, an analysis of the measures with respect to this aspect has to be done. If their feasibilities are not enough, other statistical measures of higher order have to be considered and analyzed. One possibility can be the application of the three-point probability function, whose counterparts of first and second order are already shown in this thesis, cf. section 7.2.1. Additionally, the Minkowski valuations can be serve as a suitable higher order measure, since they allow for a rather mechanical interpretation. They have a closer correlation to measures usually applied for the description of engineering structures as e.g. the first and second moment of area. In 3D the four (scalar) Minkowski functionals are the volume, the area, the integrated mean curvature, and the Euler characteristic. More details on this topic can be found in Mecke and Buchert [144] and Mecke [143].

A further topic should be the parameterization of the inclusion morphology in the SSRVEs, which serves as degrees of freedom in the overall least square functional during the optimization process. The straightforward extension to the three-dimensional description by sampling-points is not an advisable method. For that method the processing from the sampling points to a binary representation, which is done several times during the optimization, is too complex and, consequently, it will increase the computational time. Additionally, the expected complexity of the inclusion geometry in the three-dimensional case and therefore the highly increased number of degrees of freedom in the geometry are arguments against this strategy. It may be a more suitable approach to consider generalized ellipsoids for the geometrical description of the inclusion morphology of SSRVEs. Thereby, the points on the surface of the ellipsoid satisfy the equation

$$\sum_{i=1}^{d} \left(\frac{|\boldsymbol{v}_i \cdot (\boldsymbol{x} - \boldsymbol{x}_\mathrm{C})|}{r_i} \right)^{p_i} = 1 \,. \tag{7.50}$$

The parameterization of such a geometrical object is given by the spatial dimension d, the center position $\boldsymbol{x}_\mathrm{C}$, the directions $\boldsymbol{v}_i$ of the principal axis of the ellipsoid, the principal radii r_i and the exponents p_i. A crucial part is the choice of the parameter p_i, since it determines the shape of the surface, i. e. convexity for $p_i \geq 1$ or concavity for $p_i < 1$. The special choice of $p = 2$ result in a smooth and strictly convex hull, a "normal" ellipse ($d = 2$) or ellipsoid ($d = 3$). Furthermore, $p = 1$ yields a parallelogram, for $n \to 0$ the surface nears the center $\boldsymbol{x}_\mathrm{C}$ and for $p \to \infty$ the ellipsoid becomes a rectangular shape. The origin of this kind of mathematical description goes back to the French mathematician Gabriel Lamé (1795–1870), who introduce the description of a superellipse, also refer to as Lamé curve.

For the purpose of verification of the construction of 3D SSRVEs real target structures must be obtained. In the two-dimensional case the imaging of steel microstructure is a well established technique and good results can be achieved by several methods, e. g. scanning electron microscope (SEM) and electron backscatter diffraction (EBSD). But the reconstruction of three-dimensional structures is a task, which required considerable efforts. On that account the department for microstructure physics and metal forming at the "Max-Plank Institut für Eisenforschung GmbH" has developed a 3D orientation electon microscopy technique. This 3D electron backscatter diffraction (3D EBSD) method provides cross sectional information including a metallographic characterization of the considered material. Thereby a joint high-resolution field emission SEM/EBSD setup is coupled with a focused ion beam system (FIB) and provides a set of cross-sectional planes of the considered dual-phase steel. The equipment and the geometric arrangement is shown in Figure 7.33a. The sample of the considered dual-phase steel is mounted on a tiltable holder inside the equipment. During the investigation the sample is tilt between two positions: the cutting and the EBSD position. In the cutting position the FIB system milling thin layers (10 nm - 1 μm thick) from the investigated surface of the sample. The other position is used for the EBSD analysis, where an electron beam is focused onto the milled surface and the back scatter diffraction patterns are monitored by the EBSD camera. Due to different diffraction patterns several properties of the sample can be analyzed, e. g. crystal orientations and grain size. Additionally, a reconstruction of the in-plane morphology of the ferritic matrix and the martensitic inclusion phase are possible based on this back scatter diffraction patterns. Such micrographs are exemplarily depicted in Figure 7.33b. For more details concerning the 3D EBSD method we refer to Bastos et al. [17], Konrad et al. [131], Zaefferer et al. [256]. In Figure 7.33c the three-dimensional reconstruction of the dual-phase steel is shown resulting from the stacking of the cross-sectional data. Such representation can be used as target structure for the determination of the statistical measures, which are needed for the 3D SSRVE construction, as well as for the application in FE-simulations to obtain stress-strain relations as references for the verification of the 3D SSRVE method, the so-called "overkill" solutions.

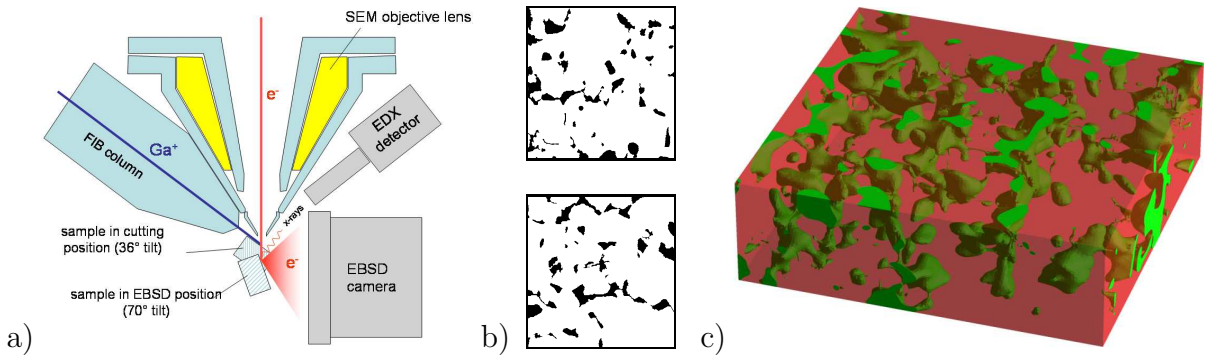

Figure 7.33: 3D EBSD: a) technical setup, cf. Konrad et al. [131], and b) two examples of obtained cross-sections of a dual-phase steel. The micrographs are color-coded with respect to the phases (white: ferrite, black: martensite). c) Geometrical reconstruction of three-dimensional microstructure based on cross-sectional EBSD data.

8 Summary

The investigation of numerical simulations of heterogeneous materials using the Finite Element Method was presented in this thesis. Thereby, the treatment of the geometrical description of the considered materials and bodies formed the essential part. In the first part the three-dimensional reconstruction of patient specific arteries was investigated and used in several FE-simulations. The construction of statistically similar representative volume elements (SSRVE), which serve as analogous models for real microstructures in multiscale simulations, was developed for the application to two-phase steels.

Starting from the continuum mechanical framework including stress and strain definitions as well as balance principles we discussed several basic aspects for the design of constitutive material models. In this context we treated the representation theorems considering anisotropic tensor functions, since the mechanical behavior of arterial walls exhibits a transverse isotropy. For the numerical treatment using the Finite Element Method several isotropic and anisotropic polyconvex free energy functions were given and the notion of polyconvexity regarding material stability and the existence of solutions were briefly reviewed. Based on the definition of the strong and weak form of the boundary value problem the Finite Element Method was introduced and resulted in the corresponding linearization and approximation. For the simulation of incompressible materials, e. g. biological soft tissue, the standard finite element formulations showed some well-known problems and, consequently, we discussed the extension of the standard approach to a 3-field formulation. Since the reconstruction of complex geometries often result in a large number of degrees of freedom in the finite element discretization, we introduced a parallel solution procedure, the finite element tearing and interconnecting (FETI) method, to enable the efficient solution of such a large system of equations.

An introduction to the composition of *human arteries* and their diseases including possible treatments gave an overview of the considered material in the first part of this thesis. Afterwards, several medical imaging techniques were described, which are suitable to get data for a geometrical reconstruction of the arterial wall, and additionally we discussed the main mechanical characteristics of the considered material. Based on these properties the continuum mechanical modeling of the material behavior was shown and the corresponding parameters were adjusted to experimental data. Then, the focus was set on the reconstruction of patient specific arterial geometries. The necessary data for the reconstruction were obtained on the one hand from intravascular ultrasound examination postprocessed by the virtual histology (VH IVUS) and on the other hand by angiographic X-ray imaging. The first mentioned method delivers cross-sectional information of the arterial wall containing the histology of the arterial wall. Then, the output of the filtering and segmentation processes of the VH IVUS images was combined with the three-dimensional path of the artery, which was obtained from the angiographic X-ray imaging. Based on this patient specific geometry the discretization by finite elements was performed and used in several finite element simulation, where the arterial wall was loaded with an internal hydrostatic pressure. These simulations were done for two-dimensional and three-dimensional geometries and the results were compared to each other. Since in the course of the treatment regarding the arteries several assumptions were made, we discussed the limitations and necessary extensions of the presented modeling. As example, the consideration of residual stresses, a more differentiated resolution of the plaque components and the coupling to blood flow simulation were mentioned as possible extensions.

In the second main part the application of *two-phase steels* to multiscale computations was investigated. Exemplarily, the two-phase composition of a dual-phase steel this kind of steel – it consists of a (weaker) ferritic and a (harder) martensitic phase – was introduced including its mechanical properties, which are a high strength and a good formability. Additionally, the metallographic treatment obtaining the microstructural composition of such steel was discussed. Afterwards we gave a possible constitutive modeling for the individual phases of a two-phase steel using the finite J_2-plasticity model. Since in most applications the length scale between the microstructural multiphase composition (micrometer) and the macroscopic dimension of structural components (centimeter to meter) differs strongly, we decided to apply a homogenization method, the direct micro-macro transition approach, to the numerical simulation of such materials. In common, the crucial part of this treatment is the estimation of the representative volume element (RVE), on which the microscopic boundary value problem is founded. On that account, we proposed a method to construct an analogous geometrical model for the real microstructure exhibiting similar mechanical behaviors but is characterized by a lower geometrical complexity. These models are called statistically similar representative volume elements (SSRVE) and their lower complexity results in a lower number of degrees of freedom in the finite element discretization. Consequently, the numerical effort in a multiscale computation is significantly reduced. The basic idea of this method is to construct these SSRVEs in such a way, that their statistical measures characterizing the inclusion morphology are similar to the values determined from the real microstructure of the steel. A least-square functional, which weights the difference between the statistical measures of the real structure and the SSRVE, was formulated and the minimization of this problem was done by an optimization procedure. Several numerical problems considering macroscopic homogeneous and inhomogeneous boundary value problems using a multiscale framework showed the verification of this method and the numerical efficiency compared to the application of "standard" RVEs. Finally, we discussed several aspects regarding the extension of the proposed SSRVE method to three-dimensional microstructures. Thereby, the application of additional statistical measures of higher order, another type for the parameterization of the inclusion morphology in the SSRVE and the reconstruction of three-dimensional microstructures of dual-phase steels was focused on.

A Matrix Representation of Special Tensors.

The symmetry of the right Cauchy-Green tensor $\boldsymbol{C}$, i.e., in index notation $C^{AB} = C^{BA}$, and the constitutive equation for the second Piola-Kirchhoff stresses

$$\boldsymbol{S} = 2\,\partial_C \psi \tag{A.1}$$

yields the symmetry of $\boldsymbol{S}$, i.e., $S^{AB} = S^{BA}$. In general, the associated tangent moduli $\mathbb{C} = 4\,\partial^2_{CC}\psi$ is represented by 81 independent components:

	11	22	33	12	23	13	21	32	31
11	$\mathbb{C}_{1111}$	$\mathbb{C}_{1122}$	$\mathbb{C}_{1133}$	$\mathbb{C}_{1112}$	$\mathbb{C}_{1123}$	$\mathbb{C}_{1113}$	$\mathbb{C}_{1121}$	$\mathbb{C}_{1132}$	$\mathbb{C}_{1131}$
22	$\mathbb{C}_{2211}$	$\mathbb{C}_{2222}$	$\mathbb{C}_{2233}$	$\mathbb{C}_{2212}$	$\mathbb{C}_{2223}$	$\mathbb{C}_{2213}$	$\mathbb{C}_{2221}$	$\mathbb{C}_{2232}$	$\mathbb{C}_{2231}$
33	$\mathbb{C}_{3311}$	$\mathbb{C}_{3322}$	$\mathbb{C}_{3333}$	$\mathbb{C}_{3312}$	$\mathbb{C}_{3323}$	$\mathbb{C}_{3313}$	$\mathbb{C}_{3321}$	$\mathbb{C}_{3332}$	$\mathbb{C}_{3331}$
12	$\mathbb{C}_{1211}$	$\mathbb{C}_{1222}$	$\mathbb{C}_{1233}$	$\mathbb{C}_{1212}$	$\mathbb{C}_{1223}$	$\mathbb{C}_{1213}$	$\mathbb{C}_{1221}$	$\mathbb{C}_{1232}$	$\mathbb{C}_{1231}$
23	$\mathbb{C}_{2311}$	$\mathbb{C}_{2322}$	$\mathbb{C}_{2333}$	$\mathbb{C}_{2312}$	$\mathbb{C}_{2323}$	$\mathbb{C}_{2313}$	$\mathbb{C}_{2321}$	$\mathbb{C}_{2332}$	$\mathbb{C}_{2331}$
13	$\mathbb{C}_{1311}$	$\mathbb{C}_{1322}$	$\mathbb{C}_{1333}$	$\mathbb{C}_{1312}$	$\mathbb{C}_{1323}$	$\mathbb{C}_{1313}$	$\mathbb{C}_{1321}$	$\mathbb{C}_{1332}$	$\mathbb{C}_{1331}$
21	$\mathbb{C}_{2111}$	$\mathbb{C}_{2122}$	$\mathbb{C}_{2133}$	$\mathbb{C}_{2112}$	$\mathbb{C}_{2123}$	$\mathbb{C}_{2113}$	$\mathbb{C}_{2121}$	$\mathbb{C}_{2132}$	$\mathbb{C}_{2131}$
32	$\mathbb{C}_{3211}$	$\mathbb{C}_{3222}$	$\mathbb{C}_{3233}$	$\mathbb{C}_{3212}$	$\mathbb{C}_{3223}$	$\mathbb{C}_{3213}$	$\mathbb{C}_{3221}$	$\mathbb{C}_{3232}$	$\mathbb{C}_{3231}$
31	$\mathbb{C}_{3111}$	$\mathbb{C}_{3122}$	$\mathbb{C}_{3133}$	$\mathbb{C}_{3112}$	$\mathbb{C}_{3123}$	$\mathbb{C}_{3113}$	$\mathbb{C}_{3121}$	$\mathbb{C}_{3132}$	$\mathbb{C}_{3131}$

(A.2)

Due to the symmetry of $\boldsymbol{C}$ the following symmetry properties of $\mathbb{C}$ are valid

$$\mathbb{C}_{ABCD} = \mathbb{C}_{BACD} = \mathbb{C}_{ABDC} = \mathbb{C}_{BADC},$$

so that we can reduce $\mathbb{C}$ first to the form depending on 36 components:

	11	22	33	12	23	13
11	$\mathbb{C}_{1111}$	$\mathbb{C}_{1122}$	$\mathbb{C}_{1133}$	$\frac{1}{2}(\mathbb{C}_{1112}$ $+\mathbb{C}_{1121})$	$\frac{1}{2}(\mathbb{C}_{1123}$ $+\mathbb{C}_{1132})$	$\frac{1}{2}(\mathbb{C}_{1113}$ $+\mathbb{C}_{1131})$
22	$\mathbb{C}_{2211}$	$\mathbb{C}_{2222}$	$\mathbb{C}_{2233}$	$\frac{1}{2}(\mathbb{C}_{2212}$ $+\mathbb{C}_{2221})$	$\frac{1}{2}(\mathbb{C}_{2223}$ $+\mathbb{C}_{2232})$	$\frac{1}{2}(\mathbb{C}_{2213}$ $+\mathbb{C}_{2231})$
33	$\mathbb{C}_{3311}$	$\mathbb{C}_{3322}$	$\mathbb{C}_{3333}$	$\frac{1}{2}(\mathbb{C}_{3312}$ $+\mathbb{C}_{3321})$	$\frac{1}{2}(\mathbb{C}_{3323}$ $+\mathbb{C}_{3332})$	$\frac{1}{2}(\mathbb{C}_{3313}$ $+\mathbb{C}_{3331})$
12	$\frac{1}{2}(\mathbb{C}_{1211}$ $+\mathbb{C}_{2111})$	$\frac{1}{2}(\mathbb{C}_{1222}$ $+\mathbb{C}_{2122})$	$\frac{1}{2}(\mathbb{C}_{1233}$ $+\mathbb{C}_{2133})$	$\frac{1}{4}(\mathbb{C}_{1212}$ $+\mathbb{C}_{1221}$ $+\mathbb{C}_{2112}$ $+\mathbb{C}_{2121})$	$\frac{1}{4}(\mathbb{C}_{1223}$ $+\mathbb{C}_{1232}$ $+\mathbb{C}_{2123}$ $+\mathbb{C}_{2132})$	$\frac{1}{4}(\mathbb{C}_{1213}$ $+\mathbb{C}_{1231}$ $+\mathbb{C}_{2113}$ $+\mathbb{C}_{2131})$
23	$\frac{1}{2}(\mathbb{C}_{2311}$ $+\mathbb{C}_{3211})$	$\frac{1}{2}(\mathbb{C}_{2322}$ $+\mathbb{C}_{3222})$	$\frac{1}{2}(\mathbb{C}_{2333}$ $+\mathbb{C}_{3233})$	$\frac{1}{4}(\mathbb{C}_{2312}$ $+\mathbb{C}_{2321}$ $+\mathbb{C}_{3212}$ $+\mathbb{C}_{3221})$	$\frac{1}{4}(\mathbb{C}_{2323}$ $+\mathbb{C}_{2332}$ $+\mathbb{C}_{3223}$ $+\mathbb{C}_{3232})$	$\frac{1}{4}(\mathbb{C}_{2313}$ $+\mathbb{C}_{2331}$ $+\mathbb{C}_{3213}$ $+\mathbb{C}_{3231})$
13	$\frac{1}{2}(\mathbb{C}_{1311}$ $+\mathbb{C}_{3111})$	$\frac{1}{2}(\mathbb{C}_{1322}$ $+\mathbb{C}_{3122})$	$\frac{1}{2}(\mathbb{C}_{1333}$ $+\mathbb{C}_{3133})$	$\frac{1}{4}(\mathbb{C}_{1312}$ $+\mathbb{C}_{1321}$ $+\mathbb{C}_{3112}$ $+\mathbb{C}_{3121})$	$\frac{1}{4}(\mathbb{C}_{1323}$ $+\mathbb{C}_{1332}$ $+\mathbb{C}_{3123}$ $+\mathbb{C}_{3132})$	$\frac{1}{4}(\mathbb{C}_{1313}$ $+\mathbb{C}_{1331}$ $+\mathbb{C}_{3113}$ $+\mathbb{C}_{3131})$

(A.3)

which appears in a more compact form as

	11	22	33	12	23	13
11	$\mathbb{C}_{1111}$	$\mathbb{C}_{1122}$	$\mathbb{C}_{1133}$	$\mathbb{C}_{1112}$	$\mathbb{C}_{1123}$	$\mathbb{C}_{1113}$
22	$\mathbb{C}_{2211}$	$\mathbb{C}_{2222}$	$\mathbb{C}_{2233}$	$\mathbb{C}_{2212}$	$\mathbb{C}_{2223}$	$\mathbb{C}_{2213}$
33	$\mathbb{C}_{3311}$	$\mathbb{C}_{3322}$	$\mathbb{C}_{3333}$	$\mathbb{C}_{3312}$	$\mathbb{C}_{3323}$	$\mathbb{C}_{3313}$
12	$\mathbb{C}_{1211}$	$\mathbb{C}_{1222}$	$\mathbb{C}_{1233}$	$\mathbb{C}_{1212}$	$\mathbb{C}_{1223}$	$\mathbb{C}_{1213}$
23	$\mathbb{C}_{2311}$	$\mathbb{C}_{2322}$	$\mathbb{C}_{2333}$	$\mathbb{C}_{2312}$	$\mathbb{C}_{2323}$	$\mathbb{C}_{2313}$
13	$\mathbb{C}_{1311}$	$\mathbb{C}_{1322}$	$\mathbb{C}_{1333}$	$\mathbb{C}_{1312}$	$\mathbb{C}_{1323}$	$\mathbb{C}_{1313}$

(A.4)

Since the additional relation

$$\frac{\partial^2 \psi}{\partial C_{AB} \partial C_{CD}} = \frac{\partial^2 \psi}{\partial C_{CD} \partial C_{AB}}$$

holds, it follows the well-known matrix representation of $\mathbb{C}$ with 21 independent components:

	11	22	33	12	23	13
11	$\mathbb{C}_{1111}$	$\mathbb{C}_{1122}$	$\mathbb{C}_{1133}$	$\mathbb{C}_{1112}$	$\mathbb{C}_{1123}$	$\mathbb{C}_{1113}$
22		$\mathbb{C}_{2222}$	$\mathbb{C}_{2233}$	$\mathbb{C}_{2212}$	$\mathbb{C}_{2223}$	$\mathbb{C}_{2213}$
33			$\mathbb{C}_{3333}$	$\mathbb{C}_{3312}$	$\mathbb{C}_{3323}$	$\mathbb{C}_{3313}$
12				$\mathbb{C}_{1212}$	$\mathbb{C}_{1223}$	$\mathbb{C}_{1213}$
23		*sym*			$\mathbb{C}_{2323}$	$\mathbb{C}_{2313}$
13						$\mathbb{C}_{1313}$

(A.5)

This is the representation of $\mathbb{C}$ in the most general case of anisotropic elasticity, namely the triclinic case. The vector representations of $\boldsymbol{S}$ and $\boldsymbol{C}$ are then given by

$$\begin{aligned} \boldsymbol{S} &= [S_{11} \quad S_{22} \quad S_{33} \quad | S_{12} \quad S_{23} \quad S_{13}]^T , \\ \boldsymbol{C} &= [C_{11} \quad C_{22} \quad C_{33} \quad | 2\,C_{12} \quad 2\,C_{23} \quad 2\,C_{13}]^T . \end{aligned}$$

B Definition of Convexity Conditions

In general the following implications hold for the subclasses of the convexity:

$$\textit{convexity} \;\Rightarrow\; \textit{polyconvexity} \;\Rightarrow\; \textit{quasiconvexity} \;\Rightarrow\; \textit{rank-one convexity}$$

The converse implications are not true; for more information we refer to Dacorogna [53], Šilhavý [232] and reference therein. Here, we only summarize the definition regarding the different notions of convexity. For further information we refer to e. g. Ball [6; 7], Marsden and Hughes [142], Dacorogna [53] and Šilhavý [232] and the references in the following.

For a scalar-valued tensor functions in terms of the deformation gradient $\boldsymbol{F}$, the corresponding convexity condition reads

$$\psi(\lambda \boldsymbol{F}_1 + (1-\lambda)\boldsymbol{F}_2) \leq \lambda\psi(\boldsymbol{F}_1) + (1-\lambda)\psi(\boldsymbol{F}_2) \quad \forall\, \boldsymbol{F}_1, \boldsymbol{F}_2 \in \mathbb{R}^{3\times 3},\ \lambda \in [0,1]\,, \tag{B.1}$$

cf. e.g. Schröder [191]. Note, strictness can be achieved in the previous and the following conditions by $<$ instead $\leq$, $\boldsymbol{F}_1 \neq \boldsymbol{F}_2$ and $\lambda \in]0,1[$.

Definition of Polyconvexity: $\boldsymbol{F} \mapsto \psi(\boldsymbol{F})$ is polyconvex if and only if there exists a function $P : \mathbb{R}^{3\times 3} \times \mathbb{R}^{3\times 3} \times \mathbb{R} \mapsto \mathbb{R}$ (in general non-unique) such that

$$\psi(\boldsymbol{F}) = \mathcal{P}(\boldsymbol{F}, \operatorname{Cof}\boldsymbol{F}, \det\boldsymbol{F})\,, \tag{B.2}$$

and the function $\mathbb{R}^{19} \mapsto \mathbb{R},\ (\boldsymbol{F}, \operatorname{Cof}\boldsymbol{F}, \det\boldsymbol{F}) \mapsto \mathcal{P}(\boldsymbol{F}, \operatorname{Cof}\boldsymbol{F}, \det\boldsymbol{F})$ is convex for all points $\boldsymbol{X} \in \mathbb{R}^3$.

Note that the arguments $(\boldsymbol{F}, \operatorname{Cof}\boldsymbol{F}, \det\boldsymbol{F})$ are the essential elements in the definition of the transport theorems (2.13), (2.14) and (2.15). For a better understanding of the notion of polyconvexity we consider an energy function equal to the third principal invariant in terms of $\boldsymbol{F}$, i.e. $\psi(\boldsymbol{F}) = \det\boldsymbol{F} \quad \forall\, \boldsymbol{F} \in \mathbb{R}^{3\times 3}$. Although the function is non-convex with respect to $\boldsymbol{F}$, it is polyconvex because $\psi(\boldsymbol{F}) = \mathcal{P}(\det\boldsymbol{F}) = \det\boldsymbol{F}$ is convex with respect to its argument $(\det\boldsymbol{F})$. Finally, the setup of an energy function in the additive form

$$\psi(\boldsymbol{F}) = \mathcal{P}_1(\boldsymbol{F}) + \mathcal{P}_2(\operatorname{Cof}\boldsymbol{F}) + \mathcal{P}_3(\det\boldsymbol{F}) \tag{B.3}$$

is polyconvex, if $\mathcal{P}_i$, $i = 1,2,3$ are convex in the associated variable, cf. Corollary 3.2 in Hartmann and Neff [92], Schröder and Neff [193].

Definition of Quasiconvexity: The elastic stored energy is quasiconvex whenever for all $\mathcal{B}_0 \subset \mathbb{R}^3$, all constant $\boldsymbol{F} = \bar{\boldsymbol{F}} \in \mathbb{R}^{3\times 3}$ and all $\boldsymbol{w} \in C_0^\infty(\mathcal{B}_0)$, satisfying $\boldsymbol{w} = \boldsymbol{0}$ on $\partial\mathcal{B}_0$, the integral inequality

$$\int_{\mathcal{B}_0} \psi(\bar{\boldsymbol{F}} + \operatorname{Grad}\boldsymbol{w})\ \mathrm{d}V \geq \int_{\mathcal{B}_0} \psi(\bar{\boldsymbol{F}})\ \mathrm{d}V = \psi(\bar{\boldsymbol{F}}) \times \operatorname{Vol}(\mathcal{B}_0) \tag{B.4}$$

is valid, Morrey [154].

Together with fulfillment of the growth condition $\psi(\boldsymbol{F}) \leq c_1\|\boldsymbol{F}\|^p + c_2$ with $c_1 > 0$ and $c_2, p > 1$ the quasiconvexity yields a sufficient condition for sequential weak lower semicontinuity (s.w.l.s.).

Definition of Rank-One Convexity: The energy function $\psi(\boldsymbol{F})$ is rank-one convex whenever

$$\psi(\boldsymbol{F} + \lambda\boldsymbol{\eta}\otimes\boldsymbol{\zeta}) \;\leq\; \psi(\boldsymbol{F}) + \lambda[\psi(\boldsymbol{F} + \boldsymbol{\eta}\otimes\boldsymbol{\zeta}) - \psi(\boldsymbol{F})] \tag{B.5}$$

holds $\forall\ \boldsymbol{F} \in \mathbb{R}^{3\times3}$, $\forall\ \boldsymbol{\eta}, \boldsymbol{\zeta} \in \mathbb{R}^3\backslash\{\boldsymbol{0}\}$, $\lambda \in [0,1]$. This condition has the same form as the convexity definition (B.1) until the term $\Delta\boldsymbol{F} = \boldsymbol{F}_1 - \boldsymbol{F}_2$ is replaced by $(\boldsymbol{\eta} \otimes \boldsymbol{\zeta})$. The previous definition can be reformulated for once differentiable $\psi(\boldsymbol{F})$ to

$$[\boldsymbol{P}(\boldsymbol{F}) - \boldsymbol{P}(\boldsymbol{F} + \boldsymbol{\eta} \otimes \boldsymbol{\zeta})] : (\boldsymbol{\eta} \otimes \boldsymbol{\zeta}) \ \leq\ 0 \quad \forall\ \boldsymbol{F} \in \mathbb{R}^{3\times3},\ \forall\ \boldsymbol{\eta}, \boldsymbol{\zeta} \in \mathbb{R}^3\backslash\{\boldsymbol{0}\}\ . \tag{B.6}$$

Thus, $\psi(\boldsymbol{F})$ is rank-one convex if the first Piola-Kirchhoff stresses are monotone increasing with respect to all rank-one deformation tensors. If $\psi(\boldsymbol{F})$ is twice differentiable, i.e. $\partial^2_{\boldsymbol{F}\boldsymbol{F}}\psi(\boldsymbol{F}) =: \mathbb{A}$, the alternative rank-one convexity condition reads

$$(\boldsymbol{\eta} \otimes \boldsymbol{\zeta}) : \mathbb{A} : (\boldsymbol{\eta} \otimes \boldsymbol{\zeta}) \ \geq\ 0 \quad \forall\ \boldsymbol{F} \in \mathbb{R}^{3\times3},\ \forall\ \boldsymbol{\eta}, \boldsymbol{\zeta} \in \mathbb{R}^3\backslash\boldsymbol{0}\ , \tag{B.7}$$

which is referred to as Legendre-Hadamard-Ellipticity.

C Incremental and variational quantities for the $\bar{\boldsymbol{F}}$-approach

During the derivation of the $\bar{\boldsymbol{F}}$-approach in section 3.6 several mathematical transformation are done, whose intermediate steps are omitted for reasons of clarity and comprehensibility. For the reader who want to figure out the details of these steps we give here some essential relations. As mentioned in the relevant section we consider the operators

$$\bar{\boldsymbol{F}} = \underbrace{J^{-1/3}\boldsymbol{F}}_{\boldsymbol{F}_{\text{iso}}}\underbrace{\Theta^{1/3}\mathbf{1}}_{\bar{\boldsymbol{F}}_{\text{vol}}} = \left(\frac{\Theta}{J}\right)^{1/3}\boldsymbol{F} \qquad \bar{\boldsymbol{C}} = \bar{\boldsymbol{F}}^T\bar{\boldsymbol{F}} = \left(\frac{\Theta}{J}\right)^{2/3}\boldsymbol{F}^T\boldsymbol{F}\,, \tag{C.1}$$

which are associated to the deformation gradient $\boldsymbol{F}$ and the right Cauchy-Green tensor $\boldsymbol{C}$. Thereby we consider $J = \det\boldsymbol{F}$ and the volume dilatation Θ as a element-wise constant quantity. For the three-field formulation of the weak form (3.54) in terms of the unknown fields $\boldsymbol{u}$, J, Θ, we need the variations and for the subsequent linearization the incremental forms of the operator $\bar{\boldsymbol{C}}$, i.e.

$$\begin{aligned}
\delta_{\boldsymbol{u}}\bar{\boldsymbol{C}} &= \left(\frac{\Theta}{J}\right)^{2/3}\delta\boldsymbol{C}\,, & \Delta_{\boldsymbol{u}}\bar{\boldsymbol{C}} &= \left(\frac{\Theta}{J}\right)^{2/3}\Delta\boldsymbol{C}\,,\\
\delta_J\bar{\boldsymbol{C}} &= -\frac{2}{3}\left(\frac{\Theta}{J}\right)^{2/3}\left(\frac{\delta J}{J}\right)\boldsymbol{C}\,, & \Delta_J\bar{\boldsymbol{C}} &= -\frac{2}{3}\left(\frac{\Theta}{J}\right)^{2/3}\left(\frac{\Delta J}{J}\right)\boldsymbol{C}\,,\\
\delta_\Theta\bar{\boldsymbol{C}} &= \frac{2}{3}\left(\frac{\Theta}{J}\right)^{2/3}\left(\frac{\delta\Theta}{\Theta}\right)\boldsymbol{C}\,, & \Delta_\Theta\bar{\boldsymbol{C}} &= \frac{2}{3}\left(\frac{\Theta}{J}\right)^{2/3}\left(\frac{\Delta\Theta}{\Theta}\right)\boldsymbol{C}\,.
\end{aligned} \tag{C.2}$$

Additionally the linearization requires the increment of the variations in the latter equations, i.e.

$$\begin{aligned}
\Delta_{\boldsymbol{u}}\delta_{\boldsymbol{u}}\bar{\boldsymbol{C}} &= \left(\frac{\Theta}{J}\right)^{2/3}\Delta\delta\boldsymbol{C}\,,\\
\Delta_J\delta_{\boldsymbol{u}}\bar{\boldsymbol{C}} &= -\frac{2}{3}\left(\frac{\Theta}{J}\right)^{2/3}\frac{\Delta J}{J}\delta\boldsymbol{C}\,,\\
\Delta_\Theta\delta_{\boldsymbol{u}}\bar{\boldsymbol{C}} &= \frac{2}{3}\left(\frac{\Theta}{J}\right)^{2/3}\frac{\Delta\Theta}{\Theta}\delta\boldsymbol{C}\,,\\
\Delta_{\boldsymbol{u}}\delta_J\bar{\boldsymbol{C}} &= -\frac{2}{3}\left(\frac{\Theta}{J}\right)^{2/3}\frac{\delta J}{J}\Delta\boldsymbol{C}\,,\\
\Delta_J\delta_J\bar{\boldsymbol{C}} &= \frac{2}{3}\left(\frac{\Theta}{J}\right)^{2/3}\left(\frac{5}{3}\frac{\Delta J\delta J}{J^2} - \frac{\Delta\delta J}{J}\right)\boldsymbol{C}\,,\\
\Delta_\Theta\delta_J\bar{\boldsymbol{C}} &= -\frac{4}{9}\left(\frac{\Theta}{J}\right)^{2/3}\frac{\Delta\Theta}{\Theta}\frac{\delta J}{J}\boldsymbol{C}\,,\\
\Delta_{\boldsymbol{u}}\delta_\Theta\bar{\boldsymbol{C}} &= \frac{2}{3}\left(\frac{\Theta}{J}\right)^{2/3}\frac{\delta\Theta}{\Theta}\Delta\boldsymbol{C}\,,\\
\Delta_J\delta_\Theta\bar{\boldsymbol{C}} &= -\frac{4}{9}\left(\frac{\Theta}{J}\right)^{2/3}\frac{\delta\Theta}{\Theta}\frac{\Delta J}{J}\boldsymbol{C}\,,\\
\Delta_\Theta\delta_\Theta\bar{\boldsymbol{C}} &= \frac{2}{3}\left(\frac{\Theta}{J}\right)^{2/3}\left(-\frac{1}{3}\frac{\Delta\Theta\delta\Theta}{\Theta^2} + \frac{\Delta\delta\Theta}{\Theta}\right)\boldsymbol{C}\,.
\end{aligned} \tag{C.3}$$

References

[1] H. Abè, K. Hayashi, and M. Sato, editors. *Data book on mechanical properties of living cells, tissues, and organs*. Springer, Tokio, 1996.

[2] M. Auer, R. Stollberger, P. Regitnig, F. Ebner, and G. Holzapfel. 3-d reconstruction of tissue components for atherosclerotic human arteries using ex vivo high-resolution mri. *IEEE Transactions on medical Imaging*, 25:345–357, 2006.

[3] S. Balay, V. Eijkhout, W. D. Gropp, L. C. McInnes, and B. F. Smith. Efficient management of parallelism in object oriented numerical software libraries. In E. Arge, A. M. Bruaset, and H. P. Langtangen, editors, *Modern Software Tools in Scientific Computing*, pages 163–202. Birkhäuser Press, 1997.

[4] S. Balay, J. Brown, , K. Buschelman, V. Eijkhout, W. D. Gropp, D. Kaushik, M. G. Knepley, L. C. McInnes, B. F. Smith, and H. Zhang. PETSc users manual. Technical Report ANL-95/11 - Revision 3.1, Argonne National Laboratory, 2010.

[5] S. Balay, J. Brown, K. Buschelman, W. D. Gropp, D. Kaushik, M. G. Knepley, L. C. McInnes, B. F. Smith, and H. Zhang. PETSc Web page, 2011. http://www.mcs.anl.gov/petsc.

[6] J. Ball. Convexity conditions and existence theorems in nonlinear elasticity. *Archive for Rational Mechanics and Analysis*, 63:337–403, 1976.

[7] J. M. Ball. Constitutive inequalities and existence theorems in nonlinear elastostatics. In R. Knops, editor, *Nonlinear Analysis and Mechanics*, volume 1, pages 187–241. Heriot-Watt Symposium, 1977.

[8] D. Balzani. *Polyconvex anisotropic energies and modeling of damage applied to arterial walls*. Phd-thesis, University Duisburg-Essen, Verlag Glückauf Essen, 2006.

[9] D. Balzani. Simulation of deformation, damage and residual stresses in arterial walls. *Advanced Engineering Materials*, 10(4):315–321, 2008.

[10] D. Balzani, P. Neff, J. Schröder, and G. Holzapfel. A polyconvex framework for soft biological tissues. Adjustment to experimental data. *International Journal of Solids and Structures*, 43(20):6052–6070, 2006.

[11] D. Balzani, J. Schröder, and D. Gross. Simulation of discontinuous damage incorporating residual stresses in circumferentially overstretched atherosclerotic arteries. *Acta Biomaterialia*, 2(6):609–618, 2006.

[12] D. Balzani, J. Schröder, and D. Brands. FE^2-simulation of microheterogeneous steels based on statistically similar RVE's. In *Proceedings of the IUTAM Symposium on Variational Concepts with applications to the mechanics of materials, September 22-26, 2008, Bochum, Germany*, 2009.

[13] D. Balzani, D. Brands, J. Schröder, and C. Carstensen. Sensitivity analysis of statistical measures for the reconstruction of microstructures based on the minimization of generalized least-square functionals. *Technische Mechanik*, 30:297–315, 2010.

[14] D. Balzani, D. Böse, D. Brands, R. Erbel, A. Klawonn, O. Rheinbach, and J. Schröder. Parallel simulation of patient-specific atherosclerotic arteries for the enhancement of intravascular ultrasound diagnostics. *Engineering Computations*, 29(8), 2011. Accepted 01/2012 for publication, EarlyCite.

[15] G. Baretton, C. Kirkpatrick, and B. Bültmann. Arteriosklerose – Atherosklerose. In W. Böcker, H. Denk, and P. Heitz, editors, *Pathologie*, volume 3, chapter 20.2, pages 484–493. Elsevier GmbH, München, Urban & Fischer Verlag, 2004.

[16] H.-J. Bargel and G. Schulze, editors. *Werkstoffkunde (7. Auflage)*. Springer Berlin / Heidelberg, 2000.

[17] A. Bastos, S. Zaefferer, D. Raabe, and C. Schuh. Characterization of the microstructure and texture of nanostructured electrodeposited NiCo by use of electron backscatter diffraction (EBSD). *Acta Materialia*, 54:2451– 2462, 2006.

[18] K. J. Bathe. *Finite Elemente Methoden*. Springer, 1986.

[19] M. Beran. *Statistical continuum theories*. Wiley, 1968.

[20] D. Bergel. *The visco-elastic properties of the arterial wall*. PhD thesis, University of London, 1960.

[21] W. Bergmann. *Werkstofftechnik - Teil 1: Grundlagen*. Carl Hanser Verlag München Wien, 2000.

[22] B. Bersch. *Experimentelle Untersuchung der Beziehung zwischen dem Koronarkalkgehalt der Gefäßwand und der Absorption von β-Strahlung im Rahmen der koronarvaskulären Brachytherapie: Eine Studie mit intravaskulärem Ultraaschall in vitro*. PhD thesis, Universität Duisburg-Essen, 2005.

[23] D. Bertsekas. *Constrained Optimization and Lagrange Multiplier Methods*. Academic Press, New York, 1982.

[24] J. Betten. *Tensorrechung für Ingenieure*. Teubner-Verlag, Stuttgart, 1987.

[25] J. Betten. Anwendungen von Tensorfunktionen in der Kontinuumsmechanik anisotroper Materialien. *Zeitschrift für angewandte Mathematik und Mechanik*, 78 (8):507–521, 1998.

[26] J. P. Boehler. On irreducible representations for isotropic scalar functions. *Zeitschrift für angewandte Mathematik und Mechanik*, 57:323–327, 1977.

[27] J. P. Boehler. Lois de comportement anisotrope des milieux continus. *Journal de Mécanique*, 17(2):153–190, 1978.

[28] J. P. Boehler. A simple derivation of respresentations for non-polynomial constitutive equations in some cases of anisotropy. *Zeitschrift für angewandte Mathematik und Mechanik*, 59:157–167, 1979.

[29] J. P. Boehler, editor. *Application of tensor functions in solid mechanics*. Number 292 in CISM courses and lectures. Springer-Verlag, Wien, 1987.

[30] D. Böse, C. von Birgelen, and R. Erbel. Intravascular ultrasound for the evaluation of therapies targeting coronary atherosclerosis. *Journal of the American College of Cardiology*, 49(9):925–932, 2007.

[31] D. Brands, A. Klawonn, O. Rheinbach, and J. Schöder. Modelling and convergence in arterial wall simulations using a parallel FETI solution strategy. *Computer Methods in Biomechanics and Biomedical Engineering*, 11:569–583, 2008.

[32] D. Brands, J. Schröder, A. Klawonn, O. Rheinbach, D. Böse, and R. Erbel. Numerical simulation of aterial walls based on IVUS–data. *Proceedings in Applied Mathematics and Mechanics*, 9:75–78, 2009.

[33] W. Brekelmans, R. Smit, and H. Meijer. Prediction of the mechanical behaviour of nonlinear heterogeneous systems by multi-level finite element modelling. *Computer Methods in Applied Mechanics and Engineering*, 155:181–192, 1998.

[34] J. Bresenham. Algorithm for computer control of a digital plotter. *IBM Systems Journal*, 4(1):25–30, 1965. reprinted in Interactive Computer Graphics, Herbert Freeman ed., 1980, and Seminal Graphics: Pioneering Efforts That Shaped The Field, Rosalee Wolfe ed., ACM SIGGRAPH, 1998.

[35] S. Brinkhues, D. Balzani, and G. Holzapfel. Simulation of damage hysteresis in biological soft tissues. *Proceedings of Applied Mathematics and Mechanics*, 9:155–156, 2009.

[36] S. Brinkhues, A.-K. Tielke, and J. Schröder. Sensitivity analysis of plaque components within arterial wall simulations. *Proceedings of Applied Mathematics and Mechanics*, 10(1):73–74, 2010.

[37] W. Brown. Solid mixture permettivities. *Journal of Computational Physics*, 23: 1514–1517, 1955.

[38] V. A. Buryachenko. *Micromechanics of heterogeneous materials*. Springer Verlag, 2007.

[39] P. Canham, H. Finlay, J. Dixon, D. Boughner, and A. Chen. Measurments from light and polarised light microscopy of human coronary arteries fixed at distending pressure. *Cardiovascular Research*, 23:973–982, 1989.

[40] T. Carew, R. Vaishnav, and D. Patel. Compressibility of the arterial wall. *Circulation Research*, 23:61–68, 1968.

[41] P. Chakraborti and M. Mitra. Microtructure and tensile properties of high strength duplex ferrite-martensite (dfm) steels. *Material Science and Engineering*, 466:123–133, 2007.

[42] S. Chen and J. Carrol. 3-d reconstruction of coronary arterial tree to optimize angiographic visualization. *IEEE Transactions on Medical Imaging*, 19:318–336, 2000.

[43] R. P. Choudhury and Z. A. Fayad. Imaging of atherosclerosis. Coronary wall imaging with MRI. *Journal of Cardiovascular Risk*, 9:263–270, 2002.

[44] C. Choung and Y. Fung. Compressibility and constitutive equations of arterial wall in radial compression experiments. *Journal of Biomechanics*, 17:35–40, 1984.

[45] C. Chuong and Y. Fung. On residal stress in arteries. *Journal of Biomechanical Engineering*, 108:189–191, 1986.

[46] P. Ciarlet and G. Geymonat. Sur les lois de comportement en élasticité non-linéaire compressible. *Les Comptes Rendus de l'Académie des Sciences*, 295:423–426, 1982.

[47] P. G. Ciarlet. *Mathematical Elasticity, Volume 1: Three Dimensional Elasticity*. Elsevier Science Publishers B.V., North Holland, 1988.

[48] J. Clark and S. Glagov. Structural integration of the arterial wall. *Laboratory Investigation*, 40(6):587–602, 1979.

[49] J. Clark and S. Glagov. Transmural organization of the arterial media. The lamellar unit revisited. *Arteriosclerosis, Thrombosis, and Vascular Biology*, 5:19–34, 1985.

[50] R. J. E. Clausius. Über eine veränderte Form des zweiten Hauptsatzes der mechanischen Wärmetheorie. *Annalen der Physik*, 93(12):481–506, 1854.

[51] B. D. Coleman and W. Noll. On the thermostatics of continuous media. *Archive for Rational Mechanics and Analysis*, 4:97–128, 1959.

[52] A. R. Conn, K. Scheinberg, and L. N. Vicente. *Introduction to derivative-free optimization*, volume 8 of *MPS/SIAM Series on Optimization*. Society for Industrial and Applied Mathematics (SIAM), Philadelphia, PA, 2009. ISBN 978-0-898716-68-9.

[53] B. Dacorogna. *Direct Methods in the Calculus of Variations.*, volume 78 of *Applied Mathematical Sciences*. Springer, Berlin, first edition, 1989.

[54] R. G. Davies. Influence of martensite composition and content on the properties of dual phase steels. *Metallurgica and Materials Transactions A*, 9:671–679, 1978.

[55] T. A. Davis. A column pre-ordering strategy for the unsymmetric-pattern multifrontal method. *ACM Transaction on Mathematical Software*, 30(2):165–195, June 2004. URL `http://doi.acm.org/10.1145/992200.992205`.

[56] R. de Boer and J. Schröder. *Tensor calculus for engineers with applications to continuum and computational mechanics*. Springer, manuscript, to be published in 2011.

[57] J. A. de Brux, H. F. Dorn, J. B. Duguid, H. Hamperl, W. S. Hartroft, J. Higginson, J. F. A. McManus, T. Miyaji, J. C. Paterson, C. Restrepo, J. P. Strong, A. I. Strukov, C. Tejada, H. Ungar, and P. N. Wahi. Classification of atherosclerotic lesions. Technical Report 143, World Health Organization, 1958.

[58] E. A. de Souza Neto, D. Peric, M. Dutko, and D. R. J. Owen. Design of simple low order finite elements for large strain analysis of nearly incompressible solids. *International Journal of Solids and Structures*, 33:3277 – 3296, 1996.

[59] J. W. Demmel, S. C. Eisenstat, J. R. Gilbert, X. S. Li, and J. W. H. Liu. A supernodal approach to sparse partial pivoting. *SIAM J. Matrix Analysis and Applications*, 20(3):720–755, 1999.

[60] M. Y. Desai and J. A. Lima. Imaging of atherosclerosis using magnetic resonance: state of the art and future directions. *Current Atherosclerosis Reports*, 8:131–129, 2006.

[61] DESTATIS. Sterbefälle insgesamt 2009 nach den 10 häufigsten Todesursachen der International Statistical Classification of Diseases and Related Health Problems (ICD-10). Statistic, Statistisches Bundesamt Deutschland, 2010. URL `http://www.destatis.de`. visited on 8. Jan. 2011.

[62] W. Drugan and J. Willis. A micromechanics-based nonlocal constitutive equation and estimates of represantative volume element size for elastic composites. *Journal of the Mechanics and Physics of Solids*, 44:497–524, 1996.

[63] E. N. Dvorkin, D. Pantuso, and E. A. Repetto. A formulation of the MITC4 shell element for finite strain elasto-plastic analysis. *Computer Methods in Applied Mechanics and Engineering*, 125:17–40, 1995.

[64] V. Ebbing. *Design of Polyconvex Energy Functions for All Anisotropy Classes*. PhD thesis, Institut für Mechanik, Abteilung Bauwissenschaften, Fakultät für Ingenieurwissenschaften, Universität Duisburg-Essen, 2010.

[65] A. Ehret and M. Itskov. Modeling of anisotropic softening phenomena: Application to soft biological tissues. *International Journal of Plasticity*, 25:901–919, 2009.

[66] R. Erbel, N. Reinsch, B. Plicht, and S. Möhlenkamp. Diagnostik und Prävention kardiovaskulärer Erkrankungen. *Herz*, 32:351–355, 2007.

[67] A. C. Eringen. *Mechanics of continua*. John Wiley & Sons, 1967.

[68] A. Fallahi. Microstructure-properties correlation of dual phase steels produced by controlled rolling process. *Journal of Materials Sciences and Technology*, 18(5): 451–454, 2002.

[69] C. Farhat, M. Lesoinne, P. LeTallec, K. Pierson, and D. Rixen. FETI-DP: A dual-primal unified FETI method - part i: A faster alternative to the two-level FETI method. *International Journal for Numerical Methods in Engineering*, 50:1523–1544, 2001.

[70] J. Fessler and A. Macovski. Object-based 3-d reconstruction of arterial trees from magnetic resonance angiograms. *IEEE Transactions on Medical Imaging*, 10(1): 25–39, 1991.

[71] H. Finlay, L. McCullough, and P. Canham. Three-dimensional collagen organization of human brain arteries at different transmural pressures. *Journal of Vascular Research*, 32:301–312, 1995.

[72] L. Formaggia, D. Lamponi, and A. Quarteroni. One-dimensional models for blood flow in arteries. *Journal of Engineering Mathematics*, 47:251–276, 2003.

[73] L. Formaggia, A. Quarteroni, and A. Veneziani. In *Cardiovascular Mathematics*, volume 1 of *Modeling and simulation of the circulatory system*. Springer, 2009.

[74] C. Freischläger. *Konzepte zur Formulierung versteifungsfreier Volumenelemente*. PhD thesis, Universität Fridericiana zu Karlsruhe, 2000.

[75] M. Frigo and S. G. Johnson. The design and implementation of FFTW3. *Proceedings of the IEEE*, 93(2):216–231, 2005. Special issue on "Program Generation, Optimization, and Platform Adaptation".

[76] R. Fuchs. Zur Physiologie und Wachstumsmechanik des Blutgefäßsystems. *Archiv für die gesamte Physiologie*, 28, 1900.

[77] Y. Fung. *Biomechanics – Mechanical properties of living tissues*. Springer, New York, Berlin, Heidelberg, 1993.

[78] T. Gasser, R. Ogden, and G. Holzapfel. Hyperelastic modelling of arterial layers with distributed collagen fibre orientations. *Journal of the Royal Society Interface*, 3:15–35, 2006.

[79] T. C. Gasser and G. A. Holzapfel. A rate-independent elastoplastic constitutive model for (biological) fiber-reinforced composites at finite strains: Continuum basis, algorithmic formulation and finite element implementation. *Computational Mechanics*, 29(4-5):340–360, 2002.

[80] M. W. Gee, C. Förster, and W. A. Wall. A computational strategy for prestressing patient-specific biomechanical problems under finite deformation. *International Jorunal for Numerical Methods in Biomedical Engineering*, 26:52–72, 2010.

[81] M. Geers, V. Kouznetsova, and W. Brekelmans. Multi-scale first-order and second-order computational homogenization of microstructures towards continua. *International Journal for Multiscale Computational Engineering*, 1:371–386, 2003.

[82] S. A. I. Ghesquiere. *The role of phospholipases in atherosclerosis*. PhD thesis, Department of Molecular Genetics, Cardiovascular Research Institute Maastricht, Maastricht University, The Netherlands, 2006.

[83] S. Ghosh, K. Lee, and S. Moorthy. Multiple scale analysis of heterogeneous elastic structures using homogenization theory and voronoi cell finite element method. *International Journal of Solids and Structures*, 32:27–62, 1995.

[84] R. Glowinski and P. Le Tallec. Augmented lagrangian and operator-splitting methods in nonlinear mechanics. *Mathematics of Computation*, 58(197):451–452, 1992.

[85] G. Görge, J. Ge, C. von Birgelen, and R. Erbel. Intravasaler Ultraschal – Der neue Goldstandard? *Zeitschrift für Kardiologie*, 87:575–585, 1998.

[86] J. Grace and A. Young. *The algebra of invariants*. Cambridge University Press, Cambridge, 1903.

[87] S. Greenwald, J. Moore, A. Rachev, T. Kane, and J.-J. Meister. Experimental investigation of the distribution of residual strains in the artery wall. *Journal of Biomechanical Engineering*, 119:438–444, 1997.

[88] G. B. Gurevich. *Foundations of the theory of algebraic invariants.* Nordhoff, 1964.

[89] C. Guy and D. ffytche. *An Introduction To The Principles Of Medical Imaging.* Imperial College Press, 2005. Revised Edition.

[90] P. Halmos. *Finite-dimensional Vector Spaces.* Van Nostrand, New York, 1958.

[91] H.-C. Han and Y.-C. Fung. Longitudinal strain of canine and porcine aortas. *Journal of Biomechanics*, 28(5):637–641, 1995.

[92] S. Hartmann and P. Neff. Polyconvexity of generalized polynomial type hyperelastic strain energy functions for near incompressibility. *International Journal of Solids and Structures*, 40:2767–2791, 2003.

[93] Z. Hashin. Analysis of composite materials - a survey. *Journal of Applied Mechanics*, 50:481–505, 1983.

[94] D. Hilbert. Ueber die Theorie der algebraischen Formen. *Mathematische Analen*, 36:473–534, 1890.

[95] D. Hilbert. Ueber die vollen Invariantensysteme. *Mathematische Analen*, 42:313–373, 1893.

[96] R. Hill. A theory of the yielding and plastic flow of anisotropic metals. *Proceedings of the Royal Society London A*, 193:281–297, 1948.

[97] R. Hill. *The mathematical theory of plasticity.* Oxford Clarendon Press, 1950.

[98] R. Hill. On uniqueness and stability in the theory of finite elastic strains. *Journal of the Mechanics and Physics of Solids*, 5:229–241, 1957.

[99] R. Hill. Elastic properties of reinforced solids: some theoretical principles. *Journal of the Mechanics and Physics of Solids*, 11:357–372, 1963.

[100] G. Holzapfel. Determination of material models for arterial wallls from uniaxial extension tests and histological structure. *Journal of Theoretical Biology*, 238:290–302, 2006.

[101] G. Holzapfel and D. Kiousis. Interaction of balloon catheter-stent systems with atherosclerotic lesions: a computational study. In N. Chakfé and B. Durand, editors, *ESVB 2009 New Technologies in Vascular Biomaterials. Connecting Biomaterials to Arterial Structures*, chapter 7, pages 89–111. Europrot, Strasbourg, France, 2009.

[102] G. Holzapfel and R. Ogden. Modelling the layer-specific 3d residual stresses in arteries, with an application to the human aorta. *Journal of the Royal Society Interface*, 7:787–799, 2010.

[103] G. Holzapfel and R. Ogden. Review: Constitutive modelling of arteries. *Proceedings of the Royal Society London A*, 466:1551–1597, 2010.

[104] G. Holzapfel, M. Stadler, and C. Schulze-Bauer. A layer-specific three-dimensional model for the simulation of balloon angioplasty using magnetic resonance imaging and mechanical testing. *Annals of Biomechanical Engineering*, 30:753–767, 2002.

[105] G. Holzapfel, G. Sommer, T. Gasser, and P. Regitnig. Patient-specific biomechanical analysis of plaque rupture during balloon angioplasty using MRI and mechanical testing. In *Human Biomechanics 2006, Congress of the Czech Society of Biomechanics*, 2006.

[106] G. A. Holzapfel. *Nonlinear solid mechanics, a continuum approach for engineering.* Wiley, 2000.

[107] G. A. Holzapfel and R. W. Ogden, editors. *Mechanics of biological tissue.* Springer-Verlag, Heidelberg, 2006.

[108] G. A. Holzapfel and R. W. Ogden, editors. *Biomechanical Modelling at the Molecular, Cellular and Tissue Levels.* Number 508 in CISM Courses and Lectures. Springer Verlag, Wien, New York, 2009.

[109] G. A. Holzapfel and R. W. Ogden, editors. *Biomechanics of soft tissue in cardiovascular systems.* Number 441 in CISM Courses and Lectures. Springer-Verlag, Wien, 2003.

[110] G. A. Holzapfel, T. Gasser, and R. Ogden. A new constitutive framework for arterial wall mechanics and a comparative study of material models. *Journal of Elasticity*, 61:1–48, 2000.

[111] G. A. Holzapfel, T. Gasser, and R. Odgen. Comparison of a multi-layer structural model for arterial walls with a fung-type model, and issues of material stability. *Journal of Biomechanical Engineering*, 126:264–275, 2004.

[112] E. Hornbogen, G. Eggeler, and E. Werner. *Werkstoffe (9. Auflage)*. Springer-Verlag Berlin Heidelberg, 2008.

[113] H. C. Hu. On some variational principles in the theory of elasticity and the theory of plasticity. *Science Sinica*, 4:33–54, 1955.

[114] J. Humphrey. Continuum biomechanics of soft biological tissues. *Proceedings of the Royal Society of London, Series A : Mathematical, Physical and Engineering Science*, 459:3–46, 2002.

[115] J. Humphrey, J. Eberth, W. Dye, and R. Gleason. Fundamental role of axial stress in compensatory adapations by arteries. *Journal of Biomechanics*, 41(1):1–8, 2009.

[116] J. D. Humphrey. *Cardiovascular solid mechanics. Cells, tissues, and organs.* Springer-Verlag, New York, 2002.

[117] Junqueira and Carneiro. *Histologie.* Springer, 1991.

[118] P. Kalita and R. Schaefer. Mechanical models of artery walls. *Archive of Computational Methods in Engineering*, 15:1–36, 2008.

[119] G. Karypis, K. Schloegel, and V. Kumar. ParMETIS - Parallel graph partitioning and sparse matrix ordering. Version 3.1. Technical report, University of Minnesota, Department of Computer Science and Engineering, August 2003.

[120] D. Kiousis, T. Gasser, and G. Holzapfel. A numerical model to study the interaction of vascular stents with human atherosclerotic lesions. *Annals of Biomechanical Engineering*, 35:1857–1869, 2007.

[121] A. Klawonn. FETI domain decomposition methods for second order elliptic partial differential equations. *GAMM-Mitteilungen*, 29(2):319–341, 2006.

[122] A. Klawonn and O. Rheinbach. A parallel implementation of dual-primal FETI methods for three dimensional linear elasticity using a transformation of basis. *SIAM Journal on Scientific Computing*, 28(5):1886–1906, 2006.

[123] A. Klawonn and O. Rheinbach. Inexact FETI-DP methods. *International Journal for Numerical Methods in Engineering*, 69:284–307, 2007.

[124] A. Klawonn and O. Rheinbach. Highly scalable parallel domain decomposition methods with an application to biomechanics. *Zeitschrift für angewandte Mathematik und Mechanik*, (1):5–32, July 2010. doi: 10.1002/zamm.200900329.

[125] A. Klawonn and O. Widlund. Dual-primal FETI methods for linear elasticity. *Communications On Pure & Applied Mathematics*, 59:1523–1572, 2006.

[126] J. Klingensmith, E. Tuzcu, S. Nissen, and D. Vince. Validation of an automated system for luminal and medial-adventital border detection in three-dimnesional intravascular ultrasound. *International Jounral of Cardiovascular Imaging*, 19:93–104, 2003.

[127] S. Klinkel. *Theorie und Numerik eines Volumen-Schalen-Elementes bei finiten elastischen und plastischen Verzerrungen.* PhD thesis, Universität Fridericiana zu Karlsruhe, 2000.

[128] S. Klinkel and S. Govindjee. Using finite strain 3D-material models in beam and shell elements. *Engineering Computations*, 19(8):902–921, 2002.

[129] T. G. Kolda, R. M. Lewis, and V. Torczon. Optimization by direct search: new perspectives on some classical and modern methods. *SIAM Rev.*, 45(3):385–482 (electronic), 2003. ISSN 0036-1445.

[130] A. König and V. Klauss. Virtual histology. *Heart*, 93:977–982, 2007.

[131] J. Konrad, S. Zaefferer, and D. Raabe. Investigation of orientation gradients around a hard laves particle in a warm rolled Fe3Al-based alloy by a 3D EBSD-FIB technique. *Acta Materialia*, 54:1369–1380, 2006.

[132] J. K. Koo and G. Thomas. Thermal cycling treatments and microstructures for improved properties of Fe-0.12% C-0.5% Mn steels. *Material Science and Engineering*, 24:187–198, 1976.

[133] V. Kouznetsova. *Computational homogenization for the multi-scale analysis of multi-phase materials.* PhD thesis, Technische Universiteit Eindhoven, 2002.

[134] V. Kouznetsova, W. Brekelmans, and F. Baaijens. An approach to micro-macro modeling of heterogeneous materials. *Computational Mechanics*, 27:37–48, 2001.

[135] J. Kownatzki. 3D-Rekonstruktion einer Arterienverengung mittels biplanarer Angiographie und intravaskulären Ultraschall. Diplomarbeit, Fachbereich Mathematik, Universität Duisburg-Essen, 2008.

[136] E. Kröner. Allgemeine Kontinuumstheorie der Versetzung und Eigenspannung. *Archive of Rational Mechanics and Analysis*, 4:273–334, 1960.

[137] R. Krstić. *Human microscopic anatomy.* Springer, 1991.

[138] E. Lee. Elasto-plastic deformation at finite strains. *Journal of Applied Mechanics*, 36:1–6, 1969.

[139] J. Leung, A. Wright, N. Cheshire, J. Crane, S. Thom, A. Hughes, and Y. Xu. Fluid structure interaction of patient specific adbdominal aortic aneurysms: a comparison with solid stress models. *BioMedical Engineering OnLine*, 5(33):1–15, 2006.

[140] B. Lu and S. Torquato. Lineal-path function for random heterogeneous materials. *Physical Reviews A*, 45:922–929, 1992.

[141] M. M. Mäkelä and P. Neittaanmäki. *Nonsmooth Optimization: Analysis and Algorithms with Applications to Optimal Control.* World Scientific Publishing Co. Inc., 1992. ISBN 981-02-0773-5.

[142] J. Marsden and J. Hughes. *Mathematical Foundations of Elasticity.* Prentice-Hall, 1983.

[143] K. R. Mecke. Additivity, convexity, and beyond: Application of minkowski functionals in statistical physics. In K. R. Mecke and D. Stoyan, editors, *Statistical Physics and Spatial Statistics: The Art of Analyzing and Modeling Spatial Structures and Pattern Formation*, number 554 in Lecture Notes in Physics. Springer, 2000.

[144] K. R. Mecke and H. Buchert, T.and Wagner. Robust morphological measures for large-scale structure in the universe. *Astronomy & Astrophysics*, Vol. 288:697–704, 1994.

[145] J. Merodio and P. Neff. A note on tensile instabilities and loss of ellipticity for a fiber-reinforced nonlinearly elastic solid. *Archives of Mechanics*, 58:293–303, 2006.

[146] J. Merodio and R. Ogden. Instabilities and loss of ellipticity in fiber-reinforced compressible non-linearly elastic solids under plane deformation. *International Journal of Solids and Structures*, 40:4707–4727, 2003.

[147] C. Miehe. *Kanonische Modelle multiplikativer Elasto-Plastizität. Thermodynamische Formulierung und Numerische Implementation.* PhD thesis, Universität Hannover, Institut für Baumechanik und Numerische Mechanik, Bericht-Nr. F93/1, 1993. Habilitationsschrift.

[148] C. Miehe and E. Stein. A canonical model of multiplicative elasto-plasticity formulation and aspects of the numerical implementation. *European Journal of Mechanics, A/Solids*, 11:25–43, 1992.

[149] C. Miehe, J. Schotte, and J. Schröder. Computational micro-macro-transitions and overall moduli in the analysis of polycrystals at large strains. *Computational Materials Science*, 16:372–382, 1999.

[150] C. Miehe, J. Schröder, and J. Schotte. Computational homogenization analysis in finite plasticity. simulation of texture development in polycrystalline materials. *Computer Methods in Applied Mechanics and Engineering*, 171:387–418, 1999.

[151] C. Miehe, J. Schröder, and M. Becker. Computational homogenization analysis in finite elasticity: Material and structural instabilities on the micro- and macroscales of periodic composites and their interaction. *Computer Methods in Applied Mechanics and Engineering*, 191:4971–5005, 2002.

[152] M. Mooney. A theory of large elastic deformation. *Journal of Applied Physics*, 11: 582–592, 1940.

[153] B. Moran, M. Ortiz, and C. F. Shih. Formulation of implicit finite element methods for multiplicative finite deformationplasticity. *International Journal for Numerical Methods in Engineering*, 29:483–514, 1990.

[154] C. B. Morrey. Quasi–convexity and the lower semicontinuity of multiple integrals. *Pacific Journal of Mathematics*, 2:25–53, 1952.

[155] J. C. Nagtegaal, D. M. Parks, and J. R. Rice. On numerically accurate finite element solutions in the fully plastic range. *Computer Methods in Applied Mechanics and Engineering*, 4:152–177, 1974.

[156] A. Nair, B. D. Kuban, E. M. Tuzcu, P. Schoenhagen, S. E. Nissen, and D. G. Vince. Coronary plaque classification with intravascular ultrasound radiofrequency data analysis. *Circulation*, 106:2200–2206, 2002.

[157] A. Nair, M. Margolis, B. Kuban, and D. Vince. Autmated coronary plaque characterisation with intravascular ultrasound backscatter: ex vivo validation. *EuroIntervention*, 3:113–120, 2007.

[158] P. Neff. *Mathematische Analyse multiplikativer Viskoplastizität*. Ph.D. Thesis, Technische Universität Darmstadt, Shaker Verlag, ISBN:3-8265-7560-1, Aachen, 2000.

[159] J. A. Nelder and R. Mead. A simplex method for function minimization. *The Computer Journal*, 7:308–313, 1965.

[160] S. Nissen and P. Yock. Intravascular ultrasound: novel pathophysiological insights and current clinical applications. *Circulation*, 103:604–616, 2001.

[161] W. Noll. *The foundations of mechanics and thermodynamics*. Springer, 1974.

[162] E. Oñate and R. Owen, editors. *Computational Plasticity*, volume 7 of *Computational Methods in Applied Sciences*. Springer Verlag, 2 edition, 2007.

[163] M. O'Connell, S. Murthy, S. Phan, C. Xu, J. Buchanan, R. Spilker, R. Dalman, C. Zarins, W. Denk, and C. Taylor. The three-dimensional micro- and nanostructure of the aortic medial lamellar unit measured using 3d confocal & electron microscopy imaging. *Matrix Biology*, 27(3):171–181, 2008.

[164] H. Oettel and H. Schumann, editors. *Metallografie – mit einer Einfhrung in die Keramografie*. Wiley-VCH, 15 edition, 2011.

[165] R. W. Ogden. Large deformation isotropic elasticity: on the correlation of theory and experiment for incompressible rubber-like solids. *Proceedings of the Royal Society of London*, 326(1567):565–584, 1972.

[166] R. W. Ogden. Large deformation isotropic elasticity: on the correlation of theory and experiment for compressible rubber-like solids. *Proceedings of the Royal Society of London*, 328(1575):567–583, 1972.

[167] R. W. Ogden. *Non-linear elastic deformations*. Dover Publications, 1984.

[168] J. Ohser and F. Mücklich. *Statistical analysis of microstructures in materials science*. J Wiley & Sons, 2000.

[169] H. Oktay, T. Kang, J. Humphrey, and G. Bishop. Changes in the mechanical behavior of arteries following balloon angioplasty. asme 1991 biomechanics symposium, AMD-vol. 120. *American Society of Mechanical Engineers*, 120, 1991.

[170] M. Ostoja-Starzewski. The use, misuse, and abuse of stochastic random media. In *Proceedings of European Conference on Computational Mechanics*, 2001.

[171] T. Passerini, M. de Luca, L. Formaggia, A. Quarteroni, and A. Veneziani. A 3d/1d geometrical multiscale model of cerebral vasculature. *Journal of Engineering Mathematics*, 64:319–330, 2009.

[172] D. Patel and D. Fry. The elastic symmetry of arterla segments in dogs. *Circulation Research*, 24:1–8, 1969.

[173] E. Peña and M. Doblaré. An anisotropic pseudo-elastic approach for modelling mullins effect in fibrous biological materials. *Mechanics Research Communications*, 36(7):784–790, 2009.

[174] D. Peric, D. Owen, and M. Honnor. A model for finite strain elasto-plasticity based on logarithmic strains: Computational issues. *Computer Methods in Applied Mechanics and Engineering*, 94:35–61, 1992.

[175] G. Povirk. Incorporation of microstructural information into models of two-phase materials. *Acta Metallurgica*, 43/8:3199–3206, 1995.

[176] G. Prause, S. DeJong, C. McKay, and M. Sonka. Towards a geometrically correct 3-d reconstruction of tortuous coronary arteries based on biplane angiographiy and intravascular ultrasound. *International Journal of Cardic Imaging*, 13(6):451–462, 1997.

[177] A. Quarteroni and A. Valli. *Domain decomposition methods for partial differential equations*. Oxford Science, Oxford, 1999.

[178] A. Reuss. Berechnung der Fließgrenze von Mischkristallen aufgrund der Plastizitätsbedingung für Einkirstalle. *Zeitschrift für angewandte Mathematik und Mechanik*, 9:49–58, 1929.

[179] O. Rheinbach. *Parallel Scalable Iterative Substructuring: Robust Exact and Inexact FETI-DP Methods with Applications to Elasticity.* Phd thesis, University Duisburg-Essen, Fachbereich Mathematik, 2006.

[180] O. Rheinbach. Parallel iterative substructuring in structural mechanics. *Archive of Computational Methods in Engineering*, 16:425–463, 2009. ISSN 1134-3060.

[181] J. Rhodin. Architecture of the vessel wall. In D. Bohr, A. Somlyo, and J. H.V. Sparks, editors, *Handbook of Physiology*, chapter 2: The Cardiovascular System, Volume II: Vascular Smooth Muscle, pages 1–31. American Physiological Society, 1980.

[182] R. Rivlin. Further remarks on the stress–deformation relations for isotropic materials. *Archive for Rational Mechanics and Analysis*, 4:681–702, 1955.

[183] R. S. Rivlin. Large elastic deformations of isotropic materials II. Some uniqueness theorems for pure homogeneous deformation. *Philosophical Transactions of the Royal Society of London*, 240:491–508, 1948.

[184] M. Roach and A. Burton. The reason for the shape of distensibility curve of arteries. *Canadian jorunal of biochemistry and physiology*, 35(8):681–690, 1957.

[185] R. A. Robb. *Biomedical Imaging, Visualization and Analysis.* Wiley-Liss, Inc., 2000.

[186] R. Ross. The gordon wilson lecture: Atherosclerosis - a response to injury gone awry. *Transactions of the American Clinical and Climatological Association*, 93: 78–86, 1982.

[187] C. Roy. The elastic properties of the arterial wall. *Journal of Physiology*, 3:125–159, 1881.

[188] M. Sarwar and R. Priestner. Influence of ferrite-martensit mirostructural morphology on tensile properties of dual-phase steel. *Journal of Materials Science*, 31: 2091–2095, 1996.

[189] R. B. Schock. Intra-aortic balloon catheter having a collapsible variable diameter inner tube. Patent 6830559, Datascope Investment Corp., United States, 2004.

[190] H. Schramm and J. Zowe. A version of the bundle idea for minimizing a nonsmooth function: Conceptual idea, convergence analysis, numerical results. *SIAM Journal on Optimization 2*, 1(1):121–152, 1992. ISSN 1052-6234.

[191] J. Schröder. *Homogenisierungsmethoden der nichtlinearen Kontinuumsmechanik unter Beachtung von Instabilitäten.* Bericht aus der Forschungsreihe des Instituts für Mechanik (Bauwesen), Lehrstuhl I, Universität Stuttgart, 2000. Habilitationsschrift.

[192] J. Schröder. Anisotropic polyconvex energies. In J. Schröder and P. Neff, editors, *Poly-, Quasi- and Rank-One Convexity in Applied Mechanics*, number 516 in CISM Courses and Lectures, pages 53–105. Springer-Verlag, 2010.

[193] J. Schröder and P. Neff. Invariant formulation of hyperelastic transverse isotropy based on polyconvex free energy functions. *International Journal of Solids and Structures*, 40:401–445, 2003.

[194] J. Schröder and P. Neff, editors. *Poly-, Quasi- and Rank-One Convexity in Applied Mechanics*. Number 516 in CISM Courses and Lectures. Springer-Verlag, 2010.

[195] J. Schröder, D. Balzani, and D. Gross. Aspects of modeling and computer simulation of soft tissues: Applications to arterial walls. *Materialwissenschaft und Werkstofftechnik*, 36(12):795–801, 2005.

[196] J. Schröder, P. Neff, and D. Balzani. A variational approach for materially stable anisotropic hyperelasticity. *International Journal of Solids and Structures*, 42(15): 4352–4371, 2005.

[197] J. Schröder, D. Balzani, and D. Brands. Approximation of random microstructures by periodic statistically similar representative volume elements based on lineal-path functions. *Archive of Applied Mechanics*, 81(7):975–997, 2010. ISSN 0939-1533.

[198] B. Schultze-Jena. Über die schraubenförmige Struktur der Arterienwand. *Gegenbaurs Morpholigische Jahrbuch*, 83:230–246, 1939.

[199] I. Schur. *Vorlesungen über Invariantentheorie*. Springer-Verlag, Berlin, 1968.

[200] H. P. Schwefel. *Evolution and Optimum Seeking.* Wiley, 1996.

[201] B. Shekhonin, S. Domogatsky, V. Muzykantov, G. Idelson, and V. Rukosuev. Distribution of type i, iii, iv and v collagen in normal and artherosclerotic human arterial wall: Immunomorphological characteristics. *Collagen and Related Research*, 5:355–368, 1985.

[202] F. Silver, D. Christiansen, and C. Buntin. Mechanical properties of the aorta: A review. *Critical Reviews in Biomedical Engineering*, 17:323–358, 1989.

[203] F. Simo and R. Taylor. Quasi-incompressible finite elasticity in principal stretches. continuum basis and numerical algorithms. *Computer Methods in Applied Mechanics and Engineering*, 85(3):273–310, 1991.

[204] J. Simo. A framework for finite strain elastoplasticity based on maximum plastic dissipation and the multiplicative decomposition: Part i. continuum formulation. *Computer Methods in Applied Mechanics and Engineering*, 66:199–219, 1988.

[205] J. Simo. Algorithms for static and dynamic multiplicative plasticity that preserve the classical return mapping schemes of the infinitesimal theory. *Computer Methods in Applied Mechanics and Engineering*, 99:61–112, 1992.

[206] J. Simo. Numerical analysis and simulation of plasticity. In P. Ciarlet and J. Lions, editors, *Handbook of numerical analysis*, number 6. Elsevier Science, 1998.

[207] J. Simo and F. Armero. Geometrically non-linear enhanced strain mixed methods and the method of incompatible modes. *International Journal for Numerical Methods in Engineering*, 33:1413–1449, 1992.

[208] J. Simo and T. Hughes. *Computational Inelasticity.* Springer-Verlag., 1998.

[209] J. Simo, R. Taylor, and K. Pister. Variational and projection methods for the volume constraint in finite deformation elasto-plasticity. *Computer Methods in Applied Mechanics and Engineering*, 51:177–208, 1985.

[210] J. C. Simo, R. L. Taylor, and P. Wriggers. A note on finite-element implementation of pressure boundary loading. *Communications in Applied Numerical Methods*, 7: 513–525, 1991.

[211] R. Smit, W. Brekelmans, and H. Meijer. Prediction of the mechanical behavior of nonlinear heterogeneous systems by multi-level finite element modeling. *Computer Methods in Applied Mechanics and Engineering*, 155:181–192, 1998.

[212] G. Smith. On isotropic integrity bases. *Archive of Rational Mechanics and Analysis*, 18:282–292, 1965.

[213] G. Smith. On isotropic functions of symmetric tensors, skew-symmetric tensors and vectors. *International Journal of Engineering Science*, 9:899–916, 1971.

[214] G. F. Smith. On a fundamental error in two papers of C.-C. Wang "On representations for isotropic functions, Parts I and II". *Archive for Rational Mechanics and Analysis*, 36:161–165, 1970.

[215] M. Sonka, X. Zhang, M. Siebes, M. S. Bissing, S. C. DeJong, S. M. Collins, and C. R. McKay. Segmentation of intravascular ultrasound images: a knowledge-based approach. *Transactions on Medical Imaging*, 14(4):719–732, 1995.

[216] A. Spencer, editor. *Continuum theory of the mechanics of fibre-reinforced composites*. Number 282 in CISM Courses and Lectures. Springer-Verlag, Wien, 1984.

[217] A. J. M. Spencer. Theory of invariants. In A. Eringen, editor, *Continuum Physics*, volume 1, pages 239–353. Academic Press, 1971.

[218] J. Ståhlhand, A. Klarbring, and G. Holzapfel. Smooth muscle contraction: mechanochemical formulation for homogeneous finite strains. *Prog. Biophys. Molec. Biol.*, 96:465–481, 2008.

[219] J. Staubesand. Anatomie der Blutgefäße. I. Funktionelle Morphologie der Arterien, Venen und arterio-venösen Anastomosen. In M. Ratschow, editor, *Angiology*, chapter 2, pages 23–82. Thieme, Stuttgart, 1959.

[220] E. Stein and F.-J. Barthold. Elastizitätstheorie. In G. Mehlhorn, editor, *Der Ingenieurbau: Grundwissen*, number 4. Ernst and Sohn, 1996.

[221] M. Stroeven, H. Askes, and L. Sluys. A numerical approach to determine representative volumes for granular materials. In *Fifth World Congress on Computational Mechanics (WCCM V)*. Vienna University of Technology, 2002.

[222] P. M. Suquet. Local and global aspects in the mathematical theory of plasticity. In A. Sawczuk and G. Bianchi, editors, *Plasticity today: modelling, methods and applications*, pages 279–310. Elsevier, 1985.

[223] S. Tavares, P. Pedroza, J. Teodósio, and T. Gurova. Mechanical properties of a quenched and tempered duals phase steel. *Scripta Materialia*, 40(8):887–892, 1999.

[224] R. L. Taylor. FEAP - A Finite Element Analysis Program. Users manual, Structural Engineering, Mechanics and Materials, Department of Civil and Environmental Engineering, University of California, Berkeley, 2009. URL `http://www.ce.berkeley.edu/projects/feap/`. visited on 19. Mar. 2011.

[225] K. Terada and N. Kikuchi. Nonlinear homogenization method for practical applications. In S. Ghosh and M. Ostoja-Starzewski, editors, *Computational Methods in Micromechanics*, volume 212, pages 1–16. American Society of Mechanical Engineers, 1995.

[226] A.-K. Tielke. Sensitivity analysis of plaque components within arterial wall simulations based on patient specific data. Diplomarbeit, Institut für Mechanik, Universität Duisburg-Essen, 2009.

[227] S. Torquato. *Random heterogeneous materials. microstructure and macroscopic properties*. Springer, 2002.

[228] A. Toselli and O. B. Widlund. Domain Decomposition Methods – Algorithms and Theory. In *Springer Series in Computational Mathematics*, volume 34. Springer-Verlag, Berlin Heidelberg New York, 2005.

[229] C. Truesdell and W. Noll. Encyclopedia of physics. In S. Flügge, editor, *The nonlinear field theories of mechanics*. Springer, 1965.

[230] R. Vito and S. Dixon. Blood vessel constitutive models – 1995-2002. *Annual Review of Biomedical Engineering*, 5:413–439, 2003.

[231] W. Voigt. *Lehrbuch der Kristallphysik*. Teubner, 1966.

[232] M. Šilhavý. *The mechanics and thermodynamics of continuous media*. Springer, 1997.

[233] A. Wahle. Präzise dreidimensionale Rekonstruktion von Gefäßsystemen aus biplanen angiographischen projektionen und deren klinische anwendung. *VDI Fortschritt-Berichte. Reihe 17:Biotechnik*, 152, 1997.

[234] A. Wahle, E. Wellnhofer, I. Murgaragu, H. Sauer, H. Oswald, and E. Fleck. Assessment of diffuse coronary artery disease by quantitative analysis of coronary morphology based upon 3-d reconstruction from biplane angiograms. *IEEE Transactions on Meical Imaging*, 14:230–241, 1995.

[235] A. Wahle, G. Prause, S. DeJong, and M. Sonka. Geometrically correct 3d-reconstruction for Intravascular Ultrasound Images by fusion with biplane angiography - Methods and validation. *IEEE-Transactions on Medical Imaging.*, 87(98): 1–14, 1999.

[236] A. Wahle, G. Prause, C. von Birgelen, R. Erbel, and M. Sonka. Fusion of Angiography and Intravascular Ultrasound In-vivo: Establishing the Absolute 3d-Frame Orientation. *IEEE Transactions on Biomedical Engineering, special issue on Biomedical Data Fusion*, 46:1176–1180, 1999.

[237] B. Waller, C. Pinkerton, and J. Slack. Intravascular ultrasound: A histological study of vessels during life. The new "gold standard" for vascular imaging. *Circulation*, 85:2305–2310, 1992.

[238] C.-C. Wang. On a general representation theorem for constitutive relations. *Archive for Rational Mechanics and Analysis*, 33:1–25, 1969.

[239] C.-C. Wang. On representations for isotropic functions. Part I. Isotropic functions of symmetric tensors and vectors. *Archive for Rational Mechanics and Analysis*, 33: 249–267, 1969.

[240] C.-C. Wang. On representations for isotropic functions. Part II. Isotropic functions of skew-symmetric tensors, symmetric tensors, and vectors. *Archive for Rational Mechanics and Analysis*, 33:268–287, 1969.

[241] C.-C. Wang. A new representation theorem for isotropic functions: An answer to professor G. F. Smith's Criticism of my papers on representations for isotropic functions. Part 1. Scalar-valued isotropic functions. *Archive for Rational Mechanics and Analysis*, 36:166–197, 1970.

[242] C.-C. Wang. A new representation theorem for isotropic functions: An answer to professor G. F. Smith's Criticism of my papers on representations for isotropic functions. Part 2. Vector-valued isotropic functions, symmetric tensor-valued isotropic functions, and skew-symmetric tensor-valued isotropic functions. *Archive for Rational Mechanics and Analysis*, 36:198–223, 1970.

[243] C.-C. Wang. Corrigendum to my recent papers on "Representations for isotropic functions". *Archive for Rational Mechanics and Analysis*, 43:392–395, 1971.

[244] K. Washizu. On the variational principles of elasticity and plasticity. Technical Report 2518, Aeroelastic and Structures Research Laboratory, Massachusetts Institute of Technology, Cambridge, March 1955.

[245] K. Washizu. *Variational Methods in Elasticity and Plasticity.* Pergamon Press, Oxford, 2 edition, 1975.

[246] G. Weber and L. Anand. Finite deformation constitutive equations and a time integration procedure for isotropic, hyperelastic-viscoelastic solids. *Computer Methods in Applied Mechanics and Engineering*, 79:173–202, 1990.

[247] H. Weizsacker and P. Pinto. Isotropy and anisotropy of the arterial wall. *Journal of Biomechanics*, 21:477–487, 1988.

[248] H. Weyl. *The classical groups, their invariants and representation.* Princeton Univ. Press, Princeton, New Jersey, 1946.

[249] WHO. The top ten causes of death. Fact sheet 310, World Health Organization, 2008. URL `http://www.who.int/mediacentre/factsheets/fs310_2008.pdf`. visited on 7. Jan. 2011.

[250] H. Wienecke, D. Böse, M. Haude, H. Eggebrcht, T. Konorza, C. Naber, and R. Erbel. Koronare Stents - Von der Idee zum High-Tech-Implantat. *Medizinische Klinik*, 100: 505–511, 2005.

[251] B. Wolters, M. Rutten, G. Schurink, U. Kose, J. de Hart, and F. van de Vosse. A patient-specific computational model of fluid-structure interaction in adbdominal aortic aneurysms. *Medical Engineering and Physics*, 27:871–883, 2005.

[252] WorldAutoSteel. UltraLight Steel Auto Body - Advanced Vehivle Comcepts (ULSAB-AVC). Overview report, International Iron and Steel Institute, 2002. URL `http://www.worldautosteel.org/uploaded/ULSAB-AVC_Overview_Rpt.pdf`. visited on 14. June 2011.

[253] WorldAutoSteel. Advanced high strength steel (ahss) - application guidelines (version 4.1). Technical report, World Steel Association, June 2009. `http://www.worldautosteel.org/uploaded/AHSS 20Application 20Guidelines 204-1 20June 202009.pdf`, visited on 14. June 2011.

[254] P. Wriggers. *Nichtlineare Finite-Element-Methoden*. Springer-Verlag, Berlin, 2001.

[255] H. Xiao. On isotropic extension of anisotropic tensor functions. *Zeitschrift für angewandte Mathematik und Mechanik*, 76(4):205–214, 1996.

[256] S. Zaefferer, S. I. Wright, and D. Raabe. Three-dimensional orientation microscopy in a focused ion beam-scanning electron microscope: A new dimension of microstructure characterization. *Metallurgica and Materials Transactions A*, 39A:374–389, 2008.

[257] J. Zeman. *Analysis of Composite Materials with Random Microstructure*. PhD thesis, University of Prague, 2003.

[258] Q.-S. Zheng. Theory of representations for tensor functions – a unified invariant approach to constitutive equations. *Applied Mechanics Reviews*, 47:545–587, 1994.

[259] Q.-S. Zheng and A. J. M. Spencer. Tensors which characterize anisotropies. *International Journal of Engineering Science*, 31(5):679–693, 1993.

[260] O. Zienkiewicz and R. Taylor. *The finite element method – for solid and structural mechanics*. Elsevier, 6 edition, 2005.

[261] T. I. Zohdi and P. Wriggers. *An introduction to computational micromechanics*. Springer Verlag Berlin Heidelberg, 2008.

Der Lebenslauf ist in der Online-Version aus Gründen des Datenschutzes nicht enthalten.

In dieser Schriftenreihe bisher erschienene Berichte:

Nr. 1 (2004) *Ein Modell zur Beschreibung finiter anisotroper elasto-plastischer Deformationen unter Berücksichtigung diskreter Rissausbreitung*, J. Löblein, Dissertation, 2004.

Nr. 2 (2006) *Polyconvex Anisotropic Energies and Modeling of Damage applied to Arterial Walls*, D. Balzani, Dissertation, 2006.

Nr. 3 (2006) *Kontinuumsmechanische Modellierung ferroelektrischer Materialien im Rahmen der Invariatentheorie*, H. Romanowski, Dissertation, 2006.

Nr. 4 (2007) *Mehrskalen-Modellierung polykristalliner Ferroelektrika basierend auf diskreten Orientierungsverteilungsfunktionen*, I. Kurzhöfer, Dissertation, 2007.

Nr. 5 (2007) *Proceedings of the First Seminar on the Mechanics of Multifunctional Materials*, J. Schröder, D. Lupascu, D. Balzani (Ed.), Tagungsband, 2007.

Nr. 6 (2008) *Zur Modellierung und Simulation diskreter Rissausbreitungsvorgänge*, O. Hilgert, Dissertation, 2008.

Nr. 7 (2009) *Least-Squares Mixed Finite Elements for Solid Mechanics*, A. Schwarz, Dissertation, 2009.

Nr. 8 (2010) *Design of Polyconvex Energy Functions for All Anisotropy Classes*, V. Ebbing, Dissertation, 2010.

Nr. 9 (2012) *Modeling of Electro-Mechanically Coupled Materials on Multiple Scales*, M.-A. Keip, Dissertation, 2012.

Nr. 10 (2012) *Geometrical Modeling and Numerical Simulation of Heterogeneous Materials*, D. Brands, Dissertation, 2012.